Dedicated to the memory of Robert Bowman.
His science and friendship are missed.

Shasta Marrero
New Mexico Institute of Mining and Technology
August, 2012

Calibration of Cosmogenic Chlorine-36

by

Shasta Marrero

Submitted in Partial Fulfillment
of the Requirements for the Degree of
Doctor of Philosophy in Earth & Environmental Science
with Specialty in Hydrology

New Mexico Institute of Mining and Technology
Socorro, New Mexico
August, 2012

ABSTRACT

The CRONUS-Earth Project is designed to improve upon the general knowledge of cosmogenic systematics and to provide the cosmogenic user community with a uniform platform for use and interpretation of all cosmogenic nuclides. Geological calibrations for all the commonly used nuclides are part of the CRONUS-Earth Project. This work focuses on the geological calibration of chlorine-36 as well as the detailed description of the CRONUScalc program, which was designed to perform cosmogenic nuclide calculations.

As cosmogenic nuclide applications continue to expand, the need for a common basis for calculation becomes increasingly important. In order to accurately compare between results from different nuclides, a single method of calculation is necessary. Currently, calculators exist for each nuclide independently (or the Al/Be pair), but these calculators are independent and the assumptions and implementation of details are not consistent among them. A new program, CRONUScalc, is presented here. This unified code presents the first method applicable to all the commonly used cosmogenic nuclides (^{10}Be, ^{26}Al, ^{36}Cl, ^{3}He, and ^{14}C). The base code predicts the concentration of a sample at a particular depth for a particular time in the past. This versatile code can be used for many applications; the code already includes scripts for calculating surface exposure age for a single sample or for a depth profile containing multiple samples. The code is available under the general public license agreement and can be downloaded and modified by advanced users to deal with specific atypical scenarios.

Chlorine-36 is a versatile cosmogenic nuclide, but has been plagued by conflicting production rates from different geological calibration studies (Phillips et al., 2001; Swanson and Caffee, 2001; Evans et al., 1997; Stone et al., 1996). The CRONUS geological calibration of chlorine-36 is an important part of achieving consistency within the cosmogenic community. The CRONUS-Earth Project has provided high-quality geological calibration sites, including Lake Bonneville, Peru, Scotland, and Copper Canyon, for a large-scale calibration of chlorine-36.

The Lake Bonneville geological calibration site is actually two individual sites that share most of the same radiocarbon chronology. The two sites are the Tabernacle Hill basalt and the Promontory Point quartzite. Both sites share the constraint of a very large, well-dated flood event. Tabernacle Hill chlorine-36 data from plagioclase mineral separates provides a consistent dataset for calcium spallation calibration. While the whole-rock samples are more scattered, the datasets are consistent across three labs and are used to calibrate the $P_f(0)$ parameter. Of all the chlorine-36 datasets from Tabernacle Hill, the mineral separates also agree best with the ages produced by helium-3 analyses of the same samples.

The Huancané geological calibration site is located high in the Peruvian Andes in the southeastern portion of Peru. As the Quelccaya ice cap advanced and retreated, boulders in the valley were plucked and redeposited with other material from the valley as moraines. Cores from boggy areas in proximity to the moraines have provided bracketing radiocarbon ages for the ice cap advances. The Huancané potassium mineral-separate data provides valuable information for chlorine-36 production rate calibration from a low latitude, high elevation site. An offset between chlorine-36 labs is unfortunate and is likely due to differing processing techniques. The UW mineral separate data was used in the final

chlorine-36 production rate calibration. The comparison between chlorine-36 and beryllium-10 data at the Huancané site generally indicates that the beryllium-10 data produces more precise results than the chlorine-36 data. However, the consistency of the beryllium data, despite varying boulder heights, confirms that there should be no problems with snow corrections, exhumation, or other shielding issues at the Huancané site.

At the Scotland site, two main areas were sampled: the Isle of Skye and the Scottish highlands. We sampled at several locations on the Isle of Skye, including the Red Cuillins, the Black Cuillins, and Kyleakin Pass. Other samples were collected on the mainland in the Scottish highlands. The CRONUS sites were chosen to be correlative with the deglaciation from the Loch Lomond Readvance. The CRONUS-Earth data from the Scotland sites are generally internally consistent. Of the 31 beryllium, 18 aluminum, 4 chlorine, and 16 carbon points, only one Be and one Al point were removed as outliers. Other than carbon, the ages calculated for all the samples using the final CRONUS calibrated production rates are consistent, with most ages overlapping within uncertainty of each other and the independent age bounds. These calibration sites, focusing on rock avalanches and scoured bedrock associated with the deglaciation at the end of the Loch Lomond readvance, provide key locations for the calibration of all the nuclides in the CRONUS project. The location at high latitude and low elevation provides a valuable point because it should be essentially independent of the scaling model used.

The Copper Canyon samples were collected from a quartz vein hosted in limestone located in the Magdalena mountains in New Mexico. The Copper Canyon site, which had many complicating factors that did not appear until later

in the study, produced a $P_f(0)$ value of 678 $\pm$ 54 n $g^{-1}yr^{-1}$. Uncertainties due to blank subtractions, water content, varying composition, and inconsistent data points contributed to the decision to classify this as a secondary site. Sensitivity studies based on the factors listed above produce values of $P_f(0)$ that vary by up to 50% compared to the nominal value of 678 n $g^{-1}yr^{-1}$. The nominal value is consistent with the value of $P_f(0)$ found as part of the main chlorine-36 CRONUS-Earth calibration presented here. Copper Canyon is not a primary chlorine-36 calibration site, but provides insight into the chlorine-36 $P_f(0)$ parameter.

Three primary sites, Lake Bonneville, Peru, and Scotland, were used to calibrate the spallation pathways (K and Ca) for chlorine-36 production yielding production rates of 56.0 $\pm$ 2.2 at ^{36}Cl (g Ca)$^{-1}yr^{-1}$ for Ca spallation and 157 $\pm$ 6 at ^{36}Cl (g K)$^{-1}yr^{-1}$ for potassium spallation. The third major production rate parameter for the low-energy production pathway, $P_f(0)$, was calibrated separately using secondary CRONUS-Earth data from the Bonneville and Baboon Lakes sites and yielded a value of 704 $\pm$ 141 n (g air)$^{-1}yr^{-1}$. There was significant uncertainty associated with the third pathway due to the presence of site-to-site variability and possible factors to explain this are discussed in detail.

The resampling of the Puget Lowlands site allowed for the analysis of samples comparable to those presented in Swanson and Caffee (2001). The new analyses, performed by two different labs, are consistent with the calibrated production rates produced in this study and are therefore not consistent with the previously published rates in Swanson and Caffee (2001). The most likely source for this discrepancy is a systematic analytical problem with the original samples.

The chlorine-36 calibration uses the CRONUScalc program, an open-source multi-nuclide Matlab program that helps with the interpretation of cosmogenic

nuclide results, to produce the results. Chlorine-36 muon production rate parameters consistent with the code were recalculated from published profiles for both Ca and K. The minimum uncertainty on the chlorine-36 technique was assessed independently for the spallation and $P_f(0)$ calibrations using a secondary dataset with independent ages. The goodness of fit for the spallation calibration is reported as well. The uncertainty associated with the chlorine-36 technique is assessed using a combination of analytical uncertainty and the scatter in the secondary dataset when the dataset is aged using the final parameters.

Keywords: Cosmogenic nuclide; chlorine-36; calibration

ACKNOWLEDGMENTS

One of the main things I learned while working on my dissertation is that collaboration on scientific projects is important. I could not have completed my dissertation without the help of many amazingly talented people.

Thanks to my advisor, Fred Phillips, for his unending support and patience, and helping me to become a scientist. The rest of my committee, including Nelia Dunbar, Bruce Harrison, Andy Campbell, and John Stone (University of Washington), has encouraged me as well and I thank you all for your practical outlook and advice.

The CRONUS-Earth Project not only funded my MS and PhD work, but provided an incredible opportunity to collaborate with and learn from all the experts in the cosmogenic nuclide field. I would like to thank all the CRONUS-Earth collaborators who helped in various ways throughout the project especially John Stone, Nat Lifton, Meredith Kelly, Brian Borchers, Michelle Hinz, Rob Aumer, Adam Hudson, and Lisa Majkowski-Taylor. I would also like to thank Tom Vogel at Michigan State for working with me on XRF rush orders and special requests.

Many thanks to the entire NMT/E&ES community, especially Nelia Dunbar & Lynn Heizler for their microprobe expertise, Bill McIntosh for his advice on mineral separation and the loan of a paleomag drill, and Pat, Leigh, and other office people for helping me to navigate campus paperwork. A huge thanks to

my lab assistants, especially Natalie Earthman, who helped me keep up on the unending pile of samples and dishes. After the lab work is done, writing becomes life and I would not have made it through without my writing group, Laura & Amy.

Thanks to my parents and grandparents for their support, despite the fact that they weren't always completely sure what I was working on. Thanks to my younger sister for the moral support. I was so happy to be able to share a PhD experience with her, despite the fact that she defended her PhD 13 days before me! Finally, thanks to my husband, Nico, for cooking meals and doing dishes for the last six months as well as his unwavering support in every other way.

"All is well that ends eventually..."

-Nico Marrero

This dissertation was typeset with LaTeX[1] by the author.

[1]The LaTeX document preparation system was developed by Leslie Lamport as a special version of Donald Knuth's TeX program for computer typesetting. TeX is a trademark of the American Mathematical Society. The LaTeX macro package for the New Mexico Institute of Mining and Technology dissertation format was written for the Tech Computer Center by John W. Shipman.

CONTENTS

LIST OF TABLES

LIST OF FIGURES

This dissertation is accepted on behalf of the faculty of the Institute by the following committee:

Fred M Phillips, Advisor

I release this document to the New Mexico Institute of Mining and Technology.

Shasta Marrero Date

CHAPTER 1

INTRODUCTION

1.1 Introduction and Motivation

In-situ terrestrially produced cosmogenic nuclides are becoming commonplace tools in an increasing number of applications in scientific fields, including geomorphology and geochronology. In geomorphology, cosmogenic nuclides can be used to investigate the mechanisms and rates of formation or degradation of features in the landscape, specifically erosion rate and landform evolution. For geochronology, cosmogenic nuclides can provide dates on surfaces that cannot be dated by traditional means (i.e. carbon-14 dating), dating fault scarps, or looking at events indicating climate change (i.e. glacial sequences) that could have significant impacts on society.

Despite the widespread use of cosmogenic nuclides, there are still significant inconsistencies in the field that typically stem from the lack of a coherent system for the processing and interpretation of cosmogenic nuclides. The NSF-funded CRONUS-Earth (Cosmic-Ray prOduced NUclide Systematics on Earth) project is designed to address differences in the systematics of cosmogenic nuclides and provide the cosmogenic user community with a uniform platform for use and interpretation of all cosmogenic nuclides. My role in this project was to provide raw chlorine-36 sample data for a set of calibration sites, produce production rate parameters for chlorine-36 in conjunction with other researchers, and to

co-write the Matlab code used to do cosmogenic nuclide calculations for ^{36}Cl and for other nuclides.

Cosmic-ray interactions with minerals at the earth's surface produce in-situ cosmogenic nuclides. These surfaces can be dated and used to investigate processes in the natural world, assuming the production rates of the nuclides are also known. The production of cosmogenic nuclides is dependent on the sample position and orientation in space (i.e., coordinates and dip/direction of dip of the sample) and the original incoming cosmic-ray flux, which varies over space and time (Gosse and Phillips, 2001). The production also decreases with increasing depth in the sample material due to attenuation of the cosmic-ray flux through interactions with matter. The interaction of neutrons with minerals produces cosmogenic nuclides through several types of reactions. The most common reaction is spallation, which is defined for these purposes as an energetic reaction where a target nucleus is bombarded by an incoming cosmic-ray particle (commonly a neutron) resulting in lighter nucleus and other byproducts (Dunai, 2010). Another reaction is the interaction of a muon with the target nucleus to produce a cosmogenic nuclide (Heisinger et al., 2002b,a). A third type of reaction is the absorption of a low-energy neutron by a nucleus (Phillips et al., 2001), which is only relevant for cosmogenic nuclides in the production of chlorine-36 and helium-3 (and also calcium-41). The production rate of this pathway for chlorine-36 is calibrated with the parameter $P_f(0)$, defined in detail in Section 2.4.2.

The relationship between total production and depth can be nearly exponential for some nuclides, such as beryllium-10, or significantly more complex, as for chlorine-36. Cosmogenic beryllium-10 is produced through spallation and muon absorption in a single mineral, leading to an almost-exponential decrease

in production with depth. For chlorine-36, the significant production mechanisms and targets are more complex and include four different spallation reactions (target nuclei: Ca, K, Ti, Fe), low-energy neutron capture by chlorine-35, and muon capture by two elements (target nuclei: Ca, K). The large number and type of reactions forming chlorine-36 leads to a complicated production scenario that is intimately linked to the composition of a sample. Although all of these variables are generally accounted for in the current modeling of chlorine-36 systematics, there is still significant work remaining to improve upon the current understanding of this technique.

Chlorine-36 is unique among the cosmogenic nuclides because of its versatility. Beryllium-10 and aluminum-26, for example, require pure quartz separates in order to determine surface-exposure ages. Chlorine-36, on the other hand, can be measured either in whole-rock samples or in any mineral phase with sufficient amounts of potassium, calcium, or chlorine. This technique also allows limestone surface exposure age dating, which is impossible using other cosmogenic nuclides. The typical applicable age range of chlorine-36 is between 5 ka and 500 ka. This range covers a gap in dating techniques where features are too old for radiocarbon and too young for argon dating. The above-mentioned qualities make chlorine-36 a worthwhile tool for earth scientists. One way that this valuable tool could be improved is by increasing the accuracy of chlorine-36 dating techniques and providing this information to the user community.

Geological calibration studies on chlorine-36 production rate parameters date back to 1986 (Phillips et al., 1986) and have been continually revisited as new calibration locations, techniques, or models become available. The published geological calibration studies on chlorine-36 production rates are summarized in

Table 1.1, with the discrepancies between the resulting production rates shown graphically in figure 1.1. Ideally, the production rates for each pathway would be in agreement with the production rates calibrated by other researchers. However, it is clear that there are significant discrepancies, ranging up to 40% in some cases, within each of the pathways. Unfortunately, the lack of agreement among previously published chlorine-36 production rates discourages wider use of the technique. The discrepancies between the rates have been attributed to many factors including mineralogy/composition (Evans, 2001), scaling (Swanson and Caffee, 2001), independent age constraints (Gosse and Phillips, 2001; Swanson and Caffee, 2001), preparation methods (Gosse and Phillips, 2001; Schimmelpfennig et al., 2009), differences in partitioning chlorine-36 between pathways (Licciardi et al., 2008; Schimmelpfennig et al., 2009), or new technological methods (Marrero, 2009), among others. Despite the numerous possibilities for the source of the discrepancies, there is no consensus on the underlying cause(s).

Regardless of the source of the discrepancies, the differences in published production rate parameters limit the applicability of the technique. Until the discrepancy is resolved, advances of the chlorine-36 technique, and the fields that use it, will be hindered. In an attempt to determine the sources of the problems in previous calibrations and obtain accurate production rate parameters, a new calibration was designed that addressed as many of the proposed discrepancy sources as possible.

1.2 Improvements in this Calibration

This calibration is designed to address as many of the previously cited issues for the chlorine-36 production rate discrepancy as possible. The improve-

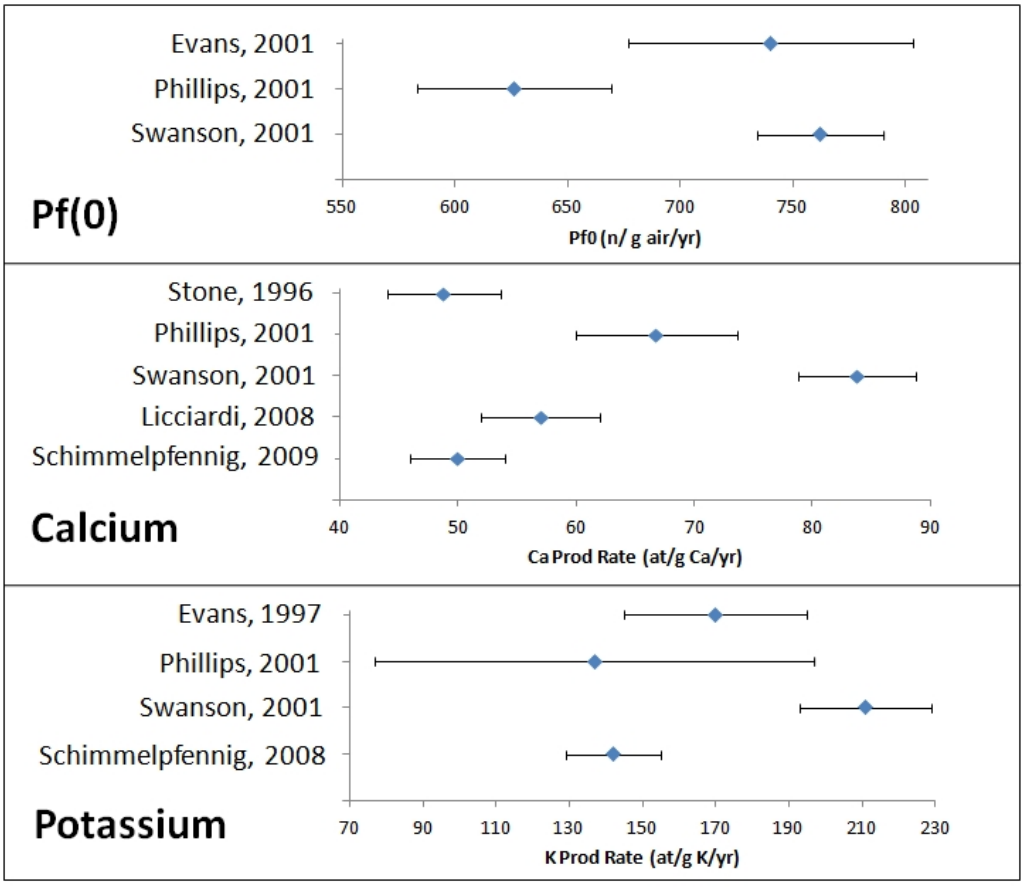

Figure 1.1: Graphical comparison of Ca, K, and $P_f(0)$ production rates from previously published geological calibration studies. References are abbreviated. Full references are as follows: Evans (2001); Phillips et al. (2001); Swanson and Caffee (2001); Stone et al. (1996); Licciardi et al. (2008); Schimmelpfennig et al. (2009); Schimmelpfennig (2009); Evans et al. (1997).

Source	Location	Landform	h	Lat	Age	Meth.	Ψ
Phillips et al. (2001)	Utah	Basalt Flow	1445	39°N	16.5	WR	Ca: 66.8 ± 6.8
	Idaho	Basalt flow	1367-1798	44°N	2.1-13.7		
	New Mexico	Basalt flow	2058-2578	35°N	3-18.2		K: 137 ± 60
	Wales	Boulder on beach	375	52 °N	11.8		
	Ellesmere Island	Glacial erratic boulder	80-100	80°N	9		$P_f(0)$: 626 ± 43
	Northwest Territories	Glacial polished bedrock	20	68°N	14.8		
	Arizona	Meteor Crater ejecta	1730	35°N	49		
Evans et al. (1997)	Sierra Nevada	Glacial bedrock	3000-3600	38°N	13.1	MS	K: 170 ± 25
	Scotland	Glacial bedrock	520	58°N	11.6		
	Antarctica	Bedrock	2000-2200	70°S	SS		K: 241 ± 9
Stone et al. (1996)	Utah	Basalt flow	1445	39 °N	17.3	MS	Ca: 48.8 ± 4.8
Evans (2001)	Scotland	Glacial bedrock	520	58 °N	11.6	MS	$P_f(0)$: 740 ± 63
Swanson and Caffee (2001)	WA state	Moraine boulders and glacial bedrock	10-140	48°N	15.5	WR	Ca: *91 ± 5; K: *228 ± 18; $P_f(0)$: 762 ± 28
Licciardi et al. (2008)	Iceland	Basalt flow	30-500	64 °N	4-10	WR	Ca: 57 ± 5
Schimmelpfennig (2009)	Sicily	Basalt flow	2000	38°N	10	MS	Ca: 50 ± 4
	Argentina	Basalt flow	2300-2500	36 °S	15		K: 142 ± 13

Table 1.1: Summary of previous chlorine-36 calibration studies. h indicates the elevation in meters. Method is the method used to prepare the samples: WR indicates whole rock samples and MS indicates mineral separates. $P_{\mathrm{m,k}}$ is the production rate for nuclide m from target k as calibrated from the study (as published). All studies shown here used Lal (1991) scaling. *Indicates that the production rate includes muons. Units for Ca are atoms (g Ca)$^{-1}$ yr^{-1}, K are atoms (g K)$^{-1}$ yr^{-1}, and $P_f(0)$ are fast neutrons (g air)$^{-1}$ yr^{-1}.

ments to this calibration as compared to previous calibrations includes the expansion of the latitude/elevation range, the better independent age constraints on the site, and the use of both mineral separates and whole rock samples.

A brief summary of the pertinent information for the CRONUS-Earth chlorine-36 sites is shown in Table 1.2. The CRONUS sites have the advantage of representing a large range of altitudes (300-4900 m above sea level), lithologies (examples include basalt, quartz, and granite), and latitudes (14°S and 34-57°N). Previous studies had a smaller range of latitudes and elevations than those represented in this study, as shown in figure 1.3. Mainly, the addition of the low latitude, high elevation site is critical to this calibration. This increased range of latitude and elevation helps to discriminate between the possible scaling models, as discussed in Section 2.6.

The age range at many of the calibration sites is limited to the range appropriate for radiocarbon dating, which provides critical constraints on the calibration. Therefore, for each site listed above, there will be an individual examination of each limiting age based on the available radiocarbon dates. These limiting ages will ultimately determine, to some extent, the uncertainties placed on the final production rate parameters through the uncertainties determined using the orthogonal distance regression method, discussed in the methods chapter, Chapter 3.

The compositions of the rocks chosen for this calibration also have particular importance. Production must be constrained for each main production pathway (spallation from Ca, spallation from K, and neutron activation on Cl), so the rocks must contain the target elements, preferably with negligible contributions from the other pathways. The ternary diagram in Figure 1.4 shows the

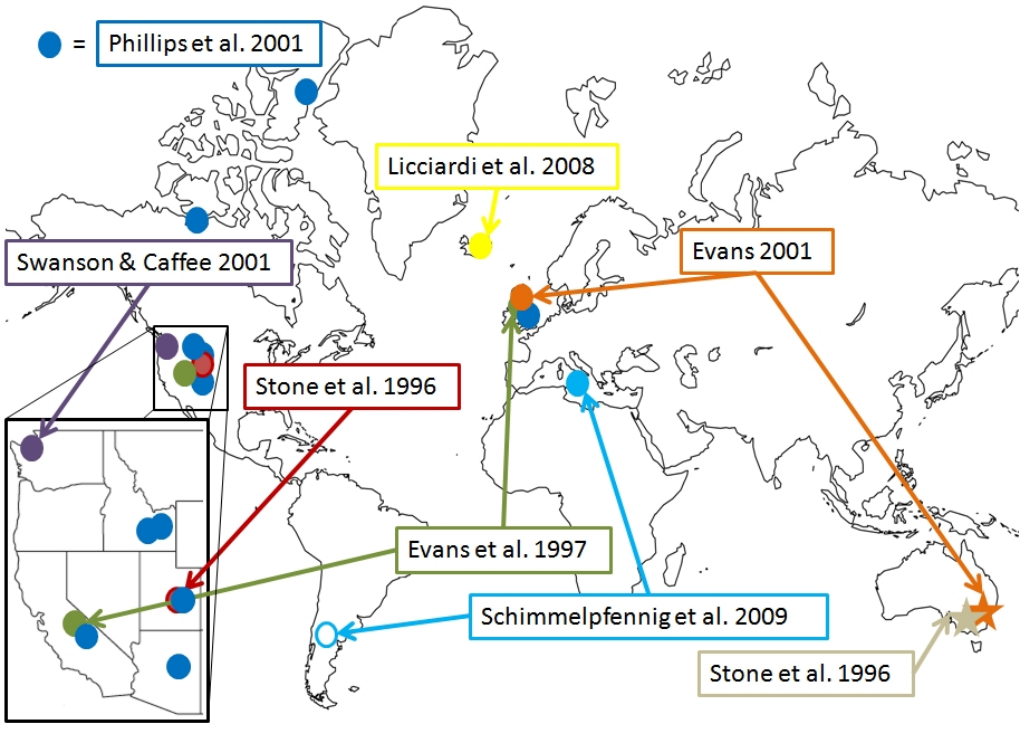

Figure 1.2: Map showing locations of all the previous chlorine-36 calibration locations (color-coded to correspond with the reference label). The inset shows all the studies in the western US. Sites indicated by stars are muon calibration locations. The open circle indicates that the study was performed by the author, but only published in a dissertation and not the final publication.

Site Name	Chapter	Landform	Lithology	Elev [m]	Lat	Age [ka]	Path
Tabernacle Hill, UT	4	Basalt Flow	Basalt	1460	39°N	18.2	Ca, Cl
Scotland	5	Rock Avalanche	Gabbro, granite	300	57°N	11.7	K, Ca
Huancané, Peru	6	Moraine	Rhyolite tuff	4900	14°S	12.32	K, Cl
Copper Canyon, NM	7	SS Profile	Quartz	2200	34°N	SS	Cl

Table 1.2: CRONUS-Earth chlorine-36 primary calibration site summary. Chapter refers to the chapter number in the dissertation where the site is discussed in detail. 'Elev' is the elevation, 'Lat' is the latitude, and 'Path' refers to the production pathways that were possible at each site based on lithology. 'SS' indicates that the site is at steady-state.

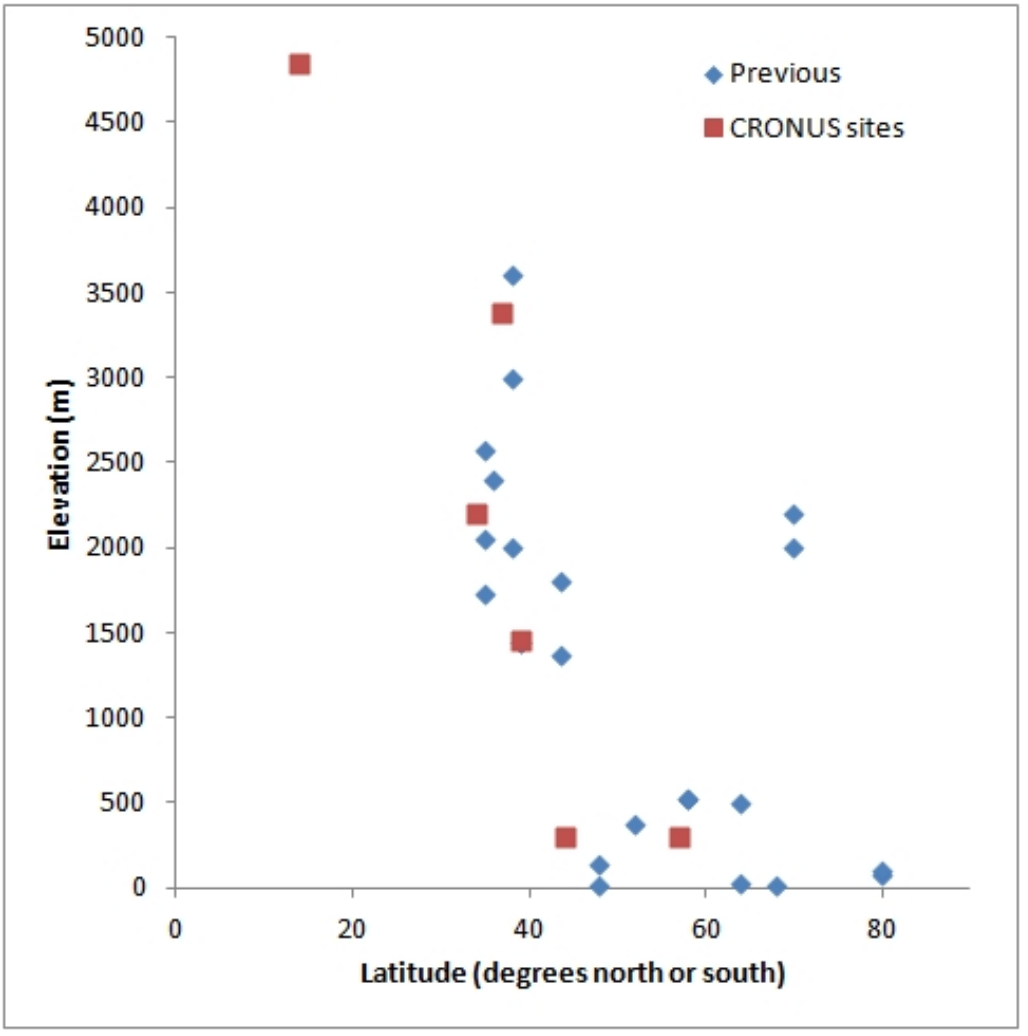

Figure 1.3: Plot showing latitude and elevation for the previously published calibrations and the CRONUS-Earth sites. The figure includes both primary and secondary CRONUS-Earth sites.

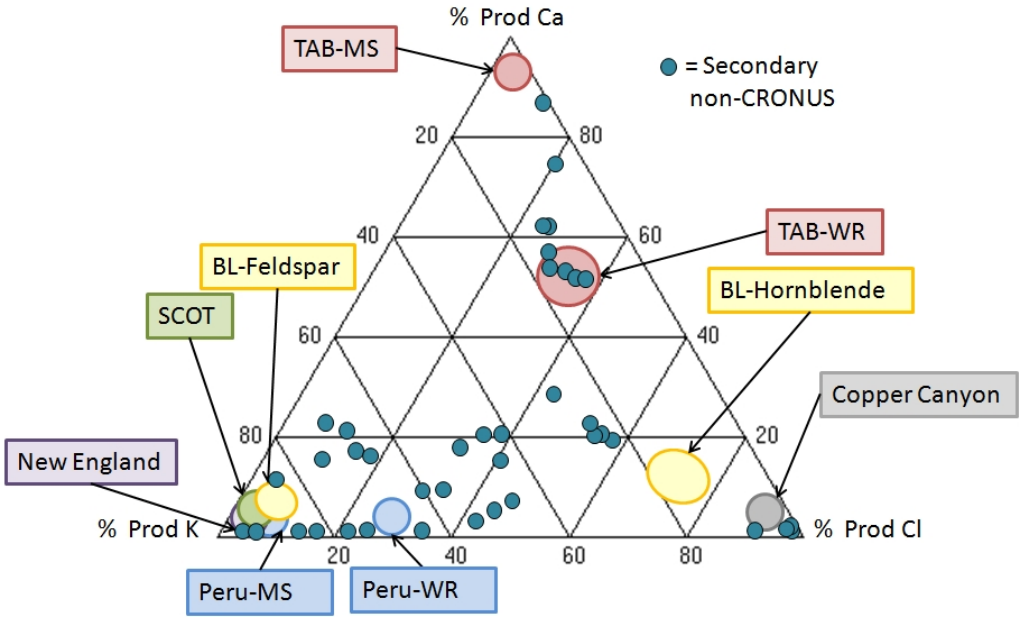

Figure 1.4: Ternary diagram showing the CRONUS-Earth sample compositions. The figure includes both primary and secondary CRONUS-Earth data. Secondary non-CRONUS sites are shown as unlabeled smaller blue circles. Abbreviations refer to the site: TAB - Tabernacle Hill, UT; BL - Baboon Lakes, CA; Peru - Huancané, Peru; SCOT - Isle of Skye and Scottish Highlands, Scotland; New England - Littleton-Bethlehem moraine; Copper Canyon - Copper Canyon, NM. Additional abbreviations refer to the composition of the samples: MS - plagioclase or feldspar mineral separates; WR - whole rock.

percent production from each main pathway for each calibration site. On this diagram, the best calibration samples will plot in the corners of the diagram where production from a pathway is isolated from that of other target elements. Ideally, there would be at least three sites for each pathway; however, the high-quality CRONUS sites were limited in number. CRONUS-Earth chlorine-36 secondary sites, those not used in the calibration but used for comparison purposes, are also shown on the diagram.

1.3 Calibration Organization

The production of robust chlorine-36 production rate parameters is the main goal of the CRONUS-Earth chlorine-36 calibration effort. Using Ca and K spallation-dominated sample data from the high-quality sites selected by the CRONUS-Earth committee, the spallation calibration produces relatively robust results for the production rates. The calibration of the $P_f(0)$ parameter is a more complicated issue than the calibration of spallation production rates. The $P_f(0)$ calibration included the Copper Canyon site, designed to calibrate the $P_f(0)$ value using a depth profile and using measurements of both chlorine-36 and beryllium-10. The list of CRONUS-Earth sites is relatively small, so additional published datasets were incorporated into a secondary dataset in order to test the calibrated parameters and realistically assess the uncertainty of the technique.

A significant portion of the 40% discrepancy between the production rates can by credited to a single study, Swanson and Caffee (2001), that produced very discrepant production rates when compared to all other chlorine-36 production rate calibrations. If the Swanson and Caffee (2001) study is eliminated from the list of valid chlorine-36 calibrations, the discrepancy among the previous calibrations is reduced to only 27%, at most. Part of the goal of the CRONUS-Earth project was to return to the Puget Sound locality and collect samples from the same or similar boulders as those sampled by Swanson and Caffee (2001) in order to either reproduce the results or else determine what caused the discrepancy. The reanalysis of samples representative of the Swanson and Caffee (2001) is an important goal of the project, despite the fact that this is only a secondary goal.

A sensitivity analysis for chlorine-36 helped to identify the most influential input parameters. This provided information on the magnitude of uncertainties

necessary for the current calibration samples. While this exercise only provided minimum uncertainties for a particular sample, it was still useful to determine which parameters have the largest influence on the sample age. Additionally, this identified which parameters may warrant further investigation to reduce uncertainties on future samples.

The final results of the calibration are being incorporated into the CRONUScalc program, a multi-nuclide, modular Matlab code that allows for the prediction of concentrations in samples, calibration, and surface exposure age calculation for both surface samples and multi-sample depth profiles. The CRONUScalc code is the underlying code used to run a suite of online exposure age calculators. The final chlorine-36 production rates will be used in the chlorine-36 online calculator. These production rates, in addition to those produced for other nuclides, are immediately available to the cosmogenic user community through the online calculator.

1.4 Dissertation Organization

This dissertation is centered around a single, large-scale chlorine-36 calibration. Due to the nature of the work, there are numerous independent sites that need to be discussed individually as well as other small projects that are included in the dissertation. In Chapter 2, I address the background material necessary to understand cosmogenic nuclides by describing the theory and equations that are used in the CRONUScalc program. The methods used during this investigation, including the laboratory, field, and mathematical modeling methods for the project, are discussed in Chapter 3.

Each main site used for chlorine-36 calibration is discussed in a separate chapter. Each chapter includes sections on the geologic history, the radiocarbon or other age constraints, the site characteristics that make it desirable for this study, and the presentation of the site results. The site chapters include Lake Bonneville, UT (Chapter 4); Scotland (Chapter 5); Huancané, Peru (Chapter 6); and Copper Canyon, NM (Chapter 7).

The final chapter, Chapter 8, brings all of the information together to discuss the full chlorine-36 calibration. This chapter presents the combined results of all the sites as final production rates. There is a lengthy discussion of the calibration of the $P_f(0)$ production rate parameter and the factors affecting that calibration that are not applicable to the other pathways. The discussion of the results for the project to resample and compare to the Swanson and Caffee (2001), a input parameter sensitivity analysis, and a comparison of the ratios of chlorine:beryllium in identical samples is discussed in this chapter as well. The end of the calibration chapter includes sections on future work and conclusions for the entire dissertation.

There are many figures concerning the aging of cosmogenic samples presented in the chapters discussed above. In all cases, the sample ages are shown with error bars representing the one-sigma uncertainty. The depicted uncertainty accounts for only the propagated uncertainties on input parameters and does not include other factors, such as uncertainties due to the production rate parameters or scaling. All chlorine-36 sample ages are presented in this way unless otherwise stated.

CHAPTER 2

COSMOGENIC NUCLIDE SYSTEMATICS AND THE CRONUSCALC PROGRAM

2.1 Abstract

As cosmogenic nuclide applications continue to expand, the need for a common basis for calculation becomes increasingly important. In order to accurately compare between results from different nuclides, a single method of calculation is necessary. Currently, calculators exist for each nuclide independently (or the Al/Be pair), but these calculators are independent and the assumptions and implementation of details are not consistent among them. A new program, CRONUScalc, is presented here. This unified code presents the first method applicable to all the commonly used cosmogenic nuclides (^{10}Be, ^{26}Al, ^{36}Cl, ^{3}He, and ^{14}C). The base code predicts the concentration of a sample at a particular depth for a particular time in the past. This versatile code can be used for many applications; the code already includes scripts for calculating surface exposure age for a single sample or for a depth profile containing multiple samples. The code is available under the general public license agreement and can be downloaded and modified by advanced users to deal with specific atypical scenarios.

Note: This chapter is designed to be submitted for publication and several sections have been written by coauthors (Brian Borchers and Rob Aumer).

2.2 Introduction

The CRONUS-Earth Project is an NSF-funded project intended to improve many aspects of cosmogenic isotope use and help create a consistent, accurate use of the technique within the community. One important part of that project is the creation of a code that can consistently perform necessary calculations for different scaling schemes and that is applicable to all the commonly used nuclides (^{10}Be, ^{26}Al, ^{36}Cl, ^{3}He, ^{14}C). The program presented here, called CRONUScalc, is a joint effort by the CRONUS project to address the problems in previous codes. This calculator directly incorporates much of format and function of the Al/Be code written by Balco et al. (2008), but it extends the functionality beyond Al/Be as well as reworking some parts of the original code. The new CRONUScalc code keeps the original modular format, but has updated the code with functions to do production/accumulation calculations, calibrations, and surface and depth profile exposure ages.

Previous calculators have been created for ^{36}Cl (Phillips and Plummer, 1996; Schimmelpfennig et al., 2008), ^{3}He (Goehring et al., 2010b), and ^{10}Be/^{26}Al (Balco et al., 2008), and others (Dunne et al., 1996; Vermeesch, 2007). In each of these cases, the calculator was valid for up to two nuclides and the range of functionality (scaling and other assumptions) varied among the different implementations, leading to significant inconsistencies between nuclides. CRONUScalc is modularized so that nuclide-independent factors are calculated using the same code, which provides consistent results for all nuclides.

The base code of CRONUScalc predicts the cosmogenic nuclide concentration in a sample (of either finite or point thickness) at a given depth at a particular

time in the past. This function allows great versatility in earth science applications. CRONUScalc can be used to predict concentrations of a suite of nuclides for a variety of purposes. The code is published under the GNU General Public License, version 2 terms so the basic code can be modified to output many different parameters and can be downloaded and modified to suit a user's particular needs.

The wide range of possible applications of the general code is impossible to predict. However, the code has been used to create two specific calculators to address the common need to calculate surface exposure ages from unknown samples. The two calculators that are included with the code are a single-sample surface exposure age calculator and a multi-sample depth profile calculator.

The fundamental theory and assumptions that have gone into the code are described in this paper. There are significant improvements and new features in CRONUScalc as compared to previous calculators, including a more accurate method of integration through time and depth, a modular format, updated geomagnetic history, newly produced calibration datasets, updated and calibrated muon production model, and the ability to calculate ages for single samples at depth or perform a calibration.

2.3 Code Systematics

The sections below describe the fundamental theory behind the code. In general, the theoretical sections briefly describe all the relevant equations, but focus on the modifications or complete revisions as compared to the code described in Balco et al. (2008). In many places, the summary equations are presented and discussed in the main text, while additional parameters, especially equations for

calculating fundamental properties of the atmosphere or subsurface, are included in the appendix. Equations in the appendix are indicated by an A in front of the equation number. This section includes cosmic rays, production equations, nuclide-specific considerations, scaling, and the surface and depth profile details.

2.3.1 Cosmic Rays

Cosmic rays originate primarily from Milky Way galaxy supernova, but also from the sun and other energetic phenomena (Dunai, 2010; Gaisser, 1990; Gosse and Phillips, 2001; Pigati and Lifton, 2004). The main cosmogenic particle reaching the atmosphere is protons (87% of the nucleonic cosmic-ray flux), with a smaller portion of the comic-ray flux composed of alpha particles (12%) and other heavier nuclei (Dunai, 2010). These incoming particles have a wide range of energies, with typical energies ranging from a few MeV to 10^{20} eV (Dunai, 2010). Over long periods (10Ma), the mean energy spectrum of the cosmic rays and the integrated flux has been shown to be relatively constant (Leya et al., 2000).

As the incoming cosmic-ray particles reach the top of the atmosphere, they interact with the earth's magnetic field. Only particles with sufficiently high energy and the correct trajectory will actually reach the earth's surface. The rigidity of a particle (R) is given by Equation 2.1. In the equation for rigidity, p is the particle momentum, c is the speed of light, and e is the particle charge.

$$R = pc/e \tag{2.1}$$

The cutoff rigidity, the minimum threshold for the particle energy necessary in order to penetrate the field normal to the magnetic field, is the standard

parameter used to organize the effect of the dipole field on location (Dunai, 2010; Gosse and Phillips, 2001; Lifton et al., 2005). The cutoff rigidities are related to geomagnetic latitude, having very low values near the poles ($>58^{\circ}$ at sea level), resulting in admittance of all cosmic-ray particles, and increasing cutoff rigidities moving towards the equator (Lifton et al., 2005). This is discussed further in the scaling section, 2.6.

The complexity of the paths of cosmic-ray particles due to interaction of looping trajectories with the solid earth results in an area where there are both allowed and forbidden trajectories in an alternating pattern known as the penumbra (Hillas, 1972). In order to determine where this region is and its effects on the cosmic-ray flux, reverse particle tracking (or trajectory tracing) is performed for particles within 20 km of the earth's surface to determine the effective cutoff rigidity of a location (Shea and Smart, 1983; Dunai, 2010; Lifton et al., 2005). The effective cutoff rigidity is used in scaling models to parameterize the cosmic-ray flux of a site.

After the primary cosmic-ray particles reach the top of the atmosphere, they interact with atmospheric particles and create a cascade of secondary particles. As these secondary particles are produced and the cascade moves further down through the atmosphere, several trends are apparent: the energy of the secondary particles is decreased, the total flux of particles is decreased, and the flux becomes dominated by neutrons due to the ionization losses of protons (Dunai, 2010). During these reactions, muons are also produced by energetic incoming particles high in the atmosphere (Eidelman, 2004). Unlike the hadronic component of the flux, the mesonic flux increases and then reaches a plateau as the cascade moves down through the atmosphere because muons do not interact as

strongly as neutrons and are lost very slowly through ionization (Gaisser, 1990). When they reach the earth's surface, the muons comprise the majority of the particles in the incoming cosmic-ray flux (Lal, 1988), but contribute less to surface production than do neutrons due to their lower propensity for nuclear interactions.

The intensities of the energies of the neutrons that reach the earth's surface determine the rate of the cosmogenic-nuclide-producing reactions. The neutrons, which compose 98% of the nucleonic flux at the earth's surface (Dunai, 2010), have peaks in the energy spectrum at 100 MeV, 1-10 MeV, and $<$1 eV (Dunai, 2010; Goldhagen et al., 2002). Figure 2.1 shows the neutron energy spectrum that reaches the earth's surface. The neutron energies discussed in this paper will be categorized as high ($>$10 MeV), epithermal ($<$0.1 MeV and $>$0.5 eV), or thermal ($<$0.5 eV). While these conventions follow other papers in the field (Gosse and Phillips, 2001; Schimmelpfennig et al., 2008), there are no consistent classifications and the actual energies associated with the categories can vary (Dunai, 2010).

2.3.2 Scaling of Cosmic-Ray Flux

In order to determine the production of a particular cosmogenic nuclide, it is necessary to determine the incoming flux at that specific location. However, as there are only limited observations of cosmic-ray flux at the earth's surface, it is necessary to create models that predict the incoming cosmic-ray flux any location. These models are called "scaling models" and seven different models have been proposed. These are discussed in detail in section 2.6. The three main categories of scaling models are based on the underlying method of calibrating the model. The first model by Lal (1991) was based on cosmic-ray emulsion data and

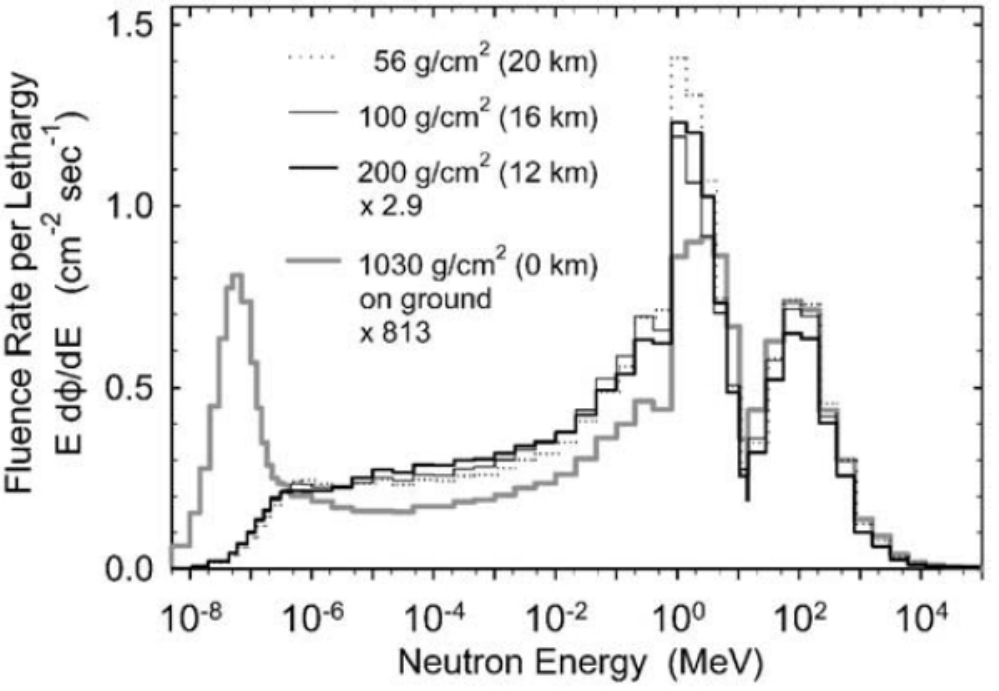

Figure 2.1: The spectrum of cosmic-ray-produced neutrons reaching the earth's surface (Goldhagen et al., 2002). The units of fluence rate is a measure of the total number of particles crossing over a sphere with a unit cross-section per unit time and lethargy is simply the natural logarithm of energy.

some neutron monitor data. The second model relies on only neutron monitor data. The third category does not rely on calibration to a fixed set of data points but, instead, is completely based on analytical equations based on physics modeling, although this model has been tested against the neutron energy spectrum datasets.

The analytical equations that comprise the Sato et al. (2008) model for the incoming cosmic-ray flux allows for a new scaling model, including the breakdown of the incoming flux into different energy levels. The incoming cosmic-ray flux of Sato et al. (2008) matches well with surface measurements, as seen in Figure 2.2. The predicted spectrum shows the same energy pattern as the measurements by Goldhagen et al. (2002). The equations in Sato et al. (2008) have been incorporated using the implementation by Lifton (Lifton, 2012).

The energy breakdown of the cosmic-ray flux provides information that is not available using the traditional neutron-monitor based scaling schemes (e.g. Dunai (2000); Lifton et al. (2005); Desilets and Zreda (2001)). This, in turn, allows for the inclusion of reaction cross-sections for each nuclide, resulting in the ability to incorporate nuclide/reaction-dependent cross-sections into the scaling models. The nuclide-dependent scaling incorporates both proton and neutron spectra for each nuclide. For all nuclides, there is more than one reaction that produces the nuclide, so a cross-section is required for each reaction being considered. The neutron cross-sections are shown in Figure 2.3. For further information on the nuclide-dependent scaling, see the scaling discussion in section 2.6.

2.4 Production Equations

The standard reference that describes the equations for production of cosmogenic nuclides is Gosse and Phillips (2001). The equations given in the paper

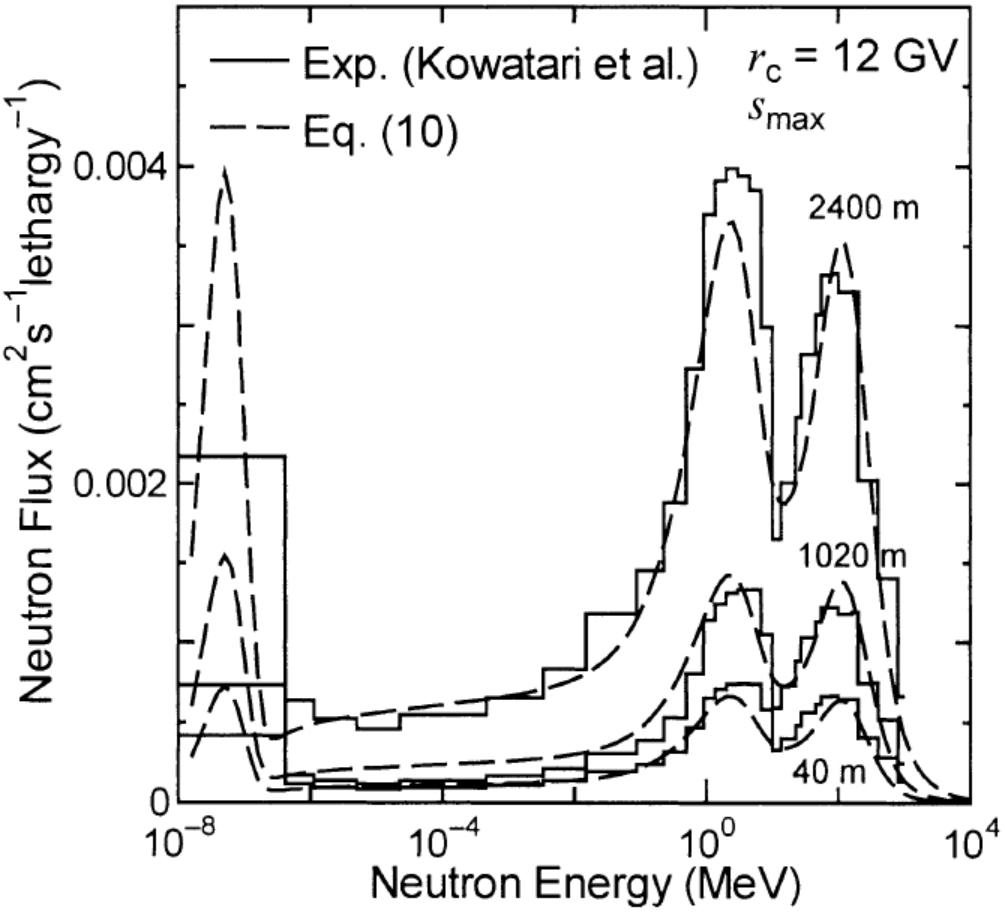

Figure 2.2: Calculated neutron spectrum from Sato and Niita (2006) ("Eq. (10)" in the figure) compared to data from Mt. Fuji ("Exp. (Kowatari et al.)" in the figure).

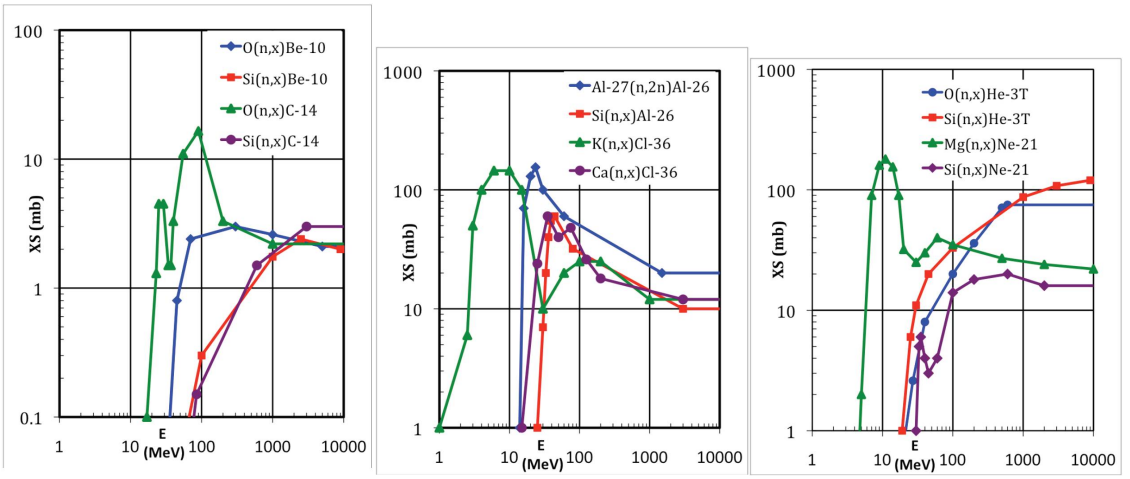

Figure 2.3: Estimated neutron reaction cross-sections (in millibarns) for common cosmogenic-nuclide producing reactions. Cross-sections between points were found using linear interpolation on a log-log plot. (a) Reaction cross-sections for reactions producing ^{10}Be from Si and O as well as reactions producing ^{14}C from Si and O. (b) Reaction cross-sections for production of ^{26}Al as well as production of ^{36}Cl from Ca and K. (c) Reaction cross-sections for the production of ^{3}He from Si and O and the production of ^{21}Ne from Mg and Si. All cross-sections originally published in Reedy (2011).

have provided the baseline for numerous applications of cosmogenic nuclides. New research has provided modification and revision of the existing theory and the revised equations are presented here. CRONUScalc is an implementation of these equations, both from Gosse and Phillips (2001) and from newer sources, and the purpose of this paper is to systematically document them, without need for the reader to refer back to numerous prior publications. The details below are discussed in general terms for production of nuclide, k, while details specific to a particular nuclide are discussed in later sections.

2.4.1 Spallation

Spallation occurs when a high-energy nucleon interacts with a target nucleus with enough energy to break nuclear bonds and fragment the nucleus into

several smaller pieces. During the creation of cosmogenic nuclides, one of these resultant pieces is the nuclide of interest. Cosmogenic nuclide production from spallation follows a well-established exponential decrease with depth. At the surface, this is typically the dominant production mechanism. All the nuclides discussed in this paper are produced through at least one spallation pathway. The formula for the instantaneous production rate from spallation ($P_{s,m}$) is (Gosse and Phillips, 2001; Schimmelpfennig et al., 2008):

$$P_{\mathrm{s,m}}(Z) = S_T \sum S_{el,s} P_{\mathrm{m,k}}(0) \mathrm{C_k} \exp\left(-\frac{Z}{\Lambda_{\mathrm{f,e}}}\right) \tag{2.2}$$

Where $P_{\mathrm{m,k}}$ is the production rate of species m by spallation of element k; S_T is the topographical shielding factor; $S_{el,s}$ is the scaling factor for spallation reactions for the particular reaction of interest; C_{k} is the concentration of the element k; and $\Lambda_{\mathrm{f,e}}$ is the effective attenuation length for fast neutrons. The production is summed for all target elements k that produce nuclide m to give the total spallation production rate.

Attenuation Length The particle attenuation length is the passage length through a medium required to attenuate the original intensity of the cosmic-ray beam by a factor of e^{-1} (Gosse and Phillips, 2001). This value varies depending on the type of particle (neutron, muon) and the associated energy level (fast, thermal, epithermal, etc.). For neutrons, the main factor is the energy level, with higher energy particles able to penetrate further into the subsurface than lower energy particles.

The apparent attenuation length is an important parameter because it quantifies the depth to which the nucleonic component can penetrate and cause production within a sample. The apparent attenuation length is defined with respect

to a flat sample with no topographical shielding. When the apparent attenuation length is adjusted to account for the dip of the sample surface and the topographical shielding, the result is the effective attenuation length, $\Lambda_{f,e}$. The effective attenuation length is the parameter that should be used in calculations pertaining to production from a particular sample.

Typically, as the topographic shielding increases, the effective attenuation length increases (Dunne et al., 1999). The spectrum of neutron energy varies depending on the azimuth angle. The highest energy cosmic rays are vertically incident upon the sample and the flux is dominated by these rays (in Dunai (2010) Dorman et al., 1999). As incident angle decreases going from vertical to horizontal, the intensity of the cosmic rays decreases due to the increasing apparent atmospheric depth (Dunai, 2010). The equation for this change in intensity is shown in equation 2.3. As the topography typically blocks out only cosmic rays near the horizon, the average energy of the remaining cosmic rays increases. The sample dip also contributes to a change in the effective attenuation length and shielding, as described in Dunne et al. (1999).

$$I(\theta) = I_0 \sin^m \theta \tag{2.3}$$

Where I is the intensity and θ is the inclination angle from the horizontal. The exponent m has been experimentally fit in several papers with significant differences in the results, as discussed in Dunai (2010). The most commonly cited value is 2.3 $\pm$ 0.5 (Nishiizumi et al., 1989), although Lal (1958) also gives a value of 2.3. However, Conversi and Rothwell (1954), cited by Lal, give a value of 2.1 $\pm$ 0.3 for 60 MeV nucleons (2.6 $\pm$ 0.2 for 750 MeV). In other studies, values of 2.5 $\pm$ 0.5 to 3.0 $\pm$ 0.5 (Barford and Davis, 1952), 3.5 $\pm$ 1.2 (Heidbreder et al., 1971),

and 2.65 (Masarik et al., 2000) have also been provided. Muons follow a similar trend, although the exponent needed to describe them is 2 (Eidelman, 2004).

In order to calculate the appropriate effective attenuation length, it is necessary to consider the sample location and the dip and shielding. A separate shielding calculator has been developed to simplify the calculation of the topographic shielding factor as well as the appropriate effective attenuation length. The values for the apparent attenuation length, Λ_f, for fast nucleonic particles range from 121 to >170 g/cm2 (Dunai, 2000). Some recent studies for Be use a value of 177 (Farber et al., 2008; Schimmelpfennig et al., 2008). However, it is understood that the value is constant at a particular site, but changes from site to site as altitude and elevation change. The attenuation length model accounts for the latitude and elevation of a sample. If shielding information is included, the effective attenuation length is modified accordingly.

The attenuation-length model in CRONUScalc is based on atmospheric attenuation lengths calculated from the PARMA model of Sato et al. (2008), adjusted upward by 11.1% to account for systematic differences between atmospheric and lithospheric attenuation. The exact percentage adjustment was calculated based on an inverse relationship between attenuation length and macroscopic cross-sections of the materials. To derive this from basic physics principles (J. Stone, pers. comm., February 14, 2012), we start by calculating the radius of an element, which can be estimated by $r = r_0 A^{1/3}$ where A is the atomic weight and r_0 is an experimentally determined constant. Using the radius (r) and the density ($\rho = N_A/A$, where N_A is Avagadro's number), the cross-sectional area of the nuclei in the material can be calculated (Equation 2.4) with units of cm^2/g, which simplifies to Equation 2.5.

$$area = \frac{N_A}{A}\pi(r_0 A^{1/3})^2 \tag{2.4}$$

$$area = \pi N_A r_0^2 A^{-1/3} \tag{2.5}$$

Another assumption is that the attenuation length (calculated here as the mean-free path) is related to the inverse of the macroscopic cross-section (A_m) by Equation 2.6 with units of g/cm^2.

$$A_m = \frac{1}{\pi N_A r_0^2} A^{1/3} \tag{2.6}$$

Using these principles, the estimated relationship between the attenuation lengths in air (A_{air}) and rock (A_{rock}) is given by the final equation as $(\mathrm{A}_{air}/\mathrm{A}_{rock})^{1/3}$, where A is the average atomic weight of the material. Figures 2.4 and 2.5 show the variations incorporated into the code for the apparent attenuation length. When possible, these values should be adjusted to account for horizon obstructions. The full table of values can be found in Appendix A.3.

The shielding/attenuation length calculator is a relatively simple model, but it should be sufficient for surface and near-surface samples. For typical surface samples, attenuation length changes result in only small changes in the production rate or age. When compared to the depth-profile fitting of several profiles, the calculator provides reasonable attenuation lengths to within $\sim$10%. However, when depth profiles are available, the attenuation length should still be one of the fitted parameters to ensure the most accurate value. Use of the surface shielding calculator to estimate attenuation lengths for depth profiles or other deep samples should be approached with caution.

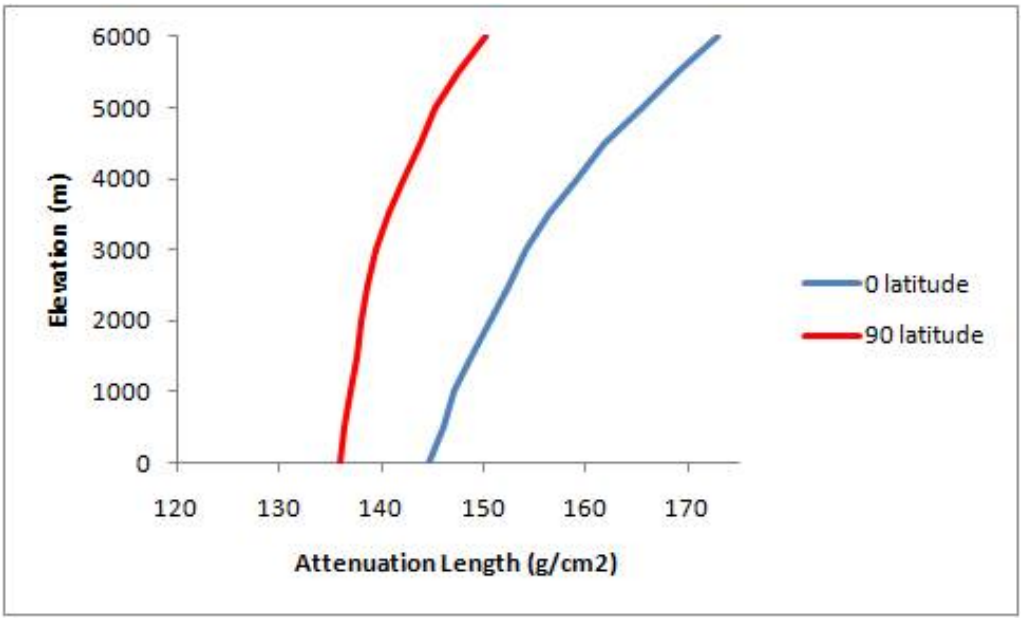

Figure 2.4: The change in attenuation length with changing elevation. These changes are shown for both zero and 90° latitude.

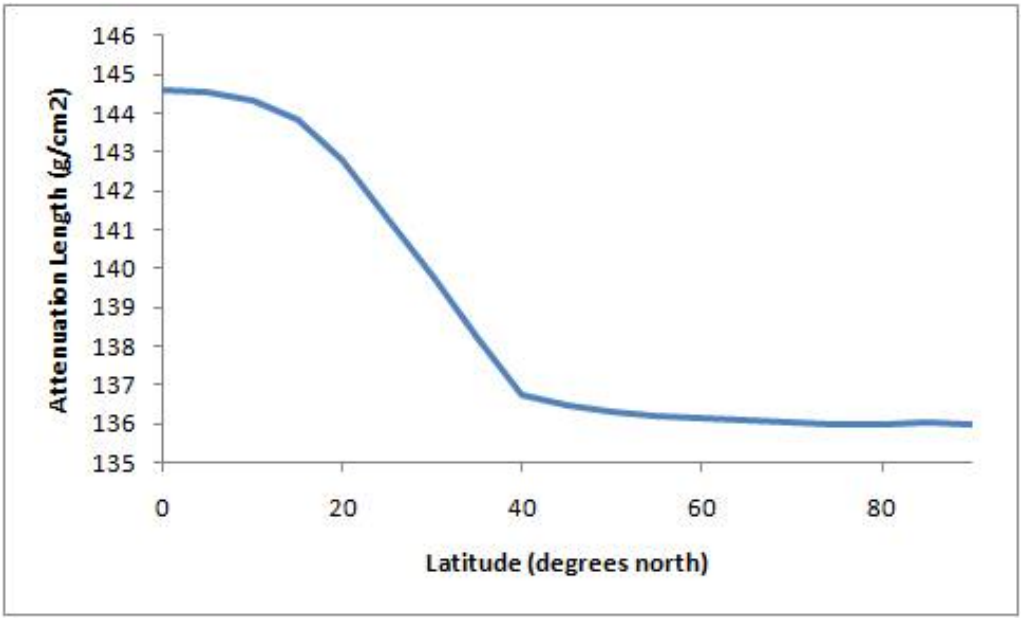

Figure 2.5: The change in attenuation length with changing latitude. Shown for 0 degrees longitude and sea level.

2.4.2 Epithermal Neutrons

Low-energy cosmogenic nuclide production, including that from thermal and epithermal neutrons, does not follow an exponential pattern with depth due to the atmosphere-ground interface effects. The general form for the production of the cosmogenic nuclide of interest from epithermal neutrons is shown in Equation 2.7. The epithermal neutron attenuation length ($\Lambda_{eth,ss}$, Equation 2.8) accounts for both moderation and absorption of epithermal neutrons and parameterizes the effective depth of penetration of the epithermal neutron flux (Gosse and Phillips, 2001).

$$P_{eth,ss,m} = f_{eth,ss,m}\Gamma_{eth,ss,m} = \frac{f_{eth,ss,m}}{\Lambda_{eth,ss}}\Phi_{eth,ss,total}(Z)(1 - p(E_{th})_{ss}) \tag{2.7}$$

Where: $f_{eth,ss,m}$ is the fraction of epithermal neutrons absorbed that are taken up by target element k to produce nuclide m (eqn A.15). $\Gamma_{eth,ss,m}$ is the total rate of epithermal neutron absorption. $\Phi_{eth,ss,total}$ is the epithermal neutron flux (eqn 2.12).

$$\Lambda_{eth,ss} = [\bar{\xi}_{bulk}(I_{eff,ss} + \Sigma_{sc,ss})]^{-1} = \Sigma_{eth,ss}^{-1} \tag{2.8}$$

$\bar{\xi_{ss}}$ is the average macroscopic log decrement energy loss per neutron collision (eqn A.28). $I_{eff,ss}$ is the macroscopic resonance integral for absorption of epithermal neutrons in the subsurface (eqn A.16). $\Sigma_{sc,ss}$ is the macroscopic neutron scattering cross-section in the subsurface and is defined in Equation A.27.

The distribution of epithermal neutrons in the subsurface can be described by Equation 2.9. The epithermal neutrons are assumed to be produced entirely

from the moderation of both spallation and evaporation neutrons and are assumed to be in temporal equilibrium with the high-energy flux (Gosse and Phillips, 2001).

$$D_{eth,ss}\frac{d^2\Phi_{eth,ss}}{dZ^2} = \frac{\Phi_{eth,ss}}{\Lambda_{eth,ss}} - R_{eth,ss}P_f \tag{2.9}$$

The diffusion coefficient for epithermal neutrons in the subsurface ($D_{eth,ss}$) is defined in Equation A.9, with the corresponding parameter in the atmosphere, defined in Equation A.10. $R_{eth,ss}$ is the normalization factor for the epithermal neutron production rate (eqn A.25). P_f is the production rate of epithermal neutrons from fast neutrons, with the value at the surface represented as $P_f(0)$.

The observed subsurface, epithermal neutron flux, $\Phi_{eth,ss}$, at a particular point is the balance of exponential production with depth against the loss of neutrons through diffusion at the rock/air interface as well as loss through absorption and moderation. The hypothetical epithermal neutron flux in the subsurface assuming that there is no boundary (all material is the same as the subsurface) is indicated by $\Phi^*_{eth,ss}$ and is given in Equation 2.10. The difference between the hypothetical equilibrium flux in the air ($\Phi^*_{eth,a}$) and the hypothetical equilibrium flux in the subsurface ($\Phi^*_{eth,ss}$) is $\Delta\Phi^*_{eth,ss}$. The physical cause of the difference between the fluxes (no interface vs interface) is the effect of diffusion. This is shown mathematically in Equation 2.11 and graphically in Figure 2.6.

$$\Phi^*_{eth,ss}(Z) = P_f(0)\frac{R_{eth,ss}}{\Sigma_{eth,ss} - D_{eth,ss}/\Lambda^2_{f,e}} \tag{2.10}$$

$$\Delta\Phi^*_{eth,ss} = \Phi^*_{eth,a} - \Phi^*_{eth,ss} = -\Delta\Phi^*_{eth,a} \tag{2.11}$$

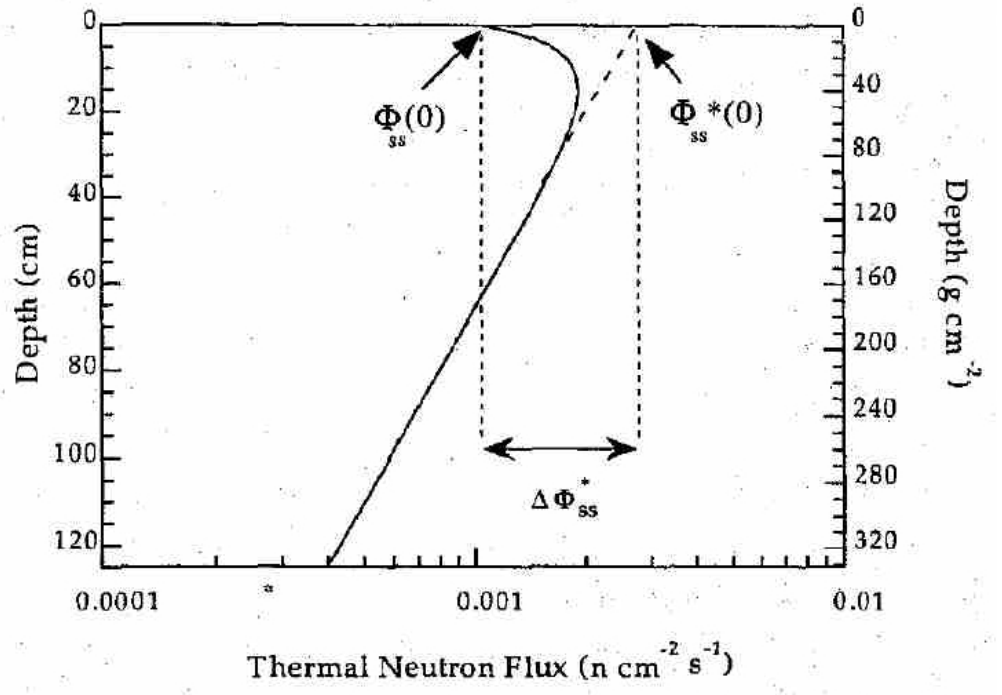

Figure 2.6: Graphical definition of quantities Φ, Φ^*, and $\delta\Phi$ (Evans, 2001). The thermal neutron production profile in granite, as calculated in Evans (2001), is plotted as a function of depth. The granite composition was taken from Liu et al. (1994).

For the purposes of this initial solution, photodisintegration and other neutron-producing interactions are neglected. The diffusion-like behavior of low-energy neutrons means that the diffusion equation, in addition to the production equations, must be solved in order to predict the appropriate amount of cosmogenic nuclide from this type of production. The solution to the coupled differential equations (originally solved in Phillips et al. (2001)) yields Equation 2.12.

$$\Phi_{eth,ss} = S_T S_{el,eth} \Phi^*_{eth,ss} exp(-\frac{Z}{\Lambda_{f,e}}) + (F\Delta\Phi)^*_{eth,ss} exp(-\frac{|Z|}{L_{eth,ss}}) \tag{2.12}$$

The physical meaning of the $(F\Delta\Phi)^*_{eth,ss}$ term (Equation 2.13) is the difference between the actual observed flux (with an interface present) and the flux that would be observed at the surface (Z=0) if all materials were the same as those in the subsurface. This can also be formulated for the air, as seen in Equation A.12. $L_{eth,ss}$ (eqn A.19) is the diffusion length for epithermal neutrons in the subsurface and the corresponding parameter in the atmosphere, $L_{eth,a}$, is shown in Equation A.20. $S_{el,eth}$ is the scaling factor for epithermal reactions for this nuclide.

$$(F\Delta\Phi)^*_{eth,ss} = \frac{\Delta\Phi^*_{eth,ss} D_{eth,a}/L_{eth,a} - \Delta\Phi^{**}_{eth,a} D_{eth,ss}/\Lambda_{f,e}}{D_{eth,a}/L_{eth,a} + D_{eth,ss}/L_{eth,ss}} \tag{2.13}$$

Where:

$$\Delta\Phi^{**}_{eth,a} = \Delta\Phi^*_{eth,ss} - \frac{D_{eth,a}}{D_{eth,ss}} \Phi^*_{eth,a} \tag{2.14}$$

2.4.3 Thermal Neutrons

The production equations for thermal neutron pathways are analogous to those for epithermal neutrons. In the general production equation, the form is

very similar with other terms being replaced by values calculated for thermal neutrons instead of epithermal neutrons. The production rate ($P_{th,m}$) for thermal neutrons is shown in Equation 2.15 (Gosse and Phillips, 2001).

$$P_{th,ss,m} = f_{th,ss,m}\Gamma_{th,ss,m} = \frac{f_{th,ss,m}}{\Lambda_{th,ss}}\Phi_{th,ss,total}(Z) \tag{2.15}$$

Where $f_{th,ss,m}$ is the fraction of absorbed thermal neutrons that are taken up by element k to produce nuclide m (eqn A.32); $\Gamma_{th,ss,m}$ is the total rate of thermal neutron absorption; $\Phi_{th,ss,total}$ is the thermal neutron flux (eqn 2.17); and $\Lambda_{th,ss}$ is the effective thermal neutron attenuation length and is defined in Equation A.33.

The distribution for thermal neutrons in the subsurface (Equation 2.16) is also similar to that of epithermal neutrons, except that the thermal neutron source is assumed to be only neutrons moderated from the epithermal energy range.

$$D_{th,ss}\frac{d^2\Phi_{th,ss}}{dZ^2} = \frac{\Phi_{th,ss}}{\Lambda_{th,ss}} - R_{th,ss}\frac{p(E_{th})_a}{\Lambda_{eth,ss}}[\Phi^*_{eth,ss}exp(-\frac{Z}{\Lambda_{f,e}}) + (F\Delta\Phi)^*_{eth,ss}exp(-\frac{|Z|}{L_{eth,ss}})] \tag{2.16}$$

Where $D_{th,ss}$ (Equation A.29) is diffusion coefficient for thermal neutrons; $R_{th,ss}$ is the ratio of thermal neutron production in the rock to that in the atmosphere and is defined in Equation A.38. The term $p(E_{th})_a$ is the resonance escape probability of a neutron from the epithermal energy range in the atmosphere (Equation A.24), with the corresponding subsurface term shown in Equation A.23.

The equations described above can be solved for the thermal neutron flux using the same boundary conditions assumed in the epithermal problem. The

thermal neutron flux, discounting muon-induced neutrons, is shown in Equation 2.17.

$$\Phi_{th,ss} = S_T S_{el,th} \Phi^*_{th,ss} exp(-\frac{Z}{\Lambda_{f,e}}) + (\mathscr{F}\Delta\Phi)^*_{eth,ss} exp(-\frac{|Z|}{L_{eth,ss}}) + (\mathscr{F}\Delta\Phi)^*_{th,ss} exp(-\frac{|Z|}{L_{th,ss}}) \quad (2.17)$$

where:

$$\Phi^*_{th,ss} = \frac{p(E_{th})_a R_{th,ss} \Phi^*_{eth,ss}}{\Lambda_{eth,ss}(\Sigma_{th,ss} - \frac{D_{th,ss}}{\Lambda^2_{eth,ss}})} \quad (2.18)$$

$$(\mathscr{F}\Delta\Phi)^*_{eth,ss} = \frac{p(E_{th})_a R_{th,ss} (F\Delta\Phi)^*_{eth,ss}}{\Lambda_{eth,ss}(\Sigma_{th,ss} - D_{th,ss}/L^2_{eth,ss})} \quad (2.19)$$

$$(\mathscr{F}\Delta\Phi)^*_{th,ss} = [D_{th,a}(\frac{\Phi^*_{th,a}}{\Lambda_{f,e}} - \frac{(\mathscr{F}\Delta\Phi)^*_{eth,a}}{L_{eth,a}}) - D_{th}(\frac{\Phi^*_{th,ss}}{\Lambda_{f,e}} - \frac{(\mathscr{F}\Delta\Phi)^*_{eth,ss}}{L_{eth,ss}}) + \frac{D_{th,a}}{L_{th,a}}(\Delta\Phi^*_{th,ss} + \Delta(\mathscr{F}\Delta\Phi)^*_{eth,ss})]/(\frac{D_{th,ss}}{L_{th,ss}} + \frac{D_{th,a}}{L_{th,a}}) \quad (2.20)$$

In Equation 2.20, additional parameters of $\Delta\Phi^*_{th,ss}$ and $\Delta(\mathscr{F}\Delta\Phi)^*_{eth,ss}$ are described in Equations A.31 and A.4, respectively. $S_{el,th}$ is the scaling factor for thermal reactions for this particular nuclide.

2.4.4 Muons

Muon contributions to total production are typically small at the surface, but become increasingly important at depth. Sampling sites with large erosion

rates or possible pre-exposure concerns will be especially dependent on correct muon production formulations, as will depth profiles (Stone et al., 1998). The original CRONUS-Earth calculator (Balco et al., 2008) implemented the Heisinger et al. (2002a,b) muon model as an improvement over the commonly-cited formulation in Stone et al. (1998). However, data collected by J. Stone (pers. comm., April 15, 2012) have demonstrated that the model and parameters given in Heisinger et al. (2002a,b) overestimate actual muon production of ^{10}Be at depth by up to factor of two when compared to deep profile data. Figure 2.7 shows this overprediction for the CRONUS-Earth Beacon Heights site. New data at depth from the CRONUS-Earth project has allowed for the calibration of relevant muon production parameters leading to an improved muon production model.

The new Sato et al. (2008) scaling model, combined with the previous Heisinger muon production equations and CRONUS-Earth data, has been employed to formulate a new hybrid muon production model that combines aspects of each of these models. The Sato/Heisinger muon code is modified by N. Lifton from the Heisinger muon implementation described in Balco et al. (2008) and supplemental materials (Balco, 2007). The procedure followed by the code is summarized here along with the relevant equations. The CRONUScalc muon module initially calculates the omnidirectional flux at SLHL and the site of interest using the Sato PARMA equations (Sato et al., 2008). The omnidirectional flux is converted to the vertical flux at SLHL using the equation presented in Heisinger et al. (2002b) and shown here in Equation 2.21. This formulation is only valid down to 200,000 g/cm^2 and the alternate formulation provided in Balco (2007) should be used for deeper applications.

$$\phi_{\nu,0}(Z) = \frac{a}{(Z+b)[(Z+1000)^{1.66}+c}e^{dZ} \tag{2.21}$$

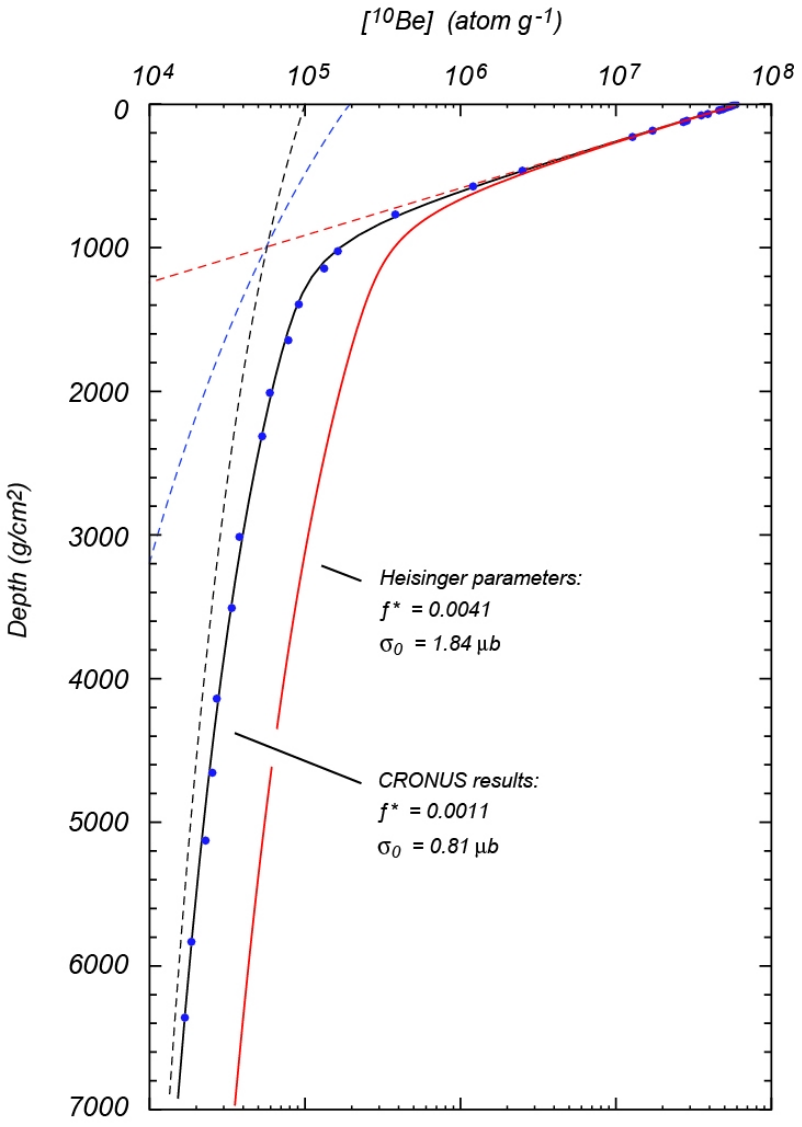

Figure 2.7: Figure showing the overprediction of muon production using the Heisinger model. The red line shows the original Heisinger parameters and the solid line indicates the newly calibrated model. The blue points are the measured depth profile samples. The different pathways are shown by the dashed red (spallation), blue (negative muon), and black (fast muon) lines. Figure provided by J. Stone (pers. comm., April 15, 2012).

where the coefficients are as follows:$a = 5.401 \times 10^7$, $b = 21000$, $c = 1.567 \times 10^5$, $d = -5.5 \times 10^{-6}$.

The stopping rate of the vertically incident muons is calculated by its equivalence to the range spectrum of the muons at the surface. Equation 2.22 shows this calculation.

$$R_{\nu,0}(Z) = \frac{d}{dz}(\phi_{\nu,0}(Z)) = -5.401 \times 10^7 [\frac{bc\frac{da}{dz} - a(\frac{db}{dz}c + \frac{dc}{dz}b)}{b^2c^2}] \tag{2.22}$$

Where $a = exp^{-5.5\times10^{-6}}z$; $b = (z + 21000)$; $c = (z + 1000)^{1.66} + 1.567 \times 10^5$; $\frac{da}{dz} = -5.5 \times 10^{-6}e^{-5.5\times10^{-6}z}$; $\frac{db}{dz} = 1$; $\frac{dc}{dz} = 1.66(z + 1000)^{0.66}$.

The muon flux at the surface is scaled based on the Sato/Lifton model (Lifton, 2012). The scaling is done by computing the muon flux at the site and at a reference location (SLHL) and dividing the site flux by the reference flux. Each discretized muon energy level is scaled independently, leading to a set of muon scaling factors, one for each energy level. The negative muon flux is scaled as a single unit and is not discretized by energy. The scaling factors are built into the results from the muon module and so are not used in the production code later.

The vertical muon flux as a function of depth at the site is found by numerically integrating the stopping rate from infinite depth to the depth of interest (Equation 2.23). This formulation is not appropriate for greater depths.

$$\phi_\nu(Z) = \int_Z^\infty R_\nu(x)dx \tag{2.23}$$

The vertical muon flux is converted to total muon flux at the site using the formula in Heisinger et al. (2002b) (Equation 2.24), but modified to use depth units of g/cm^2 by Balco et al. (2008); Balco (2007), as shown in Equation 2.25.

$$\phi(\mathrm{Z},\theta) = \phi_\nu(\mathrm{Z}) cos^{n(\mathrm{Z})}\theta \tag{2.24}$$

$$n(\mathrm{Z}) = f - g\ln(\frac{\mathrm{Z}}{100} + 42) + \mathrm{Z} * h \tag{2.25}$$

Coefficients for the previous equation are: f=3.21, g=0.297, $h = 1.21 \times 10^{-5}$.

The total muon flux at a given depth ($\phi_\mu(\mathrm{Z})$) is given by Equation 2.26.

$$\phi_\mu(\mathrm{Z}) = \frac{2\pi}{n(\mathrm{Z}+\delta\mathrm{Z})+1}\phi_\nu(\mathrm{Z}) \tag{2.26}$$

The total muon stopping rate as a function of depth (R(Z)) can be calculated by Equation 2.27. The total stopping rate in muons * g^{-1} s^{-1} is converted to the negative muon stopping rate by accounting for the percentage of all stopped muons that are negative stopped muons (44%) and then converting the units to muons * g^{-1} yr^{-1}. In both flux calculations, total muon flux and stopped negative muon flux, the values are calculated so that the flux is a positive value.

$$\begin{aligned} R(\mathrm{Z}) = \frac{2\pi}{n(\mathrm{Z}+\delta\mathrm{Z})+1}R_\nu(\mathrm{Z}) - \phi_\nu(\mathrm{Z})(-2\pi) \\ (n(\mathrm{Z}+\delta\mathrm{Z})+1)^2[\frac{-0.297\times10^{-2}}{\frac{\mathrm{Z}+\delta\mathrm{Z}}{100}+42} + 1.21\times10^{-5}] \end{aligned} \tag{2.27}$$

Fast Muon Production Production from fast muons as a function of depth is calculated using the formulas in Heisinger et al. (2002b), with the general production described in Equation 2.28.

$$P_{\mu,fast} = S_T \phi_{\mu,total}(\mathrm{Z}) \beta(Z) (\bar{E}(Z))^{\alpha} \sigma_0 \mathrm{N}_{t,i} \tag{2.28}$$

Where β is a function of depth and is shown in Equation 2.30 and $\bar{E}$ is defined as the mean muon energy at a given depth Z and is shown in Equation 2.31. $\mathrm{N}_{t,i}$ is the number density of the atoms in the target element (in units of at/g). This value is a constant for each nuclide unless the composition of the target changes, as it does for chlorine-36.

In Heisinger et al. (2002b), the σ_{190} parameter is used to calculate the value for σ_0 using Equation 2.29, which is, in turn, used to calculate the production from muons for a particular nuclide, as shown in Equation 2.28. The value for alpha (α) is a fixed value that determines how strongly the cross-section is dependent on energy, with low values indicating a weaker dependence and higher values a stronger dependence. Heisinger et al. (2002b) recommends a value of $\alpha \approx 0.75$, but mentions that values between 0.75-1.3 are possible. Preliminary work by Keyong Kim (John Stone, pers. comm., April 15, 2012) on deep ^{10}Be and ^{26}Al samples indicates that higher values of α are preferable. Existing data allows any value between 0.75 and 1.3 so the CRONUS-Earth project chose a value of α = 1.0, which simplifies the math. The value of σ_{190} can be measured experimentally and Heisinger et al. (2002b) reports these values for many of the nuclides of interest including ^{26}Al, ^{10}Be, ^{14}C, and ^{36}Cl from calcium. Note that there is no value for ^{36}Cl from potassium. When these values are used to calculate predicted values for measured depth profiles, there are significant discrepancies.

Knowing that the values predicted by Heisinger et al. (2002b) do not match the measured values, the value of σ_0 was selected as the calibration parameter. This was done mainly for two reasons. First, σ_0 is the only nuclide-dependent

parameter in the fast production equation, so it is the logical choice. Second, by directly calibrating the σ_0 parameter, any reliance on the conversion from σ_{190} to σ_0 is eliminated. Equation 2.29 was used to calculate initial starting parameters for the σ_0 calibration.

$$\sigma(E) = \sigma_0 E^{\alpha} \tag{2.29}$$

Where:

$$\beta = 0.846 - 0.015log(\frac{Z}{100} + 1) + 0.003139(log(\frac{Z}{100} + 1)^2) \tag{2.30}$$

$$\bar{E} = 7.6 + 321.7. * (1 - exp(-8.059x10^{-6}Z)) + 50.7(1 - exp(-5.05 \times 10^{-7}Z)) \tag{2.31}$$

Slow Negative Muon Capture Production Production from slow negative muon capture ($P_{\mu-}$) is described by Equation 2.32, originally from Charalambus (1971) and discussed in detail for chlorine-36 in Stone et al. (1998). The production rate depends on the stopping rate of negative muons ($\phi_{\mu-}$) as well as the nuclide-dependent factors ($f_{i,C}$, $f_{i,D}$, f_i^*). $f_{i,D}$ is the fraction of muons stopped by element k and absorbed by the nucleus before decay of the muon. $f_{i,C}$, the compound factor, represents the probability that the muon will be captured by a target element within the bulk rock. The formula for the compound factor is taken from Charalambus (1971) and is consistent with the values cited in Heisinger et al. (2002a). In the case of nuclides measured in a target mineral of constant composition, the compound factor is a constant parameter; however, for elements where the target

mineral composition may vary, this is a compositionally dependent value. The value for $f_{i,C}$ can be calculated using the formula in Equation A.40 and the values in von Egidy and Hartmann (1982).

$$P_{\mu-} = S_T \phi_{\mu-}(Z) f_{i,C} f_{i,D} f_i^* \tag{2.32}$$

f_i^* is the probability for particle emission to the radionuclide and has been calibrated for Al, Be, Cl (K and Ca). The chlorine-36 calibrations are discussed in chapter 8 and we use the best-fit results here instead of the values published in Heisinger et al. (2002a,b). All the muon calibrations, including Al, Be, and Cl, are discussed in the CRONUS-Earth muon calibration paper (Stone and Borchers, 2012). There are currently no profiles to use for calibration of carbon-14, so the values presented in Heisinger et al. (2002a,b) are used in the code.

Muon-induced Neutrons As the muon reactions occur in the subsurface, neutrons are produced as a by-product. In order to calculate the nuclide production due to muogenic neutrons, it is necessary to know the muon flux. Due to the new capabilities of the Sato/Heisinger muon model, the quantification of fluxes has improved and they need no longer be estimated using a simple exponential approximation (Stone et al., 1998), as was previously done in most models, including the Phillips and Plummer (1996); Schimmelpfennig et al. (2009) calculators, but are directly calculated using Equation 2.33. The muon module, described in the previous section, is used to calculate the negative muon stopping rate ($\phi_{\mu-}$(Z)) and total muon flux ($\phi_{\mu f}(Z)$) terms at a given depth.

$$P_{n,\mu}(\mathrm{Z}) = Y_s \phi_{\mu-}(Z) + 5.8 \times 10^{-6} \phi_{\mu f}(Z) \tag{2.33}$$

where Y_s is the average neutron yield per stopped negative muon (Fabryka-Martin, 1988).

Near the atmosphere/subsurface interface, muon-induced low-energy neutrons are assumed to follow the same distribution as the spallation-induced neutrons. Although the muon-induced neutron flux near the surface is not in equilibrium with the production rate due to diffusion, the diffusion is occurring based on the total concentration of neutrons at the surface. The dominant source of neutrons is spallation reactions, so the muons are assumed to follow the same pattern as the spallation-induced neutrons, leading to the incorporation of the muogenic neutrons into the epithermal neutron flux as shown in Equation 2.34.

$$\begin{aligned}\Phi_{\text{eth,ss}}(Z) &= S_T S_{el,eth} \Phi^*_{\text{eth,ss}} \exp\left(-\frac{Z}{\Lambda_{\text{f,e}}}\right) \\ &\quad +(1+R_\mu(0)R_{\text{eth,ss}})(F\Delta\Phi)^*_{\text{eth,ss}} \exp\left(-\frac{Z}{L_{\text{eth,ss}}}\right) \\ &\quad +R_\mu(Z)\Phi^*_{\text{eth,ss}} \end{aligned} \tag{2.34}$$

There are two different values used in the code for the muon-induced neutron factor, R_μ. $R_\mu(Z)$ is defined in Equation 2.35. In the parts of the equation dealing with epithermal neutrons, the surface production rate of the muogenic neutrons ($R_{mu}(0)$) is used because of the assumption that the production follows the same trend as the spallogenic neutrons. For the parts of the equation dependent on the attenuation at depth of the muon flux, the actual values for $R_{mu}(Z)$ are calculated from the muon module and used in the equation.

$$R_\mu(Z) = \frac{S_{el,\mu} P_{n,\mu}(Z)}{S_{el,eth} P_f(0) R_{eth}} \tag{2.35}$$

The code calculates the epithermal neutron flux and the subsequent cosmogenic nuclide production by combining the muon-induced neutrons with the original epithermal neutron production equation, Equation 2.12, to produce the total epithermal neutron production for nuclide m, as shown in Equation 2.36.

$$\begin{aligned} P_{\mathrm{eth,ss,m}}(\mathrm{Z}) &= S_T S_{el,eth} \frac{f_{\mathrm{eth,ss}} \Phi_{\mathrm{eth,ss,total}}}{\Lambda_{\mathrm{eth,ss}}} = \frac{f_{\mathrm{eth,ss}}}{\Lambda_{\mathrm{eth,ss}}} \Bigg\{ \Phi^*_{\mathrm{eth,ss}} \exp\left(-\frac{\mathrm{Z}}{\Lambda_{\mathrm{f,e}}}\right) \\ &\quad + (1 + R_\mu(0) R_{\mathrm{eth,ss}}) (F\Delta\Phi)^*_{\mathrm{eth,ss}} \exp\left(-\frac{z}{L_{\mathrm{eth,ss}}}\right) \\ &\quad + R_\mu(\mathrm{Z}) \Phi^*_{\mathrm{eth,ss}} \Bigg\} \end{aligned} \tag{2.36}$$

Similar considerations for muon-induced neutrons must be made for the thermal energy range. Some of the epithermal-range neutrons produced by muon interactions lose enough energy to become thermal neutrons. The contribution of these muon-induced neutrons to the thermal flux is shown in Equation 2.37. Once again, the muon-induced neutrons are assumed to follow the same trends as the spallogenic neutrons and are scaled appropriately using only the surface value of $R'_\mu(Z)$ for the spallogenic parts of the equation. For the neutron-dependent term, the actual values for each depth are calculated. The final equation for the thermal neutron flux is shown in Equation 2.38.

$$R'_\mu(Z) = \frac{p(E_{th})_a}{p(E_{th})} R_\mu(Z) \tag{2.37}$$

$$\Phi_{th,ss,total} = S_T S_{el,th}\Bigg\{\Phi^*_{\text{th,ss}}\exp\left(-\frac{\text{Z}}{\Lambda_{\text{f,e}}}\right) + (1+R'_\mu(0))(\Im\Delta\Phi)^*_{\text{eth,ss}}\exp\left(-\frac{\text{Z}}{L_{\text{eth,ss}}}\right) + (1+R'_\mu(0)R_{\text{th,ss}})(\Im\Delta\Phi)^*_{\text{th,ss}}\exp\left(-\frac{\text{Z}}{L_{\text{eth,ss}}}\right) + R'_\mu(\text{Z})\Phi^*_{\text{th,ss}}\Bigg\} \quad (2.38)$$

The total production of cosmogenic nuclide k via thermal neutron pathways is described by combining Equation 2.38 with Equation 2.15 and yields an equation for total production with depth from thermal neutrons, shown in Equation 2.39.

$$\begin{aligned} P_{\text{th,ss,m}}(\text{Z}) &= S_T S_{el,th}\frac{f_{\text{th}}\Phi_{\text{th,ss,total}}}{\Lambda_{\text{th,ss}}} = \frac{f_{\text{th}}}{\Lambda_{\text{th,ss}}}\Bigg\{\Phi^*_{\text{th,ss}}\exp\left(-\frac{\text{Z}}{\Lambda_{\text{f,e}}}\right) \\ &+(1+R'_\mu(0))(\Im\Delta\Phi)^*_{\text{eth,ss}}\exp\left(-\frac{\text{Z}}{L_{\text{eth,ss}}}\right) \\ &+(1+R'_\mu(0)R_{\text{th}})(\Im\Delta\Phi)^*_{\text{th,ss}}\exp\left(-\frac{\text{Z}}{L_{\text{eth,ss}}}\right) \\ &+R'_\mu(\text{Z})\Phi^*_{\text{th,ss}}\Bigg\} \end{aligned} \quad (2.39)$$

2.4.5 Radiogenic Production

Radiogenic production in the subsurface is assumed to be in equilibrium with the concentrations of uranium (U) and thorium (Th) in the rock. This component is quantified using measured concentrations of U and Th and the method

described in Fabryka-Martin (1988), which is based on the formulations developed by Feige et al. (1968). The uranium and thorium α-decay chain members produce alpha particles (α) as they decay. The alpha particles react with light nuclei in the rock matrix to produce low-energy neutrons. In turn, the neutrons can react with target elements in the rock in the same way that cosmogenically-produced neutrons react to produce nuclides such as chlorine-36. The equations for calculating this contribution to the total nuclide inventory within a sample are provided in detail in Fabryka-Martin (1988) and are summarized here.

The radiogenic production of nuclides is shown in Equation 2.40. The elements with the maximum yield of neutrons due to alpha particle reaction are Be, B, F, and Li. However, due to the low concentration of these elements in most rocks, the largest concentrations of neutrons result from targets with larger matrix concentrations, such as Al, Si, Mg, O, and Na. In the samples for this study, the concentrations of the elements listed in Appendix A.2 were measured with the exception of oxygen (O) and hydrogen (H). The concentrations of both O and H were calculated from the oxide measurements performed on the other elements.

Although the concentrations of the largest producers of neutrons are the most important elements to quantify, the remaining rock matrix composition must still be quantified in addition to the elements listed above so that all elements can be used to calculate the stopping power of the rock. In particular, there are several elements, such as boron and gadolinium, that have large thermal neutron absorption cross-sections, meaning that they have a large probability of absorbing neutrons (radiogenically formed and cosmogenically formed neutrons) (Fabryka-Martin, 1988). This decreases the actual amount of chlorine-36 formed within the rock because these other elements intercept the neutrons prior

to formation of chlorine-36. The concentrations of all the measured elements are included in these calculations of the properties of the rock. A table of nuclear properties for all the elements included in sample analysis is shown in Appendix A.2. The original table presented in Fabryka-Martin (1988) had several typos that have now been corrected using the information in Mughabghab (2006) and Schimmelpfennig et al. (2009).

$$P_r = P_{eth,r} f_{eth} + P_{th,r} f_{th} \tag{2.40}$$

Where P_r is the total radiogenic production from all mechanisms in a particular sample. $P_{eth,r}$ is the total radiogenic epithermal neutron production (Equation 2.41) and $P_{th,r}$ is the total radiogenic thermal neutron production (Equation 2.42).

$$P_{eth,r} = (P_{n,\alpha} + P_{n,sf})(1 - p(E_{th})) \tag{2.41}$$

$$P_{th,r} = (P_{n,\alpha} + P_{n,sf})(p(E_{th})) \tag{2.42}$$

where $P_{n,\alpha}$ is the production rate of neutrons from alpha particles in neutrons g^{-1} yr^{-1} (Equation 2.43). $P_{n,sf}$ is the neutron production rate due to the spontaneous fission of ^{238}U and can be calculate as 0.429*[U], where [U] is the concentration of uranium in ppm.

$$P_{n,\alpha} = X[U] + Y[Th] \tag{2.43}$$

Where [Th] is the thorium concentration in ppm. X and Y are neutron production factors related to the light isotope composition of the rock matrix and

are described in Equations 2.44 and 2.45, respectively. These were originally described by Feige et al. (1968).

$$X = \frac{\sum kS_k F_{k,bulk} Y_n^U}{\sum kS_k F_{k,bulk}} \tag{2.44}$$

$$Y = \frac{\sum kS_k F_{k,bulk} Y_n^{Th}}{\sum kS_k F_{k,bulk}} \tag{2.45}$$

Where S_k is the mass stopping power of element k for α-particles of a given energy. Y_n^U and Y_n^{Th} are the neutron yields of element i per ppm U or Th in equilibrium. $F_{k,bulk}$ is the fractional abundance of element k in ppm in the bulk rock.

2.5 Accumulation

Instantaneous production rates, such as those described above, must be integrated in both time and thickness in order to calculate the production in a real sample. In many common solutions, this is done analytically or with additional scaling factors to account for the finite thickness of a sample. In the CRONUScalc program, this integration is done numerically, which is more accurate for depth integrations and makes it simple to incorporate time-dependent scaling and production rates.

For a given age, an appropriate time step, Δt, is found such that the erosion rate is small for that period and the changes in time-dependent production rates are not too large. The sample begins at depth and the cosmogenic inventory within the sample is tracked during its migration to the surface. For each time step, the current scaling factors and production rates are found for the sample.

The inventory accounts for the decay of all previously produced nuclide inventory (the first term in Equation 2.46) as well as the production and decay of the nuclide during the current time step (second term in Equation 2.46).

$$N_{tot} = N_{prev} exp^{-\lambda \Delta t} + P_{tot} * f_{decay} \tag{2.46}$$

Where N_{tot} is the total inventory in the sample up to the current time step; N_{prev} is the inventory from all previous time steps; λ is the decay constant for the nuclide; P_{tot} is the instantaneous production rate of the nuclide from all mechanisms; and f_{decay} is the decay factor (Equation 2.47) that accounts for the fact that a small amount of the nuclide produced at the beginning of the time period will have decayed by the end of the period.

$$f_{decay} = \frac{1 - exp^{-\lambda \Delta t}}{\lambda} \tag{2.47}$$

After the nuclide is produced, the samples are "eroded" by updating the depths for the sample by using the erosion rate and the time step, as shown in Equation 2.48.

$$D_{new} = D_{previous} - \Delta t * \epsilon \tag{2.48}$$

Where D_{new} is the new depth, D_{prev} is the previous sample depth, and ϵ is the erosion rate of the surface.

These steps are repeated from t=-age, with the sample at depth, until t is equal to the year sampled, when the sample reaches the surface. The inventory is then returned by the module and used in any number of other functions, such as surface or depth-profile calculators, or simply returned to the user.

2.6 Scaling

Cosmogenic nuclide scaling applies the physics governing the modulation of the cosmic ray flux by atmospheric mass and the terrestrial and solar magnetic fields to provide production rates as a function of location and exposure time. Numerous scaling models have been proposed in order to correct for latitude, elevation, atmospheric pressure anomalies, geomagnetic field changes, non-dipole effects, and solar modulation. For all the details of the scaling models themselves, please see the original papers (cited in Table 2.1); for details of implementation, please see the description in Balco (2007) and Lifton (2012).

The fundamental correction for elevation and latitude is the key part of each scaling model. The first scaling model to implement this was Lal (1991). Eventually, Stone (2000) reformulated the original equations to take atmospheric pressure, instead of elevation, as an input. This is still a commonly cited scaling model. However, the original, time-independent Lal/Stone scaling (abbreviated as St in the code) does not account for changes in production rate that we know are occurring through time due to changes in the geomagnetic field.

The production rates of cosmogenic nuclides are a function of the magnetic field strength. As the geomagnetic field of the earth changed in the past, production rates of the nuclides also changed. This fact has led to the development of scaling models that incorporate the geomagnetic history of the earth. Dunai (2000) (Du) , Desilets et al. (2006b); Desilets and Zreda (2003) (De) , and Lifton et al. (2005, 2008) (Li), and Sato et al. (2008) (Sa) have all implemented different models to incorporate the changing magnetic field. Following Balco et al. (2008), we have also provided the time-dependent Lal scaling (Lm, including geomagnetic effects as described in Nishiizumi et al. (1989)) in order to differentiate between the geomagnetic effects and other differences in the models.

Abbr.	Reference	Description
St	Lal (1991); Stone (2000)	Time-independent (constant production rate). Based on two different types of neutron detection methods (photographic emulsions and neutron monitors). Scaling factor inputs are geographic latitude and atmospheric pressure, based on the Stone (2000) modification.
Lm	Lal (1991); Nishiizumi et al. (1989)	Time-dependent version of St based on time-variation in the dipole magnetic field intensity, as formulated by Nishiizumi et al. (1989).
Li	Lifton et al. (2005, 2008)	Time-dependent model based on neutron monitor measurements and incorporating dipole and non-dipole magnetic field fluctuations and solar modulation. The scaling factor is based on actual atmospheric pressure, solar modulation, and a cutoff rigidity calculated using trajectory tracing.
Du	Dunai (2000, 2001a,b)	Time-dependent model based on neutron monitor measurements and incorporating dipole and non-dipole magnetic field fluctuations. The scaling factor is based on an analytically calculated cutoff rigidity and atmospheric pressure. A long-term mean for solar modulation is used in this model.
De	Desilets et al. (2006b); Desilets and Zreda (2003)	Time-dependent model based on neutron monitor measurements and incorporating dipole and non-dipole magnetic field fluctuations. The scaling factor is based on a cutoff rigidity calculated using trajectory tracing and the actual atmospheric pressure.
Sf	Lifton (2012); Sato et al. (2008)	Time-dependent model based on equations from a nuclear physics model and incorporating dipole and non-dipole magnetic field fluctuations and solar modulation. The scaling factor is based on actual atmospheric pressure, solar modulation, and a cutoff rigidity calculated using trajectory tracing. The total flux (protons+neutrons) is used to scale all reactions.
Sa	Lifton (2012); Sato et al. (2008)	Time-dependent model based on equations from a nuclear physics model and incorporating dipole and non-dipole magnetic field fluctuations and solar modulation. The scaling factor is based on actual atmospheric pressure, solar modulation, and a cutoff rigidity calculated using trajectory tracing. Nuclide-dependent scaling by incorporating cross-sections for the different reactions.

Table 2.1: Table of scaling models, including abbreviations, original references, and a brief description of each model.

Time period (kyr)	Model name	Reference
3-7ka	CALS7k	Korte and Constable (2005)
7-18ka	GLOPIS-75	Laj et al. (2004)
18ka-2Ma	PADM2M	Ziegler et al. (2011)

Table 2.2: Geomagnetic history used in all the scaling models.

In CRONUScalc, the geomagnetic history is consistent across all scaling models, even though each model uses the history in a slightly different manner. This information is available in the code and can be modified directly if a different geomagnetic history is necessary. References for the current geomagnetic history being used can be found in Table 2.2. The Lifton et al. (2005) and the more recent model presented in Lifton (2012) (Sa) also incorporate the effects of solar modulation into the scaling model.

In each scaling model that incorporates geomagnetic effects, the appropriate input is cutoff rigidity. However, each scaling model implements the rigidity cutoff calculations differently (summary of these differences in Schimmelpfennig (2009)). See each original scaling reference for the equations for cutoff rigidity. In the program, each scaling model discussed up to this point is taken directly from Balco et al. (2008) and complete descriptions can be found in the original calculator supplemental material (Balco, 2007).

A recent model by Sato et al. (2008) provides an energy-dependent breakdown of incoming cosmic rays at any point on the earth's surface and has led to the creation of a new scaling model. While the equations in Sato et al. (2008) were not originally intended for this purpose, Lifton has modified the Sato model to incorporate the geomagnetic models and the solar modulation effects so that it can be used as a cosmogenic nuclide scaling model (Lifton, 2012). Using this combined model, referred to as the Lifton/Sato model (abbreviated Sf to distinguish

it from the previous Lifton et al. (2005) scaling model), we are able to calculate the neutron and muon flux at any site given the latitude, longitude, and elevation by calculating the combined proton and neutron flux at the site of interest and dividing by the flux at a reference location (SLHL).

The energy-dependent calculations in the Sf model provide the opportunity to create a nuclide-dependent scaling model (Sa) in addition to the "flux-only" model presented above. Nuclide-dependent scaling incorporates physics modeling of the atmosphere and experimental measurements of cross-sections to scale each nuclide based on its reaction energies. This should produce a better prediction of the production from each nuclide, although there is some debate as to the validity of nuclide-dependent scaling given our current level of analytical uncertainty (Schimmelpfennig et al., 2011). Although geologically based production rates are used in the code, the physics-based production rates are used to scale each reaction. The cross-sections were determined using beam irradiation experiments and are interpolated between measurements (Reedy, 2011). The cross-sections for a particular reaction at a particular energy are then multiplied by the incoming flux of neutrons at that energy. This yields the physics-based production rate for a particular reaction and energy. The individual physics-based production rates at each energy are then integrated to yield a complete physics-based production rate for the nuclide, adding the reactions together to produce a single production rate for each nuclide. This is summed for both protons and neutrons. The physics-based production rate is calculated both at the site (the specific latitude, longitude, and elevation) and at the reference location (SLHL). The site production rate is then divided by the reference production rate to yield the nuclide-dependent scaling factor. For all nuclides, this is done for each reaction. In the case of chlorine-36, this results in six nuclide-dependent scaling factors for chlorine, including two low-energy scaling factors to scale thermal and

epithermal neutron production. In all other non-Lifton/Sato scaling models, the nuclide-dependent scaling factors still appear in the code, but all are set equal to the single scaling factor produced by the selected scaling model. The cutoff rigidity used in the Lifton/Sato scaling models are the same as the Lifton model discussed above.

Examining results from multiple scaling models for any particular site allows users to assess the confidence in the age results. Goodness of fit with the scaling models is discussed in the CRONUS calibration papers (Borchers and Stone, 2012). Results from all the scaling models are available in the CRONUScalc program and users are encouraged to look at the variability between models when assessing results from a particular site.

While there are seven different spallation scaling models, CRONUScalc uses only one muon scaling model to adjust for latitude and elevation. Muons were not directly scaled in any of the original models, so we use the newest, calibrated muon model for muon production. The Sato/Heisinger muon model is discussed fully in Section 2.4.4. The Sato/Heisinger muon production model does not directly use a scaling factor. Instead, the scaled production rates are produced directly by the code because scaling occurs inside the code.

A new input to the code is the "year collected" that allows the scaling models to account for the time of exposure more completely. In previous calibrations, the independent age constraints have been listed as "before present." For radiocarbon analyses, this is actually "years before 1950." The calibrations have been updated accordingly and now list independent ages as "years before 2010" and the aging routines in CRONUScalc now integrate production through the collection year. For most samples, this is not a critical change, but does provide a more

accurate estimate of production or age, which will only become more important through time. The sample is assumed to have been processed shortly after collection or to have been stored where continued production and decay would be insignificant. For some nuclides, such as ^{14}C, the change from integration to 1950 through 2010 could make a measurable difference in the predicted concentration.

2.7 Nuclide-Specific Considerations

While the cosmogenic nuclides share many similarities in terms of production pathways, they are each produced by a different combination of pathways and there are other individual issues that need to be addressed. In the following sections, the specific pathways for production, uncertainties, and other issues are documented for each of the major four code modules representing five nuclides.

Each nuclide is produced by one or more of the pathways discussed in the previous section. The most common reactions are shown in Table 2.3 for the common nuclides and their common target minerals.

2.7.1 Aluminum-26 & Beryllium-10

Beryllium-10 is the most commonly used cosmogenic nuclide and also provides the most consistent datasets. ^{26}Al is also produced in quartz and is commonly processed in the same samples as ^{10}Be. Both nuclides are produced in quartz through only two mechanisms: spallation and muogenic production. Muogenic production of ^{10}Be and ^{26}Al accounts for only $\sim$3.6% and $\sim$4.5%[1] of total surface production, respectively (Heisinger et al., 2002b).

[1]The predictions of Heisinger et al. (2002b) have been shown to overpredict measured concentrations, so these values are approximations only.

Nuclide	**Reaction**
^{3}He	Spallation: O, Mg, Si, Ca, Fe, Al
	^{6}Li(n,α)^{3}He
^{10}Be	^{16}O(n,4p3n)^{10}Be
	^{28}Si(n,x)^{10}Be
	^{16}O(μ^{-},αpn)^{10}Be
	^{28}Si(μ^{-},x)^{10}Be
^{14}C	^{16}O(μ^{-},2p)^{14}C
	^{16}O(n,2pn)^{14}C
	^{17}O(n,α)^{14}C
	^{28}Si(n,x)^{14}C
^{26}Al	^{28}Si(n,2pn)^{26}Al
	^{28}Si(μ^{-},2n)^{26}Al
^{36}Cl	^{40}Ca(n,2n3p)^{36}Cl
	^{39}K(μ^{-},p2n)^{36}Cl
	^{40}Ca(μ^{-},α)^{36}Cl
	^{35}Cl(n,μ^{-})^{36}Cl
	^{39}K(n,α)^{36}Cl

Table 2.3: Common reactions producing cosmogenic nuclides (Gosse and Phillips, 2001). The symbolism is as follows for the X(a,b)Y reaction: X is the target element, a is the particle interacting with the target, b is emitted during the reaction, and Y is the final nuclide product. Reactions are only shown for the pathways discussed in the paper. For beryllium, aluminum, and carbon, only reactions possible in a quartz target mineral are shown.

When aluminum-26 and beryllium-10 are both being analyzed far a particular sample, they can be processed in the same quartz split. The code is designed similarly to Balco et al. (2008) in order to allow the samples to have data from either beryllium-10 or aluminum-26, or both nuclides in any sample. The production rates for both nuclides have only been determined reliably in quartz, so this is the only lithology supported by CRONUScalc.

Additional information, such as erosion rate or burial history, can be determined if more than one nuclide is analyzed in a sample (Bierman, 1994; Granger, 2001). The common Al/Be pair is frequently used for these investigations. In the near future, CRONUScalc (and the accompanying user interface) will be designed to calculate and plot useful information for a couple of the most frequent paired studies, such as determining erosion rate or burial history.

For information on the production rates used in the calculator, see the CRONUS-Earth spallation production rate calibration paper (Borchers and Stone, 2012) and the CRONUS-Earth muon calibration paper (Stone and Borchers, 2012).

2.7.2 Chlorine-36

Cosmogenic chlorine-36 is produced by the full range of pathways discussed in the production systematics section above. The main three pathways are spallation (Ca, K, Ti, Fe), low-energy neutron absorption (Cl), and muogenic production (Ca, K, Ti, Fe).

There have been production rate discrepancies of up to 40% cited between different production rate studies in the past. The CRONUS-Earth project is addressing these issues and much of this is discussed in Chapter 8. For spallation

production rates, only CRONUS data is used in the calibration and the resulting production rates appear to be very robust and have small uncertainties. For the low-energy neutron production pathway, there are more possible complicating factors, such as water content or geometry, which are discussed in detail below. CRONUS-Earth data and legacy data are being combined to thoroughly address these issues and produce a $P_f(0)$ value that provides the most reasonable results for the largest number of samples.

Water content in the sample can change the low-energy neutron flux and can therefore affect the production of chlorine-36 through the low-energy pathway. Water acts to thermalize higher energy neutrons as well as absorb lower energy neutrons (Evans, 2001). Despite the clear evidence of this potentially large effect on sample ages or calibrations, the water content of the rock is usually estimated and not measured (Dep et al., 1994a). In samples where the water content of the rock is measured, the water content of the surrounding few meters of rock or soil may also be contribute to the moderation of low-energy neutrons (Zreda et al., 2008). Environmental water content of surface rocks (i.e., pore water) usually varies as a function of season and time since the most recent precipitation event, and therefore even measurement of the water content at the time of sampling does not adequately constrain the long-term average water content.

The importance of water content was demonstrated by Dep et al. (1994b) where the modeled thermal neutron flux and chlorine-36 production are shown for samples with identical compositions but with varying water contents of 1%, 2% and 4%. In the study, the thermal neutron flux increases by 20% with each increase in water content and total production increases by approximately 7% with each increase. These values indicate the significant uncertainty that could

be introduced by imprecise water contents. Dep et al. (1994b) also mentions the increase in uncertainty in porous rock types where water content could vary significantly through time.

The above evidence indicates that water content can play a large role in the production of chlorine-36 via the low-energy neutron pathway, especially if snow or other known water sources are present for a significant period of time. Ideally, dating of chlorine-36 samples would be done on mineral separates to eliminate the uncertainty associated with this pathway (Schimmelpfennig et al., 2009). The $P_f(0)$ value that was obtained during the CRONUS-Earth calibration has a larger uncertainty than the other parameters, likely due to differences in geometry or water content, as discussed above. The calibration indicates that a single value of $P_f(0)$ is appropriate for most sites. However, whole-rock chlorine-36 is commonly performed on only a small number of lithologies and settings, so the calibration may be skewed towards the values obtained in those lithologies, such as basalts. This single $P_f(0)$ value may not be appropriate for every site and individual considerations must be accounted for in advanced calculations. For the lowest uncertainty, mineral separates should be used if possible.

For nuclides that can be produced from neutrons released during radioactive decay of elements like uranium, the production from these reactions is calculated and subtracted prior to any other calculations. The assumption is that the material has come to equilibrium with the production and absorption of neutrons. The equilibrium concentrations of the cosmogenic nuclides are calculated using the formulas in Fabryka-Martin (1988). That amount is subtracted from the measured concentration. In most studies, the rocks (not the exposure age) are sufficiently old that the assumption of equilibrium is reasonable. Even for

younger features, such as a newly-erupted basalt, the assumption of equilibrium is reasonable due to equilibration with the uranium and thorium concentrations prior to eruption, so long as the magma did not undergo differentiation or mixing that changed its U and Th contents less than ~ 0.5 Ma prior to sampling.

For chlorine-36, there are numerous input parameters including compositional parameters. The code allows for the input of a "target" composition, which is only the five chlorine-36 producing elements, in addition to the traditional "bulk rock" composition, which is the whole rock composition prior to any processing. The bulk rock composition includes trace element data, such as boron and uranium, that allows for the appropriate calculation of neutron absorption properties of the rock and radiogenic subtraction.

Isotope Dilution Mass Spectrometry (IDMS) Isotope Dilution Mass Spectrometry (IDMS) is a standard method for highly accurate elemental and isotopic analysis. In cosmogenic nuclide applications it is commonly used for analysis of ^{36}Cl and elemental Cl. The process includes adding a "spike" of known isotope ratio that has been enriched in one of the stable chlorine isotopes, either ^{35}Cl or ^{37}Cl. In either case, the ratios of ^{36}Cl/^{35}Cl and ^{35}Cl/^{37}Cl are measured at the accelerator. The stable chloride concentration and the ^{36}Cl concentration of the rock can both be back-calculated using the ratios from the accelerator and the dissolution information of the spike and sample mass. The process is described in detail in Desilets et al. (2006a).

When using IDMS for chlorine, there is a correlation between the uncertainties in stable chloride concentration and the uncertainties on chlorine-36 concentration. In order to produce the correct uncertainties from raw laboratory results, a set of additional codes were created to handle this calculation. This code

is external to the main CRONUScalc program, but is distributed with the code. It is designed to assist the user in calculating the correct concentrations of ^{36}Cl and Cl and correctly assigning their uncertainties. A linearized uncertainty method was used to calculate the stable chlorine concentration. However, the traditional error propagation does not work for low-Cl samples due to the non-linear response in this range, so uncertainties are calculated using a Monte Carlo method. In the Monte Carlo code, the uncertainty in the stable chlorine concentration is calculated 10,000 times using the nominal inputs (spike mass, sample mass, spike concentration, etc.) and a random uncertainty. The random uncertainty added to each input is calculated by multiplying the given uncertainty in that parameter by a random number generated from a normal distribution with mean of one and standard deviation of one. For samples with high chlorine concentrations, the Monte Carlo result is essentially the same as the linearized approximations; however, at low chlorine concentrations, the uncertainties can be a significant percentage of the total concentration (>90%). The IDMS calculator is discussed in more detail in Appendix D.1.

For information on the chlorine-36 production rates used in the code, see the final chapter of this dissertation, Chapter 8.

2.7.3 Carbon-14

Production of cosmogenic carbon-14 is primarily from the spallation of oxygen, but also other elements including Mg, Al, and Si (Dunai, 2010). Unlike beryllium-10, muons contribute significantly (14%)[2] to the cosmogenic production at the surface and increasingly at depth (Heisinger et al., 2002b). Quartz is

[2]Muon production by Heisinger et al. (2002b) calculates predicted ^{10}Be concentrations that are significantly too large when compared with data from deep cores, so this percentage is possibly too high as well.

the only commonly measured lithology, although it is possible to measure cosmogenic ^{14}C in other lithologies (Handwerger et al., 1999; Dunai, 2010). Carbon-14 has a short half-life and therefore reaches saturation relatively quickly ($\sim$20 kyr) (Lifton et al., 2001). Due to these factors, ^{14}C is well-suited to short-term erosion rate studies and young burial history studies (Dunai, 2010).

There are significant problems with the reproducibility of ^{14}C analyses, leading to larger uncertainties in the production rate parameters. This applies especially to earlier methods of pyrolysis or hydrolysis, as discussed in Lifton et al. (2001). The newer method used by Lifton et al. (2001) is a stepped combustion method, but significant scatter is still seen in some results. This results in larger uncertainties on the production rate parameters, as calibrated by the CRONUS-Earth Project.

In CRONUScalc, only the production of ^{14}C in quartz by spallation and muons is available. This should provide adequate functionality for the majority of ^{14}C users. For information on the ^{14}C production rates used in the calculator, see the CRONUS-Earth spallation production rate calibration paper (Borchers and Stone, 2012).

2.7.4 Helium-3

Cosmogenic helium-3 is produced primarily by spallation reactions on most elements present in a rock (Mg, Si, Fe), but also through low-energy neutron production on lithium. Typically, production via the lithium low-energy pathway is only important in high-lithium rocks (Dunai, 2010). Currently, CRONUScalc only incorporates the spallation production for helium-3. There is no measurable contribution to production via muon pathways (Kurz, 1986; Dunai, 2010). For

most applications, helium-3 is measured in olivine or pyroxene because quartz and plagioclase do not quantitatively retain helium (Cerling, 1990). Currently, only a single production rate from the combined olivine and pyroxene dataset has been calibrated so only these two mineralogies are included in CRONUScalc.

When measuring helium-3, the inherited (magmatic) component must be subtracted from the measured concentration in order to examine only the cosmogenically produced helium-3. This is done through crushing and then stepwise heating of each sample (Kurz, 1986; Cerling, 1990). The input needed for CRONUScalc is the cosmogenic atoms of helium-3 per gram. CRONUScalc assumes that any corrections for blanks or inherited component have already been performed.

The production rate of helium-3 is dependent on the mineral phase, the dataset, and the scaling model. The data used for helium-3 calibration includes both official CRONUS data as well as high-quality external datasets. The sites included in the calibration are based entirely on the compilation by Goehring et al. (2010b). For information on the ^{3}He calibration, see the CRONUS-Earth spallation production rate calibration paper (Borchers and Stone, 2012).

Future versions of the calculator may provide the option of entering compositional information in order to account for the low-energy production in the sample. This would increase the applicability of CRONUScalc to helium samples with higher Li contents.

2.8 Discussion & Cautions

2.8.1 Atmosphere and Elevation Relationships

The relevant inputs are both elevation and atmospheric pressure for the sample. Elevation, which is more easily measured and can be found on a topographic map even after sampling, is the traditional input for these codes. The additional pressure input is necessary because it is the more accurate measure of the sample location in the atmosphere. If the sample pressure is not independently determined, it can be converted using one of the common atmospheric relationships. The ERA40 code is the interpolation of comprehensive global observations and analyses over a 45 year period, as discussed in Kållberg et al. (2007). This module is available with the code in order to facilitate this conversion. The production-rate calibrations were all done using pressures determined by ERA40 and it is recommended that this conversion be used unless there is a specific reason to suspect a different pressure relationship. In some rare cases, the actual site pressure varies from the predictions discussed above. For these sites, the best choice is to directly input the estimated average site pressure over the lifetime of the sample exposure. This is best done only by advanced users familiar with the information necessary to make the best estimate (climate models of past variability, etc.).

Uncertainty in the sample pressure is a significant contributor to sample uncertainty. The uncertainty associated with the pressure based on uncertainties in elevation are quite small ($<$1 hPa for elevation uncertainties up to 15 m). This results in only a small amount of total uncertainty on the sample age ($<$1%). A more realistic source of uncertainty associated with pressure is the difference between the current pressure and the integrated pressure over the exposure time of

the sample. The pressure history through time is not a factor that can be accurately calculated. Our assumption that the pressure has remained relatively constant through time adds additional uncertainty. We have added an uncertainty of 5 hPa to account for this and this addition results in uncertainties of 2-5% for most samples.

2.8.2 Uncertainties Due to Scaling

Not all scaling models fit the data equally well. For each nuclide, a single dataset was used to produce a production rate for each combination of scaling model and nuclide. As part of the beryllium-10 calibration, the fit of each scaling model tot he data will be produced. In order to accurately assess uncertainty due to scaling models, results from multiple models should be compared. A second issue associated with scaling is the uncertainty from determining the scaling factor at a new location that is not a calibration site. The exact uncertainty due to scaling is unknown at a new location, but an estimate can be obtained using "leave-one-out cross-validation" (see Borchers and Stone (2012) for details).

2.8.3 Program Evolution

The code is designed to produce a predicted concentration at a particular depth for the specified nuclide. This is done using a function called `predNXX` or `predNXXdepth`, where XX represents the desired nuclide (i.e. `predN36depth` calculates production of chlorine-36). There are a few preliminary code modules necessary to build the inputs required for the main code. These include creating constants (`physpars`), calculating scaling factors (`scalefacsXX`), organizing the

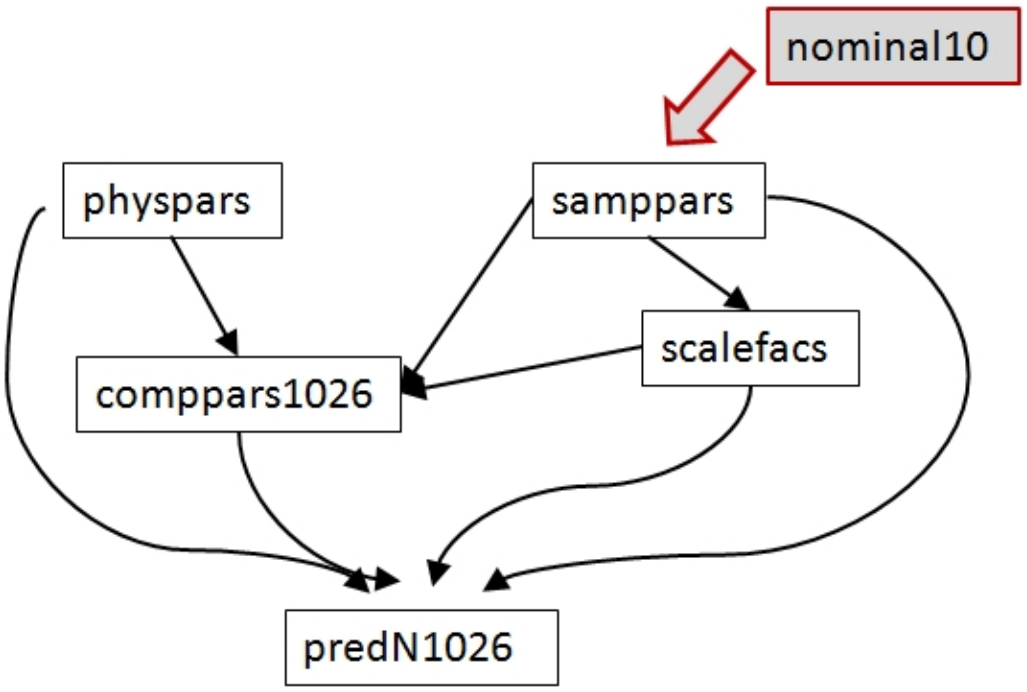

Figure 2.8: Data flow diagram showing the relationship between different parts of the code for a beryllium-10 sample. Inputs include the nominal inputs (`nominal10`) and the uncertainties on each of those inputs (`uncerts10`, not shown). Other code pieces (`physpars`, `samppars10`, `comppars10`, and `scalefacs10`) set up the correct variables for the upper-level code pieces. `predN36` predicts the concentration for a given age and depth.

input parameters (`sampparsXX`), and computing sample-dependent parameters that are needed in production calculations (`compparsXX`). These are not discussed in detail here, but can be found in the function appendix. `PredNXX` uses all this preliminary information in order to predict concentrations of the nuclide. This is summarized in Figure 2.8.

This program has several differences as compared to previous calculators. The CRONUScalc program is designed to work for all the commonly used nuclides, including ^{10}Be, ^{26}Al, ^{3}He, ^{36}Cl, and ^{14}C, with ^{21}Ne to be added soon. The modular nature of the program means that the scaling models are all applied in an identical manner to each nuclide, avoiding any possible inconsistencies from

errors in coding or using two different calculators for cross-nuclide comparisons. The addition of a new scaling model by Lifton/Sato (Lifton, 2012) allows for a physics-based calculation of the incoming cosmic-ray flux as well as nuclide-dependent scaling models that incorporate the individual nuclide reaction cross-sections.

This versatile program is able to calculate production and accumulation for any given sample as well as perform calibrations and calculate surface sample and depth-profile ages. This is the first calculator to provide both surface sample and depth-profile aging abilities based on the same underlying code. Included in the surface calculator is the ability to age a single sample at depth.

Other features that are not clearly visible when using the program are the new integration method and the improved muon production formulation. Previous calculators relied on analytical solutions to integrate over depth. In this program, a numerical depth integration is performed, which removes approximations necessary in the analytical solution to the depth integration. This results in a more accurate inventory of accumulated nuclide in the sample. The new muon production is scaled by both elevation and latitude, based on the Lifton/Sato scaling model (Lifton, 2012), and includes new production rate parameters calibrated from deep profiles for ^{10}Be, ^{26}Al, and ^{36}Cl (from both Ca and K). Both of these features are not visible in the upper levels of the program, but they improve the overall performance.

Finally, although this paper discusses primarily the code behind the program, there is an online interface for the surface and depth-profile calculators available to the public. This simplifies the process and makes the technique available to a much broader range of users. The online calculator provides at least two

different assessments for uncertainty, one from the analytical propagation of uncertainties based on the age derivatives and one that includes the more realistic uncertainties proposed by the CRONUS-Earth project based on comparison of real-world data to the predictions of this program. The interface and instructions for its use will be discussed in a future paper.

2.8.4 Calibration Technique

The production rates incorporated into the CRONUScalc code are the results from the CRONUS-Earth Project calibration. The spallation calibration for all nuclides is discussed in detail in Borchers and Stone (2012). The calibration used orthogonal distance regression instead of the traditional least-squares fit used in previous calibrations. The least-squares method typically assumes that there are no uncertainties on the independent variable. This calibration improves upon previous calibrations by using orthogonal distance regression (ODR). Generally, ODR allows both dependent variables (in this case, sample data) and independent variables (e.g., radiocarbon age constraints) to have uncertainty in the curve-fitting process by minimizing the orthogonal distances to the curve instead of minimizing purely vertical or horizontal distances to the curve (Boggs et al., 1987). The use of ODR for the calibration of surface samples can provide a better fit to the data leading to smaller overall uncertainties in the calibrated parameters.

2.9 Surface Sample Calculator

Most researchers employing cosmogenic nuclides have been using individually coded or publicly available surface exposure-age calculators. This calculator has an advantage because it is designed for use with all the common

nuclides. The Balco et al. (2008) calculator put the Al/Be cosmogenic nuclide community on a consistent platform. However, this did not apply to any other nuclides and the code did not fully propagate uncertainties. This code, and the associated calculator, is an improvement due to the multi-nuclide capability, full propagation of uncertainties, and the new ability to work with single samples at depth.

Using the equations given in the previous sections, we can compute the rate of production of a cosmogenic nuclide at any depth within the subsurface at any point in the past. This production rate varies over time due to time-dependent scaling as well as varying due to changes in depth caused by erosion or aggradation. While the nuclide is accumulating it is also continuing to decay- the radioactive decay rate must be subtracted from the production rate. The time-dependent production rate can be numerically integrated over time in order to predict the concentration of the cosmogenic nuclide at a specific depth after a specified exposure history. By averaging the accumulated production at depths throughout the thickness of a sample, we can predict the average concentration of the cosmogenic nuclide as a function of the exposure age of the sample.

2.9.1 Computing the Exposure Age

To compute the exposure age of a sample, we begin by computing the sample-specific saturation concentration. This is done by predicting the accumulated concentration in the sample after a very long exposure (for ^{14}C, 50 kyr is generally sufficient, although a longer period like 2 million years is more appropriate for long-lived nuclides like ^{10}Be and ^{26}Al). If the measured concentration of the cosmogenic nuclide is close to or exceeds the saturation concentration, then

it is not possible to determine an exposure age for the sample because the sample is effectively saturated. If not, then we use the bisection method to find an age at which the predicted concentration matches the measured concentration of the nuclide.

The actual functions that are used to calculate the age of a chlorine-36 surface sample are shown in Figure 2.9. The data flow diagram shows the inputs, main code that is called, and the underlying code that is used during the calculations. The data flow is very similar for all other nuclides. The inputs to the code, `nominalXX`, include the location information (lat/long/elev/pressure), site information (erosion rate, shielding, attenuation length), and sample information (thickness, density, depth to top of sample, cosmogenic nuclide concentration, and year collected). For chlorine-36, additional information about the composition of the target and bulk rock are required as inputs, as is the covariance between the uncertainties on ^{36}Cl and stable Cl, which is its own input variable, `cov36`. All the details of the inputs for all nuclides are discussed in Appendix D.2. Uncertainties are allowed on every input parameter and are included in the `uncertsXX` parameter. The main inputs, `nominalXX`, are used by the function `cl36ageraw` to compute only the exposure age of the sample, while `cl36age` uses the uncertainties on the input parameters and the covariance between the ^{36}Cl and stable Cl uncertainties to compute the overall uncertainty on the sample. Within `cl36ageraw`, the variables are set up using a set of lower-level codes (`physpars`, `sampparsXX`, `compparsXX`, `scalefacsXX`). The variables are then used by `computeage36`, which uses the bisection method to find the matching concentrations. Those concentrations are predicted using the `predNXX` code. The best-fit age is then returned to `cl36age`, which then calculates the uncertainties and returns the final result to the user. Details on the outputs for each nuclide are included in Appendix D.3.

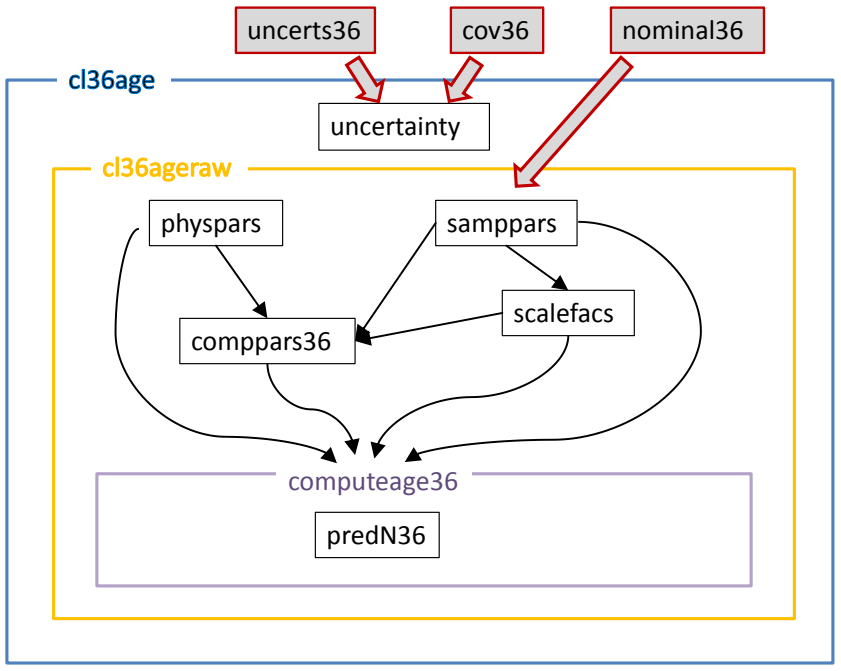

Figure 2.9: Data flow diagram showing the inputs and code used to age a chlorine-36 surface sample. Shaded boxes indicate inputs to the code. Arrows indicate where outputs are used by other code pieces. Inputs include the nominal inputs (`nominal36`), the uncertainties on each of those inputs (`uncerts36`), and the covariance between the total chlorine concentration and the ^{36}Cl concentration (`cov36`). Other code pieces (`physpars`, `samppars36`, `comppars36`, and `scalefacs36`) set up the correct variables for the upper-level code pieces. `computeage36` uses `predN36`, which predicts the concentration for a given age and depth, to calculate the best-fit age for a sample. The wrapper scripts, `cl36ageraw` and `cl36age`, perform all the calculations for sample aging without and with uncertainty calculations, respectively.

2.9.2 Input Uncertainties and Derivatives

The computed exposure age for a sample depends on a number of other sample parameters, including its thickness and density, the assumed erosion rate, the assumed atmospheric pressure at the exposure site, etc. For each of these parameters, we compute the derivative of the computed exposure age with respect to the parameter by finite difference approximation. If the user supplies uncertainties for these parameters, then we can use these derivatives to propagate the uncertainties in the parameters into an uncertainty on the computed exposure age (Bevington and Robinson, 1992).

The code allows for extensive quantification of the uncertainties associated with a sample. The commonly reported uncertainty, that from AMS analysis, only represents the minimum uncertainty in the age of an unknown. There are uncertainties in the other measurements (chemical concentrations, field measurements, etc.), production rates, scaling, and laboratory processing. Each of these sources adds a small amount of uncertainty to the age of the sample. There is the option to add uncertainties to every input parameter in the `uncertsXX` input parameter. This is a new feature unavailable in other single-sample surface exposure age calculators. This idea was addressed in the multi-sample depth profile calculator using Monte Carlo methods presented by Hidy et al. (2010), but is treated more systematically here.

Based on a sensitivity analysis with realistic uncertainties on all the parameters, there are some uncertainties that are insignificant. For example, realistic uncertainties on latitude are not important when compared to uncertainties on the concentration. Other variables that realistically do not require uncertainties include longitude, shielding, and year collected. On the other hand, relatively

large uncertainties are expected on parameters such as erosion rate and water content because these require estimation and some knowledge of the site and can rarely be precisely calculated.

When comparing different nuclide results, especially those from different sites, all uncertainties must be assessed in a consistent manner. The uncertainties from scaling and methodological considerations become primary issues. The CRONUS project has done a series of interlaboratory studies (details in Jull et al. (2011); Jull and Scott (2012)) to address the uncertainties that arise solely from different processing techniques and accelerator measurements. These results were used to incorporate realistic uncertainty into the samples used for calibration.

2.10 Depth Profile Calculator

The depth profile calculation is formulated as a Bayesian inverse problem. This approach has several advantages. First, unlike using a classical statistics approach to parameter estimation, the Bayesian approach treats unknown parameters as a random variables. Doing so allows the resulting fitted parameters to be reported as expected values, accompanied by a probability distribution. Second, this approach allows the user to submit prior information or expert knowledge, influencing the solution. The selection of a informative[3] prior will strongly bias the resulting posterior distribution. Therefore the responsible user is obligated to report the effect that different priors have on their solution. Third, from a computational standpoint, the method presented in the next section is not susceptible to the convergence failures that iterative line-search solvers can encounter in certain cases.

[3]The word informative is used to describe a distribution in which most to the probability is clustered over a relatively small range.

Performing the depth profile calculation requires the simultaneous estimation of three parameters: age (t), erosion rate (ϵ), and inheritance (inh). The steps necessary for the computations are summarized here. First, an evenly spaced, 3-dimensional grid over the parameters of age, erosion rate, and inheritance is created. Note that the spacing is consistent only within each dimension and the parameter range for each is specified by the user. Second, the misfit χ^2 value is calculated at each node (each age, erosion rate, and inheritance point) using Equation 2.49.

$$\chi^2_{t,\epsilon,inh} = \sum_{i}^{n} \left(\frac{x_i}{\sigma_i} \right)^2 \tag{2.49}$$

where

$$x_i = ConcPred_{t,\epsilon,inh} - ConcMeas_i$$

Next, the approximated χ^2 hyper-surface is transformed into a likelihood surface using Equation 2.50.

$$L(\mathbf{x}|\boldsymbol{\theta}) = \prod_{i=1}^{n} \left(\frac{1}{\sqrt{2\pi\sigma_i}} \right) \cdot \exp\left(-\frac{\chi^2_{t,\epsilon,inh}}{2} \right). \tag{2.50}$$

Finally, the joint posterior from the likelihood we use Bayes rule, shown in Equation 2.51.

$$p(\boldsymbol{\theta}|\mathbf{x}) = \frac{L(\mathbf{x}|\boldsymbol{\theta})\pi(\boldsymbol{\theta})}{\int_{-\infty}^{\infty} L(\mathbf{x}|\boldsymbol{\theta})\pi(\boldsymbol{\theta})d\boldsymbol{\theta}}. \tag{2.51}$$

Where $\pi(\boldsymbol{\theta})$ is the joint prior distribution set by the user on the following parameters: age, erosion rate, and inheritance. A trapezoidal integration scheme is used to calculate the denominator, leaving the joint posterior density, $p(\boldsymbol{\theta}|\mathbf{x})$.

When assigning uncertainties to a solution, it is important to determine if any multiple interactions exist between erosion rate, age and inheritance. To display these interactions, the calculator produces 3 pairwise 2-D contour plots of the joint posterior distribution with contours of 68% and 95% regions of probability. For example, integrating $p(\boldsymbol{\theta}|\mathbf{x})$ over inheritance gives the probability distribution shown in Equation 2.52. This effectively marginalizes the joint posterior over one of the three parameters. An example of the resulting 2-D contour plots are shown in Figure 2.10, along with the predicted versus measured profile plot.

$$p(er, age|\mathbf{x}). \tag{2.52}$$

The best-fitting solution is the lowest chi-squared value over the entire three-dimensional grid. This is called the maximum a posterior (MAP) solution. In the 2-D pairwise plots, the MAP solution and the apparent 2-D best-fit solution do not always coincide due to the interaction of the parameters with the third dimension. The direct calculation of posterior probabilities eliminates the need for Markov Chain Monte Carlo, as was used by Hidy et al. (2010). In contrast to Hidy et al. (2010), this code also computes a posterior probability distribution, allowing for an assessment of the probability of the resulting age being within particular age bounds.

2.11 Conclusion

The CRONUScalc program, designed simply to predict sample concentrations at a particular depth, is intended to be versatile and work quickly for the

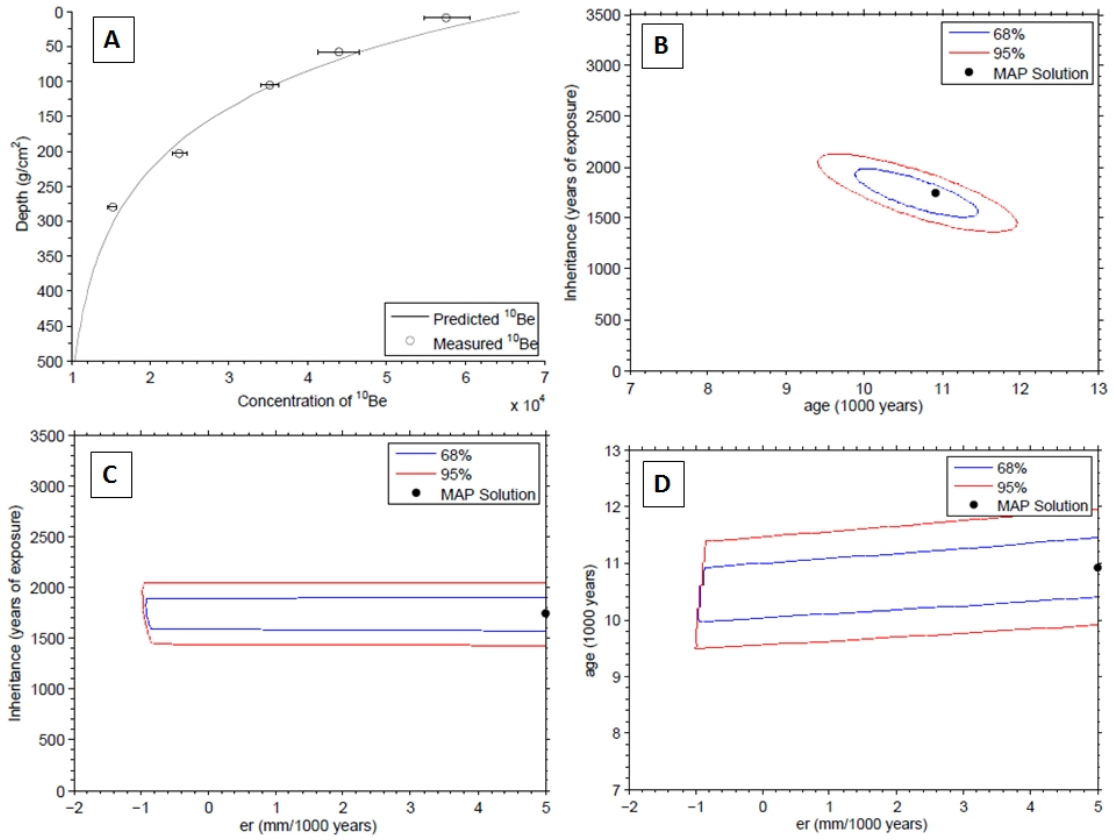

Figure 2.10: Example of the profile and pairwise plots produced by the depth profile calculator. The example is a beryllium-10 profile published by Goehring et al. (2010a) and used as an example in Aumer (2010). MAP solution is the best-fitting 3-D solution. 68% and 95% contours are the confidence intervals for the chi-squared values. (A) Figure shows the measured data and the predicted profile with depth; (B) Figure shows the confidence intervals for the plot of the inheritance and age; (C) Figure shows the confidence intervals for the plot of the inheritance and erosion rate; (D) Figure shows the confidence intervals for the plot of the age and erosion rate.

largest number of possible applications without sacrificing accuracy. However, the code is available under a public license, so advanced users can modify the code to work for an unusual scenario. The multi-nuclide code's modular format allows for all the features, such as scaling models, to be applied identically to all nuclides. The obvious new features, including a new scaling model that performs nuclide-dependent scaling, and the hidden new features, including a new muon production formulation and more accurate integration methods, improve the performance of this program over other cosmogenic nuclide calculators. The additional options to perform surface and depth-profile aging or to perform calibrations offers many options to the user.

As results from the CRONUS-Earth Project and other calibrations continue to be released, the code can be updated to reflect the most recent improvements. While the code is complete now and can be adapted to many different functions, there are future plans to develop an online calculator for these particular functions in order to remove any necessity of a Matlab license or knowledge of coding and make the code easily available to the general cosmogenic isotope user community.

CHAPTER 3

METHODS

In order to go from a calibration plan to final results, there are many different methods involved. The sample sites themselves must be picked and the individual samples collected. Those samples are then physically and chemically prepared, including measurements to determine composition. The prepared samples are then sent to the accelerator for analysis. The results from the accelerator are used in calibrations, as discussed in the calibration chapter. Details for each of these procedures is detailed below.

3.1 Sampling

The geological calibration portion of the CRONUS-Earth Project involved the work of many collaborating scientists. In this case, the sample sites were agreed upon by the entire group, while the individual samples at a specific location were determined by the smaller group of researchers who collected the samples. In both cases, the highest standards, as described in detail in the CRONUS sampling document (CRONUS, 2005), were used to select the sites.

3.1.1 Cosmogenic Nuclide Calibration Site Requirements

The principle site-selection criterion was a well-constrained age by another method. In order to perform a geologic calibration, independent confir-

mation of the age of the site was necessary. The uncertainty in that age must also be very small in order to produce an accurate production rate. In this case, the duration of the event had to be very small in order to reduce the possible uncertainty in the final production rate.

An ideal calibration location has multiple lithologies so all nuclides can be calibrated because not all nuclides can be processed from a single lithology. For example, helium-3 is commonly measured on olivine, while beryllium-10 analysis requires quartz. Ideally, lithologies would be present for analysis of all the main cosmogenic nuclides, including beryllium-10, aluminum-26, neon-21, helium-3, chlorine-36, and carbon-14.

In a practical sense, it is difficult to meet all these requirements precisely at a single geological location. The goal of this geological calibration was to use the best possible surface to calibrate all the nuclides simultaneously. In most previous calibrations, only a single nuclide was measured at any given site (examples include Phillips et al., 2001; Goehring et al., 2010b, 2011; Evans et al., 1997; Stone et al., 1996). In a limited number of studies (Licciardi et al., 2006, 2008; Nishiizumi et al., 1989), nuclides have been compared at a single location. However, one of the CRONUS Project goals was an internuclide comparison in order to answer lingering questions about scaling and production.

3.1.2 Individual Sample Requirements

Once the geological calibration site was selected, individual samples representing the desired geomorphic surface were collected. Calibration samples require strong constraints on parameters such as erosion rate and shielding while

avoiding the need for other complicated corrections, such as those for edge effects. Any uncertainties in sample parameters are carried through into uncertainty on the final production rates. The individual sample sites were chosen based on desirable characteristics decided upon by the CRONUS-Earth committee. These characteristics include high relative topographic location to avoid shielding from ash or soil or nearby objects, original surface texture to avoid eroded samples, and a sample location which was not near edges or cracks to avoid edge effects.

The high relative topography ensures that there are small or no shielding corrections for either topography, such as nearby tumuli or slopes, or cover by other material, such as ash from eruption or soil (Gosse and Phillips, 2001). The cover material is usually eroded or blown off of topographic highs and accumulates in depressions in the landscape (Zreda and Phillips, 1994). Careful sampling avoids obvious depressions where this might be a problem. In areas where cover was suspected, samples were collected from dipping surfaces to ensure that no material accumulated on the surface.

Samples with original surface texture were preferred as they indicate very small amounts of erosion. If the original surface texture, such as pahoehoe ropes, glacial polish, or wave polish, was preserved, it indicated that little erosion ($\ll 1$ cm) has occurred at that particular location (Cerling and Craig, 1994a). Finally, in order to get samples that were not near edges (Gosse and Phillips, 2001), a rock saw was used to take samples from the center of boulders or tumuli. If there were cracks, chisels were also used. Also, a rock saw provides a more consistent depth. The Bonneville site samples were collected with a rock saw and chisel, while all the other sites were collected using either the traditional hammer and

chisel or the drilling and explosives technique (used at the Peru site). The choice of collection method was due either to the difficulty of access of some sites (e.g., Huancané moraine, Baboon Lakes moraines) or due to a need to minimize the environmental impact of the sampling (e.g., Scotland, Puget Sound).

3.2 Physical & Chemical Processing

After collection in the field, the original rock samples were sent to the preparing lab, which varied by sample location. New Mexico Tech performed the initial sample preparation for the Huancané samples and Copper Canyon samples, while PRIME Lab at Purdue University prepared the Scotland, Bonneville, New England, and Baboon Lakes samples. University of Washington prepared the samples from the Puget Lowlands. The samples were photographed in detail, weighed, and density was determined for the samples. Part of each sample was crushed to fine sand size and homogenized using a commercial sample splitter according to the procedure outlined in Appendix B.2. The remainder of the sample was left as whole rock for future tests or other unforeseen needs. The homogeneous aliquots were mailed to the participating laboratories (see Table 3.1).

Starting with the homogeneous aliquot, a representative aliquot was obtained using a sample splitter. All the NMT samples presented in this work were chemically prepared in the laboratory in Socorro, New Mexico, using the procedure outlined below. This procedure was modified from Zreda and Phillips (1994). The entire process is described in detail in Appendix C.2, although a brief summary is presented here.

Laboratory	^{36}Cl MS	^{36}Cl WR	^{10}Be [–]	^{26}Al [–]	^{14}C [–]	^{3}He [–]
TAB	UW	NMT Dal Purdue				WHOI
PPT		NMT	UW LDEO LLNL UC Berk	UW LDEO UC Berk	UA	
Peru	NMT UW	NMT	UW LDEO Dart	UW		
Scotland	UW		UW Purdue	UW	UA	
NZ*			LDEO		LDEO	
NE	UW		UW LDEO	UW LDEO		
BL	UW NMT	NMT	UW			
PUG	NMT	NMT Purdue	UW	UW		

Table 3.1: Table showing the CRONUS sample processing labs for each site. (*) Site was used as a primary site but was not collected as part of the CRONUS-Earth Project. Sites above the double line are primary sites and those below are secondary. WR-Whole rock, MS-Mineral separates. Labs are identified as follows: UW-University of Washington, NMT-New Mexico Tech, WHOI-Woods Hole Oceanographic Institute, Dal-Dalhousie, Purdue-Purdue University, LLNL-Lawrence Livermore National Lab, LDEO-Lamont Doherty Earth Observatory, UC Berk-University of California Berkeley, Dart-Dartmouth, UA-University of Arizona.

The samples were leached with dilute nitric acid to remove carbonates and organic material and clean up the outer surfaces of the sample (Stone et al., 1996). At low pH, anion adsorption can cause meteoric chloride to adhere to the outer mineral surfaces. After rinsing the samples in water, a dilute base (1% NaOH for 15-60 min) was used to raise the pH and cause the chloride anions to desorb from the surface. The samples were then rinsed to neutral pH.

Using a sample splitter, a small, quantitative fraction of the leached sample was obtained and then ground to a powder. This sample was sent for XRF (X-Ray Fluorescence) to determine the major elements and an additional analysis by ICP-OES (Inductively Coupled Plasma-Optical Emission Spectroscopy) to measure elements such as uranium, thorium, and gadolinium. Some of this powder was also reserved for a chloride determination in the laboratory. For all quartz samples (Copper Canyon site), samples were split and sent for traditional XRF and ICP-OES after the initial leaching, then samples were etched with HF ICP-OES analysis was performed at the Bureau of Geology on campus in order to determine the target elements in the sample.

In the case of mineral separates, samples were physically prepared after the whole-rock sample aliquots were taken. The mineral separates were prepared by magnetic separation and then density separation using lithium metatungstate (LMT) heavy liquid. The exact preparation for the magnetic and density separations varied depending on which fraction was needed. For example, in order to obtain a feldspar separate, the Peru whole-rock material was magnetically separated and the non-magnetic fraction (containing both quartz and feldspar) was then further separated using a 2.58 g/cm^3 liquid. The 'float' portion was the desired feldspar separate. Once separated, the relatively mono-lithologic samples

were purified using an iterative process involving 1-15% HF and an ultrasonic bath. Samples were verified as clean by microscrope. The samples then followed the same steps as whole rock samples for chemical processing.

Chlorine concentrations were estimated by an in-house chlorine determination process that used an ion-specific electrode in a two-ring diffusion cell (Aruscavage and Campbell, 1983; Elsheimer, 1987). This provided an estimate of the concentration of chloride in each sample that was used to determine the amount of sample to dissolve and the amount of chlorine-35 spike to add. The chlorine-35 spike is an NaCl salt solution with the chlorine component being 99.96% ^{35}Cl. The addition of this spike to the sample allowed for more accurate measurement of the ^{36}Cl/^{35}Cl and the ^{35}Cl/^{37}Cl ratios at the AMS (Accelerator Mass Spectrometry) facility as well as an accurate measurement of the total chloride within the rock due to the use of IDMS (Isotope Dilution Mass Spectrometry). The AMS technique is discussed in detail in Section 3.3 while IDMS is covered in more detail in Section 3.5. The in-house calculated chloride concentration was used only as an estimate for initial dissolution and the more accurate IDMS results were used in the final age calculations.

The estimated chloride concentrations were used in conjunction with two computer programs, CHLOE (Phillips and Plummer, 1996) and an in-house program called LabCalcs, to calculate the amount of sample to dissolve and the amount of chlorine-35 spike to be added. This calculation is based on the age and erosion rate of the sample and is necessary to make sure the final ^{36}Cl/^{35}Cl and the ^{35}Cl/^{37}Cl sample ratios will be within the measurement capabilities of the AMS facility. The appropriate amount of sample was split out using the sample splitter and then the spike was weighed and added to the sample. The sample

was then dissolved using concentrated nitric and hydrofluoric acids. After dissolution, silver chloride (AgCl) was precipitated out of the sample and purified through successive dissolution and reprecipitations. Sulfur, an interfering isobar of chlorine-36 during AMS analysis, was removed through precipitation and syringe filtration during the purification steps as barium sulfate using a barium nitrate solution. Then the final silver chloride samples were rinsed, dried, packaged, and sent to the AMS laboratory for analysis.

3.3 Accelerator Mass Spectrometry (AMS) for Chlorine

The first AMS measurements of chlorine-36 were performed by Elmore et al. (1979). Although the samples were water and not rock, the technique is essentially the same for cosmogenic samples. The analytical technique originally designed by Elmore et al. (1979) has been updated and a more current description is included in Elmore and Phillips (1987) and Muzikar et al. (2002). The methods presented here are summarized from a combination of these publications. The basic principle behind the accelerator is that the targets (samples) are ionized, accelerated by an electric field, and then separated based on both charge and mass using a magnetic field (Muzikar et al., 2002).

The prepared AgCl samples were sent to the Purdue PRIME Lab for analysis by AMS. The AgCl sample was carefully packed into a brass target preloaded with AgBr. The sample is placed into the target and tamped down to create a flat target surface in the center. The individual targets are loaded onto a wheel and the wheel is placed into the ion source in preparation for measurement.

A cesium sputter source (1 in Figure 3.1) is used to produce negative ions from the target, in this case Cl^-. The negative ions are then accelerated to an

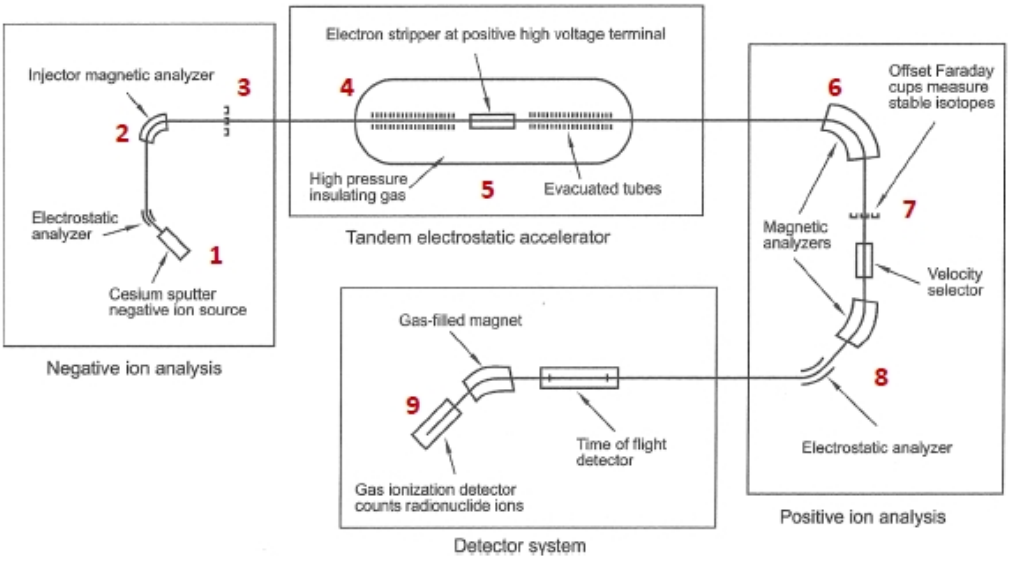

Figure 3.1: Figure showing generalized layout of a tandem accelerator, similar to the one used in this study (Muzikar et al., 2002). Numbers correspond to discussion in the text.

energy range of 40-100 keV using an electric field. The accelerated ions are passed through an injector magnet (2 in Figure 3.1) that selects for the desired mass. The ions pass into the first stage of the tandem Van de Graaf accelerator, where they are accelerated again to several MeV (4 in Figure 3.1).

In the center of the Van de Graaf accelerator, the terminal is kept at a very high potential as compared to either end. The negative ions pass through a foil stripper (5 in Figure 3.1) that removes electrons from the ions and also breaks up any molecules present in the beam. The now-positively charged ions are repelled by the terminal, accelerating the particles to energies in the range of tens of MeV.

Both the stable isotopes and the rare isotope are measured as part of AMS. The stable isotope ratio is measured as electrical current using Faraday cups since the stable ion beam is large enough to produce a readily measurably current. The stable isotopes are measured at two places: the low-energy Faraday cup (3 in Fig-

ure 3.1) and after acceleration by the Van de Graaf accelerator at the high-energy Faraday cup (7 in Figure 3.1). The measurement at the low-energy cup are more reliable and are used as the final results. The second measurement is typically slightly lower than the low end measurement, although larger differences in the measurement can indicate other problems with the accelerator.

The remainder of the line is dedicated to separation and measurement of the rare isotope, ^{36}Cl in this case. The counting is done individually using a gas ionization detector. Precautions are taken to reduce the effects of isobars that interfere with the measurement of the rare isotope. This is done in in several ways. First, the electric fields allow only negative ions to reach the detector. This eliminates interference from ^{36}Ar, which does not form a negative ion. Second, the injector magnet is selective for molecules of a particular value of ME/q^2 (M=mass, E=kinetic energy, q=charge). Any molecules not conforming to this requirement are not correctly deflected and do not continue down the line. This same procedure occurs again after the molecules have been stripped, providing an extra selectivity step. Third, the stripper causes molecules to dissociate, eliminating molecules that have the same mass/charge as the isotope of interest. Fourth, an electrostatic analyzer and a Wien filter (8 in Figure 3.1) are used to filter out particles based on E/q and velocity, respectively. Finally, the gas ionization detector (9 in Figure 3.1) measures the rate of energy loss of the ion and can reject isobars of the desired nuclide. For example, ^{36}S (Z=16) loses energy more slowly than ^{36}Cl (Z=17) because of the difference in Z (nuclear charge) (Muzikar et al., 2002). The discrimination in the final step only works if the number of atoms of the interfering isobar in the beam is not overwhelming, which emphasizes the need to perform sufficient sulfur cleanup steps during the sample preparation process.

The rare isotope concentration in a sample cannot be directly calculated because the ions are not quantitatively retained in the beam. Instead, the ratios of $^{36}Cl/^{35}Cl$ and $^{35}Cl/^{37}Cl$ are measured at the accelerator and are used later in the IDMS calculations (Section 3.5) to determine the actual concentration of total chloride and chlorine-36 in the sample. The stable isotope currents are measured in a Faraday cup while the rare isotope, ^{36}Cl in this case, is measured by individual atom-counting using the gas-ionization detector. In order to measure the isotope ratios, the current from the Faraday cup detector is selected alternately with the radioisotope counting rate (Elmore and Phillips, 1987). The stable isotope current is measured before and after each rare isotope measurement (Susan Ma, pers. comm., March 2011).

The raw accelerator results require pre-processing before distribution to the sample submitter. A series of blanks and standards are run at the beginning of each wheel in addition to one standard or blank being run after every 3-5 samples. Some corrections are performed automatically by the software, including dead time, normalization, and tailing corrections (Susan Ma, pers. comm., March 2011). The normalization is performed based on the measurement of the known-ratio standards that are consistently analyzed. In the case of a batch of samples with very large sulfur counts, further sulfur corrections may be performed. This was not the case in any of the samples presented in this work.

3.4 Inductively Coupled Plasma (ICP) Procedure

Some samples, specifically the Copper Canyon samples, required an in-house ICP analysis in order to determine the target element compositions of the

dissolved material. This was performed following the dissolution procedure provided by J. Stone (pers. comm., June 14, 2010) and then following the in-house procedure at the Bureau of Geology on the New Mexico Tech campus. These steps are outlined below.

The 0.25 g sample aliquots were dissolved in a Teflon beaker (with lid) in 5 mL concentrated HF. In order to avoid the need for redissolution of the material, 1 mL of 10% sulfuric acid was added to the sample. This evaporates to a small amount of concentrated sulfuric acid, but does not disappear completely. For the Copper Canyon samples, it was necessary to double the amount of HF used, probably due to the larger grain size being dissolved. The samples were placed on the hotplate (275°F) overnight. The samples were quantitatively transferred to a test tube for ICP analysis. They were each diluted to 10 mL using 1% nitric acid.

The samples were transported to the Bureau of Geology for the ICP measurement. Three measurement standard solutions were created by diluting purchased standard solutions in the same 1% nitric acid solution. For each level (high, medium, and low concentrations), there was only one solution containing all four target elements. The standard solutions were designed to be comparable to the expected concentrations in the rock samples. The known concentration of these standard solutions were entered into the ICP computer.

The in-house ICP procedure was followed for all samples. Generally, the blanks were analyzed first, then the solution standards. To test the operation of the machine and verify results, known geological samples (Bureau of Geology standards) were analyzed. If all measurements were within tolerance of normal, the samples were analyzed. A blank and the high and low standards were run

after every 5-7 samples. If there were any inconsistencies with a measurement, blanks and standards were rerun and then the samples were rerun and only the final measurement was used. The Copper Canyon sample measurements were obtained during two different runs on the ICP.

3.5 Verification of Isotope Dilution Mass Spectrometry (IDMS)

The analysis of low-Cl samples is common, especially when processing mineral separates. The NMT samples were prepared using the Isotope Dilution Mass Spectrometry (IDMS) technique, described in (Desilets et al., 2006a) as well as Section 3.5 of the dissertation. In order to confirm that the accelerator is able to measure these samples, which commonly have higher $^{35}Cl/^{37}Cl$ ratios than high-Cl samples, a dilution test that had Cl concentrations ranging from 2.5 to 252 ppm was designed. These standard solutions were carefully prepared from Week's Island Halite. The samples were designed to have a range of Cl values as well as a range of $^{35}Cl/^{37}Cl$ ratios. Two different ^{35}Cl solutions (spike) with different isotope ratios were also tested. The two spike samples represent one with pure ^{35}Cl and one in which the ^{35}Cl spike was mixed with Week's Island Halite (i.e., $^{35}Cl/^{37}Cl$ ratio) natural in order to obtain a diluted spike. These are referred to as 'pure' and 'diluted' spike in this discussion.

The processing of IDMS results requires the raw AMS results and the sample dissolution information. The stable Cl and ^{36}Cl concentrations, including a Monte Carlo error estimation in each and the covariance between them, are outputs from the CRONUScalc "`spiketoconc`" routine. Two formulas are needed in order to calculate total chlorine concentration and chlorine-36 concentration from

the AMS results. The formula for total chlorine in ppm is shown in Equation 3.1, while the equation for chlorine-36 concentration in at/g is shown in Equation 3.2.

$$Cl = \frac{1000 * C_{soln} M_{soln} Wn[A_0 - SS(1 - A_0)]}{M_{rock}[(A_0 W_{35} + (1 - A_0) * W_{37}) * (SS(1 - An) - An)]} \tag{3.1}$$

$$Rm = RS * \frac{1 + ((1 - An) * SS - An)}{A_0 - SS * (1 - A_0)} \tag{3.2}$$

Where C_{soln} is concentration of the spike solution (mg/g), M_{soln} is the mass of the spike solution (g), Wn is the atomic weight of Cl (g/mol), A_0 is the spike isotope ratio (atoms ^{35}Cl/tot atoms Cl), M_{rock} is the dissolved sample mass (g), W_{35} and W_{37} are the atomic weights of ^{35}Cl and ^{35}Cl (g/mol), respectively, SS is the measured stable/stable atomic ratio (^{35}Cl/^{35}Cl), RS is the measured rare/stable atomic ratio (^{36}Cl/tot Cl), An is the natural isotope atomic ratio (^{35}Cl/tot Cl), and R_m is the rare/stable atomic ratio of the rock (^{35}Cl/tot Cl).

Using the IDMS relationships, the IDMS chlorine concentration of the sample in ppm (Column 2 in Table 3.2) and the uncertainty on chlorine concentration (Column 3) were determined. From the initial creation of the standard and the dilutions, the actual solution concentration (Column 4) and the absolute difference between the actual solution concentration and the IDMS concentration in the sample (Column 5) were computed. The ^{35}Cl/^{37}Cl ratio is also included in the table for reference. The results are plotted in Figure 3.2 with the x-axis as the known solution concentration and the y-axis as the calculated sample concentrations, including analytical uncertainties. The inset plot is a close-up of the graph in the region of low chloride (<30ppm) where many of the mineral-separate samples would plot.

Name	Calc conc (ppm)	uncert	Meas Conc (ppm)	diff	rel diff	$^{35}Cl/^{37}Cl$
BS110610-250 pur	257.7	5.9	252.3	5.49	0.02	6.04
BS110610-100 pur	106.8	1.7	101.4	5.43	0.05	7.05
BS110610-50 pur	54.9	0.9	50.8	4.13	0.08	6.07
BS110610-25 pur	26.7	0.4	25.5	1.19	0.05	9.29
BS110610-12.5 pur B	19.0	0.8	12.1	6.86	0.57	67.07
BS110610-7.5 pur	9.1	0.7	7.3	1.72	0.23	25.32
BS110610-2.5 pur	3.0	0.0	2.5	0.42	0.17	33.71
BS110610-100 dil	99.5	6.9	101.4	1.84	0.02	6.13
BS110610-25 dil	25.1	0.5	25.5	0.40	0.02	10.71
BS110610-7.5 dil	7.6	0.8	7.3	0.28	0.04	14.97

Table 3.2: Results from the dilution test looking at AMS performance on low-Cl samples. The "calc conc" is the Cl concentration calculated from the dissolution of the standard material and dilution. "Meas conc" is the concentration determined using IDMS on the AMS results. "pur" refers to the pure ^{35}Cl spike and "dil" refers to the dilute spike batch. The sample name also has the approximate concentration shown. Relative diff (rel diff) is calculated by (calc-actual)/actual.

Overall, the IDMS concentrations agree very well with the calculated concentrations. The dilute spike appears to provide the best fit to the calculated concentrations, with an average of only a 2% difference. The range of differences for the pure spike is 2-23%, with most samples differing by $<$10%. There is one sample, 12 ppm, that shows a 57% difference when compared to the calculated concentration. Without a larger sample size, it is difficult to determine if the difference between the pure and dilute spike is due to the small sample size or the different spike. The uncertainties calculated on the stable chloride concentration from the AMS data are much smaller or equivalent to the relative differences reported here for the pure spike samples. The uncertainties calculated for the dilute spike samples are all larger than the relative differences here. The pure spike underestimates the true uncertainty in the chlorine concentration of the sample while the dilute spike is consistent with the results from this study.

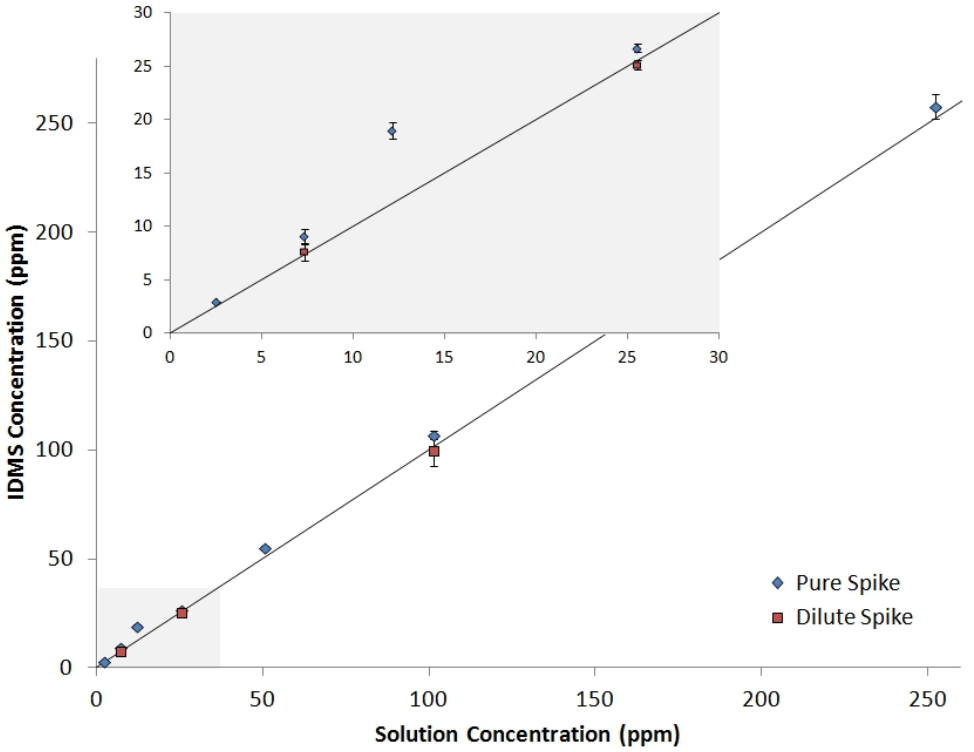

Figure 3.2: Graph of dilution test results. Gray box indicates area shown in the inset. Error bars indicate uncertainty from AMS. Symbols are smaller in the inset to show error bars.

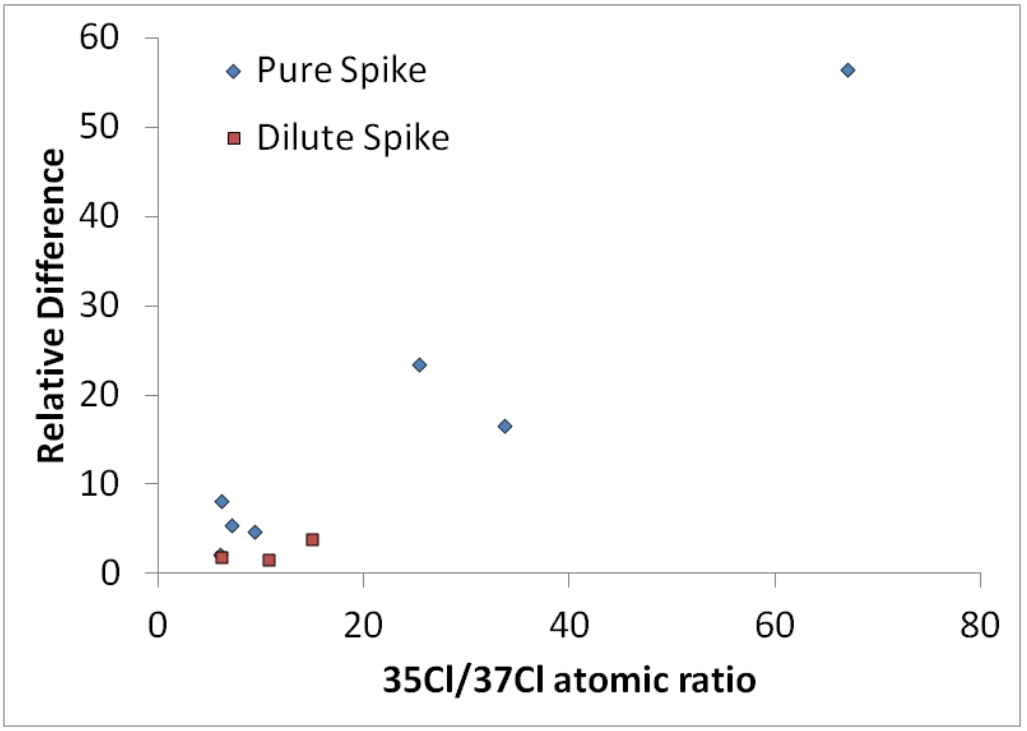

Figure 3.3: Comparison of relative difference in concentration as compared to the known concentration [(Observed-Calculated)/Calculated] vs $^{35}Cl/^{37}Cl$ atomic ratio measured in the sample.

When the results are plotted with the x-axis as the $^{35}Cl/^{37}Cl$ and the y-axis as the percent difference between the IDMS concentration and the calculated concentration (shown in Figure 3.3), there is a trend. The higher ratios correlate with the higher differences. There is not enough information to discriminate between the two different spikes. Based on this, the final measured $^{35}Cl/^{37}Cl$ ratio should be kept below 20 whenever possible.

3.6 Calculations of New Production Rates

The new production rates were calculated using the CRONUScalc code (details in Section 2). The code was used to fit the production rate parameters for calcium, potassium, and low-energy neutron production to the datasets. The

calibrations were all performed using orthogonal distance regression (ODR) and using the chi-squared statistic to check the fit of the calibration. These methods are discussed below.

3.6.1 Orthogonal Distance Regression

A typical calibration method used in the past was some variation of a least-squares fit to the calibration sample data to yield the production rate(s) of interest. That method typically assumes that there are no uncertainties on the independent variable. This calibration improves upon previous calibrations by using orthogonal distance regression (ODR). Generally, ODR allows both dependent variables (in this case, sample data) and independent variables (e.g., radiocarbon age constraints) to have uncertainty in the curve-fitting process by minimizing the orthogonal distances to the curve instead of minimizing purely vertical or horizontal distances to the curve (Boggs et al., 1987). Curve-fitting using ODR is shown graphically in Figure 3.4. The use of ODR for the calibration of surface samples can provide a better fit to the data leading to smaller overall uncertainties.

The traditional least squares minimization is of the form found in Equation 3.3 (Boggs et al., 1987).

$$min(\beta) \sum_{i=1}^{n} [f(x_i, \beta) - y_i]^2 \tag{3.3}$$

Where the sum is minimized by changing β, the input parameter is x_i, and only the observations (y_i) are assumed to have uncertainties. In this case, the measurements are the concentrations, which have uncertainties, and the input

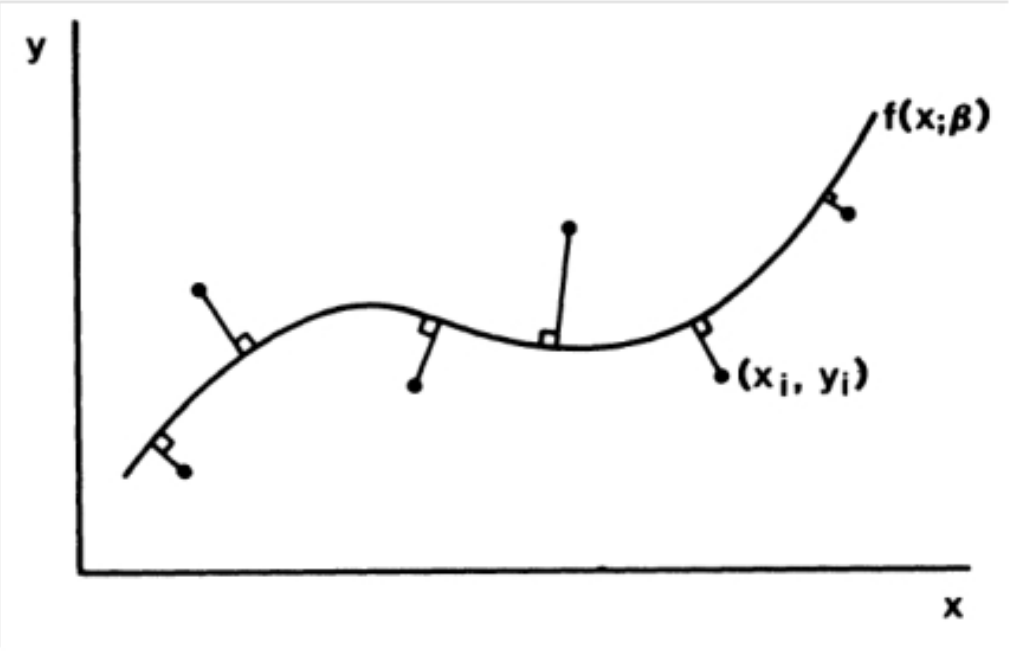

Figure 3.4: Figure illustrating the basic principle of orthogonal distance regression (ODR), where the line fit to the data minimizes the orthogonal distance between the points and the curve (Boggs et al., 1987)

parameter is the independent ages, which are assumed to be known exactly. If uncertainties (δ) are introduced for the x_i parameter (i.e., the independent age), the result is Equation 3.4 (Boggs et al., 1987).

$$min(\beta, \delta) \sum_{i=1}^{n} [(f(x_i + \delta_i; \beta) - y_i)^2 + \delta_i^2] \tag{3.4}$$

The uncertainties in this method arise from several sources. It is already known that the AMS uncertainties are not the only uncertainties in the cosmogenic method, although they have traditionally been the only ones reported. The only uncertainties that are explicitly used in the calibration are the uncertainties on the nuclide concentration and the independent age uncertainties. Uncertainties on other parameters could add to the uncertainty in the calibration, but would not be quantified even if they are included in the input parameters. These

uncertainties are relatively small in comparison to concentration uncertainties (see Section 8.23), but it important to remember that they are being accounted for in the uncertainties on either concentration or independent age.

Using ODR, samples can be allowed to have completely independently (sample-by-sample) varying ages within the bracket provided by the independent ages or they can be constrained to have a single independent age for a site. A site with a single constrained age is clearly more appropriate for a basalt flow, while independently varying ages might be more appropriate for a moraine. However, the independently varying age option could also inadvertently compensate for other mis-estimated parameters, such as varying erosion rates, so this option was not used for the CRONUS-Earth Project.

3.6.2 Chi-Squared and Reduced Chi-Squared

In order to assess the goodness-of-fit of the data to the independent age constraints, the reduced chi-squared value was calculated. This value is calculated based on the expected concentration (E) (calculated by code) and the observed concentration (O) (sample measurements). Chi-squared uses the uncertainty for each sample measurement (σ) to weight the sum of the sample results. The chi-squared (χ^2) is calculated using Equation 3.5 (Bevington and Robinson, 1992).

$$\chi^2 = \sum \frac{(O-E)^2}{\sigma^2} \tag{3.5}$$

In order to get the reduced chi-squared (χ^2_ν) value, the original chi-squared value is divided by ν, which is the number of samples minus the number of parameters being determined. In the calibrations, the number of fitted parameters

varies from 1-3. Ideally, the reduced chi-squared values should be around one if the data are close to the expected value (Bevington and Robinson, 1992). Mathematically, this is represented in Equation 3.6.

$$\chi^2_\nu = \frac{\chi^2}{\nu} \tag{3.6}$$

3.7 Blank Correction

Blank corrections were applied to all the NMT sample results discussed in this study. The blank correction consists of two parts: a total chloride correction and a chlorine-36 correction. The total chloride is assumed to be proportional to the amount of reagents that were added while the chlorine-36 blank is assumed to be independent of reagent amounts and is instead a function of the environment where the sample was processed and the procedure used. The total Cl and ^{36}Cl blanks are applied completely independently to each sample.

Blanks run with each batch of samples were used to calculate the blank subtraction for the entire batch. In general, the blank type was matched to the type of sample being run. The same spike and the same reagents, typically in the same proportions as they were used in the samples, are used for the blanks.

The total chloride blank is based on the quantities of reagents (hydrofluoric and nitric acids) added to the samples (see Schimmelpfennig et al. (2009) for additional support). To calculate the additional amount of chloride added to the sample by reagents, the blanks are treated as spiked samples and the concentration of chlorine in the blank is calculated. This is the concentration of chlorine in the reagents as found by IDMS. The concentration in the reagents is converted

into mg Cl/mL reagent. The total chloride blank subtractions typically range from 1-5% of the sample Cl.

The chlorine-36 blank is found by calculating the total chlorine-36 in the sample. In the NMT lab, there does not appear to be a strong correlation between the amount of reagents and the total ^{36}Cl in the blank (see Figure 3.5), so a single blank value that was independent of reagent amount was used. The total amount of chlorine-36 in each blank is calculated based on the AMS results and dissolution information. The blank is applied to each sample as total atoms of chlorine-36 per sample. The ^{36}Cl blank subtraction typically ranges from 1-3%, with deep samples having a larger percentage due to the much lower concentrations.

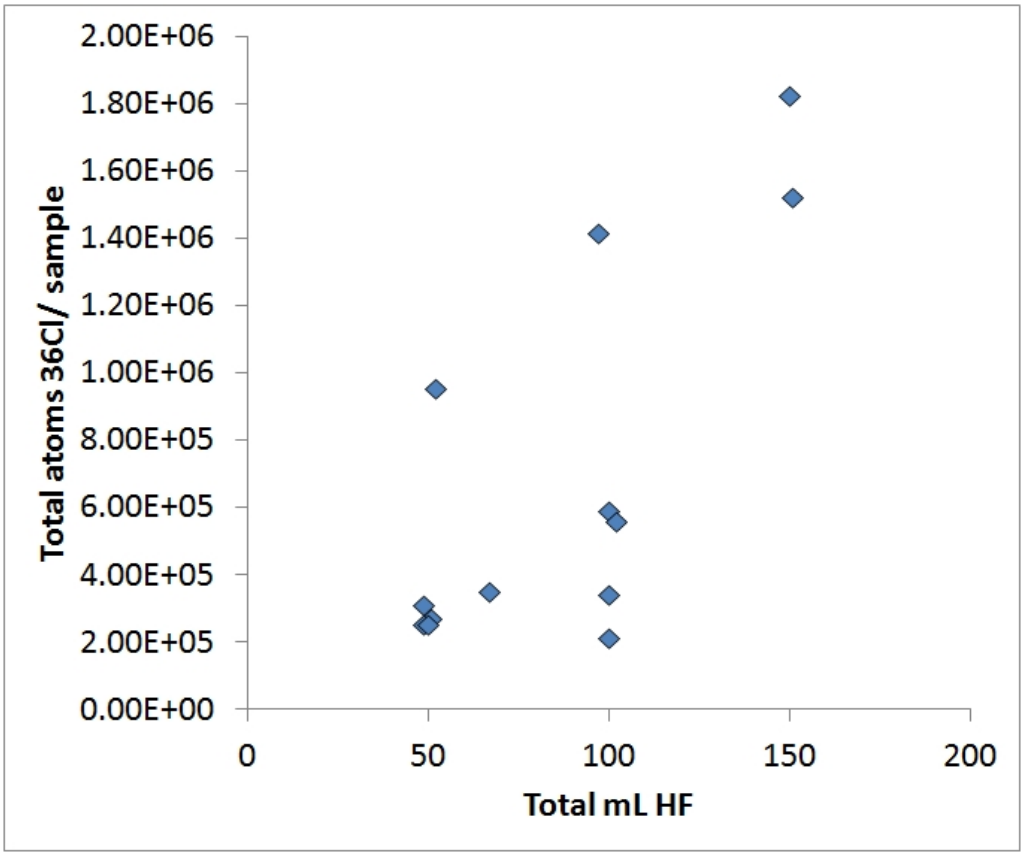

Figure 3.5: Total atoms of chlorine-36 per blank sample (y-axis) compared to the total mL of HF added to the sample (x-axis).

CHAPTER 4

LAKE BONNEVILLE - SITE DESCRIPTION AND DATA

The Lake Bonneville, Utah, geological calibration site is being used as a primary calibration site in the CRONUS-Earth project. This chapter is intended to support the main calibration chapter of this dissertation by describing the site and the resulting chlorine-36 data and assessing the quality of both. Most of the information contained herein will be published by a CRONUS-Earth investigator as part of a special volume in Quaternary Geochronology. The Lake Bonneville geological calibration site is actually two individual sites that share most of the same radiocarbon chronology. The two sites are the Tabernacle Hill basalt and the Promontory Point quartzite. Both sites share the constraint of a very large, well-dated flood event. The well-constrained chronology makes this site a good calibration site. The geologic history of Lake Bonneville will be covered first, along with the relevant radiocarbon analyses, with individual concerns being discussed in the site-specific sections later.

In this paper, all original radiocarbon ages will be reported as ^{14}C years BP, indicating years before 1950. When needed, the radiocarbon ages are calibrated using Calib 6.02 (Stuiver et al., 2005). These calibrated ages are reported as cal ka or cal years BP. In some cases, samples are reported as "years before 2010" to indicate that 60 years has been added to the calibrated radiocarbon age. When dealing with ages from cosmogenic nuclides, the ages are reported as ^{10}Be ka

or ^{36}Cl ka as necessary to avoid confusion. The cosmogenic nuclide ages are all referenced to the year 2010.

4.1 History of Lake Bonneville

Lake Bonneville was a large, closed-basin lake during the Late Pleistocene in the region that is now occupied by the Great Salt Lake (Figure 4.1). Gilbert originally identified the paleolake Bonneville (Gilbert, 1890). A detailed chronology of the fluctuations of the lake level between 30 ^{14}C ka and 12 ^{14}C ka ($\sim$33-12 cal ka) was developed later by Oviatt et al. (1992) using more than 80 radiocarbon dates (Figure 4.1).

The first transgression events in the recent paleolake history, between approximately 30 - 22 ^{14}C ka ($\sim$ 30-25 cal ka), have very little chronological information compared to the later phases of the lake history (Oviatt et al., 1992). After a period of relatively shallow occupation, the lake levels rose relatively quickly from a very low level, probably at or below the modern lake levels, to a mid-range lake level around 26.5 ^{14}C ka ($\sim$29 cal ka). The lake level oscillated over a vertical distance of about 45 m between 22-20 ^{14}C ka ($\sim$25-22 cal ka). The Stansbury shoreline was formed during these fluctuations, also known as the Stansbury oscillation (see Figure 4.2).

The final transgression leading to the Bonneville stage began around 20 ^{14}C ka (22 cal ka) (Oviatt et al., 1992). Based on lake cores, there were several smaller-scale (30-50 m) fluctuations in lake level during the transgression. However, none of these smaller fluctuations are evident in the shoreline record (Oviatt, 1997). At the end of this transgression, the lake reached its highest elevation at 1552 m. The highest shoreline, the Bonneville shoreline, formed at this elevation

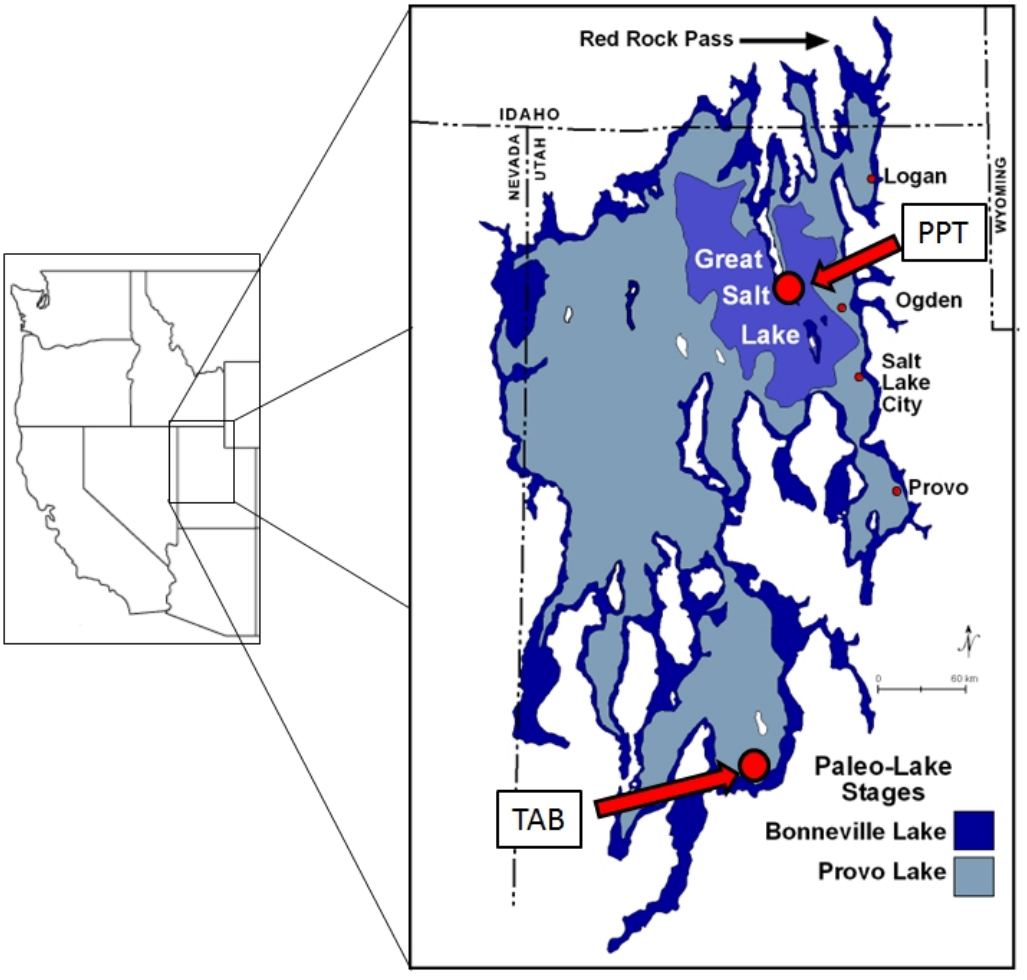

Figure 4.1: Figure showing location of Lake Bonneville in relation to the current Great Salt Lake and the sampling locations (TAB=Tabernacle Hill, PPT=Promontory Point). Also shown is the Red Rock Pass sill. (Map modified from Idaho State University (2006))

.

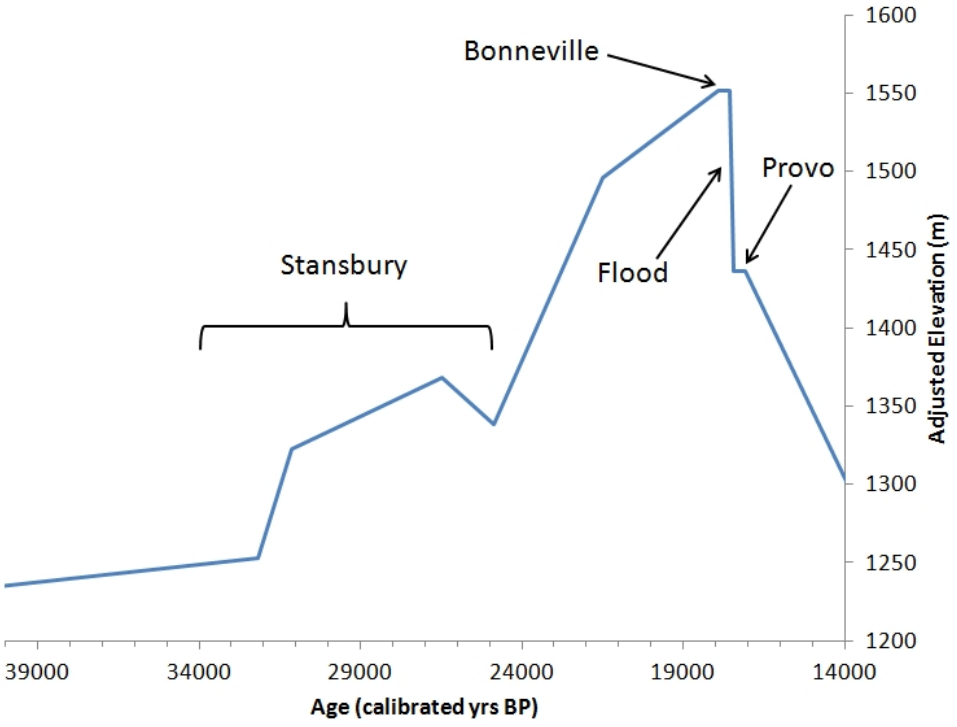

Figure 4.2: Figure showing the reconstructed water level of Lake Bonneville through time, labeled to show important events. Ages and elevations based on Oviatt and Miller (2005); Oviatt et al. (1992) with ages converted from radiocarbon to cal ka using Calib 6.02 (Stuiver et al., 2005).

when the lake level stabilized (Oviatt et al., 1992). At this point, the lake was very large, with an area of more than 52,000 km^2 (32,000 sq. miles) (DeGrey et al., 2008), and very deep, over 330 m (1000 feet) (Utah Geological Survey, 2008), to the point that waves with sufficient energy to erode bedrock were created along the fetch of the lake. The large waves allowed the lake to cut deeply into the surrounding bedrock through wave action despite the relatively short occupation of the shoreline at this elevation (Oviatt and Miller, 2005). The Promontory Point quartzite locality is on the surface of this wavecut bench.

A period of intermittent overflow at Red Rock pass continued for up to 500 years (Oviatt et al., 1992). At that point, the alluvial fan sill at Red Rock Pass (Figure 4.1) failed catastrophically and the Lake Bonneville flood engulfed the Snake River plain to the north of the lake (Oviatt et al., 1992). During this flood event, the lake level dropped approximately 100 m very rapidly, releasing almost 5000 km^3 of water (DeGrey et al., 2008). The date of the flood is discussed in the radiocarbon section. Afterwards, the lake level stabilized at the elevation of the bedrock sill at Red Rock pass and the Provo level shoreline formed. During this development, the intermittent overflow probably continued.

Sometime shortly after the flood, but during the Provo shoreline occupation, the Tabernacle Hill basalt erupted into the lake at the Provo level. It is clear from pillow basalts around the margin of the flow and other geologic evidence, that the basalt erupted into a lake approximately at the level of the Provo shoreline (Oviatt and Nash, 1989). However, the top of the basalt flow shows no evidence of eruption into water, indicating that the eruption occurred after the Bonneville flood event when the water was at the Provo shoreline level. This unique geological situation provides an excellent calibration site.

One to two thousand years of steady outflow established the main Provo shoreline (Janecke and Oaks, 2011). The history of the basin at this point is unclear, with arguments for the occupation of the Provo for a relatively short (0.5-1.0 ka) period of time (Oviatt et al., 1992), the occupation of the shoreline twice (once during the original transgression and once during regression) (Sack, 1999), or the Provo level was occupied for a much longer period than originally thought (1.5-2.5 ka) (Godsey et al., 2005; Benson et al., 2011). However, the exposure history of the Tabernacle Hill basalt is unaffected by these alternative interpretations of the lake level. The eruption occurred very early in the Provo shoreline history and an eruption during the transgressive phase would have shown evidence of eventual cover by water from the Bonneville shoreline occupation. Godsey et al. (2011) presents new radiocarbon evidence showing that Provo shoreline formation ceased at approximately 15 cal ka. Although the later chronology is not completely constrained, it is clear that the lake dropped to very low levels, possibly lower than the modern Great Salt Lake, by approximately 12 ^{14}C ka (14 cal ka) (Oviatt et al., 1992).

4.1.1 Radiocarbon constraints on the Bonneville and Provo Shorelines

The chronology for the paleo-Lake Bonneville is considered to be one of the most reliable in the world for a Pleistocene lake (Oviatt et al., 1992). Although there are numerous independent ages (radiocarbon or other methods) providing constraints on the different lake level stages, there only are a few sets of very important dates that delimit the particular events of interest. These significant ages are discussed here in detail.

The independent ages constraining the exposure age at Promontory point, the end of the wavecutting event and the abandonment of the shoreline, are based on the age of the Bonneville flood itself. The datasets that constrain this event include the relevant ages from Oviatt et al. (1992), CRONUS radiocarbon analyses from tufa samples collected from Tabernacle Hill, new radiocarbon dates from non-gastropod materials (Miller et al., 2011), and U/Th dates from carbonates in flooded cave deposits (McGee et al., 2012a,b).

Based on all prior radiocarbon ages, the CRONUS-Earth Project calculated an age for the Bonneville flood of 17.1 $\pm$ 0.3 cal ka (Brian Borchers, pers. comm., 2005 and Greg Balco, pers. comm., 2005). This age was based on the relevant 19 radiocarbon ages presented Tables 4.1 and 4.2, which are taken from Oviatt et al. (1992) and Oviatt and Miller (2005). This age and the method used to obtain it was described in Marrero (2009). The method for employed in calculating the age of the Bonneville flood was a maximum likelihood estimate, described in the methods section, and a Monte Carlo analysis. The radiocarbon ages from before the flood are listed in Table 4.1, while the ages from the Provo shoreline (after the flood) are listed in Table 4.2. Since completion of Marrero (2009), additional dates have provided new information and the age was reanalyzed as described below.

However, in a recent abstract, Miller et al. (2011) questioned the validity of dates on gastropods from Lake Bonneville based on new radiocarbon ages from the Provo shorezone that provide significantly older ages (18-17 cal ka) than the corresponding gastropod radiocarbon ages (17-15 cal ka). Another new unpublished dataset from David McGee (pers. comm., April 26, 2012) provides U/Th ages of carbonate deposits in caves of various altitudes in the Bonneville Lake area. The results indicate that carbonate deposition ceased at 18.12$\pm$0.15 ka in a

cave in the Fish Springs Range that is 40 m below the highstand level for the Bonneville shoreline (McGee et al., 2012b). By inference, this provides a minimum limiting age on the Bonneville flood. There are also additional radiocarbon and U/Th dates from the same lab that corroborate this age. These new dates and doubt about some of the original radiocarbon ages led to an extensive reanalysis of the age of the Bonneville flood as part of the CRONUS initiative.

The Tabernacle Hill basalt erupted shortly after the retreat of Lake Bonneville to the Provo stage but before the establishment of the Provo stage features such as tufa on the basalt (Oviatt and Nash, 1989). The tufa encrustations on the Tabernacle Hill basalt provide a radiocarbon constraint on the youngest possible age of the basalt flow. In May 2011, Fred Phillips collected additional tufa samples from the Tabernacle Hill basalt flow (see Figure 4.3 for location) for radiocarbon analysis by the CRONUS-Earth Project. Tufa ages can be problematic due to recrystallization so the new samples, so the new samples were collected from the ceilings of shallow rock shelters. Because the tufa formed on a basalt, which contains no carbon, the possibility of contamination from detrital carbon is low (Oviatt et al., 1992). The new tufa samples were carefully treated using the procedure described in Appendix B.1. The samples were cut into stratigraphic sections, with the 'top' being younger and the 'bottom' being older, and then they were cleaned with water, crushed, and sieved. The samples were again cleaned with water and then partially dissolved with HCl, following the procedure in Oviatt and Nash (1989), prior to CO_2 extraction and graphitization.

The new CRONUS tufa ages are shown in Table 4.3. The new radiocarbon ages do provide the oldest post-flood constraints; however, the new post-flood ages overlap with the youngest pre-flood ages. Instead of relying on all the pre-

vious radiocarbon ages presented in the table, only the pre-Bonneville ages from material other than shells are examined (specifically ages 18 and 19 in Table 4.1).

It seems clear that the new ages, including at least two different types of dating techniques, are consistent with an older age of the Bonneville flood than the generally accepted previous age. Incorporating this new information into the chronology actually leads to a larger uncertainty on the age of the flood. Based on this, an age of 18.3 $\pm$ 0.5 years before 2010 is adopted for the exposure age of Promontory Point, i.e. the flood age. Similarly, an age of 18.2$\pm$ 0.5 cal ka before 2010 is adopted for the Tabernacle Hill basalt flow.

4.2 Tabernacle Hill basalt flow

4.2.1 Geology/site description

Tabernacle Hill basalt flow (TAB), southwest of Salt Lake City and the current Great Salt Lake, is a basalt flow erupted shortly after the retreat of Lake Bonneville to the Provo stage. The flow, originally described by Gilbert (1890), is an approximately circular basalt flow (see Figure 4.3) with a central crater and surrounded by an assymetrical tuff cone and smaller cinder cones (Oviatt and Nash, 1989). The basalt flow covers approximately 17 km^2 (6.5 mi^2). Several faults, typically striking NNE, cut the basalt (see Figure 4.4). One of the larger faults cuts the basalt flow in the northern area and appears to have facilitated the opening of a vent. Pyroclastic debris spewed from the primary vent at the center cone and covered a significant local area based on the areal extent of the deposits found in the Lake Bonneville lacustrine deposits (Oviatt and Nash, 1989). The smaller vent in the north also has basaltic tuff and probably covered a more localized area with pyroclastic material.

#	Lab ID	C-14 age	C-14 Error	Cal yr Min	Cal yr Max	Lake Level	Material	Elev (m)	Stratigraphic Interpretation	Reference
11	B-50770	14420	370	16334	18557	up	Stagnicola	1535	5m below Bonneville B1 shoreline	Godsey et al. (2005)
12	B-146004	14730	140	17215	18516	up	Stagnicola	1532	30m below Bonneville shoreline	Godsey et al. (2005)
13	SI-4227C	14730	100	17263	18481	at	tufa, innermost, 18%	1552	Bonneville shoreline	*Currey et al. (1983), *Stuckenrath, R. pers comm. with Oviatt, 1979
14	B-39294	14830	160	17382	18619	up	Stagnicola	1525	sand 30 m below Bonneville shoreline	Oviatt et al. (1994)
15	B-169099	15060	50	18098	18632	up	Stagnicola	1540	6m below Bonneville shoreline	Godsey et al. (2005)
16	B-156852	15080	90	18067	18673	up	Stagnicola	1530	just below Bonneville shoreline	Godsey et al. (2005)
17	B-151451	15080	90	18067	18673	up	Stagnicola	1527	20m below Bonneville shoreline	Godsey et al. (2005)
18	W-5261	15100	140	18018	18742	down	Wood	1538	transgressive lagoon/bar complex	*Scott (1988)
19	B-23174; ETH-3518	15250	160	18088	18861	down	Charcoal	1545	pre-Bonneville soil	*Oviatt (1991)

Table 4.1: Table of relevant radiocarbon age constraints prior to the Bonneville flood. * indicates that the reference is cited in Oviatt et al. (1992). The level column values are as follows: 'at' indicates that the lake level was at or near the sample altitude, 'up' indicates that the lake level was above the sample, and 'down' indicates that the lake level was below the sample. This table is modified from Oviatt and Miller (2005). Radiocarbon ages are calibrated using Stuiver et al. (2005).

#	Lab ID	C-14 age	C-14 Error	Cal yr Min	Cal yr Max	Lake Level	Material	Elev (m)	Stratigraphic Interpretation	Reference
1	1 B-15316	13110	50	15198	15847	at	Gastropods	1420	backshore muddy sandy gravel	Godsey et al. (2005)
2	AA-19045	13290	115	15313	16240	up	Fluminicola	1426	sandy spit just below Provo shoreline	**Light (1996)
3	B-159810	13580	40	15807	16563	up	Gastropods	1436	14m below Provo shoreline	Godsey et al. (2005)
4	B-153158	13660	50	15919	16675	at	Stagnicola	1435	1.5m below Provo shoreline	Godsey et al. (2005)
5	WW-4147	13705	40	15985	16713	up	Stagnicola	1412	sandy marl 30 m below Provo shoreline	*Miller & Oviatt, unpublished
6	AA-19040	13850	115	16065	16949	up	Stagnicola	1427	Bear River delta graded to Provo shoreline	**Light (1996)
7	W-899	13900	400	15456	17891	up	mollusk shells	1426	Bear River delta graded to Provo shoreline	*Bright (1966); *Rubin and Berthold (1961)
8	WW-4148	14090	40	16397	17138	up	Stagnicola	1412	sandy marl 30 m below Provo shoreline	*Miller & Oviatt, unpublished
9	AA-19059	14290	125	16559	17672	up	Stagnicola	1439	sand just below Provo shoreline	**Light (1996)
10	B-23803	14320	90	16640	17605	at	Tufa	1436	Provo shorezone	Oviatt and Nash (1989)

Table 4.2: Table of relevant radiocarbon age constraints from the Provo shoreline indicating that they are after the Bonneville flood. * Indicates that the reference is cited in Oviatt et al. (1992). ** Indicates that the reference is cited in Oviatt and Miller (2005). The level column values are as follows: 'at' indicates that the lake level was at or near the sample altitude, 'up' indicates that the lake level was above the sample, and 'down' indicates that the lake level was below the sample. This table is modified from Oviatt and Miller (2005). Radiocarbon ages are calibrated using Stuiver et al. (2005).

#	Lab ID	C-14 age	C-14 Error	Cal yr Min	Cal yr Max	Lake Level	Material	Elev (m)	Stratigraphic Interpretation	Reference
20	AA-94394	14570	80	17379	18018	at	tufa	1445	Provo shorezone	Lifton/Hudson, 2011*
21	AA-94395	14760	80	17635	18491	at	tufa	1445	Provo shorezone	Lifton/Hudson, 2011*
22	AA-94396	14950	80	17936	18543	at	tufa	1445	Provo shorezone	Lifton/Hudson, 2011*
23	AA-94397	14970	80	17960	18547	at	tufa	1445	Provo shorezone	Lifton/Hudson, 2011*
24	AA-94399	14970	80	17960	18547	at	tufa	1445	Provo shorezone	Lifton/Hudson, 2011*
25	AA-94400	15140	90	18026	18622	at	tufa	1445	Provo shorezone	Lifton/Hudson, 2011*
26	AA-94398	15130	80	18027	18613	at	tufa	1445	Provo shorezone	Lifton/Hudson, 2011*

Table 4.3: Table of new radiocarbon age constraints from the Provo shoreline tufas on the Tabernacle Hill basalt indicating that they are after the Bonneville flood. Calibrated age ranges are the total extent of two sigma ranges before 1950. The level column values are as follows: 'at' indicates that the lake level was at or near the sample altitude, 'up' indicates that the lake level was above the sample, and 'down' indicates that the lake level was below the sample. *Radiocarbon measurement by N. Lifton and A. Hudson (2011) as part of the CRONUS-Earth Project. Radiocarbon ages are calibrated using Stuiver et al. (2005).

The classification of the Tabernacle Hill central cone as a tuff cone is evidence for the presence of a lake above the vent when it erupted. A tuff cone has a typical sequence of deposits as well as a particular geometry (Cas and Wright, 1988). This sequence typically includes volcanic breccias, followed by surge deposits intermixed with minor air-fall deposits, subsequently covered by massive air fall tuff or lapilli deposits and capped by surge deposits. The geometry of the tuff cone includes steep inner and outer slopes, a small cone diameter, and a crater floor that is above the surrounding terrain. In this case, the Tabernacle Hill central cone displays key characteristics that indicate that it is a tuff cone and was therefore erupted into water.

According to the description by Oviatt and Nash (1989), there are several features that indicate that this basalt flow was erupted into water including rounded pillows with glassy external texture and coarser internal texture and wave-rounded cobbles and boulders. The best evidence for eruption into water is the pillow basalts, which traditionally have a distinct fast-cooled outer portion with a glassy texture and a slower-cooled internal crystalline structure (Press and Siever, 2001) as seen at Tabernacle Hill. The altitude of the outer edge is 1445 m, which is approximately 3 m lower than the known Provo shoreline nearby, although this could be due to incomplete isostatic rebound or magma chamber subsidence (Oviatt and Nash, 1989). Despite the overwhelming evidence that the Tabernacle Hill basalt erupted into water, the water depth was shallow. Because there is no evidence on the top of the flow of eruption into water, it is clear that this eruption occurred after the flood that lowered the lake level from the Bonneville to the Provo stage.

During the Provo shoreline occupation, waves acted on the margins of the basalt flow causing the erosion of the edges and resulting in the presence of

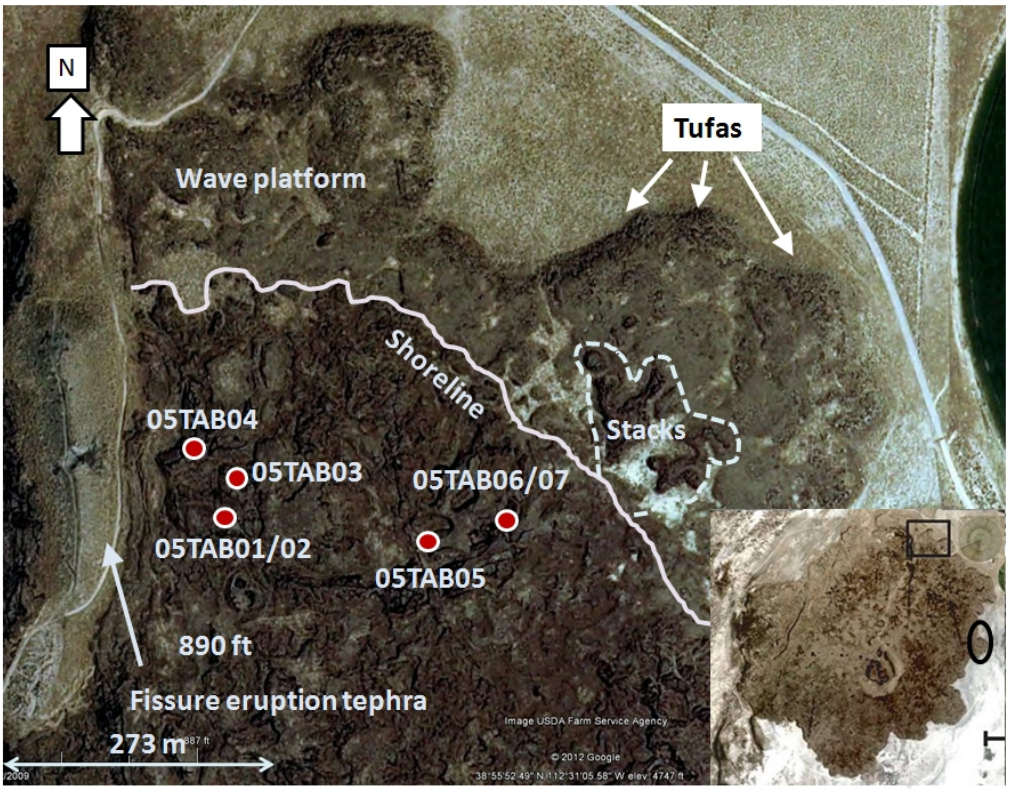

Figure 4.3: (inset) Tabernacle Hill satellite image showing the whole flow and the area in which the samples were collected. The oval indicates the tufa sampling location. (main) Closeup of the sampling area showing individual sample locations and other features, such as the shoreline, wave platform, and the tephra.

Sample	Latitude	Longitude	Elevation (m)
05TAB01	38.93	-112.522	1458
05TAB02	38.93	-112.522	1458
05TAB03	38.93	-112.523	1461
05TAB04	38.93045	-112.522	1458
05TAB05	38.92995	-112.51988	1455
05TAB06	38.930067	-112.51897	1457
05TAB07	38.930067	-112.51897	1457

Table 4.4: Location information for CRONUS-Earth Taberacle Hill samples. All samples are basalt samples with a 1.0 shielding factor and a thickness of 3 cm.

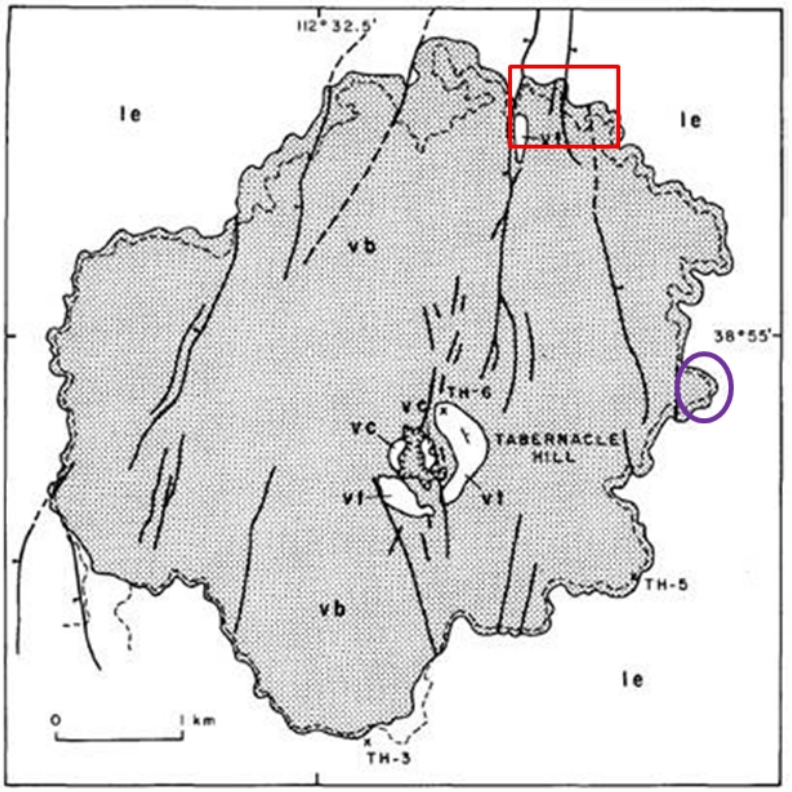

Figure 4.4: Figure showing faulting at the Tabernacle Hill basalt flow. The box indicates the sampled area. The oval indicates the location of the tufa samples. Abbreviations are vb = basalt, vt = basaltic tuff, vc = scoriaceous cinders. Hachured line indicates the volcanic crater. Faults are shown with bar and ball on downthrown side; fractures shown as heavy lines. TH sites indicate samples discussed in Oviatt and Nash (1989).

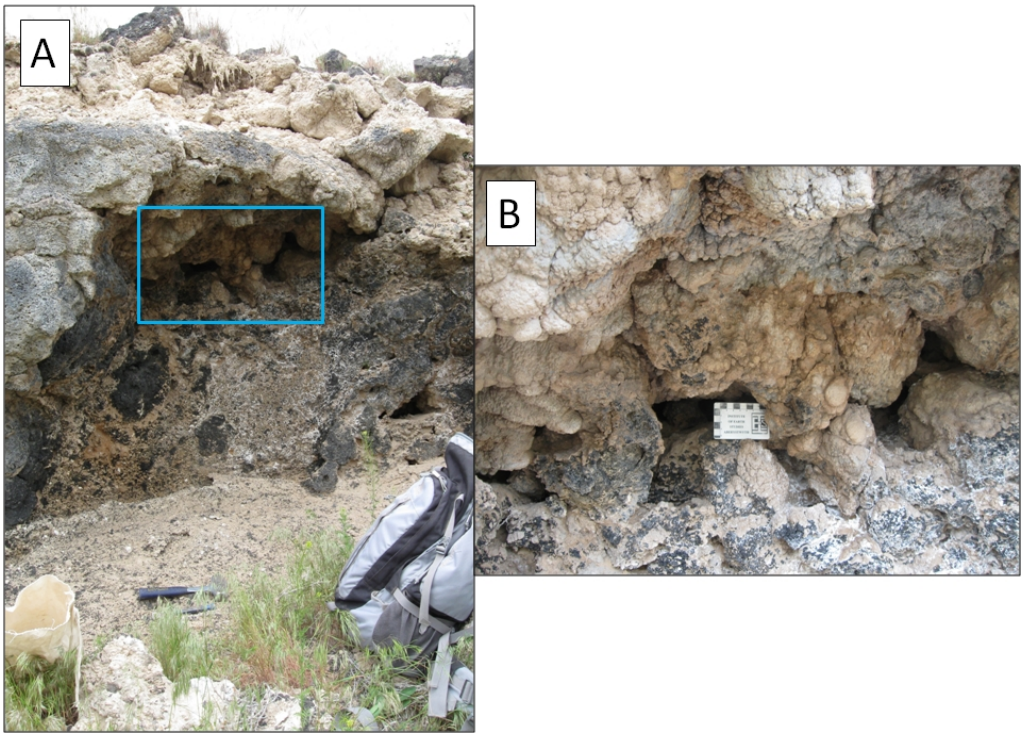

Figure 4.5: A representative tufa sample collected for radiocarbon analysis by the CRONUS-Earth project. (A) The overhang where the sample was collected. The box indicates the location of the closeup photo shown in (B). Photos by F. Phillips.

rounded cobbles at the wave margins (Oviatt and Nash, 1989). This constant-elevation margin is at the Provo shoreline elevation, clearly indicating the water level at the time. The occupation of the Provo shoreline over the years also allowed the formation of tufa on the outside edges of the basalt flow. Tufa, formed through physico-chemical and biogenic precipitation (Ford and Pedley, 1996), is commonly seen in the shorezone of lakes. In the Bonneville Lake area, the tufa encrustations typically form in areas undergoing erosion and that have little sediment input (Felton et al., 2002, 2006). This bolsters the other evidence for the shoreline at the Provo level at the time of eruption.

4.2.2 Samples Collected

Samples were collected from the north side of the volcanic cone to the east of the fissure-eruption tephra, shown on Figure 4.4. The samples were collected within 500 m of each other in an attempt to obtain samples that would be uniform in composition and exposure history. Samples were collected from areas at the tops of the tumuli (see Figure 4.6) in order to eliminate the need for a significant shielding factor and to reduce the possibility of cover by soil or ash. Previous work by Stone et al. (1996) showed little evidence of tephra cover based on his measurements. Eolian cover is a known problem for the western part of the flow, so this area was also avoided (Lifton, 2005). The samples were also taken well away from any edges formed by pressure ridges in order to reduce edge effects. A rock saw was used to make sure that samples were taken in the middle of the tumulus (see Figure 4.6). Finally, the original surface texture of pahoehoe ropes (Marrero, 2009, see photos in) was used to distinguish samples that had undergone very little erosion. Shielding information, pictures, and GPS coordinates were recorded. Seven samples of the basalt were collected along with one tufa sample. Sample names for all CRONUS samples were determined as follows: the three-letter indicator (TAB) indicates the site name, the prefix indicates the year, the suffix indicates the sample number. Any additional numbers/letters have been added by our lab to distinguish mineral separates (MS) or to indicate replicate samples. Individual sample information, including photos, is included in Appendix C.3.

4.2.3 Possible Complicating Factors

This section covers issues specific to this particular sample site. In this case, the issues include erosion, sample cover by ash, and contamination by sec-

Figure 4.6: (left) Photo showing the type of landform (top of tumulus) sampled by the CRONUS project. (right)The Tabernacle Hill samples were collected using a saw and chisel.

ondary minerals. These are covered individually below.

Erosion rates on basalts are difficult to quantify (Cerling, 1990). Basalts erode through two distinct mechanisms: gradual erosion and the spalling of entire horizontal sheets. The pahoehoe flows can be a series of horizontal layers so that spalling of the surface layer reveals a new layer that is essentially indistinguishable from the original surface (Cerling and Craig, 1994b). These secondary surfaces can have pahoehoe ropes and other indications of an uneroded surface. In the case of gradual erosion, the surface textures are worn down at a constant rate through time. The pahoehoe rope or other indicator of the exposed surface is removed. In the case of a fresh basalt flow, the gradual erosion must first strip off the shiny, friable, outer layer until the denser, inner material is reached.

The rates at which erosion occurs on basalt flows, or on any given basalt flow, is not well-constrained. Cerling and Craig (1994b) estimated that ropes cannot remain distinct with more than 1 cm of total erosion (a rate of 0.55 mm/kyr Tabernacle Hill) for ropes to remain distinct, while Dunbar (1999); Dunbar and

Phillips (2004) estimated a significantly higher erosion rate for basalts with pahoehoe ropes of 5 mm/kyr, equal to ∼8.5 cm of total erosion at Tabernacle Hill. It is also possible that higher erosion rates are appropriate for younger samples while the outer, very friable layer is removed progressively, with erosion rates slowing significantly after the denser inner material is reached (Dunbar and Phillips, 2004). Based on the fact that a 5,000 year old flow in New Mexico had already lost its shiny outer layer (Dunbar, 1999), the higher erosion rate would probably only be appropriate for the first 5,000 years or less.

The independent assessment of the Tabernacle Hill basalt flow erosion rate was difficult due to the factors presented above. Based on the geological evidence, primarily the surface texture of the sample, significant erosion did not occur. It is likely that the actual erosion rate of the Tabernacle Hill basalt is between the two estimates discussed in the previous paragraph. It seems like an appropriate integrated rate for this sample should be closer to the lower bounding erosion rate than the upper. An erosion rate of 1.0 ± 0.5 mm/kyr was used for the Tabernacle Hill erosion rate. The uncertainty was set to half of the rate to account for the large possible range of erosion rates.

Ash cover is a possible contributor to a decrease in cosmogenic production, especially because tuff cones commonly produce this material as part of the sequence (Cas and Wright, 1988). There is known eolian deposition of sand over part of the basalt flow (Lifton, 2005). These areas were specifically avoided during sampling. Samples were also taken from slightly sloping surfaces or from the tops of tumuli to avoid problems with accumulation of soil, ash, or other eolian material.

The initial ^{36}Cl results from Tabernacle Hill whole-rock samples, reported in Marrero (2009), showed significant sample-to-sample and within-sample vari-

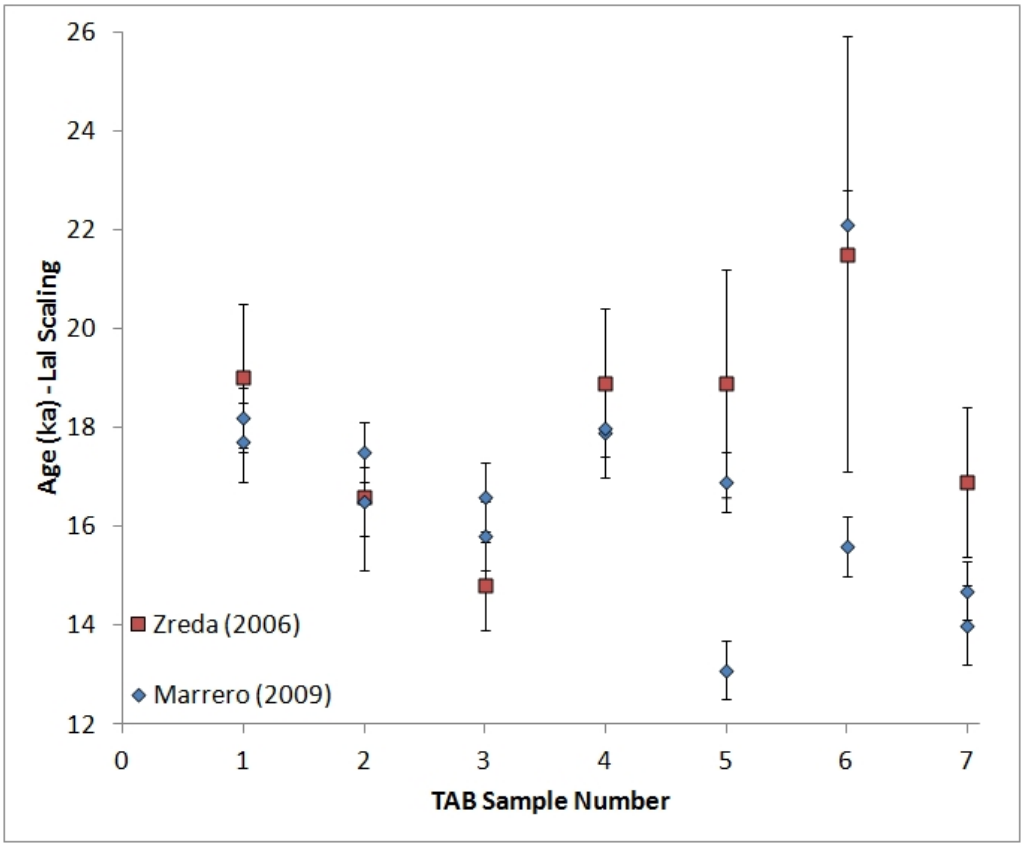

Figure 4.7: Ages for Tabernacle Hill as calculated in Marrero (2009) and the results from Zreda (pers. comm., 2006). The CHLOE program (Phillips and Plummer, 1996) was used to calculate the ages. CHLOE uses Lal (1991) scaling and the erosion rate was 0.89 mm/kyr. Production rates used to calculate these ages were from Phillips et al. (2001).

ability (see Figure 4.7). This amount of scatter was higher than expected and we proposed several possible hypotheses for the discrepancy. The hypotheses included inhomogeneities in the XRF/sample aliquots and problems with the chemical processing technique. Similar variable results were produced by Zreda (pers. comm., 2006), also plotted in Figure 4.7. It is worthwhile to note that the pattern of scatter is similar between the two datasets. Unfortunately, full information for the Zreda samples was never provided so these results are not used in any future calculations.

SiO2	TiO2	Al2O3	Fe2O3	MgO	CaO	Na2O	K2O	P2O5	LOI
(wt %)	(wt %)	(wt %)	(wt %)	(wt %)	(wt %)	(wt %)	(wt %)	(wt %)	(wt %)
7.29	0.08	1.38	0.53	0.45	30.62	0.07	0.26	0.02	58.95

Table 4.5: Composition of the Carrizozo material collected from basalt as measured by major element XRF analysis. LOI = Loss On Ignition.

Upon further inspection of the samples, secondary minerals were noted in the samples as small, white particles (see Figure 4.8). These were not noticed during the processing of the first batches of samples and these grains may have contributed to the variable results. The white particles do not fully dissolve in dilute (3-5%) or full-strength (70%) nitric acid, indicating that they are not completely composed of carbonates, as originally suspected. The particles could be zeolites or another mineral that formed from weathering processes. Zeolites are commonly associated with lavas and are formed as a weathering product (Deer et al., 1974). These hydrated aluminosilicates have a large range of possible compositions, with many containing Ca, K, or Na (Deer et al., 1974). In an attempt to collect enough of this type of material, we collected large pieces of similar-looking material from the Carrizozo basalt flow near Carrizozo, New Mexico. Under a binocular microscope, the material was very spiky. An XRF analysis of the crushed material (results in Table 4.5) showed it to be composed almost entirely of calcium and LOI (either water or CO_2). Whether the material in the Tabernacle Hill samples has a composition similar to this Carrizozo material or to a typical zeolite composition is unknown, but either composition is likely to negatively impact the results from the chlorine-36 analysis of the samples. The white material does not dissolve in the dilute (3-5%) nitric acid used to treat cosmogenic samples and must be removed using another method prior to final dissolution of the sample.

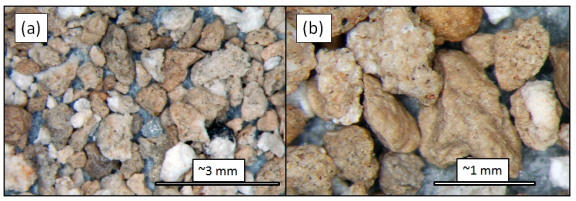

Figure 4.8: (a) Photo showing the material separated from the TAB samples. (b) Closeup of the discarded material from TAB samples.

In order to remove the white particles from the Tabernacle Hill whole-rock samples, a site-specific procedure was developed. The samples were leached in dilute nitric acid and then magnetically separated into magnetic and non-magnetic fractions. Each fraction was subjected to heavy liquid separation in order to remove the white particles, present in both portions, from each fraction. The two fractions, now with white particles removed, were combined back into a single sample and the traditional sample processing was used. For the mineral separate sample, only the phenocryst portion was separated and used as a sample. This procedure was used on all subsequent samples processed for Tabernacle Hill. These results are presented in the next section. The initial analyses reported in Marrero (2009) will not be included or discussed in the next section.

4.2.4 Tabernacle Hill Data and Discussion

Three labs, in addition to the NMT lab, processed Tabernacle Hill samples and provided the necessary information to analyze the results. John Stone (University of Washington) processed five plagioclase mineral separate samples as part of the CRONUS-Earth project. In addition to the CRONUS samples, John Stone has contributed five additional, essentially identical analyses from a previous collection trip to the same locality (labeled TH in the appendix). These samples are all included in the spallation calibration. Three labs, Gosse at Dalhousie,

Caffee at PRIME Lab at Purdue University, and NMT, processed whole-rock samples from Tabernacle Hill. The results from all these labs will be discussed.

The consistency of chlorine-36 data is impossible to assess without accounting for composition due to the production from multiple target elements. Therefore, the results will be plotted and discussed in two ways. The first method is a normalized composition diagram and the second is the calculated ages of the samples using the final production rates. Both methods rely on the final production rates to some degree. The production rates were produced without information from this analysis, so there is no circularity. This analysis simply presents the data using these two presentation styles in order to ascertain if they are consistent.

The normalized composition diagram plots the concentration of chlorine-36 from the combination of Cl and Ca (as calculated by the final production rates) divided by the weight percent CaO of the target versus the percent production from Cl. Production from K is subtracted prior to these calculations. Bulk rock, trace element, and target compositions for all Tabernacle Hill samples are shown in Appendix C.3. Ideally, all the samples would fall along a single line, with the calcium production rate found by extrapolating to 0% production by chlorine. While this is not independent of production rates, it gives a clear picture of whether or not the data are consistent for the production rate calibration. All the samples from all the labs are shown using this plot in Figure 4.9.

The site production rate for calcium for Tabernacle Hill was found by using the CRONUScalc Matlab program. Due to the fact that the samples are calcium-dominated (in mineral separates) and chlorine/calcium-dominated (whole-rock), only the calcium production rate and, less reliably, the value of $P_f(0)$ can be

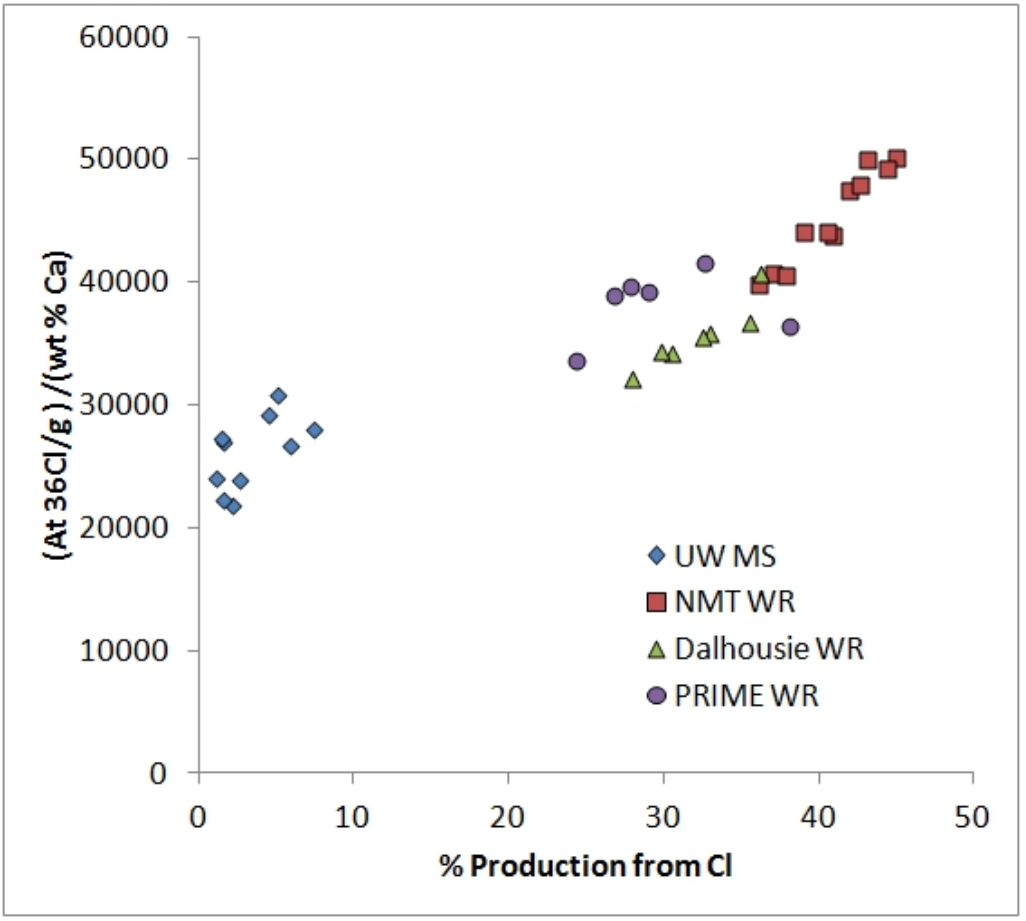

Figure 4.9: Plot showing Tabernacle Hill atoms of chlorine-36 from Ca per weight % Ca for all Tabernacle Hill basalt datasets. The plot includes mineral separates from University of Washington (John Stone) and whole rock from New Mexico Tech (Shasta Marrero), Dalhousie (John Gosse), and PRIME Lab at Purdue (Marc Caffee).

calculated from data obtained at this site. The calcium calibration results, based on only the mineral separates, were cross-checked using a manual analysis in Excel. Essentially, the production rates can be approximated by fitting a straight line through the data as they are plotted in Figure 4.9. The y-intercept at Cl equal to zero should indicate the production rate from only calcium at the site. The Matlab code accomplishes this through chi-squared minimization and selecting the best-fit parameter. The Matlab and Excel results were in very good agreement and only results from the Matlab analysis will be discussed.

The site calcium production rate (scaled to SLHL using the Lifton/Sato scaling (Lifton, 2012)) based on only the plagioclase mineral separates is 56.0 at (g Ca)$^{-1}$yr^{-1} for calcium. After the completion of the spallation calibration, the spallation production parameters were treated as constants and the whole-rock Tabernacle Hill samples were used to calibrate a value for $P_f(0)$. The value at this site is 814 based on the whole-rock samples from all labs. The details of this calibration are discussed in detail in Chapter 8.

After the final global calibration of production rates (see Chapter 8), the newly calibrated rates were used to age all the Tabernacle Hill samples. This is plotted in Figure 4.10. As described above, only the UW mineral separates were used in the spallation calibration, while the whole-rock samples from all labs were used in the determination of $P_f(0)$. The whole-rock data shows significantly more scatter than the mineral-separate data. The discrepancy may be due to differences in preparation methods between the labs, but is more likely due to the inherent differences between the production mechanisms.

The mean and standard deviation for ages of Tabernacle Hill samples using Lifton/Sato scaling (Lifton, 2012) in the CRONUScalc program is 19.1 $\pm$ 1.1

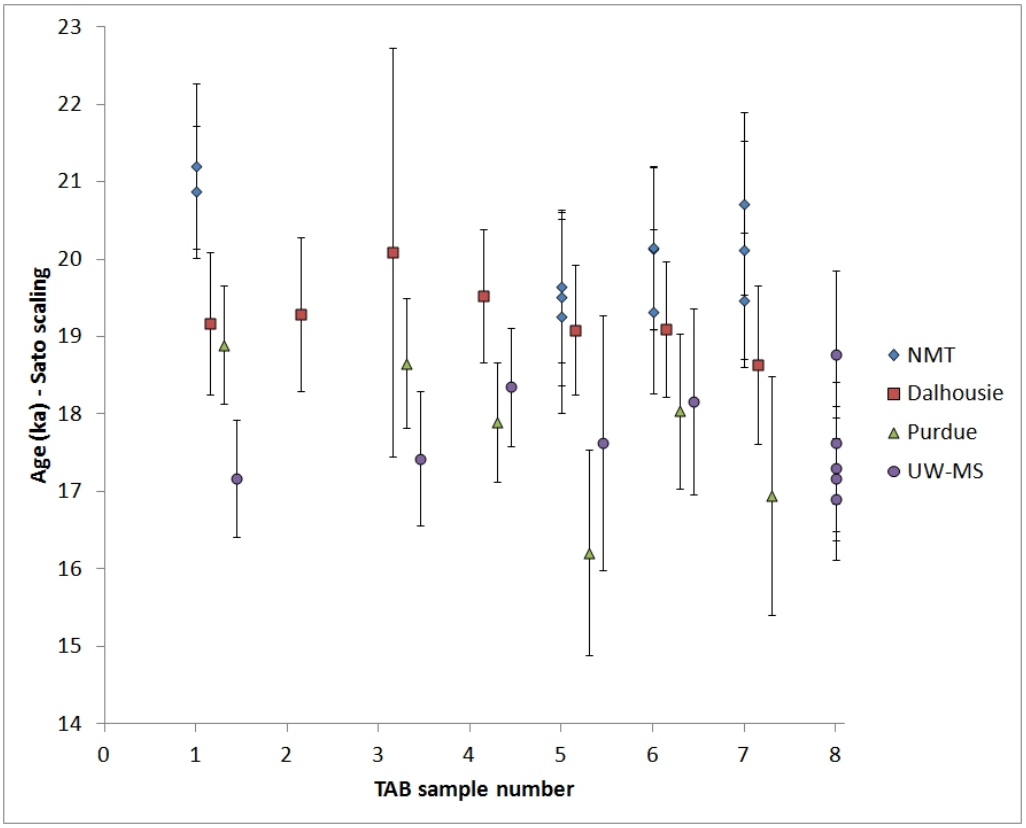

Figure 4.10: Ages of all chlorine-36 Tabernacle Hill samples from all labs using CRONUScalc with the Lifton/Sato scaling (Lifton, 2012). Note: All the raw data for the original measurements are provided in Appendix C.3. A single outlier at the NMT lab (05TAB06-1) has been removed from all analyses due to documented laboratory issues. The samples from all labs are whole-rock analyses except for the mineral separate samples from University of Washington labeled "UW-MS."

Name	Type (MS/WR)	Mean (ka)	Std Dev (ka)
NMT	WR	19.8	0.7
Dalhousie	WR	19.1	0.4
PRIME	WR	17.6	1.0
UW	MS	18.3	0.6
All WR	WR	19.1	1.1
All samples	WR & MS	18.8	1.1

Table 4.6: Table of mean and standard deviation for ages calculated using the Tabernacle Hill datasets. MS - Mineral separate; WR - Whole rock.

ka for combined whole-rock samples and 18.3 $\pm$ 0.6 ka for the mineral separates. The averages and standard deviations are broken out by laboratory in Table 4.6. The full dataset, including outliers, can be found in Appendix C.3. There is a small difference between the mean ages produced by the whole-rock samples and those produced by the mineral separates. The sample-to-sample scatter is smaller for the mineral separates than for the whole-rock samples.

The sample age variation due to changing erosion rate is relatively small compared to the uncertainties already placed on the sample ages due to all other uncertainties. The variation of the age with changing erosion rate is shown in Figure 4.11. For a sample with an erosion rate of up to 2 mm/kyr, there is only a 5% change in the sample age compared to a sample with no erosion. Based on sample site characteristics, an erosion rate of 1.0 $\pm$ 0.5 mm/kyr was chosen for this site. This seems appropriate when analyzed in the context of the sensitivity to erosion rate.

4.2.5 Comparison with other Nuclides

The only nuclide other than chlorine-36 that has been analyzed on Tabernacle Hill is helium-3. The original data and discussion can be found in Goehring

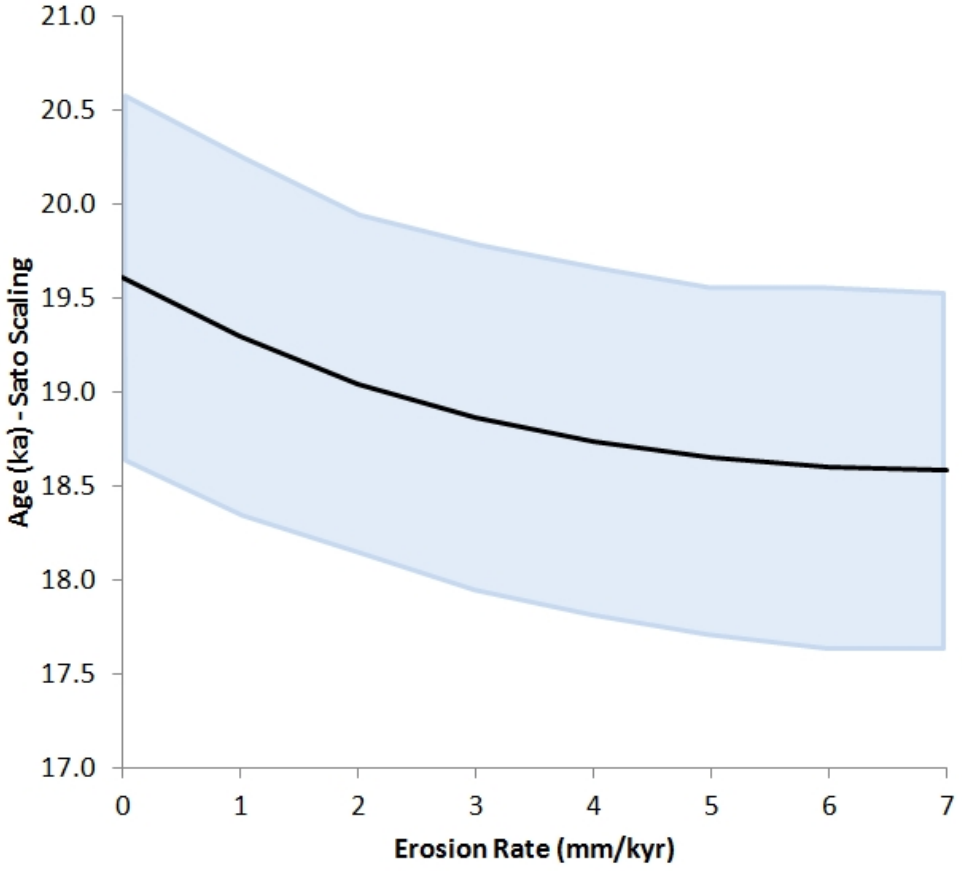

Figure 4.11: Effects of erosion rate on calculated age for a Tabernacle Hill whole-rock sample. Sample age is calculated using the Lifton/Sato scaling model (Lifton, 2012) and varying erosion rates. The shaded area represents the uncertainty bound. Sample is 05TAB05-1. Production in the sample is ∼51% from Ca, ∼11% from K, and ∼35% from Cl.

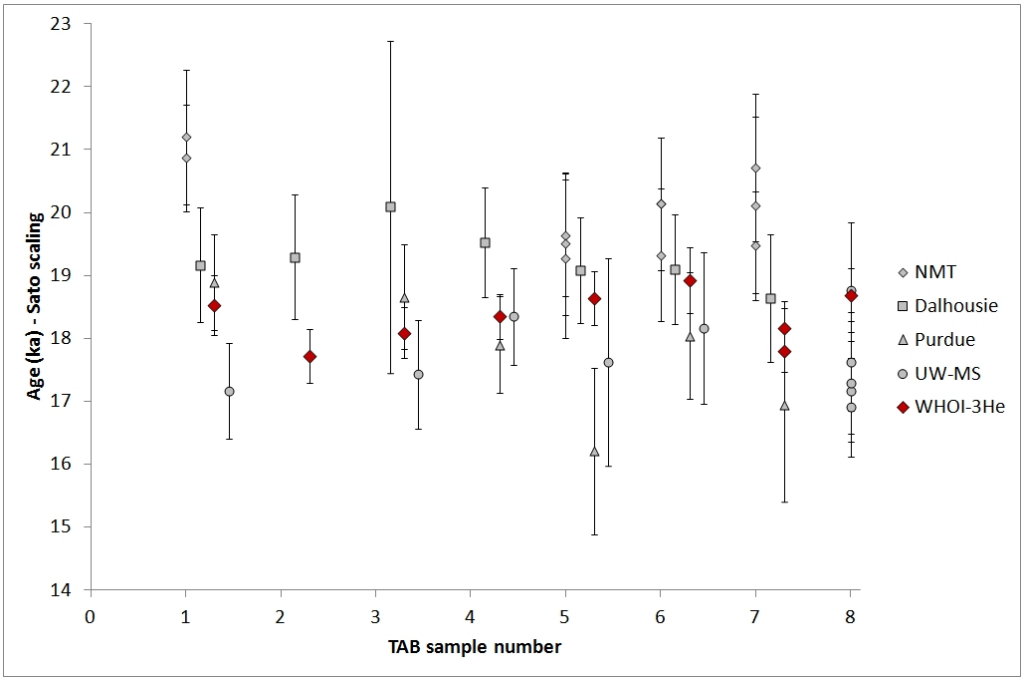

Figure 4.12: Plot of calculated ^{3}He ages in addition to all the calculated chlorine ages. Chlorine ages have been grayed out to emphasize the He samples. Ages calculated using Lifton/Sato scaling (Lifton, 2012) in CRONUScalc (see Chapter 2.

et al. (2010b). The helium-3 samples were aged using the CRONUScalc program with the Lifton/Sato scaling (Lifton, 2012). The helium-3 ages were very consistent for all of the samples (see Figure 4.12), yielding a mean of 18.3 ka and a standard deviation of 0.4 ka.

The helium ages are consistent with the chlorine-36 ages, although the mean helium-3 age is slightly lower than the mean chlorine-36 whole rock age. The mean helium-3 age is slightly higher than the plagioclase mineral-separate ages produced by Stone. This may indicate that there is a small systematic bias with the whole rock samples due to the inclusion of significant production from the thermal neutron production pathway.

4.3 Promontory Point quartzite

The Promontory Point site was originally designated as a calibration location for cosmogenic nuclides that can be measured in quartz, such as ^{10}Be, ^{26}Al, and ^{14}C. Due to the composition of these samples, it was unlikely that chlorine-36 analyses would be successful. However, the need for samples to constrain the $P_f(0)$ parameter (low K, low-Ca, high-Cl composition) was great, so this offered a possible sample location. Despite the small chance of success, samples from Promontory Point were run for chlorine-36.

4.3.1 Geology/site description

Promontory point (PPT) is at the tip of a ridge feature on the north side of the current Great Salt Lake. The two formations exposed on this bench are the late Precambrian Mutual Formation and the early Cambrian Tintic Quartzite Formation (Lifton et al., 2001). Based on the height of the remaining cliffs, erosion removed large amounts of material, on the scale of tens of meters, from this area during the Bonneville shoreline occupation (Lifton et al., 2001) (see Figure 4.13 and Figure 4.14). Joints within the quartzite facilitated the erosion (Lifton et al., 2001).

4.3.2 Samples Collected

Promontory Point sample locations were chosen based on typical cosmogenic nuclide considerations, as described in Dunai (2010), as well as several site-specific parameters. Although much of the bedrock had very little topography

Figure 4.13: Panoramic photograph showing the wave-cut bench of the Promontory Point quartzite sampling area. Photo by F. Phillips.

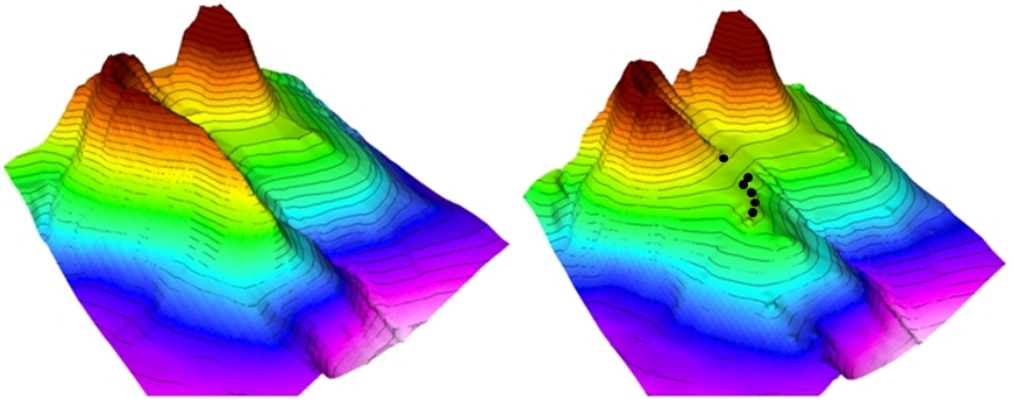

Figure 4.14: (left) Reconstruction of Promontory Point prior to erosion of the wave-cut bench and (right) the current topography. Only the sampled ridge (on the left in each figure) was reconstructed. Sample locations are shown as black dots in the image on the right. Notice that samples were collected in a transect stretching from the cliff to the far end of the bench.

(the sampled surface was sometimes less than 0.5 m above the surrounding topography), all attempts were made to sample only those bedrock outcrops that were topographically higher than the surrounding area to avoid cover by plants or soil. Samples on or near edges or large cracks were avoided to reduce any geometric issues or edge effects. Finally, the original surface texture, in this case a wave-polished patina, was sought out to reduce effects associated with erosion. The wave-polish only survives as long as there is essentially zero erosion. The sample locations, shielding, and other sample-specific information are included in Table 4.7.

Initial concerns about the timing of the erosion of the cliff led to a transect-based sampling plan. If samples closer to the lake were exposed earlier than samples closer to the cliff, they may have been subjected to larger amounts of inheritance (see Section 4.3.3). Ideally, the sampling of the bench would have been restricted to bedrock areas near the cliff because bedrock is not subject to as much possible variation in exposure history as for boulders. Unfortunately, there was a lack of bedrock close to the cliff so some wave polished boulders of similar lithology to the cliff were sampled as well in the hopes that they were eroded out close to the end of the Bonneville shoreline occupancy. 05PPT08 is an example of one of these boulders. Ultimately, samples along a transect from the cliff base to the farthest point on the bench showed no trends. The general sample transect is shown in Figure 4.14.

Descriptions for each sample, including composition, and other important sample information have been included in Appendix C.3.

Sample	Latitude	Longitude	Elevation (m)	Shielding	Thickness (cm)
05PPT01	41.2637	-112.475	1603	0.975	3
05PPT02	41.2637	-112.475	1603	0.992	3
05PPT03	41.2636	-112.476	1600	0.884	3
05PPT04	41.2636	-112.477	1598	0.982	2.5
05PPT05	41.2639	-112.475	1605	0.981	4
05PPT08	41.2638	-112.475	1606	0.884	2.5

Table 4.7: Location information for CRONUS-Earth Promontory Point samples. All samples are quartzite samples. The datum is WGS84 and shielding was calculated using azimuth/horizon pairs measured for each sample.

4.3.3 Possible Complicating Factors

Complicating factors for this site include inheritance, erosion, and sample preparation methods.

An estimation of the amount of material and total water depths covering the sampling site permit the calculation of the penetration of muons to the actual sample sites. These calculations are important because both of these factors (rock and water depths) could affect the inheritance. Water and/or rock above the sample locations would reduce the production within the samples due to absorption of the cosmic rays by the water or rock. I reconstructed the ridge by extending the general shape of the ridges exposed above the lake erosion level. My new reconstruction of the ridge shows depths of rock above the samples of 50-70m prior to the creation of the wavecut bench and 10-17m of water after the bench was created. The penetration of muons through the rock was calculated based on a depth of 13250 g/cm^2 using the CRONUScalc program and an age of 100 ka. The maximum contribution of inherited muons as compared to the modern surface production rate is 0.03% and is considered negligible for all future calculations. After the bench was cut, 10-17m of water was present over the sampling site. Cosmic rays are attenuated quickly in water and the brief duration of the

shoreline (1-2 ka at most) makes this contribution negligible. In order to collect samples least susceptible to inheritance, bedrock closest to the cliff was more desirable due to the obvious large amount of erosion. In this case, the shielding corrections necessary due to this sampling procedure introduce less uncertainty to the overall age calculation than the possible inheritance issues present at greater distances from the cliff face.

Erosion and plant cover are not an issue. The samples have wave polished surfaces (making any measurable erosion negligible) and there are no plants/trees in the area and no fractures to encourage plant growth. Erosion is discussed here only due to the sensitive sample chemistry. For this site, the age-erosion rate relationship is demonstrated in Figure 4.15. For an erosion rate of 1 mm/kyr, there is an age difference of 4-7% from the age calculated with zero erosion. This illustrates that, although these samples are made out of a more resistant material (quartzite) than the Tabernacle Hill samples, the Promontory Point sample ages are more sensitive to erosion due to the chemical composition of the samples. However, based on the very wave polish still visible on the sampled bedrock and boulders, it is clear that little-to-no erosion has taken place. A reasonable erosion rate adopted for these samples is a zero erosion rate because any measurable erosion would have removed the wave polish.

Like the Tabernacle Hill samples, the Promontory Point samples were originally presented in Marrero (2009). These samples also showed significant scatter (see Figure 4.16) and were thought to suffer from the same problem as the Tabernacle Hill samples, such as inhomogeneity in sample splitting or other laboratory problems. The samples were reprocessed as part of this work. During the previous sample preparation, black particles were noted in the samples and

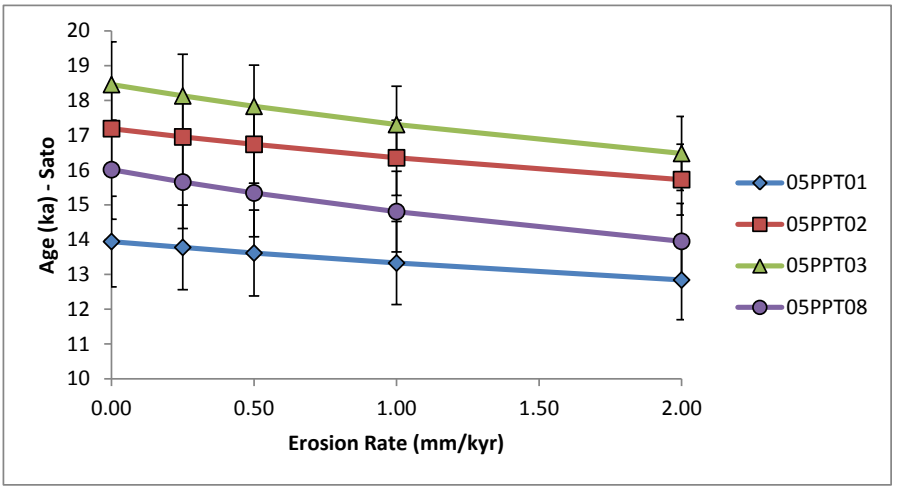

Figure 4.15: Promontory Point variation in sample ages for different erosion rates. Sample ages were calculated using Sato scaling in CRONUScalc.

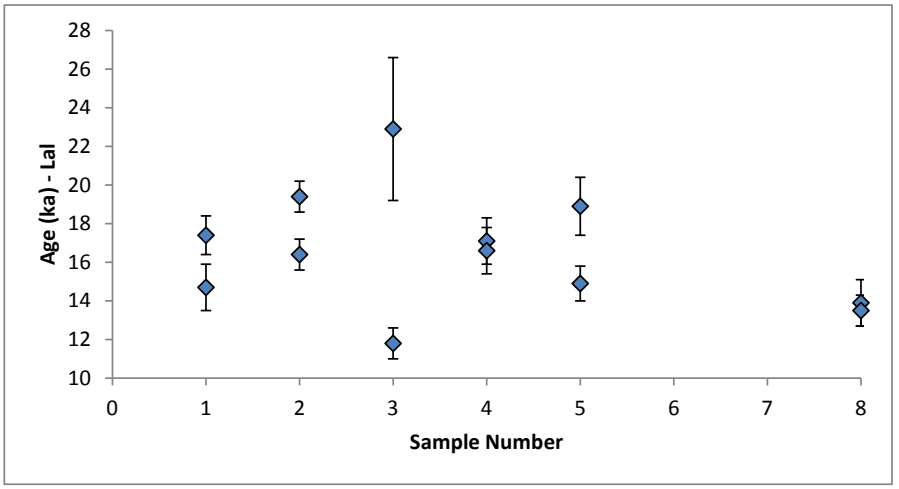

Figure 4.16: Promontory Point ages as cited in Marrero (2009). Ages were calculated using CHLOE (Phillips and Plummer, 1996), which uses Lal scaling.

sample preparation procedures were modified to deal with this material retain this material. However, other contaminating particles could also have remained in the sample, meaning that other contaminants could have contributed to the erratic results. In reprocessing the samples, the samples were rinsed following the standard lab procedure and this removed significant amounts of the black material (splits designated with an 'R' to indicate that the particles were partially removed). Density separation or acid etching were not performed. The results from the second analysis are discussed in detail in the next section.

4.3.4 Promontory Point Data and Discussion

The results from Promontory Point are aged using the final calibrated production rates (see Chapter 8) and are shown in Figure 4.17. Of the four samples, only two overlap the independent age bound and three of the four samples overlap within analytical uncertainties (although not to a large extent). These samples have very different compositions from one another (see full chemical composition in Appendix C.3), ranging from >50% production from potassium to >90% production from chlorine. There is no significant production from calcium in any of these samples.

The Promontory Point quartzite samples have insignificant concentrations of calcium and some of the samples are also very low in potassium, which should, in theory, allow for the calibration of the $P_f(0)$ production pathway from some of these surface samples as well as helping to constrain the potassium pathway. Unfortunately, the small number of samples (four) and the erratic results makes these samples undesirable for calibration. The Promontory Point sample ages also did not seem to be in line with the other sample sites yielding potassium production rates, such as Peru (see Chapter 6) and Scotland (see Chapter 5).

4.3.5 Comparison with Other Nuclides

Promontory Point has the largest number of beryllium-10 analyses from the largest number of different labs compared to all other CRONUS sites. In general, the beryllium-10 data is more consistent than the chlorine-36 data. There is no bias between samples based on the beryllium-10 results, so the scatter in the chlorine-36 data is unexpected and is not due to inheritance or erosion effects.

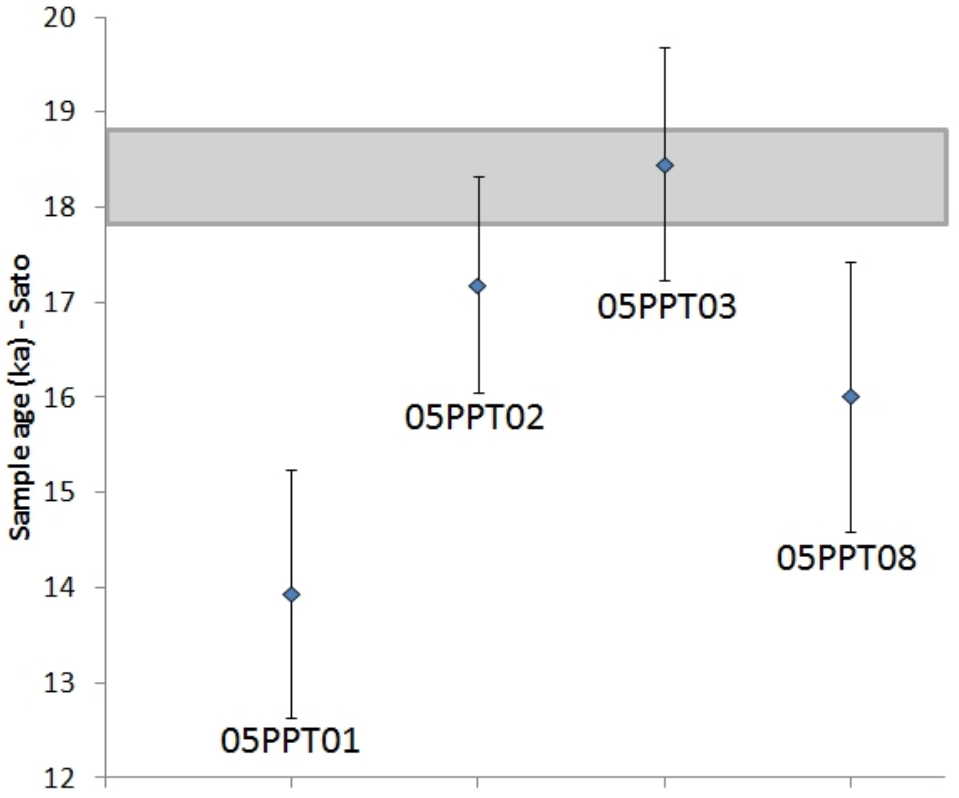

Figure 4.17: Promontory Point ages from chlorine-36 as calculated using the Sato scaling in the CRONUScalc. The gray box shows the independent age bounds. Sample points are labeled individually.

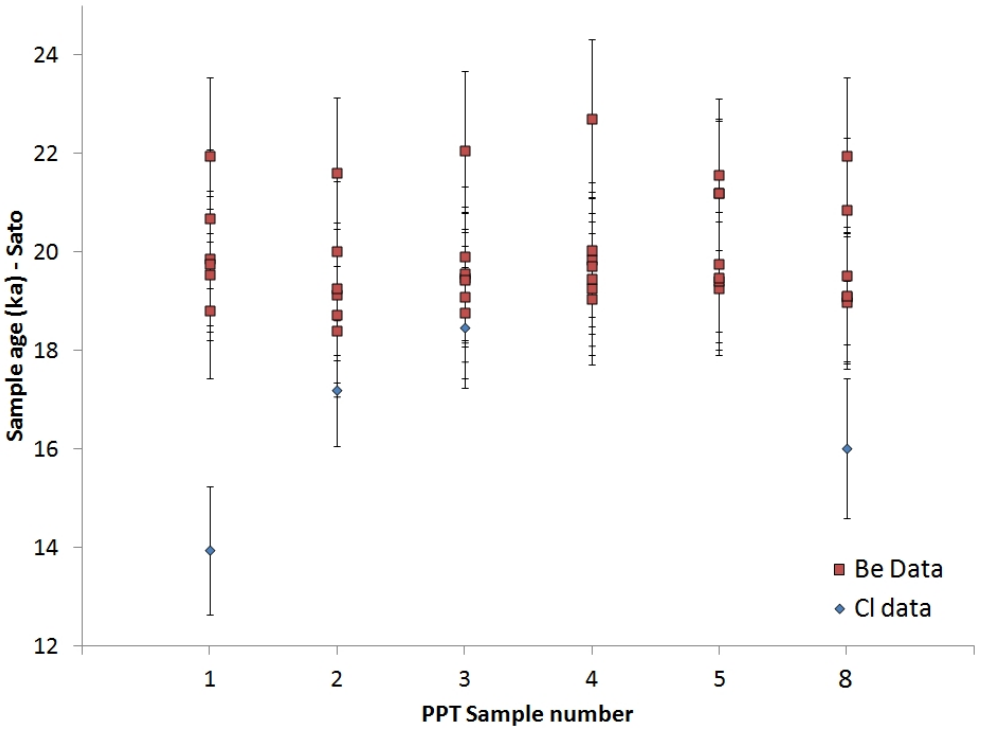

Figure 4.18: Promontory Point age comparison between chlorine-36 and beryllium-10. Calculated using the Sato scaling in the CRONUScalc.

The ages resulting from the beryllium-10 CRONUS data (as calculated using the final calibrated production rates) are compared to the chlorine-36 ages (also calculated with the final calibrated production rate) in Figure 4.18. Possible causes for the scatter are the sample preparation methods and the varying contribution of the thermal neutron pathway.

4.4 Bonneville Conclusions

The Tabernacle Hill chlorine-36 data from plagioclase mineral separates provides a consistent dataset for calcium spallation calibration. While the whole-rock samples are more scattered, the datasets are consistent across three labs and are used to calibrate the $P_f(0)$ parameter. Of all the chlorine-36 datasets from

Tabernacle Hill, the mineral separates also agree best with the ages produced by helium-3 analyses of the same samples.

The investigation to determine whether or not the Promontory Point samples could be used for chlorine-36 calibration $P_f(0)$ showed that the samples are not appropriate. The scatter of the chlorine data is significant and the discrepancy between the beryllium-10 and chlorine-36 ages provide sufficient evidence that there are likely problems with these samples. Overall, the data from Bonneville provides good calibration data for the calcium spallation production pathway and is one of the sites used for the calibration of the $P_f(0)$ parameter.

CHAPTER 5

SCOTLAND-SITE DESCRIPTION AND DATA

The Scotland geological calibration location is being used as a primary calibration site in the CRONUS-Earth project. This chapter is intended to support the main calibration chapter of this dissertation by describing the site and the resulting data and assessing the quality of both. Most of the information contained herein will be published by a CRONUS-Earth investigator as part of a special volume in Quaternary Geochronology.

In this paper, all original radiocarbon ages will be reported as ^{14}C years BP, indicating years before 1950. When needed, the radiocarbon ages are calibrated using Calib 6.02 (Stuiver et al., 2005). These calibrated ages are reported as cal ka or cal years BP. In some cases, samples are reported as "years before 2010" to indicate that 60 years has been added to the calibrated radiocarbon age. When dealing with ages from cosmogenic nuclides, the ages are reported as ^{10}Be ka or ^{36}Cl ka as necessary to avoid confusion. The cosmogenic nuclide ages are all referenced to the year 2010.

5.1 Site description

Two main areas were sampled in Scotland: the Isle of Skye and the Scottish highlands, as shown in Figure 5.1. The Isle of Skye is one of the inner Hebrides

off the west coast of Scotland and has a diverse landscape. The central area of Skye is the remainder of a Paleogene plutonic center and is part of the British Tertiary Igneous Province (Ballantyne et al., 1991). The lithology in the area ranges from Tertiary gabbros in the west, granites and sandstones in the east, to Tertiary basaltic lavas in the north. The Black Cuillins range is located in the central part of Skye (see Figure 5.2). We sampled at several locations on the Isle of Skye, including the Red Cuillins, the Black Cuillins, and Kyleakin Pass.

Other samples were collected on the mainland in the Scottish highlands. The Scottish highlands are part of the Hebridean Craton and are located to the west of the Moine thrust (Craig, 1991). The main lithology in the sampled areas was Torridonian sandstones, although there are other patches of metamorphic rocks. The Corrie Nan Arr samples consisted only of Torridon sandstone. The other site in the highlands, Maol Chean-Dearg, was composed of quartzite, likely from the Cambro-Ordovician quartzite units directly overlying the Torridonian rocks (see Figure 5.1 for outcrop locations) (Craig, 1991). Both the Isle of Skye and the Scottish highlands sites were chosen as geological calibration sites due to the beautifully-preserved glacial landforms with a well-defined timeline for formation.

During the Last Glacial Maximum, in the late Devensian ($\sim$18 ka), the entire Isle of Skye was covered by the British ice sheet (Ballantyne et al., 1998), except for a few nunatuks (Ballantyne et al., 1991). Despite the existence of some unglaciated material at the tops of peaks, the Devensian glaciation eroded significant amounts of material from the landscape.

During the cooling of the Younger Dryas, a new period of glaciation occurred and once again covered a significant part of the landscape in Scotland (see

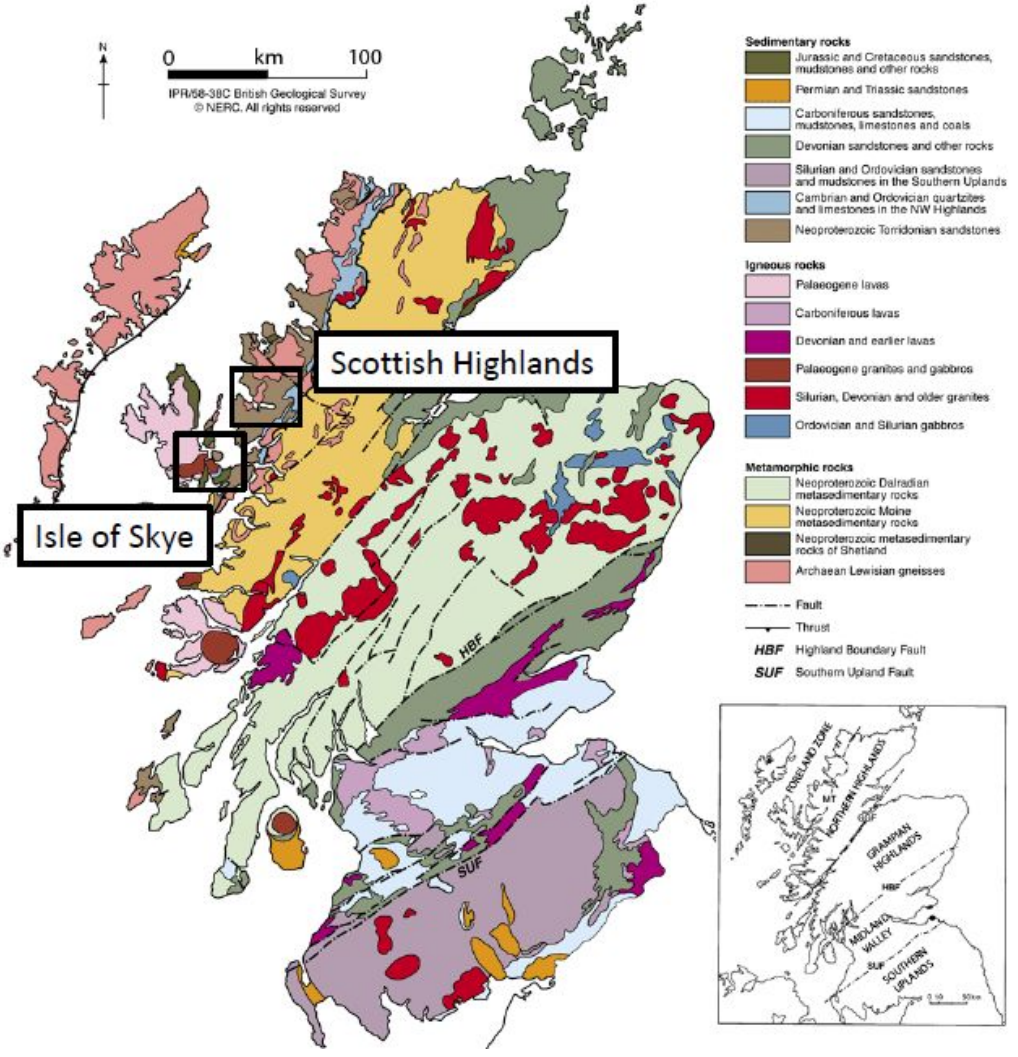

Figure 5.1: Map of the geology of Scotland (Trustees of Scottish Museums, 2012). Labeled black boxes are sample areas.

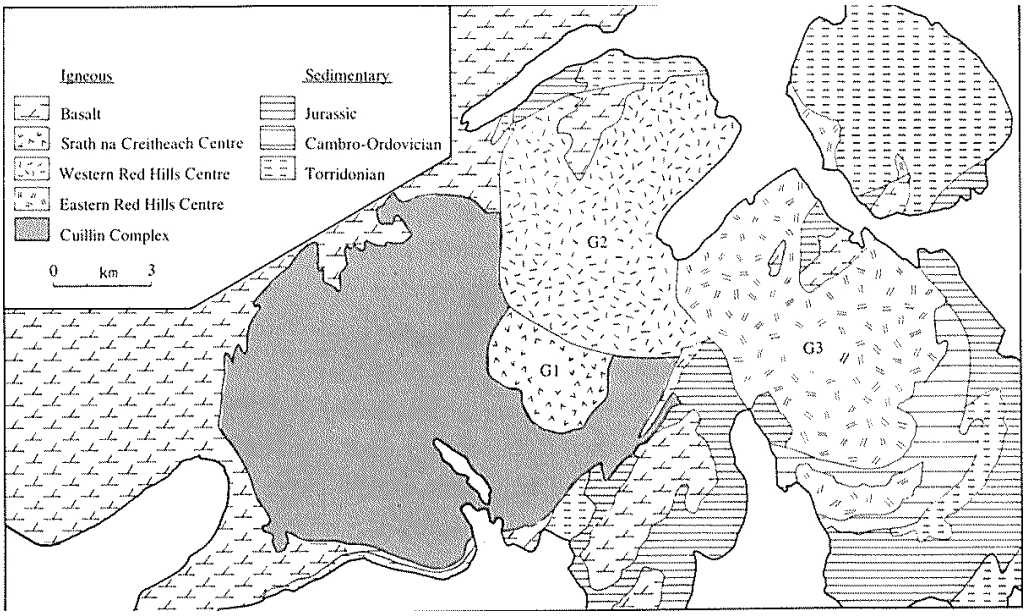

Figure 5.2: Geological map of the southern area of the Isle of Skye (Ballantyne et al., 1991).

Figure 5.3). Although these glaciers were not as extensive as the late Devensian British ice sheet, they caused the scouring of bedrock surfaces and the formation of what has become an extensively studied moraine succession (Benn et al., 1992; Ballantyne et al., 1991). During this time, a large ice cap covered the northwestern highlands of Scotland. This advance, called the Loch Lomond readvance, had a main ice cap but it also had other mountainous areas with local centers of glaciation originating from the smaller glaciers that formed in the corries (Craig, 1991). Ice fields formed in mountains on islands (such as the Isle of Skye) as well as in isolated locations on the mainland. On Skye, for example, an ice cap formed in the Cuillins and smaller glaciers formed in seven corries fringing the ice field on the west (Figure 5.4) (Ballantyne et al., 1991). The rockfalls being used as the calibration landform for this study are associated with the outlying glacial centers instead of the main ice field.

The geological calibration sites chosen for the CRONUS-Earth project are

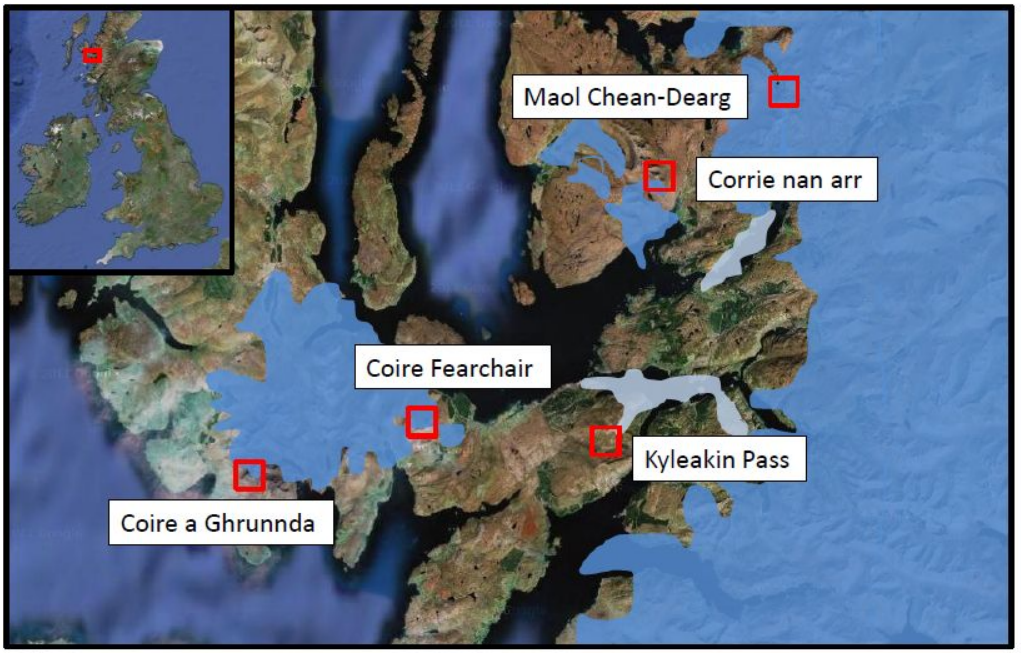

Figure 5.3: Map of the maximum ice extent of the Loch Lomond readvance in the sample areas. Light and dark blue indicates the extent of the glaciers. Modified from Golledge (2010).

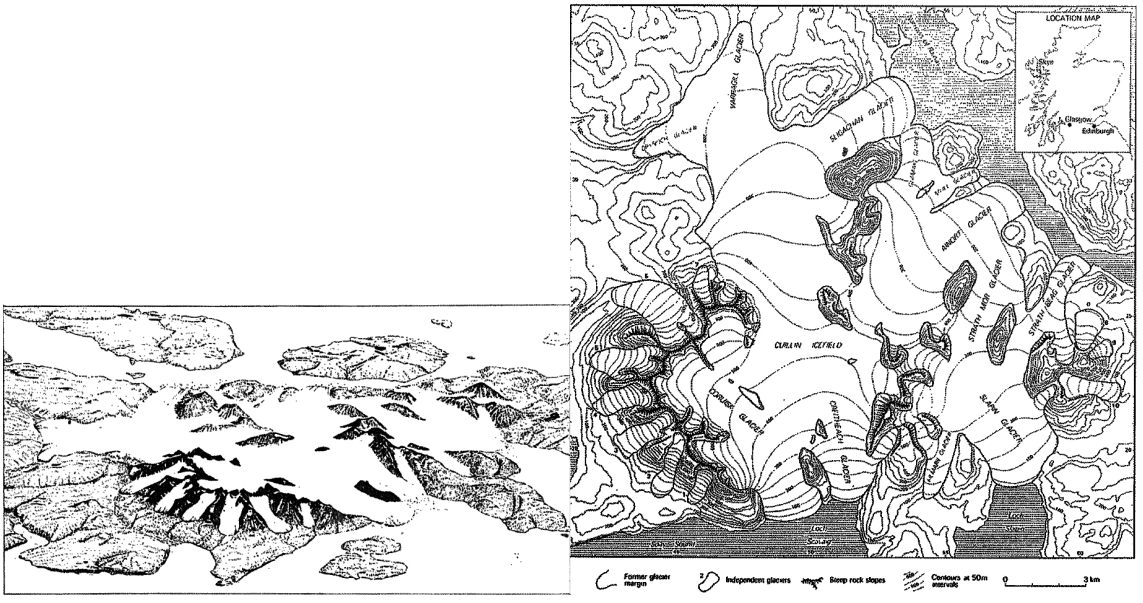

Figure 5.4: (left) Oblique view of a reconstruction of the Cuillin Icefield and corrie glaciers for the Cuillins; (right) Map of the areal extent of the same Cuillins Icefield (Ballantyne, 1989).

Figure 5.5: (left) Picture of the rockfall site in the Red Cuillins (Photo by Marc Caffee). (right) Picture of scoured bedrock at the Black Cuillins site.

of three types: 1) scoured bedrock, 2) supraglacial/subglacial boulders from rock avalanches associated with the end of the Loch Lomond readvance, and 3) terminal moraine boulders (Figure 5.5). The rock avalanches were probably caused by oversteepening of the rock walls by glacial processes (Ballantyne, 2003). Ballantyne and Stone (2004) summarize the qualities of most rock avalanches in Scotland as remaining close to the failure wall and not spreading out significantly over the flatter valley floor. In the case of the calibration samples, the rocks fell onto the glacier and were transported downstream as the glacier moved (Ballantyne, 2008). The exposure age of these rockfalls is based on the fact that the sampled rocks were not transported to the terminal part of the glacier before the glacier disappeared, indicating that the exposure prior to deglaciation should be minimal. The rocks are distributed along the length of the valleys, extending to the terminal moraine. This indicates an exposure age that coincides with the deglaciation age of the region. The scoured bedrock was also clearly exposed at the final deglaciation. For the terminal moraine samples, an age representing the maximum extent of the glacier is a better estimate of the exposure age.

Glaciers are known to be good indicators of climate change due to their sensitivity to precipitation and/or temperature depending on their location and climate regime (Oerlemans, 2005; Mark and Seltzer, 2005). Once the temperatures warmed, the glaciers retreated very quickly (Golledge, 2010). However, in order to use the Scottish glacial landforms as a geological calibration site, we need limiting ages from independent dating methods. Direct dating in the area using pollen and radiocarbon on peat has provided some bracketing ages for the moraines and glacially-scoured bedrock (Walker et al., 1988; Benn et al., 1992; Walker and Lowe, 1990; Ballantyne et al., 1991). However, due to the good correlation between the glacial movements and the record of cooling, we can correlate the cooling period from the NGRIP ice core (Rasmussen et al., 2006) with the movement of the glaciers in Scotland, reducing the window of time for the deglaciation event.

5.1.1 Independent age constraints

There have been numerous studies involving different techniques, including palynology, radiocarbon, varve counting, and chironomids, in order to determine the deglaciation age in northwestern Scotland. Each of these techniques provides a different set of constraints on the timing. The information gained from each technique is outlined separately below.

The combination of detailed geomorphic mapping and pollen studies has produced important information about the age and climate of the region during the Loch Lomond readvance. Walker et al. (1988) compared the pollen from cores taken inside and outside the mapped Loch Lomond ice margins. The oldest radiocarbon ages found within the ice margins, 9590 ± 90 and 10220 ± 150 ^{14}C yrs

(SRR-3124 and SRR-3125), yield the earliest time of accumulation of organic material and indicate that the glacier must have receded prior to these dates. The cores outside the ice margin showed significant amounts of late glacial sediment while those inside contained only Flandrian-aged sediments ($\sim$ 10 cal ka to present), which is consistent with the interpretation of deglaciation prior to 10 cal ka.

The chironomid (non-biting midge) temperature reconstructions provide a high-resolution record of summer temperatures for the region (Brooks and Birks, 2000). Previous studies using coleopteran fossils (beetles) did not provide fine enough resolution to see the smaller oscillations, such as the Younger Dryas cold period. The chironomid temperature reconstruction in southeastern Scotland by Brooks and Birks (2000) provides mean July air temperatures from approximately 14.5 cal ka to slightly after the Younger Dryas-Holocene transition. The temperature fluctuations inferred from chironomid record correlates well with the Greenland ice core (GIC) oxygen isotope curves (Rasmussen et al., 2006), indicating that it is reasonable to link the local Scottish weather patterns to the GIC. Figure 5.6 shows this correlation.

Assuming that the age control on the temperature record is correct, we can look at other geological indicators of glaciation in the region. Ballantyne (1989) provides two arguments for the Loch Lomond age of the glacial advance on the Isle of Skye. Due to the low temperatures during the Loch Lomond stadial, any area not covered by glaciers should show evidence of frost weathering, enlargement of joints, and the presence of mature relict talus slopes. Areas covered by glaciers would have been protected from these effects. None of these features can be seen inside of the ice margin, so these areas must have been covered by glaciers during the cold temperatures of the Loch Lomond readvance. A second

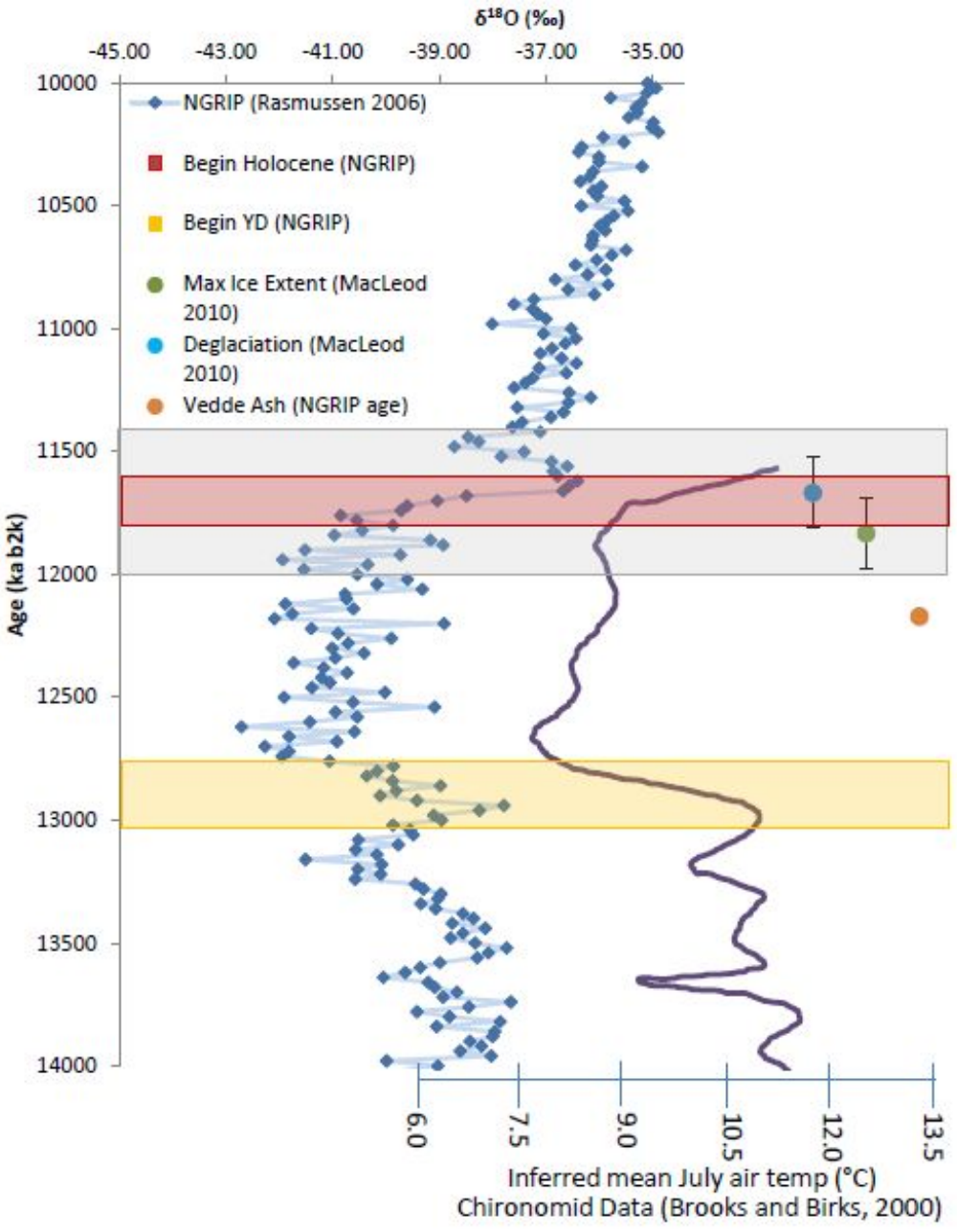

Figure 5.6: Independent age compilation. NGRIP data (δ^{18}O values shown by 20-year average points in rhombs) from Rasmussen et al. (2006); chironomid data (inferred mean July temperatures shown in solid purple line) from Brooks and Birks (2000); maximum ice extent and final deglaciation ages (shown as colored circles) from MacLeod et al. (2010). The gray box indicates the final age selected by the CRONUS-Earth project for the Scotland sites (12,690 $\pm$ 300 years before 2000). Dates from the NGRIP core are provided for the beginning and end of the Younger Dryas period.

argument for the timing of the Loch Lomond readvance is that the altitude of the marine limit is different inside and outside the glacial limit. In some areas, the higher shorelines have been erased by glacial erosion. Based on the known shoreline levels, this is consistent with a Loch Lomond age readvance as well. While these two lines of evidence are not as precise as radiocarbon ages, they do provide additional information that corroborates the the Loch Lomond readvance during the time period indicated.

A high-resolution varve record from a glacially dammed lake provides another set of age constraints on the deglaciation age. MacLeod et al. (2010) used varves from two sites, one within the ice margin and one undisturbed core outside the margin, in order to determine the timing of the maximum extent of the Loch Lomond readvance as well as the timing of the final deglaciation. The radiocarbon dates and varve counting indicated that the maximum extent of glaciers in the Loch Lomond area was later in the Younger Dryas than previously thought. This was determined to be after 12 cal ka BP based on the the timing of the near-terminal site being overrun by the glacier. The scoured bedrock regions would have been exposed as glaciers retreated. Deglaciation at this site was dated to 11,812-11,524 yr before 2000 assuming that the cessation of varve deposition due to lake drainage indicates deglaciation. These dates also correspond well with the other records of deglaciation, as seen in Figure 5.6.

The local radiocarbon age constraints provide maximum and minimum ages, but the window can be reduced by comparison to ice cores from Greenland (Rasmussen et al., 2006). By showing that the advance and retreat of the glaciers was synchronous with the changes in the Greenland ice oxygen isotope record, such as the NGRIP core, we can reduce the window for the time of glaciation

by using the cooling period determined from the core. The span of the Younger Dryas, according to the cores, is 1,193 years starting in 12,896 $\pm$ 138 and continuing to 11,703 $\pm$ 99 years before the year 2000 (Rasmussen et al., 2006). However, the resolution is such that we can look at individual excursions within this 1200 year window. The deglaciation time based on the core is 11.7 $\pm$ 0.14 ka, as seen in Figure 5.6.

Based on the information above, the outer moraines formed at the period of lowest temperatures when the glaciers were at their maximum extent, which occurred at 12.5 ka (Rasmussen et al., 2006) or after 12.0 ka (MacLeod et al., 2010). However, most of the calibration sites are not glacial moraines, but are instead scoured bedrock and supraglacial rockfalls. These features were exposed at the time of the final deglaciation, or 11,700 $\pm$ 300 cal years before 2010, which is the final age assigned to the samples for this calibration. This is consistent with the Greenland ice core transition to warmer temperatures as well as the timing for the deglaciation determined by MacLeod et al. (2010). These are all consistent with other information about paleoclimate and timing from chironomid studies, geological evidence, and pollen evidence.

5.2 Possible Complicating Factors

This section covers additional concerns at this particular site. In this case, the concerns include inheritance, the possibility of sampling reworked boulders from the larger ice sheet advance, sample cover (peat/till/snow), water effects on low-energy production, and elevation changes due to isostatic rebound. These are covered individually below.

Another possible issue related to the extent of glaciation is the possibility of inheritance due to the muonic component of the cosmic-ray flux. Muons can penetrate very deeply (tens of meters) into the subsurface. This inherited production at depth can create problems in young surface samples if insufficient material was removed during glaciation. For the samples collected on the Isle of Skye, most were likely glaciated twice in the course of the last 15,000 years. The late Devensian-age advance was very extensive, leading to large erosive forces. Additional material was also removed by the glaciers during the Loch Lomond readvance.

The possibility of inheritance differs for the different types of samples collected for the calibration. It is highly unlikely that the rockfall samples contain inherited components due to the large amounts of material removed. However, bedrock sites have a higher inheritance possibility. Moraine boulders generally have a small chance of inheritance, but there is a possibility at these sites of reworked moraine boulders from the late Devensian glaciation being sampled. Our sampling of mostly supraglacial rockfalls and bedrock instead of moraines significantly reduces the possibility of choosing reworked boulders for sampling. By understanding the local lithology and choosing only boulders matching that lithology, it is also possible to avoid erratics from previous glaciations. Reworked material does not appear to present a problem due to our strict sampling guidelines.

Cover by peat, till, snow, or other material would contribute to altering the cosmic-ray flux at the sampling sites. At one sampling site, Kyleakin Pass, the samples were downgraded from primary samples to secondary samples due to the likelihood of extended cover at the sample site. During the sampling, all

possible precautions were taken to sample dipping boulder surfaces so that the possibility of extended cover could be minimized. As no real outliers can be seen, it appears that this is unlikely to contribute to problems with the samples. The likelihood of significant snow cover is small, although possible in certain areas.

For cosmogenic nuclides produced through low-energy pathways, such as chlorine-36, the effect of water nearby or above the sample is a concern. Water absorbs energy from neutrons, changing the flux that reaches the sample. Even water from surrounding areas up to meters away can change the flux (Zreda et al., 2008). The water content in the rock is only estimated, and the water in areas surrounding the sample has not been accounted for in sample calculations. However, the only chlorine samples being processed from this site have very low chlorine-concentrations (7-40 ppm), with only 16 % or less of the production being attributed to low-energy pathways, meaning that water effects should not signficantly impact the results.

Significant changes in elevation, such as those caused by isostatic rebound, can affect production rates. There has been extensive modeling to determine the change in elevation of the entire British Isles region after the retreat of the British ice sheet. Modeling by Lambeck (1993a,b) takes advantage of the large dataset of sea level points and ice locations to create a detailed model that is dependent on earth and ice parameters and accounts for previous glaciations when looking at the loading at a specific time. Based on this modeling, it shows that the entire Isle of Skye region has not changed elevation significantly during the last 10 ka. The Isle of Skye is located in between the two locations shown in bold lines in Figure 5.7. Those locations (if averaged) yield maximum changes of sea level through the last ten thousand years ranging from 0 to -25 m. This is not enough to make

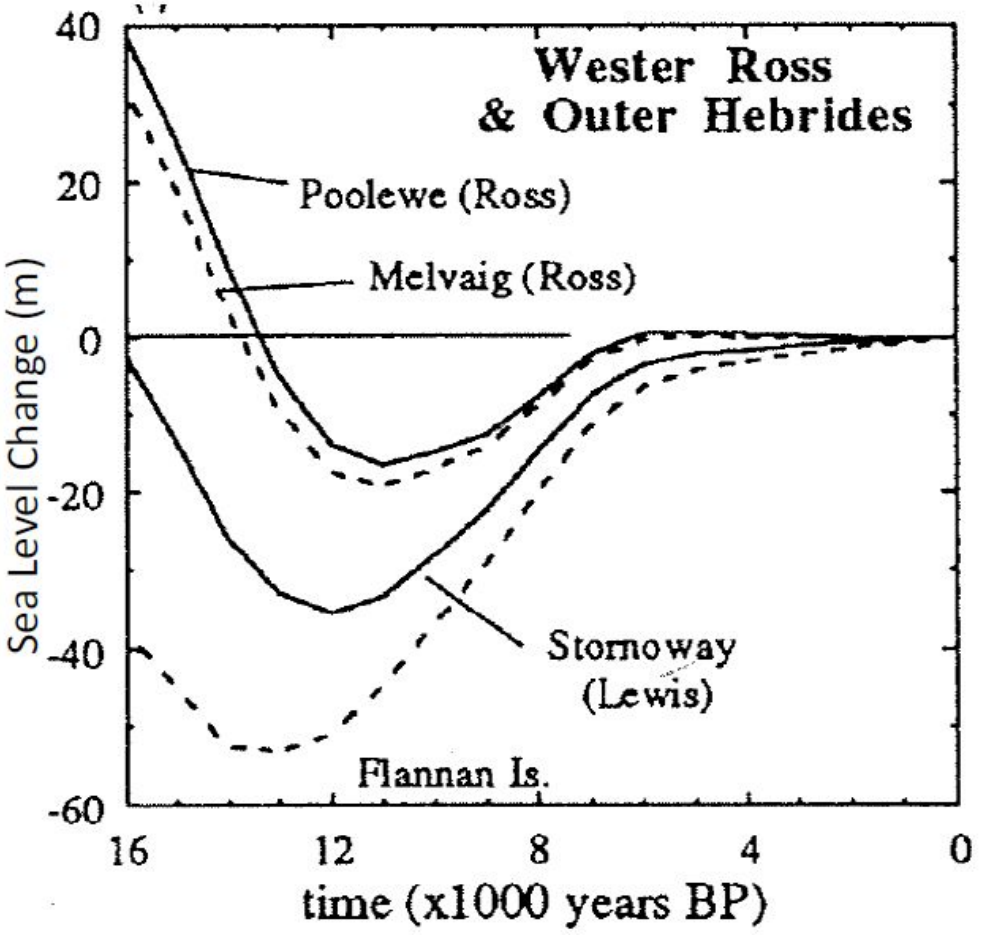

Figure 5.7: Sea level prediction for the Outer Hebrides and Wester Ross (Lambeck, 1993a).

a measurable difference in production rates. This amount of change could yield a 0-2.5% difference in age, which is on par with the measurement uncertainties in the samples. A new ice sheet reconstruction indicates that there may be some uncertainty in the thickness of the ice (Fretwell et al., 2008), although there is no new model or other evidence to indicate that a correction for elevation change due to isostatic rebound is necessary in the northwestern portion of Scotland.

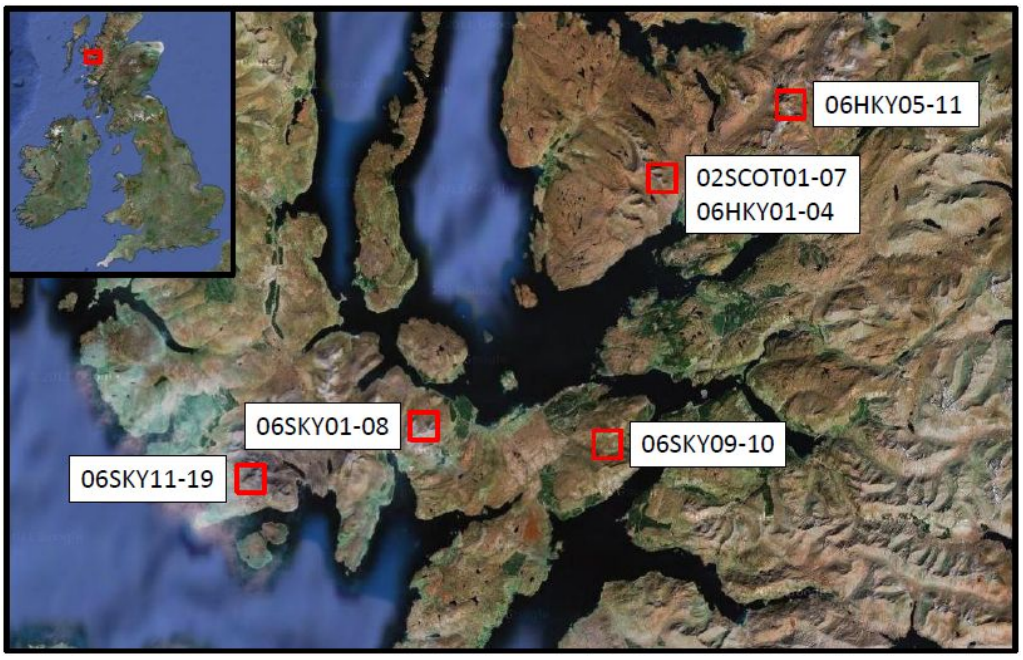

Figure 5.8: Map of sample locations for all samples discussed here. Inset shows location of sample map on map of UK (Google, 2008).

5.3 Results & Discussion

Samples for the CRONUS-Earth project were collected from five locations on the Isle of Skye and the Scottish highlands (Figure 5.8 with coordinates and other collection information in Tables 5.3 and 5.4). Samples were processed for chlorine-36, beryllium-10, aluminum-26, and carbon-14. All the information about the concentrations for each nuclide is included in Tables 5.1 and 5.2. The individual results are discussed on a site-by-site basis below.

5.3.1 Isle of Skye

Coire Fearchair, Beinn na Caillich, Red Cuillins Samples 06SKY01 through 06SKY08 were collected from the Red Cuillins at a location known as Coire Fearchair,

Sample	^{10}**Be**^{a} [at/g]	^{26}**Al**^{a} [at/g]	^{36}**Cl**^{a} [at/g]
06-SKY-01	70900 ± 2400 73200 ± 6800^{b}		176400 ± 8200
06-SKY-03	62700 ± 2000 61900 ± 4700^{b}	471000 ± 36000	
06-SKY-04	67900 ± 1900 74800 ± 7500		
06-SKY-05	70100 ± 9000^{b}		
06-SKY-06	65900 ± 2100 70300 ± 7100^{b}		141200 ± 7900
06-SKY-07	64200 ± 2100 64600 ± 5000^{b}	593000 ± 56000	147100 ± 7300
06-SKY-08	64100 ± 4200^{b}		176000 ± 8500
06-SKY-09	70200 ± 4700^{b}		
06-SKY-10	68000 ± 5400^{b}		
06-SKY-11			203000 ± 8800
06-SKY-12			209300 ± 8500 206300 ± 8300
06-SKY-14			326000 ± 13000
06-SKY-15			203000 ± 10000
06-SKY-16			181000 ± 10000
06-SKY-17			178800 ± 7900 199100 ± 9000
06-SKY-18			155500 ± 7200 127300 ± 6100
06-SKY-19			107000 ± 8100 112700 ± 7100

Table 5.1: Table of Isle of Skye, Scotland sample concentration information for all nuclides. ^{a}John Stone at Univ. of Washington (unless otherwise indicated); ^{b}PRIME Lab at Purdue Univ.

Sample	^{10}**Be**^{a} [at/g]	^{26}**Al**^{a} [at/g]	^{14}**C**^{c} [at/g]
06-HKY-01	57400 ± 1200	424000 ± 22000	119000 ± 16000
06-HKY-03A	62100 ± 1200	396000 ± 20000	109000 ± 15000 96000 ± 16000
06-HKY-04	53300 ± 1000	387000 ± 21000	120100 ± 8000
06-HKY-05	81100 ± 1400	580000 ± 22000	168800 ± 8400 146000 ± 15000 126000 ± 15000
06-HKY-06	82600 ± 2500	586000 ± 23000	180000 ± 16000 137000 ± 16000
06-HKY-07	77900 ± 1500	563000 ± 21000	148000 ± 15000 104000 ± 16000
06-HKY-08	79600 ± 1300	560000 ± 24000	149000 ± 15000
06HKY-09			143000 ± 15000
06-HKY-10	78600 ± 1400	583000 ± 22000	150000 ± 15000 111000 ± 16000
06-HKY-11	83800 ± 1200	606000 ± 22000	160000 ± 15000
02-SCOT-001-ARR-0-4cm	56500 ± 1300	392000 ± 22000	
02-SCOT-002-ARR	57400 ± 1100	454000 ± 23000	
02-SCOT-003-ARR-0-4cm	54400 ± 1200		
02-SCOT-004-ARR	57500 ± 1200	400000 ± 24000	
02-SCOT-005-ARR	58800 ± 1300	451000 ± 27000	
02-SCOT-006-ARR	56400 ± 2000	405000 ± 24000	
02-SCOT-007-ARR	59500 ± 1700	427000 ± 30000	
02-SCOT-008-ARR	57700 ± 1200	397000 ± 20000	

Table 5.2: Table of Scottish highlands, Scotland sample concentration information for all nuclides. [a]John Stone at Univ. of Washington (unless otherwise indicated); [c]Nat Lifton at Univ. of Arizona (currently at Purdue University).

Sample name	**Site Name**	**Latitude** [DD]	**Longitude** [DD]	**Elev** [m]	**Thick** [cm]	**Shield** [unitless]	λ_{eff} [g/cm^2]
06-SKY-01	Coire Fearchair	57.24081	354.02728	442	7.0	0.92	157
06-SKY-03	Coire Fearchair	57.24091	354.03189	323	8.0	0.96	174
06-SKY-04	Coire Fearchair	57.24223	354.03124	339	7.5	0.98	173
06-SKY-05	Coire Fearchair	57.24240	354.03370	322	3.5	0.99	169
06-SKY-06	Coire Fearchair	57.24249	354.03412	310	7.5	0.99	172
06-SKY-07	Coire Fearchair	57.24269	354.03515	300	6.0	0.99	165
06-SKY-08	Coire Fearchair	57.24250	354.03470	314	2.0	0.99	158
06-SKY-09	Kyleakin Pass	57.22060	354.27570	309	5.0	1.00	164
06-SKY-10	Kyleakin Pass	57.22060	354.27560	311	11.0	1.00	163
06-SKY-11	Coire a Ghrunnda	57.2014	353.7763	695	4.0	0.979	137
06-SKY-12	Coire a Ghrunnda	57.2014	353.7763	695	5.0	0.979	137
06-SKY-14	Coire a Ghrunnda	57.19946	353.78039	702	5.0	0.955	137
06-SKY-15	Coire a Ghrunnda	57.19935	353.77888	664	7.5	0.963	137
06-SKY-16	Coire a Ghrunnda	57.19958	353.77703	660	5.0	0.95	137
06-SKY-17	Coire a Ghrunnda	57.19982	353.77634	660	6.5	0.928	137
06-SKY-18	Coire a Ghrunnda	57.1895	353.76403	229	4.0	0.989	136
06-SKY-19	Coire a Ghrunnda	57.18392	353.76594	146	5.5	0.992	136

Table 5.3: The location and sample collection information for each Isle of Skye, Scotland sample, including the latitude and longitude. λ_{eff} (attenuation length) was calculated using CRONUScalc and is the effective attenuation length incorporating shielding when possible.

Sample name	**Site Name**	**Latitude** [DD]	**Longitude** [DD]	**Elev** [m]	**Thick** [cm]	**Shield** [unitless]	λ_{eff} [g/cm^2]
06-HKY-01	Corrie nan arr	57.41525	354.35359	133	3.0	0.99	165
06-HKY-03A	Corrie nan arr	57.41550	354.35338	131	5.0	0.99	167
06-HKY-04	Corrie nan arr	57.42309	354.34188	137	10.0	0.97	153
06-HKY-05	Maol Chean-Dearg	57.48742	354.55072	521	4.5	0.99	172
06-HKY-06	Maol Chean-Dearg	57.48755	354.55023	527	4.0	0.99	172
06-HKY-07	Maol Chean-Dearg	57.48778	354.55228	500	6.0	0.99	172
06-HKY-08	Maol Chean-Dearg	57.48868	354.55297	502	5.0	0.99	172
06-HKY-09	Maol Chean-Dearg	57.48863	354.55295	502	5.0	0.98	172
06-HKY-10	Maol Chean-Dearg	57.48732	354.55134	510	7.5	0.99	172
06-HKY-11	Maol Chean-Dearg	57.48743	354.55011	528	3.5	0.99	172
02-SCOT-001-ARR	Corrie nan arr	57.41413	354.35625	139	4.0	0.99	170
02-SCOT-002-ARR	Corrie nan arr	57.41413	354.35625	139	2.0	0.99	170
02-SCOT-003-ARR	Corrie nan arr	57.41413	354.35625	139	4.0	0.99	170
02-SCOT-004-ARR	Corrie nan arr	57.41512	354.35380	135	6.2	0.99	170
02-SCOT-005-ARR	Corrie nan arr	57.41512	354.35380	135	3.3	0.99	170
02-SCOT-006-ARR	Corrie nan arr	57.41525	354.35359	133	2.4	0.99	170
02-SCOT-007-ARR	Corrie nan arr	57.41525	354.35359	133	2.1	0.99	170
02-SCOT-008-ARR	Corrie nan arr	57.41525	354.35359	133	1.4	0.99	170

Table 5.4: The location and sample collection information for each Scottish highlands, Scotland sample, including the latitude and longitude. λ_{eff} (attenuation length) was calculated using CRONUScalc and is the effective attenuation length incorporating shielding when possible.

Beinn na Caillich. The site lithology is a hornblende granite. Samples 06SKY01-03 are scoured bedrock samples and samples 06SKY04-08 are all glacial boulders. Four potassium feldspar mineral separates were processed by John Stone at the University of Washington and analyzed for chlorine-36. The bulk sample composition is shown in Tables 5.5 and 5.6 and chlorine-36 target element concentrations are shown in Table 5.7.

Kyleakin Pass This location only consists of two samples (06SKY09 and 06SKY10) from the CRONUS sampling trip. The samples are both scoured bedrock samples with a composition of Torridon sandstone. These samples were downgraded from primary calibration samples to secondary samples due to the possibility of extended surface coverage. These samples are plotted here, but are not included in the main calibration dataset for beryllium-10. These samples were not analyzed for any other cosmogenic nuclides.

Coire a Ghrunnda, Black Cuillins gabbro The Black Cuillins samples, from Coire a Ghrunnda, were collected from glacial landforms including scoured bedrock and glacially-transported boulders. All the samples are gabbros and the compositions, as determined from XRF and ICP-OES, are compiled in Tables 5.5 and 5.6. Chlorine-36 target element concentrations are shown in Table 5.7. All the samples from this site were prepared at University of Washington by John Stone. Samples 06SKY11-12 are boulder samples, while 06SKY13 is a scoured bedrock sample from a cliff face. Samples 06SKY14-17 are scoured bedrock samples located near each other. Samples 06SKY18-19 are from a right lateral glacial moraine. The bedrock and boulder samples have been assigned an age of 11700 $\pm$ 300 cal ka, while the moraine samples have been assigned an age of 12400 $\pm$ 300 cal ka.

Name	SiO_2	TiO_2	Al_2O_3	Fe_2O_3	MnO	MgO	CaO	Na_2O	K_2O	P_2O_5	AW	CO_2
-	wt %	wt %	wt %	wt %	wt %	wt %	wt %	wt %	wt %	wt %	wt %	wt %
06-SKY-01-KFSP-NXHN	74.10	0.27	12.70	3.41	0.05	0.08	0.36	4.11	4.99	0.02	0.65	0.03
06-SKY-06-KFSP-NXHN	73.10	0.24	12.40	3.13	0.05	0.04	0.23	4.12	4.95	0.02	0.01	0.01
06-SKY-07-KFSP-NXHN	73.80	0.26	12.60	3.10	0.05	0.06	0.36	3.93	5.07	0.02	0.85	0.03
06-SKY-08-KFSP-NXHN	74.50	0.25	12.60	3.05	0.04	0.04	0.20	3.84	5.19	0.02	0.95	0.05
06-SKY-11-FL-NXHN	46.3	0.18	24	5.82	0.09	6.88	15.1	1.38	0.08	0.01	0.6	0.06
06-SKY-12-NXHN	46.5	0.18	24.3	6.12	0.09	6.83	14.8	1.41	0.09	0.01	0.67	0.07
06-SKY-14-FL-NXHN	46.4	0.16	24.2	6.89	0.1	7.04	14.6	1.31	0.05	0.01	0.4	0.04
06-SKY-15-FL-NXHN	46.5	0.32	21.2	7.03	0.11	10.1	13.7	1.34	0.12	0.02	0.5	0.06
06-SKY-16-FL-NXHN	46.5	0.29	22.5	7.15	0.1	8.77	13.9	1.4	0.15	0.02	0.43	0.04
06-SKY-17-NXHN	46.3	0.31	23	6.74	0.1	7.99	14	1.51	0.12	0.03	0.54	0.06
06-SKY-18-NXHN	48	0.77	20.6	8.74	0.13	5.92	12.2	2.62	0.37	0.09	0.69	0.07
06-SKY-19-NXHN	45.2	0.37	20.2	7.54	0.12	8.83	13.4	1.31	0.18	0.02	1	0.02

Table 5.5: Results of Coire Fearchair and Coire a Ghrunnda, Scotland, chlorine-36 whole rock major element analyses. All results are reported in weight percent. These analyses were used as the "bulk rock" composition for mineral separate samples of the same number. AW represents the "analytical water" in the sample. Sample composition provided by UW.

Name	Cl	B	Sm	Gd	U	Th	Cr	Li
-	[ppm]	[ppm]	[ppm]	[ppm]	[ppm]	[ppm]	[ppm]	[ppm]
06-SKY-01-KFSP-NXHN	38.70 ±	5 ± 5	14.60 ± 1	15.60 ± 1	1.85 ± 0.1	10.10 ± 0.5	5 ± 5	10 ± 3
06-SKY-06-KFSP-NXHN	7.40 ±	5 ± 5	13.00 ± 1	13.40 ± 1	1.88 ± 0.1	10.70 ± 0.5	50 ± 50	20 ± 5
06-SKY-07-KFSP-NXHN	10.70 ±	5 ± 5	11.10 ± 1	10.60 ± 1	1.98 ± 0.1	10.30 ± 0.5	5 ± 5	20 ± 2
06-SKY-08-KFSP-NXHN	22.90 ±	5 ± 5	10.10 ± 1	9.41 ± 1	2.02 ± 0.1	10.30 ± 0.5	5 ± 5	10 ± 2
06-SKY-11-FL-NXHN	30 ± 15	5 ± 5	0.5 ± 0	0.74 ± 0	0.03 ± 0.0	0.2 ± 0.1	400 ± 50	5 ± 5
06-SKY-12-SNK-NXHN	30 ± 15	5 ± 5	0.5 ± 0	0.65 ± 0	0.03 ± 0.0	0.2 ± 0.1	270 ± 50	5 ± 5
06-SKY-12-FL-NXHN	30 ± 15	5 ± 5	0.5 ± 0	0.65 ± 0	0.03 ± 0.0	0.2 ± 0.1	270 ± 50	5 ± 5
06-SKY-14-FL-NXHN	30 ± 15	5 ± 5	0.3 ± 0	0.51 ± 0	0.05 ± 0.0	0.1 ± 0.1	220 ± 50	5 ± 5
06-SKY-15-FL-NXHN	30 ± 15	5 ± 5	0.6 ± 0	0.91 ± 0	0.05 ± 0.0	0.2 ± 0.1	270 ± 50	5 ± 5
06-SKY-16-FL-NXHN	30 ± 15	5 ± 5	0.7 ± 0	1.05 ± 0	0.03 ± 0.0	0.3 ± 0.1	390 ± 50	5 ± 5
06-SKY-17-SNK-NXHN	30 ± 15	5 ± 5	0.9 ± 0	1.05 ± 0	0.03 ± 0.0	0.3 ± 0.1	340 ± 50	5 ± 5
06-SKY-17-FL-NXHN	30 ± 15	5 ± 5	0.9 ± 0	1.05 ± 0	0.03 ± 0.0	0.3 ± 0.1	340 ± 50	5 ± 5
06-SKY-18-SNK-NXHN	30 ± 15	5 ± 5	2.1 ± 0	2.62 ± 0	0.03 ± 0.0	0.3 ± 0.1	130 ± 50	5 ± 5
06-SKY-18-FL-NXHN	30 ± 15	5 ± 5	2.1 ± 0	2.62 ± 0	0.03 ± 0.0	0.3 ± 0.1	130 ± 50	5 ± 5
06-SKY-19-SNK-NXHN	30 ± 15	5 ± 5	0.7 ± 0	1.04 ± 0	0.05 ± 0.0	0.2 ± 0.1	470 ± 50	5 ± 5
06-SKY-19-FL-NXHN	30 ± 15	5 ± 5	0.7 ± 0	1.04 ± 0	0.05 ± 0.0	0.2 ± 0.1	470 ± 50	5 ± 5

Table 5.6: Results of Scotland chlorine-36 whole-rock trace element analyses. All measurements are reported in ppm. These analyses were used as the "bulk rock" trace element composition for mineral separate samples of the same number. Sample compositions reported by UW. Trace element analyses performed by ICP-OES and Cl estimated from previous analyses.

Name	K_2O	CaO	TiO_2	Fe_2O_3	Cl
-	wt %	wt %	wt %	wt %	[ppm]
06-SKY-01-KFSP-NXHN	5.79 ± 0.01	0.22 ± 0.01	0.02 ± 0.01	0.08 ± 0.01	38.70 ± 2.1
06-SKY-06-KFSP-NXHN	5.91 ± 0.01	0.14 ± 0.01	0.02 ± 0.01	0.05 ± 0.01	7.40 ± 3.0
06-SKY-07-KFSP-NXHN	6.28 ± 0.01	0.20 ± 0.01	0.02 ± 0.01	0.12 ± 0.01	10.70 ± 2.2
06-SKY-08-KFSP-NXHN	7.09 ± 0.01	0.16 ± 0.01	0.01 ± 0.01	0.05 ± 0.01	22.90 ± 2.3
06-SKY-11-FL-NXHN	0.08 ± 0.004	16.5 ± 0.165	0.04 ± 0.002	0.95 ± 0.019	16.8 ± 1.7
06-SKY-12-SNK-NXHN	0.04 ± 0.002	15.8 ± 0.158	0.48 ± 0.01	8.64 ± 0.086	28.7 ± 1.1
06-SKY-12-FL-NXHN	0.08 ± 0.004	16.3 ± 0.163	0.04 ± 0.002	0.99 ± 0.02	12.1 ± 1.3
06-SKY-14-FL-NXHN	0.05 ± 0.003	16.5 ± 0.165	0.05 ± 0.003	1.07 ± 0.011	15.2 ± 1.6
06-SKY-15-FL-NXHN	0.09 ± 0.005	15.9 ± 0.159	0.05 ± 0.003	0.92 ± 0.018	18.6 ± 2.9
06-SKY-16-FL-NXHN	0.12 ± 0.002	15.84 ± 0.158	0.054 ± 0.003	0.94 ± 0.019	29.0 ± 5.5
06-SKY-17-SNK-NXHN	0.07 ± 0.004	14 ± 0.14	0.71 ± 0.014	9.21 ± 0.092	32.7 ± 2.0
06-SKY-17-FL-NXHN	0.1 ± 0.002	16 ± 0.16	0.05 ± 0.003	1.02 ± 0.01	23.8 ± 2.3
06-SKY-18-SNK-NXHN	0.13 ± 0.003	13.5 ± 0.135	1.99 ± 0.02	14.5 ± 0.145	65.8 ± 1.9
06-SKY-18-FL-NXHN	0.27 ± 0.005	12.4 ± 0.124	0.08 ± 0.004	0.98 ± 0.02	33.1 ± 2.1
06-SKY-19-SNK-NXHN	0.07 ± 0.004	13.6 ± 0.136	0.8 ± 0.016	9.3 ± 0.093	55.8 ± 1.9
06-SKY-19-FL-NXHN	0.08 ± 0.004	15.54 ± 0.155	0.063 ± 0.003	1.39 ± 0.014	24.3 ± 3.5

Table 5.7: Table with target elements for the UW chlorine-36 samples. Target elements determined via XRF except for chlorine, which is determined using IDMS.

5.3.2 Scottish Highlands

Corrie nan arr Samples 06HKY01-04 were collected at a location known as Corrie nan arr. This location was previously sampled by Stone in 2002 and that dataset is also included in the beryllium-10 primary dataset (samples 02SCOTXXX-ARR). The rock avalanche boulders sampled carried by the glacier, but had not reached the terminus by the time of deglaciation. Most samples are supra- or sub-glacial boulders (supraglacial = 06HKY01-03, subglacial = 06HKY04, undistinguished = 02SCOT), although a few samples (02SCOT010-014) are from a terminal moraine. The concentrations in the moraine samples are indistinguishable from the other group of rockfall samples. All samples are Torridon sandstone. Sample HKY03 was removed from the beryllium calibration analysis because the concentration was >3 standard deviations from the mean of all the other samples in the Corrie nan arr site, including the samples from 2002. See Appendix C.3 for complete information for these samples.

Maol Chean-Dearg CRONUS samples 06HKY05-11 were collected at this location. All the samples are supraglacial quartzite boulders. They were processed for beryllium-10, aluminum-26, and carbon-14. These samples would have been exposed by the initial rockfall for supraglacial boulders very close to the time the area was deglaciated at the end of the Loch Lomond readvance.

5.3.3 Isle of Skye Results and Discussion

Comparing sample results across nuclides at the site cannot be done using only concentration. Instead, the final calibrated production rates and Lifton/Sato

scaling are used to produce ages for the samples. The ages are not used for any purpose other than qualitative comparison and discussion of the coherence of the samples from this site.

Beryllium-10, aluminum-26, and chlorine-36 were all analyzed as part of the CRONUS-Earth Project and results are shown in Figure 5.9. Although the scatter in the data is larger than other sites in the calibration, samples are typically, except for the aluminum outlier (06SKY07), within analytical uncertainty of the upper independent age constraint bound. This is not the case for the Coire a Ghrunnda site, discussed in detail below. The remaining chlorine-36 samples are shown independently in Figure 5.10. Three of the four samples overlap the independent age constraints, although the samples generally appear at the higher end of the acceptable range. The low elevation and high latitude of this site provides a crucial data point for all the nuclides in the calibration due to the lack of a large scaling correction. The discussion of the spallation calibrations of each of the nuclides can be found in other papers published as part of the CRONUS-Earth project.

The chlorine-36 samples from Coire a Ghrunnda are relatively consistent, although there is one outlier (06SKY14). The outlier, likely due to inheritance, is significantly more than three standard deviations away from the mean age of the other samples and is not included in any of the analyses or final calibrations. The remaining chlorine samples from this site are more scattered than the other sites, although most error bars do overlap at the one-sigma level. However, none of the error bars overlap the independent radiocarbon age bounds. This could be due to incorrect independent age assignment at this site, incorrect calcium production rates, or inheritance. The samples at this site are primarily scoured bedrock, which has a higher probability of inheritance than the other sample types.

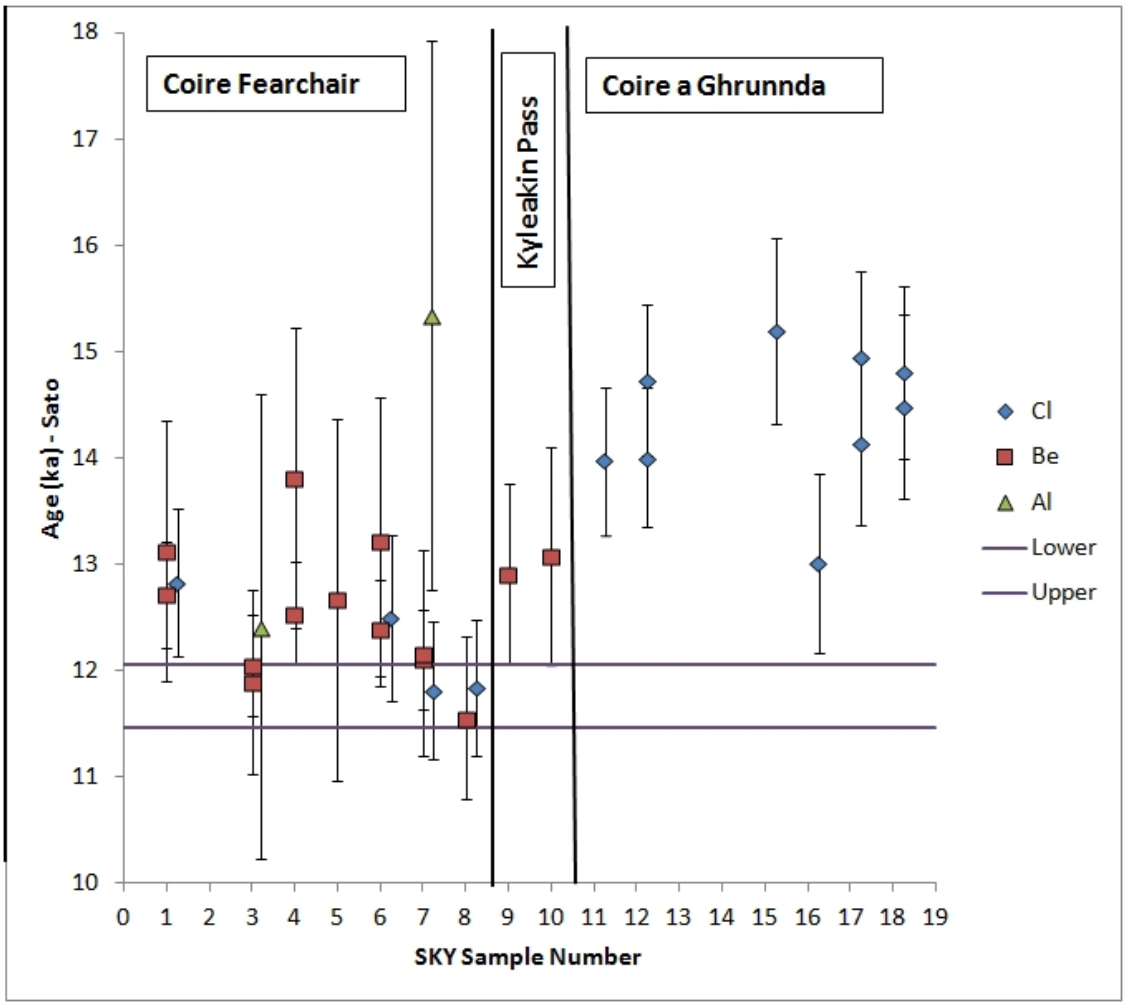

Figure 5.9: Ages from all the SKY sites (Coire Fearchair, Kyleakin Pass, and Coire a Ghrunnda) for beryllium, aluminum-26, and chlorine-36 using the Lifton/Sato scaling model. Sites are separated by black vertical lines. Uncertainties on samples represent analytical uncertainties from propagated sample uncertainties only (such as density, AMS measurements). Beryllium samples line up with the sample numbers; chlorine is plotted offset by 0.25, aluminum by 0.5 in order to make as many points visible as possible. One chlorine sample plots off graph (sample 06SKY14 has a value of 23 ± 1 ^{36}Cl ka.)

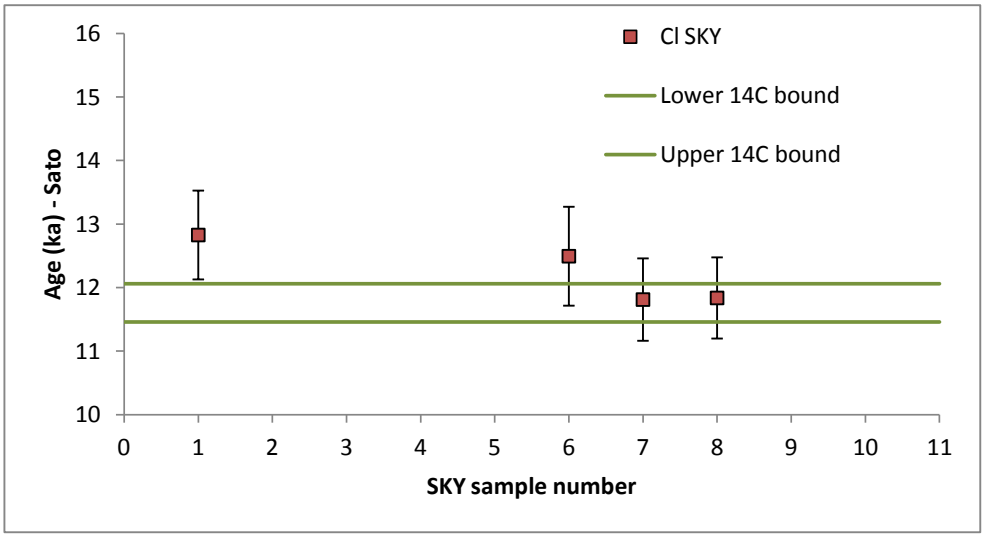

Figure 5.10: Figure showing Scotland chlorine results using Sato scaling. Also shown are the independent age constraints used for the site (green horizontal lines). Uncertainties on samples represent analytical uncertainties from AMS only.

5.3.4 Scottish Highlands Results and Discussion

All the results from the Scottish highlands samples are plotted in Figure 5.11. Due to the significant scatter in the carbon-14 dataset, Al and Be are plotted together in Figure 5.12. The aluminum and beryllium ages appear to be relatively consistent, both internally and with the independent age constraints. One exception is an outlier, sample 06HKY03. Carbon-14 results, on the other hand, show significant scatter but typically plot younger than the independent age constraints.

The HKY sites provide very internally consistent results for aluminum and beryllium calibrations. Based on the consistency for Al and Be, these sites should also provide good samples for carbon-14. This site is thus crucial to the carbon-14 calibration, despite the large scatter in the data.

5.4 Conclusion

The CRONUS-Earth data from the Scotland sites, located in the highlands as well as on the Isle of Skye, are generally internally consistent. Of the 31 beryllium, 18 aluminum, 4 chlorine, and 16 carbon points, only one Be and one Al point were removed as outliers. Other than carbon, the ages calculated for all the samples are consistent, with most ages overlapping within uncertainty of each other and the independent age bounds. These calibration sites, focusing on rock avalanches and scoured bedrock associated with the deglaciation at the end of the Loch Lomond readvance, provide key locations for the calibration of all the nuclides involved. The location at high latitude and low elevation provides a valuable point because it should be essentially independent of scaling scheme.

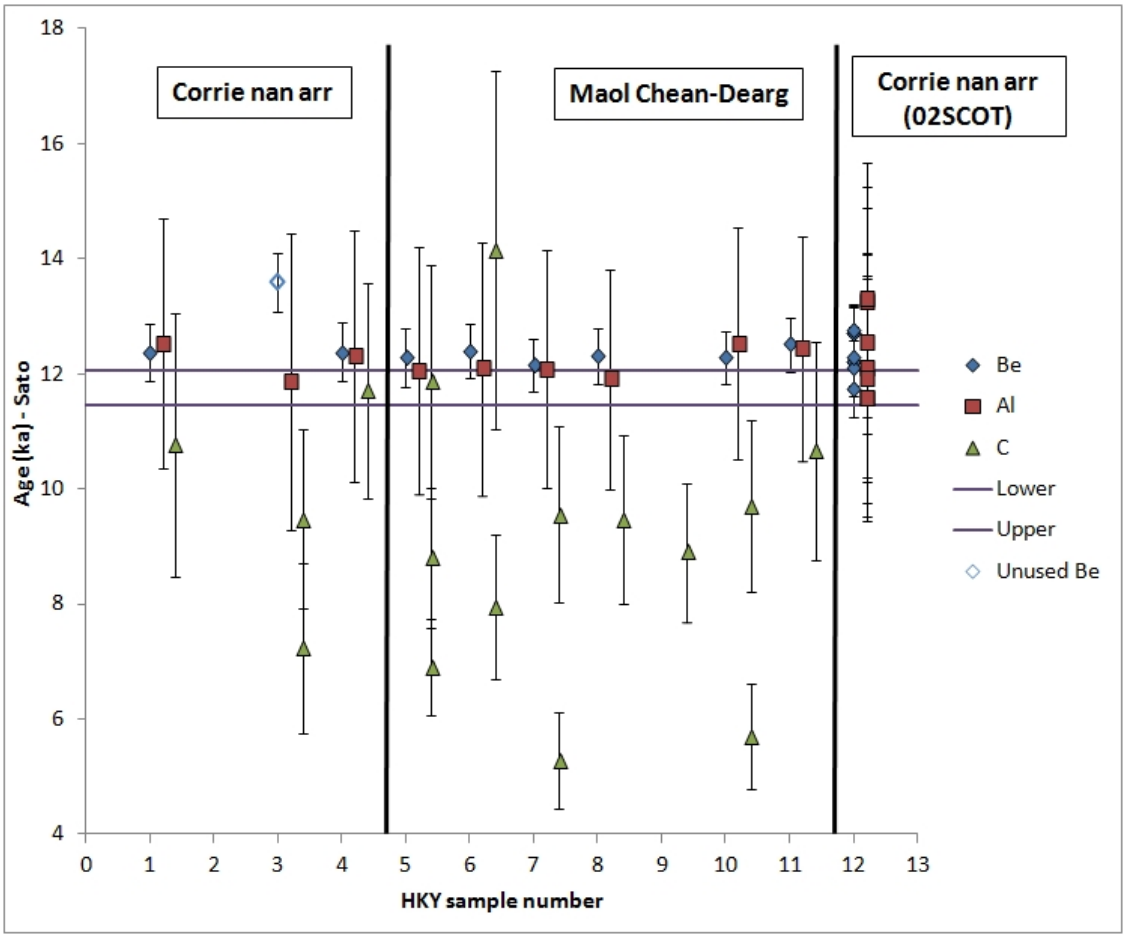

Figure 5.11: Ages from all the HKY sites for beryllium, aluminum-26, and carbon-14. Uncertainties on samples represent analytical uncertainties from AMS only. Beryllium samples line up with the sample numbers; carbon is plotted offset by 0.75, aluminum by 0.5 in order to make as many points visible as possible. Corrie nan arr samples from 2002 are plotted as sample 12. Sites are separated by vertical black lines.

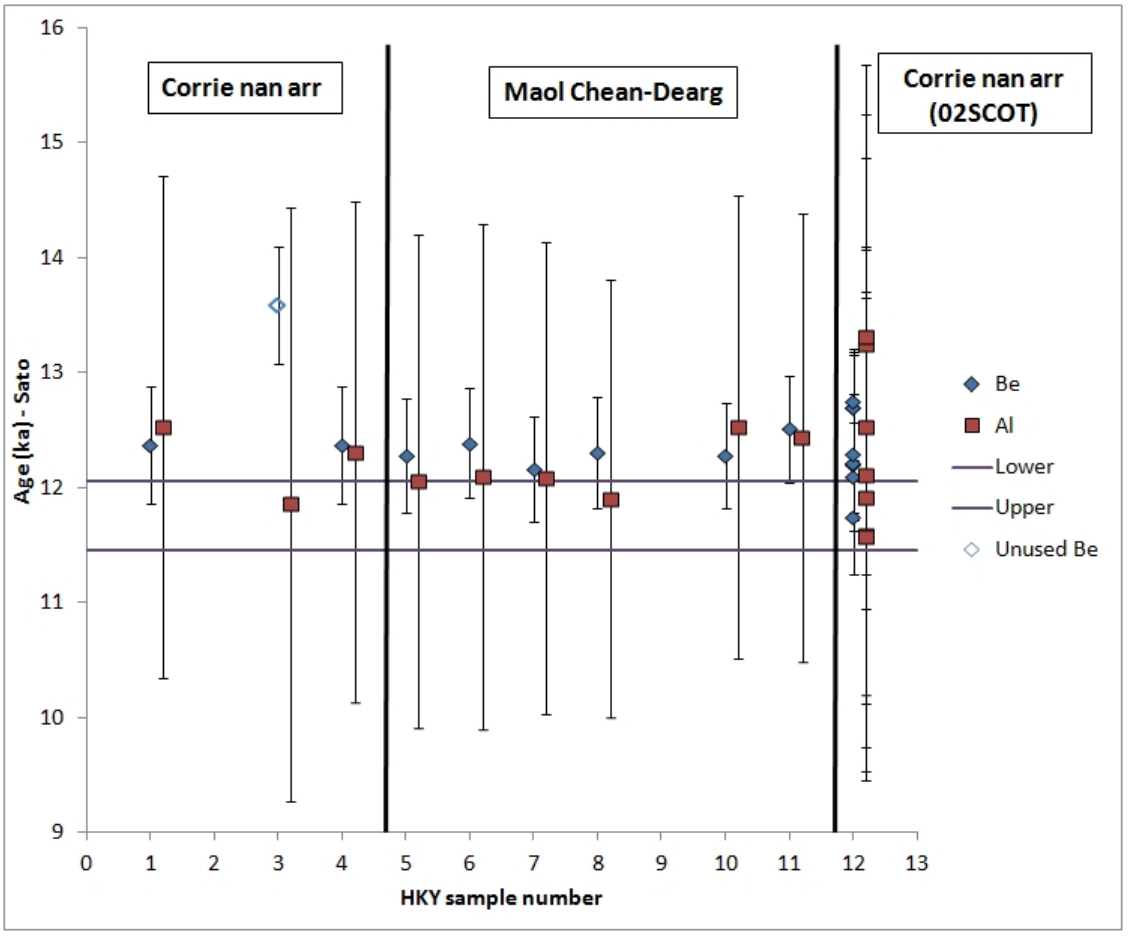

Figure 5.12: Ages from all the HKY sites for beryllium and aluminum-26. Uncertainties on samples represent analytical uncertainties from AMS only. Beryllium samples line up with the sample numbers; aluminum is plotted offset by 0.5 in order to make as many points visible as possible. Corrie nan arr samples from 2002 are plotted as sample 12.

CHAPTER 6

HUANCANÉ, PERU - SITE DESCRIPTION AND DATA

The Huancané, Peru, geological calibration site is being used as a primary calibration site in the CRONUS-Earth project. This chapter is intended to support the main calibration chapter of this dissertation by describing the site and the resulting chlorine-36 data and assessing the quality of both. Most of the information contained herein will be published by a CRONUS-Earth investigator as part of a special volume in Quaternary Geochronology.

In this paper, all original radiocarbon ages will be reported as ^{14}C years BP, indicating years before 1950. When needed, the radiocarbon ages are calibrated using Calib 6.02 (Stuiver et al., 2005). These calibrated ages are reported as cal ka or cal years BP. In some cases, samples are reported as "years before 2010" to indicate that 60 years has been added to the calibrated radiocarbon age. When dealing with ages from cosmogenic nuclides, the ages are reported as ^{10}Be ka or ^{36}Cl ka in any cases where there might be confusion. The cosmogenic nuclide ages are all referenced to the year 2010.

6.1 Site Description

The Huancané geological calibration site is located high in the Peruvian Andes in the southeastern portion of Peru (Figure 6.1). The Huancané valley is lo-

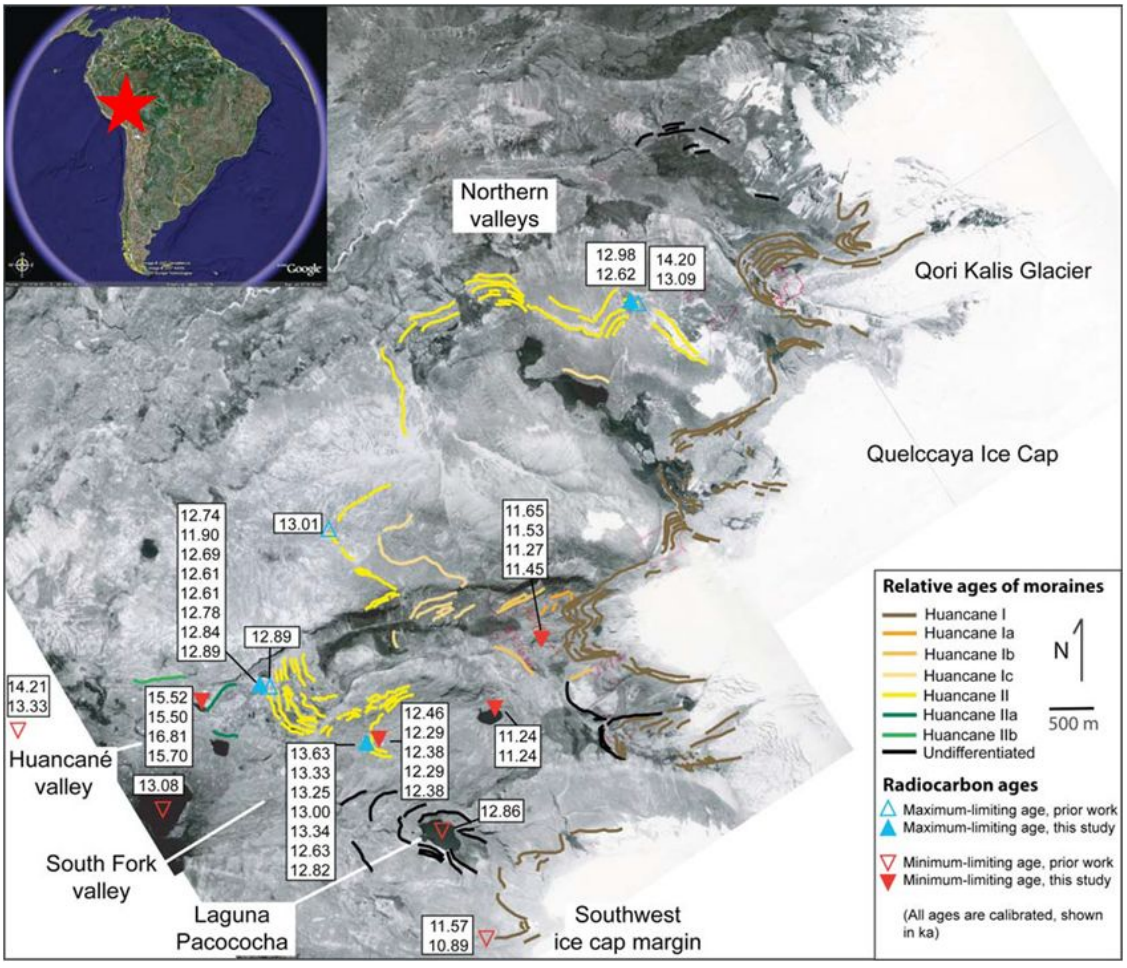

Figure 6.1: Map of moraines and radiocarbon ages at the Huancané site (Kelly et al., 2012). Radiocarbon ages are listed in the boxes. The red star on the inset map indicates the location in South America. From Kelly et al. (2012).

cated on an ignimbrite plateau (Rodbell, 2000) composed of a relatively homogeneous rhyolite tuff. As the ice cap advanced and retreated, boulders in the valley were plucked and redeposited with other material from the valley as moraines. Cores from boggy areas in proximity to the moraines have provided bracketing radiocarbon ages for the ice cap advances.

The Huancané site is particularly important to cosmogenic nuclide calibration because of its location and elevation. The largest differences between scaling

models are found at low latitudes and high elevations. The previous calibrations (i.e., Phillips et al., 2001; Fenton et al., 2011; Nishiizumi et al., 1989; Swanson and Caffee, 2001; Schimmelpfennig et al., 2008) lacked samples from locations fitting these criteria. The Huancané site provides the low latitude (-13°S) and high elevation (∼4800m) that was missing in previous studies.

The Quelccaya ice cap (Figure 6.2), which is responsible for the creation of the Huancané moraine sequence, has been extensively studied in relation to the timing of the glacial sequence as well as the forcings that cause changes in the extent of the ice cap (Mercer and Palacios, 1977; Thompson et al., 1984, 1985, 2006; Goodman et al., 2001; Rodbell, 2000; Rodbell et al., 2009). The extensive history of the ice cap provides key calibration information, specifically radiocarbon ages. There are few glacial sites with radiocarbon ages in the tropical Andes, which is mostly a result of the lack of vegetation in the harsh climate (Rodbell et al., 2009). This site is one of only two sites in the tropical Andes that have both maximum and minimum radiocarbon constraints on the glacial moraine sequence (Kelly et al., 2012). Farber et al. (2005) described the other site with limiting radiocarbon ages. The Farber site can be used as a comparison for beryllium-10 results, but only the Huancané site has chlorine-36 samples.

There are three sets of moraines in the Huancané valley and these are named the Huancané I, II, and III moraines moving from the ice cap outward (Figure 6.3). The Huancané II moraines are the source for the primary calibration samples for the CRONUS-Earth project. The majority of the bracketing radiocarbon ages are applicable to this moraine set. The Huancané I moraines have fewer radiocarbon age constraints and are not included as primary calibration samples, although results from these samples are discussed in section 6.4.5.

Figure 6.2: Photo showing the Quelccaya Ice Cap during sampling in 2008. The ice cap is responsible for the creation of the moraines in the Huancané valley (seen directly in the middle of the photo) and the South Fork Valley (seen over the head of the person on the far right). (Photo courtesy of Fred Phillips)

Lab #	^{14}C age (yr)	Cal range (ka)	Elevation (m)	Significance
I-8209	10,910 $\pm$ 160	11004-10681	4820	MAX HII
DIC-686	11,070 $\pm$ 125	11154-10856	4925	MAX HII
GX-4325	11,185 $\pm$ 185	11317-10929	5100	MAX HII

Table 6.1: Radiocarbon ages for the site from Mercer and Palacios (1977). Cal range is the one-sigma calibrated age range using Calib6.02 (Stuiver et al., 2005). All three ages provide maximum limiting ages for the Huancané II moraines (as indicated by the significance column).

6.1.1 Independent Age Constraints

Mercer and Palacios (1977) performed the initial radiocarbon analyses on samples collected near the Quelccaya ice cap. They sampled several peat deposits that were overridden by Huancané II moraines. These maximum ages (as seen in Table 6.1) ranged from 11,185-10,910 ^{14}C years BP (11317-10681 cal yr). Rodbell (2000) tightened the age constraint on the Huancané II advance when he obtained a basal radiocarbon date of 10,870 $\pm$ 70 ^{14}C years BP (AA 27032) (10881-10696 cal yr) from a core in a lake that is situated less than a kilometer from the current edge of the Quelccaya ice cap.

Kelly et al. (2012) built upon Mercer's initial work by extensively using radiocarbon dating in many locations near the Huancané moraines. Tables 6.2 and 6.3 provide information on the all the newly acquired radiocarbon dates, including radiocarbon age, calibrated age, and the significance of the sample. The key maximum limiting ages for the Huancané II moraines from their work are from two localities where peat was thrust into the bottom of the till in the outermost moraine ridge. The eight maximum limiting samples yield ages that fall between 12.9-12.6 cal ka. The minimum limiting ages are from peat deposited conformably on top of the till, yielding four ages between 12.4-12.3 cal ka. This provides a very small bracketing window between the two sets of ages. In addition, Kelly et al.

(2012) performed a maximum likelihood analysis incorporating all the available radiocarbon ages that resulted in an estimated age of the Huancané moraines of 12,320 $\pm$ 110 years before 2010.

6.2 Samples collected

A total of 21 samples were collected from various moraines for the CRONUS-Earth project (see Figure 6.3 for a map of locations and Table 6.4 for location information). Additional sample information was collected in the field, including dip, dip direction, and shielding information. The dip and direction of dip are reported directly in Table 6.4. The shielding information was used in conjunction with the CRONUScalc Matlab code to produce a shielding factor and an effective attenuation length that has been adjusted to account for the local topography and dip of the individual sample. These final calculated values are reported in Table 6.4 as well.

Samples from the Huancané site are labeled with HU08 to indicate the site and the year they were collected (2008). Of these 21 samples, 14 were from the Huancané II moraines (samples HU08-01 to -07, and HU08-10 to -16), two were collected for an erosion rate calculation from a glacially polished bedrock surface downstream from the Huancané II moraines (samples HU08-08 & -09), and five were collected from the younger Huancané I moraines (samples HU08-17 to -21). Of the 14 Huancané II samples, samples HU08-05, -07, -12, and -13 were archived in case more material was needed. The remaining ten Huancané II samples were processed for this project. Of the Huancané I samples, HU08-18, -19, & -21 were processed. All the samples designated for processing were crushed, homogenized, and distributed to participating CRONUS labs.

Sample #	Lab #	^{14}C age	Calibrated range (ka)	Rel area	Median prob (ka)	Significance
08-02-A	AA82738	10,490 $\pm$ 100	12098-12767	1	12458	Min., H-II
08-02-A	AA82738	10,400 $\pm$ 150	11757-12787	1	12286	Min., H-II
08-02-A	AA82738	10,470 $\pm$ 170	11812-12829	1	12379	Min., H-II
08-02-A	AA82738	10,400 $\pm$ 140	11807-12771	0.99	12991	Min., H-II
08-02-D	AA85307	10,450 $\pm$ 110	12032-12769	1	12384	Min., H-II
08-14b-2-19cm	AA82731	9,820 $\pm$ 90	11071-11513 11516-11613	0.91 0.05	11243	Min., H-II
08-14b-2-25cm	AA82733	9,820 $\pm$ 90	11071-11513 11516-11613	0.91 0.05	11243	Min., H-II
08A-01 SampleA	AA82730	11,780 $\pm$ 120	13360-13874	1	13628	Max., H-II
08-01B-sampleI	AA82736	10,610 $\pm$ 100	12347-12842	0.97	12633	Max., H-II
08-01B-sampleI	AA85305	10,840 $\pm$ 200	12343-13194	0.98	12815	Max., H-II
08B-01-sampleA	AA82737	11,480 $\pm$ 110	13135-13592	1	13338	Max., H-II
08A-01-sampleF	AA82740	11,470 $\pm$ 110	13125-13579	1	13329	Max., H-II
08A-01-sampleF	AA85308	11,380 $\pm$ 100	13078-13430	1	13248	Max., H-II
08-01A-sampleG	AA82741	11,060 $\pm$ 110	12848-13172	1	12996	Max., H-II

Table 6.2: Radiocarbon samples from the South Fork Valley used to constrain Huancané glacial moraine age (Kelly et al., 2012). MIN and MAX refer to whether the sample is a minimum or maximum limiting age and H-I, H-II, and H-III refer to the Huancané moraine sequence. The one-sigma calibrated range was obtained using the Calib 6.02 program (Stuiver et al., 2005). 'Rel area' is an output of the Calib 6.02 program and indicates the relative likelihood of the calibrated age range based on the radiocarbon calibration.

Sample #	Lab #	^{14}C age	Calibrated range (ka)	Rel area	Median prob (ka)	Significance
08-19A	AA82725-1	10,080 $\pm$ 90	11283-11990	1	11648	Min., H-II
08-19A	AA82725-2	9,980 $\pm$ 140	11283-11990	1	11534	Min., H-II
08-19B1	AA85305	9,850 $\pm$ 50	11156-11411	0.95	11266	Min., H-II
08-19B2	AA85306	9,930 $\pm$ 120	11129-11846	0.95	11452	Min., H-II
06-02A	AA74022	10,661 $\pm$ 52	12621-12828	0.98	12737	Max., H-II
06-02A	AA79186	10,195 $\pm$ 54	11698-12090	0.98	11896	Max., H-II
06-02B	AA74023	10,614 $\pm$ 51	12574-12810 12400-12485	0.86 0.14	12691	Max., H-II
06-02B	AA79187	10,568 $\pm$ 60	12392-12781	1	12609	Max., H-II
06-02C	AA79188	10,564 $\pm$ 55	12394-12772	1	12605	Max., H-II
06-02D	AA79189	10,718 $\pm$ 60	12662-12853	1	12777	Max., H-II
06-02E	AA74024	10,828 $\pm$ 52	12790-12896	1	12842	Max., H-II
06-02G	AA74025	10,931 $\pm$ 53	12828-12955	1	12887	Max., H-II
08-12c-8.7	Beta-257780	13,120 $\pm$ 140	15184-15888	1	15518	Min., H-III
08-12c-13.5	Beta-257781	13,110 $\pm$ 140	15174-15873	1	15504	Min., H-III
08-12c-1-37-38	OS-71336	14,100 $\pm$ 100	16395-17161	1	16808	Min., H-III
08-12c-1-44-5-47	OS-71337	13,250 $\pm$ 80	15368-16069	1	15703	Min., H-III

Table 6.3: Radiocarbon samples from the Huancané Valley used to constrain Huancané glacial moraine age (Kelly et al., 2012). MIN and MAX refer to whether the sample is a minimum or maximum limiting age and H-I, H-II, and H-III refer to the Huancané moraine sequence. The one-sigma calibrated range was obtained using the Calib 6.02 program (Stuiver et al., 2005). 'Rel area' is an output of the Calib 6.02 program and indicates the relative likelihood of the calibrated age range based on the radiocarbon calibration.

Sample	**Lat** [deg]	**Long** [deg]	**Elev** [m]	**Dip** [deg]	**DD** [–]	**Atten** [g/cm^2]	**Shield** [–]	**Thick** [cm]
HU08-01	-13.94494	-70.89539	4854	16	220	164	0.997	7
HU08-02	-13.94635	-70.89241	4862	11	350	167	0.999	5
HU08-03	-13.94613	-70.89266	4859	19	342	162	0.995	6
HU08-04	-13.94545	-70.8928	4848	22	180	159	0.991	5
HU08-06	-13.94454	-70.89483	4843	6	180	169	0.999	7
HU08-08	-13.94797	-70.89786	4871	14	309	165	0.998	2
HU08-09	-13.94797	-70.89786	4871	14	309	165	0.998	2
HU08-10	-13.947	-70.88693	4860	14	194	166	0.997	3
HU08-11	-13.94715	-70.8868	4860	8	79	169	0.999	6
HU08-14	-13.94887	-70.88559	4871	7	100	170	0.996	5
HU08-15	-13.94838	-70.88537	4869	11	265	170	0.995	6
HU08-16	-13.94679	-70.88619	4867	15	264	165	0.997	6
HU08-18	-13.93855	-70.86769	4947	25	25	157	0.983	5
HU08-19	-13.93849	-70.86761	4943	*	*	170	0.994	4
HU08-20	-13.93841	-70.86769	4946	4	162	170	0.994	4
HU08-21	-13.9383	-70.86774	4947	18	120	163	0.989	4

Table 6.4: The location and sample collection information for each Peru sample, including the latitude and longitude (both without any correction for declination), elevation, dip (degrees from horizontal), dip direction, attenuation length (Λ, corrected for shielding and location), and topographic shielding factor. Samples HU08-01 through HU08-16 are from the Huancané II moraines; samples HU08-17 through HU08-21 are from Huancané I moraines. The attenuation length was calculated using the CRONUScalc program. * = Unrecorded information. Information collected by Fred Phillips and Adam Hudson.

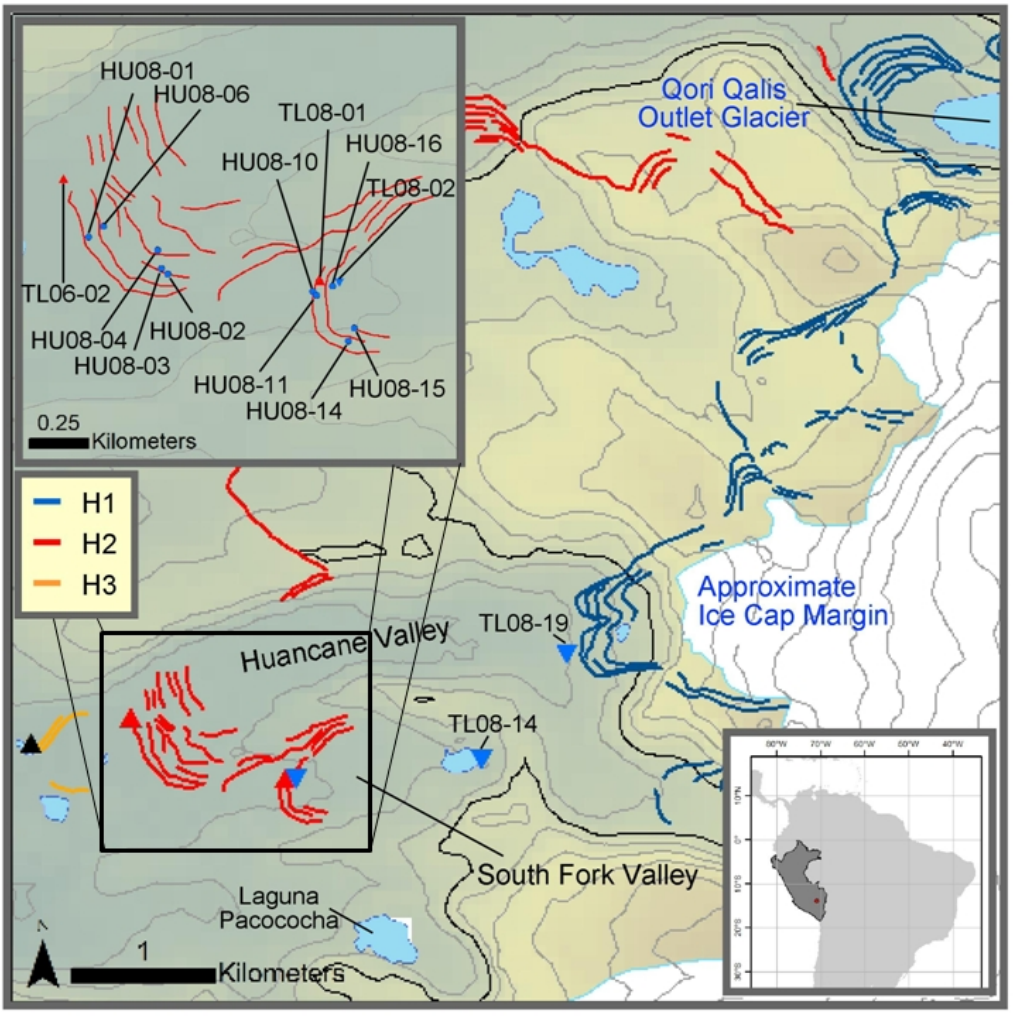

Figure 6.3: Map of sample locations at the Huancané site. H1, H2, and H3 represent the different Huancané moraines. Figure by Adam Hudson (Phillips and Hudson, 2012).

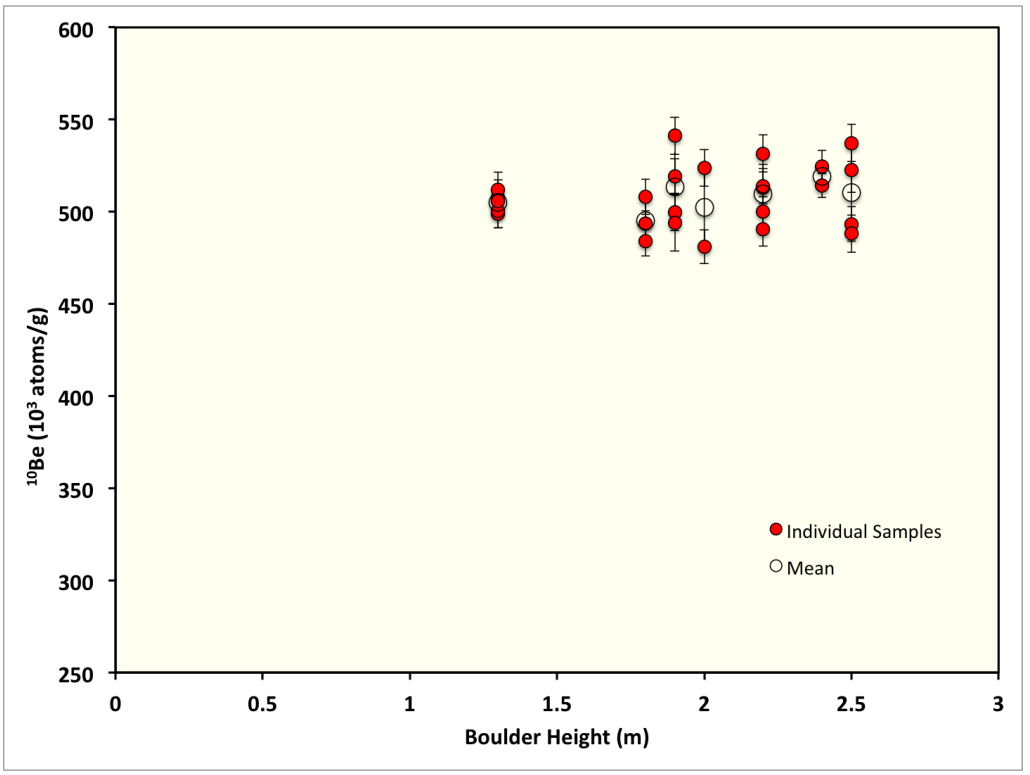

Figure 6.4: Huancané samples plotted by boulder height and beryllium concentrations.

The samples were collected from large boulders to reduce possible effects of movement after deposition and effects from exhumation. The average boulder height was 1.8m, although they ranged from 1.3 to 6.5 m. A photo (Figure 6.5) shows the typical size of sampled boulders. In order to avoid exhumation effects, only boulders at or near the crests of moraines were sampled. The relatively sharp crest shape of the moraines also indicates that significant exhumation is unlikely (Hallet and Putkonen, 1994). The cosmogenic nuclide results confirm this, showing no correlation between concentration and boulder height for beryllium-10 (see Figure 6.4).

Figure 6.5: Picture showing typical boulder size at the Huancané site. Adam Hudson in front of the HU08-16 boulder, which is 2.2 m tall.

6.3 Possible Complicating Factors

This section covers possible concerns at the Huancané site that might contribute to uncertainty or bias in the sample ages. In this case, the concerns include erosion, sample cover by vegetation/snow, stability of sample boulders, and sample preparation methods. The possible effects of each factor are covered individually below.

The sample-specific erosion rate of each boulder was determined by combining information collected in the field and the results of a local erosion study. In the field, the maximum height of resistant sections (stick-ups) above the eroded rock surface on each sampled boulder provided a minimum amount of total material removed on each boulder (Column 2 in Table 6.5). Kelly (pers. comm., April 3, 2012) performed an erosion rate study by comparing ^{10}Be concentrations from pairs of samples where polished and eroded samples were collected from the same boulder or bedrock. The difference between polished and eroded sample pairs was used to calculate the total amount of eroded material (60 mm), which corresponds to an average site erosion rate of 4.8 mm/kyr. The final erosion rates produced by combining the beryllium-10 erosion rate study and field observations range from 3.2-8.1 mm/kyr and are shown in Table 6.5.

Although ice cap records show intermittent periods of increased precipitation (Thompson et al., 1985), it is unlikely that the climate of the region would allow significant long-term snow coverage since the last glaciation (and hence, for the exposure period of the calibration samples). The largest ice cap expansion was during the Little Ice Age, producing the Huancané I moraines. Based on this, snow shielding is inferred to have been negligible. The small amount

Sample Number	Erosion depth (mm)	Erosion Rate (mm/kyr)
HU08-01	100 ± 40	8.1 ± 3.2
HU08-02	60 ± 20	4.8 ± 1.6
HU08-03	40 ± 20	3.2 ± 1.6
HU08-04	100 ± 40	8.1 ± 3.2
HU08-05	100 ± 40	8.1 ± 3.2
HU08-06	60 ± 20	4.8 ± 1.6
HU08-07	60 ± 20	4.8 ± 1.6
HU08-08	0 ± 0	0.0 ± 0.0
HU08-09	140 ± 20	10.0 ± 1.4
HU08-10	60 ± 20	4.8 ± 1.6
HU08-11	80 ± 40	6.5 ± 3.2
HU08-12	100 ± 40	8.1 ± 3.2
HU08-13	60 ± 40	4.8 ± 3.2
HU08-14	40 ± 20	3.2 ± 1.6
HU08-15	80 ± 40	6.5 ± 3.2
HU08-16	40 ± 20	3.2 ± 1.6

Table 6.5: Erosion rates for the Peru samples.The erosion rates are derived from the total erosion depth (Column 2) and the independent age of the site.

of total precipitation and the short-lived nature of the snow that does fall supports this. The necessity for a snow correction can be checked directly using the beryllium-10 concentrations. The lack of correlation between sample concentrations and boulder height (Figure 6.4), as well as a lack of correlation between surface dip and concentration (Figure 6.6) also indicates that shielding by snow has not significantly influenced nuclide production.

The effects of vegetation on the shielding of these samples are expected to be small due to the harsh climate of the tropical Andes that prevents significant vegetation, including bushes or trees that might shield incoming cosmic rays, from growing (Rodbell et al., 2009). One exception was the thin layer of lichens on most of the collected samples. The contributions of lichens to sample shielding are expected to be small due to the small thickness (1-2 mm) of the lichen layer.

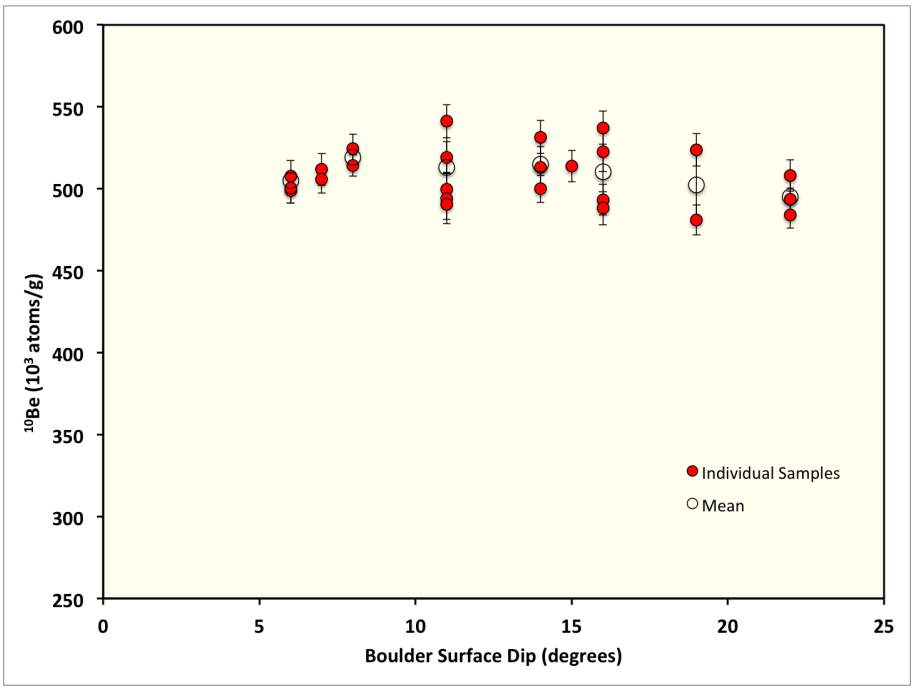

Figure 6.6: Huancané samples plotted by surface dip and beryllium concentrations.

The lichen layer was removed prior to processing, but it could have contributed to moisture retention and increased erosion.

Samples were prepared for chlorine-36 using four different laboratory procedures in an attempt to obtain samples of varying composition for the calibration. For each sample, one whole-rock analysis was run. The samples were sieved to a grain size of 250-1000 microns, leached in acid and base, and dissolved following the procedures discussed in Chapter 3. The whole rock sample preparation method maintains whatever heterogeneities were originally present between samples and allows the measurement of all the chlorine-36 production pathways in the rock.

The preparation of the mineral separates for the Huancané samples follows the general method described in the methods section (Chapter 3), but is

summarized here. Chlorine-36 mineral separates were prepared by first magnetically separating the sample into magnetic and non-magnetic fractions. The non-magnetic fraction was separated using density separation (fluid density of 2.58g/cm^2). In this separation, the floating fraction is mostly feldspar and the sinking fraction is mostly quartz. The feldspar fraction was then etched using one of three methods. The three different techniques, distinguished by suffixes on the sample name, are 1) SAN – Indicates that the samples were fully etched using 15% HF and an ultrasonic bath until no more ground mass could be seen on grains using a microscope; 2) SANreg – Indicates that the sanidine fraction was split prior to etching and this fraction was processed without etching in order to retain any ground mass present on the grains. This was an attempt to obtain a larger range of Cl contents in the samples; 3) SANetch – Indicates that the sanidine fraction (the other half of method SANreg) was significantly etched. However, most of these samples had relatively small masses and could not be etched as fully as the samples indicated in method 1. Some ground mass, which may or may not have contained Cl, remained on these samples. These three mineral separation methods produced different results due to the differing treatments. Where necessary, they are plotted as three distinct datasets in order to display the differences. In general, results from groups SAN and SANetch are consistent, while results from group SANreg are not.

6.4 Results

6.4.1 Sample Characterization

Electron microprobe performed at the New Mexico Bureau of Geology showed a hydrated volcanic-glass ground mass with very low chloride and significant potassium. The main phases identified were two distinct feldspars and

quartz. Based on these initial results, there were three possible phases for chlorine-36 mineral separate analysis (Na-Ca feldspar, K feldspar, and biotite). The Ca-Na feldspar was a small portion of the total rock and contained very little Ca, based on preliminary XRF measurements. The biotites also represented only a small and difficult-to-separate portion of the total rock. Only the potassium feldspar was a feasible mineral separate option for full chlorine-36 analysis.

The bulk-rock sample compositions are relatively homogeneous, but individual XRF and trace-element analyses were performed on each bulk-rock sample. The whole-rock XRF (Table 6.6) and trace-element (Table 6.7) analyses were used as bulk-rock measurements for the mineral-separate fractions of the same sample number. Additional measurements were performed on the dissolved fraction of mineral separates to obtain target-element concentrations, shown in Tables 6.8 and 6.9.

Very small quantities of undissolvable pink and black grains remained after the complete dissolution of the sample in HF and HNO_3. The microprobe results from these samples indicate that the pink mineral is likely topaz, while the undissolved black mineral is likely an amphibole. The only other minerals identified in the undissolved material were very small fragments of partially-dissolved grains of feldspar or quartz, as shown in Figure 6.7.

Water content for the samples was estimated based on a laboratory porosity test. Several small pieces of whole rock were weighed, dried in the oven for two weeks, weighed again, soaked in water for two weeks, and then weighed again. The porosity was estimated using the difference in mass between the wet and dry samples. The time-averaged saturation of the rocks before sampling was assumed to be 50%, yielding a volumetric fractional water content of 0.017 (i.e.,

Sample	SiO_2	TiO_2	Al_2O_3	Fe_2O_3	MnO	MgO	CaO	Na_2O	K_2O	P_2O_5	LOI
HU08-01	74.20	0.21	14.00	1.40	0.01	0.22	0.70	3.20	4.90	0.21	0.90
HU08-02	74.18	0.20	13.93	1.50	0.01	0.22	0.72	3.19	4.82	0.20	0.89
HU08-03	74.21	0.21	14.35	1.30	0.01	0.23	0.76	3.23	4.85	0.22	0.51
HU08-04	74.03	0.20	14.04	1.37	0.01	0.22	0.70	3.11	4.79	0.20	1.22
HU08-06	73.27	0.21	14.28	1.40	0.01	0.23	0.75	3.29	4.89	0.21	1.33
HU08-08	73.07	0.22	14.33	1.27	0.02	0.24	0.7	3.06	4.8	0.21	1.97
HU08-09	73.18	0.22	14.41	1.23	0.01	0.25	0.69	3.18	4.94	0.2	1.56
HU08-10	72.98	0.20	13.87	1.50	0.01	0.22	0.69	3.06	4.93	0.19	2.22
HU08-11	73.69	0.20	14.02	1.52	0.02	0.25	0.73	3.12	4.88	0.19	1.25
HU08-14	73.38	0.22	14.38	1.45	0.01	0.24	0.72	3.15	4.99	0.18	1.15
HU08-15	73.02	0.21	14.20	1.73	0.01	0.25	0.71	3.11	4.95	0.20	1.49
HU08-16	68.83	0.21	13.62	1.40	0.02	0.24	0.70	3.10	4.83	0.18	6.75
HU08-18	73.99	0.20	13.88	1.55	0.02	0.24	0.70	3.09	4.85	0.20	1.17
HU08-19	74.09	0.20	13.86	1.50	0.01	0.23	0.68	3.07	4.92	0.20	1.11
HU08-21	73.84	0.20	13.78	1.55	0.01	0.24	0.69	3.04	4.83	0.19	1.49

Table 6.6: Results of Peru chlorine-36 whole-rock major-element analyses as determined by major element XRF. All results are reported in weight percent. LOI represents the "loss on ignition" that was reported by the analyzing lab. These analyses were used as the "bulk rock" composition for mineral separate samples of the same number for both NMT and UW samples. Samples were sieved and leached prior to XRF analysis.

Sample	B	Sm	Gd	U	Th	Cr	Li
HU08-01	60	3.2	2.34	9.62	12.4	100	430
HU08-02	60	3.2	2.34	9.62	12.4	140	430
HU08-03	160	3.2	2.47	9.02	12.5	50	440
HU08-04	70	3.1	2.22	9.26	11.4	50	440
HU08-06	80	3.4	2.23	9.30	12.0	60	470
HU08-08	90	2.3	2	10.82	9.5	5	400
HU08-09	100	2.9	2.44	12	12	5	430
HU08-10	100	3.1	2.19	9.46	10.6	100	440*
HU08-11	120	3.1	2.03	8.45	11.0	110	450
HU08-14	100	2.9	1.96	8.54	10.7	50	420
HU08-15	90	2.9	2.31	10.90	11.2	130	450
HU08-16	120	3.1	1.95	8.75	10.7	50	430
HU08-18	100*	3.1*	2.19*	9.23*	11.5*	115	440*
HU08-19	100*	3.1*	2.19*	9.23*	11.5*	119	440*
HU08-21	100*	3.1*	2.19*	9.23*	11.5*	108	440*

Table 6.7: Results of Peru whole-rock trace-element analyses as determined by ICP-OES analysis. All measurements are reported in ppm. These analyses were used as the "bulk rock" trace element composition for mineral-separate samples of the same number for both UW and NMT samples. * Indicates an average of the other samples.

Sample	Target K_2O wt %	Target CaO wt %	Target TiO_2 wt %	Target Fe_2O_3 wt %	Target Cl [ppm]
HU08-01-SAN-JS	10.22	0.19	0.02	0.10	0.7
HU08-02-SAN-JS	10.25	0.23	0.02	0.03	0.5
HU08-03-SAN-JS	10.04	0.33	0.04	0.04	0.0
HU08-04-SAN-JS	10.34	0.19	0.02	0.02	0.0
HU08-06-SAN-JS	9.92	0.23	0.04	0.04	0.7
HU08-10-SAN-JS	9.84	0.25	0.02	0.02	0.6
HU08-11-SAN-JS	9.24	0.28	0.03	0.03	0.6
HU08-14-SAN-JS	9.52	0.25	0.02	0.02	2.2
HU08-15-SAN-JS	9.85	0.25	0.04	0.04	1.9
HU08-16-SAN-JS	9.55	0.28	0.06	0.05	2.4

Table 6.8: Peru chlorine-36 target-element compositions. These analyses were used as the "target" element composition. All samples are from the UW lab.

Sample	K_2O wt %	CaO wt %	TiO_2 wt %	Fe_2O_3 wt %	Cl [ppm]
HU08-02WR	4.82	0.72	0.2	1.5	98
HU08-03WR	4.85	0.76	0.21	1.3	102.1
HU08-04WR	4.79	0.7	0.2	1.37	92.6
HU08-06WR	4.89	0.75	0.21	1.4	115.5
HU08-10WR	4.93	0.69	0.2	1.5	107.8
HU08-11WR	4.88	0.73	0.2	1.52	85.3
HU08-14WR	4.99	0.72	0.22	1.45	130.5
HU08-15WR	4.95	0.71	0.21	1.73	124.8
HU08-16WR	4.83	0.7	0.21	1.4	129.8
HU08-02 SAN	6.71	0.48	0.03	0.07	17.00
HU08-03SAN	10.72	0.20	0.03	0.08	18.50
HU08-06SAN	9.55	0.24	0.03	0.07	49.20
HU08-10SAN	10.28	0.16	0.03	0.14	127.1
HU08-14SAN	8.98	0.16	0.03	0.07	19.40
HU08-15SAN	10.06	0.17	0.02	0.07	19.20
HU08-01SANetch	9.26	0.22	0.05	0.46	67.9
HU08-04SANetch	10.68	0.08	0.03	0.15	17.00
HU08-11SANetch	10.52	0.09	0.03	0.14	22.80
HU08-16SANetch	10.26	0.13	0.03	0.15	29.80
HU08-01WR	4.90	0.70	0.21	1.40	80.1
HU08-04WR	4.79	0.70	0.20	1.37	92.6
HU08-10WR	4.93	0.69	0.20	1.50	107.8
HU08-11WR	4.88	0.73	0.20	1.52	85.3
HU08-16WR	4.83	0.70	0.21	1.40	129.8
HU08-01SANreg	9.62	0.27	0.04	0.27	90
HU08-04SANreg	10.68	0.08	0.03	0.15	112.9
HU08-11SANreg	10.52	0.09	0.03	0.14	251.4
HU08-16SANreg	10.26	0.13	0.03	0.15	128
HU08-08WR	4.8	0.7	0.22	1.27	100.2
HU08-09WR	4.94	0.69	0.22	1.23	105.5
HU08-08SAN	10.49	0.06	0.04	0.15	17.8
HU08-09SAN	11.12	0.05	0.03	0.2	6.3
HU08-08QTZ	0	0	0	0	33.8
HU08-09QTZ	0	0	0	0	59
HU08-18WR	4.85	0.70	0.20	1.55	70.3
HU08-19WR	4.92	0.68	0.20	1.50	64.5
HU08-21WR	4.83	0.69	0.20	1.55	68.6
HU08-18SAN	11.29	0.07	0.03	0.08	33.8
HU08-19SAN	11.15	0.08	0.02	0.07	44.3
HU08-21SAN	10.06	0.17	0.02	0.07	31.7

Table 6.9: Peru target-element compositions as determined by major element XRF. These analyses were used as the "target" element composition. All samples are from the NMT lab.

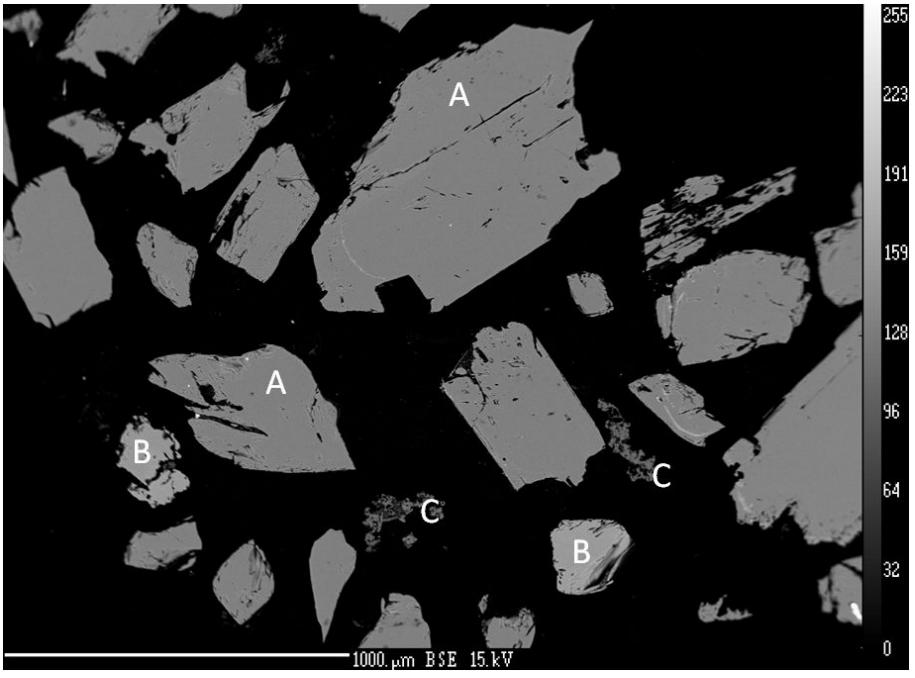

Figure 6.7: Microprobe image of undissolved material from Huancané samples. The large, darker grains are amphibole (A), the lighter grains are probably topaz (B), and the "swiss cheese" minerals are undissolved pieces of either quartz or plagioclase (C). Two examples of each type are labeled.

1.7% volumetric water content). This average was applied to all the samples at the site.

6.4.2 Chlorine-36 Results from New Mexico Tech (NMT)

The NMT chlorine-36 results from the CRONUS samples can be divided into two categories: mineral-separate samples and whole-rock samples. The mineral separates are relatively pure sanidines, while the whole rock contains all mineral phases originally present in the sample. The relevant final inventory of ^{36}Cl and stable Cl is presented in Table 6.10. The laboratory procedures for these samples are described in detail in the methods chapter, Chapter 3.

Due to inconsistency and irreproducibility, some samples were removed from the dataset. The SANreg samples were removed from the final production rate analysis due to both their anomalous values and their irreproducibility. These samples were an experimental attempt to process samples in such a way that they contained varying values of Cl, but the results were inconsistent with the other calibration samples. The matrix was not etched away on these samples, leaving the possibility that some elements, such as chlorine, could have been leached out of the matrix, which would cause inconsistent results. There are sufficient completely etched sanidine samples that the anomalous SANreg samples are not required as well. There are also two outliers in the main dataset, one each from the mineral separate and whole rock sample sets. All the unused samples are plotted as open symbols in Figure 6.13 and are not included in the final analysis.

All NMT samples had blanks subtracted from the chlorine-36 and stable chloride inventory. For the whole rock samples, the percentage of the blank

subtraction for chlorine-36 and stable chloride ranged from 8-12% and 0.8-1.4%, respectively. For the mineral separates, the chlorine-36 blank percentage was smaller (4-9%) and the stable chloride blank percentage was larger (1.1-5.5%) due to the higher chlorine-36 concentrations and lower stable chloride concentrations, respectively. The blank subtraction values were carefully calculated from blanks processed with the samples using the same lots of acid in the same proportions, whenever possible. The values of the blank subtractions were relatively consistent between batches so an average value of those blanks was applied to all the samples from NMT.

6.4.3 Chlorine-36 Results from University of Washington (UW)

Samples from the Huancané site were also prepared by John Stone at the University of Washington. The original data is in Appendix C.3. This data is included here as part of the CRONUS-Earth chlorine calibration. These samples were prepared as mineral separates only, but used the bulk rock composition and trace element concentrations from the NMT whole-rock samples. The water content calculated for the NMT samples was also applied to these samples. Target elements (Ca, K, Fe, Ti) were measured at UW using Inductively Coupled Plasma (ICP). The stable chlorine concentration was determined using AMS on a separate ^{37}Cl-spiked sample aliquot.

6.4.4 Erosion Rate Study

One pair of bedrock samples (HU08-08 and HU08-09), one glacially polished and one eroded, was collected to study erosion rates in the Huancané

Name	Raw ^{36}Cl [$\times 10^4$ at/g]	Raw Cl conc [ppm]	Covar	HF [mL]	BC Cl [ppm]	BC ^{36}Cl [$\times 10^4$ at/g]	σ_{N36}
HU08-02WR	109.50 ± 4.20	99.10 ± 1.20	12900	57	98 ± 1.6	106.4 ± 4.9	51900
HU08-03WR	91.30 ± 4.10	103.30 ± 1.20	10900	62	102.1 ± 1.6	88.8 ± 4.8	50100
HU08-06WR	96.60 ± 4.80	116.60 ± 1.70	16000	58	115.5 ± 2	94.1 ± 5.4	56600
HU08-14WR	116.60 ± 4.80	131.60 ± 1.90	22400	58	130.5 ± 2.2	114.4 ± 5.5	57900
HU08-15WR	97.80 ± 4.00	125.90 ± 1.90	19600	75	124.8 ± 2.2	95.7 ± 4.6	48500
HU08-02 SAN	100.70 ± 4.00	17.80 ± 0.60	3500	67	17 ± 1	99.3 ± 4.4	73500
HU08-03SAN	152.30 ± 4.70	19.40 ± 0.70	6000	77	18.5 ± 1.1	150.4 ± 4.9	99200
HU08-06SAN	165.60 ± 7.80	50.80 ± 0.80	10300	60	49.2 ± 1.7	162.2 ± 8.7	104000
HU08-14SAN	129.60 ± 11.40	20.50 ± 0.90	6400	53	19.4 ± 1.3	127.2 ± 11.7	146000
HU08-15SAN	136.10 ± 5.30	20.30 ± 0.80	5900	48	19.2 ± 1.3	133 ± 6.1	106100
HU08-04SANetch	154.90 ± 5.90	17.90 ± 0.30	3100	35	17 ± 0.9	151.3 ± 7	108700
HU08-11SANetch	148.00 ± 7.50	23.80 ± 0.30	3600	38	22.8 ± 1	144.2 ± 8.4	105200
HU08-16SANetch	153.40 ± 4.90	30.80 ± 0.40	5100	47	29.8 ± 1.1	149.9 ± 5.8	79200
HU08-01WR	73.50 ± 21.20	81.20 ± 18.10	963600	67	80.1 ± 18.1	71.2 ± 21.3	267400
HU08-04WR	96.20 ± 3.10	93.60 ± 1.30	11700	56	92.6 ± 1.6	93.7 ± 4	43300
HU08-10WR	96.50 ± 4.30	108.80 ± 1.70	16200	64	107.8 ± 1.9	94.4 ± 4.8	50400
HU08-11WR	88.20 ± 2.90	86.10 ± 1.10	9100	50	85.3 ± 1.4	85.7 ± 3.8	40700
HU08-16WR	98.40 ± 3.20	131.00 ± 2.70	32400	78	129.8 ± 2.9	96.3 ± 3.8	44300

Table 6.10: Final Peru chlorine-36 and stable Cl for NMT samples (Part I). "Raw" indicates that it is the original value calculated from the dissolution information and AMS results. "BC" represents the blank-corrected values. "BC σ_{36}" represents the ^{36}Cl uncertainty if the uncertainty on the stable chloride is transferred to the ^{36}Cl. The radiogenic ^{36}Cl, calculated and subtracted internally in the CRONUScalc code, is also shown. Continued in table 6.11.

Name	Raw ^{36}Cl [$\times 10^4$ at/g]	Raw Cl conc [ppm]	Covar	HF [mL]	BC Cl [ppm]	BC ^{36}Cl [$\times 10^4$ at/g]	σ_{N36}
HU08-10SAN	147.50 ± 5.60	128.50 ± 1.80	24600	56	127.1 ± 2.2	144.6 ± 6.5	70100
HU08-01SANetch	162.70 ± 9.70	69.00 ± 1.00	14000	41	67.9 ± 1.5	159.3 ± 10.4	109300
HU08-01SANreg	191.80 ± 9.00	91.90 ± 1.20	19500	56	90 ± 2.1	187.4 ± 10.1	110100
HU08-04SANreg	149.00 ± 5.80	114.70 ± 1.50	18700	39	112.9 ± 2.2	142.6 ± 8.6	90800
HU08-11SANreg	156.50 ± 6.50	253.30 ± 5.70	84000	44	251.4 ± 5.9	150.1 ± 8.7	94200
HU08-16SANreg	147.90 ± 5.70	129.40 ± 1.70	22200	42	128 ± 2.2	143.4 ± 7.3	77100
HU08-18WR	9.00 ± 0.60	71 ± 1.6	2400	121	70.3 ± 1.8	8.1 ± 1.1	10700
HU08-19WR	8.60 ± 0.70	65.3 ± 1	1000	129	64.5 ± 1.2	7.8 ± 1.1	10800
HU08-21WR	7.40 ± 0.40	69.2 ± 1.3	1400	124	68.6 ± 1.5	6.6 ± 0.8	8500
HU08-18SAN	14.60 ± 2.70	35 ± 1.1	1100	56	33.7 ± 1.6	11.6 ± 4.1	41600
HU08-19SAN	11.00 ± 1.90	45.3 ± 0.6	500	61	44.1 ± 1.2	8.5 ± 3.2	31800
HU08-21SAN	9.40 ± 1.00	32.6 ± 0.7	400	48	31.8 ± 1	7 ± 2.6	25700
HU08-08WR	208.80 ± 6.20	96.3 ± 1.7	33000	51	95.2 ± 1.9	206 ± 6.8	79700
HU08-09WR	194.70 ± 4.80	101.9 ± 1.7	32300	53	101 ± 1.9	192.3 ± 5.4	64800

Table 6.11: Final Peru chlorine-36 and stable Cl for NMT samples (Part II). "Raw" indicates that it is the original value calculated from the dissolution information and AMS results. "BC" represents the blank-corrected values. "BC σ_{36}" represents the ^{36}Cl uncertainty if the uncertainty on the stable chloride is transferred to the ^{36}Cl. The radiogenic ^{36}Cl, calculated and subtracted internally in the CRONUScalc code, is also shown.

valley. These samples were collected on a large, polished bedrock area further downstream from the Huancané II moraines. A similar beryllium-10 erosion rate study performed by Kelly (pers. comm., April 3, 2012) yielded an erosion rate of 4.8 mm/kyr. The chlorine-36 samples were split and processed using three different methods: whole rock, potassium mineral separates, and quartz mineral separates. The ages, as calculated using the final calibrated production rates from Chapter 8 and assuming zero erosion, are shown in Figure 6.8. The relative ages of the whole rock and quartz separates appear to be consistent with that expected from the pair of samples, with the polished sample yielding a higher age than the eroded sample. However, the significantly older age of the eroded sample compared to the polished sample (10 ka older than polished) indicates that there was likely an analytical problem with one or both of the mineral separate samples and so they will be discarded from further discussion. The large uncertainties on the quartz separates also makes the small differences between the sample measurements essentially meaningless, so this chlorine erosion rate discussion will focus on the whole-rock samples only.

The erosion rate necessary to bring the eroded whole-rock sample into agreement with the polished sample is 21 mm/kyr (5.0 g/cm^2/kyr). The change in age with erosion rate is shown for this whole-rock sample in Figure 6.9. It is clear that the erosion rate is much higher than the $\sim$5 mm/kyr that Kelly (pers. comm., April 3, 2012) found for beryllium. The bedrock at this site was exposed for an unknown period of time prior to the last glacial maximum, which occurred $\sim$21 ka. The glaciation during this period was extensive, as seen by deposits located a significant distance downvalley. The bedrock was covered by the glacier until deglaciation. The minimum limiting age for the deglaciation is a set of four radiocarbon dates (see Table 6.3) that have calibrated ages between 15-17 ka. The

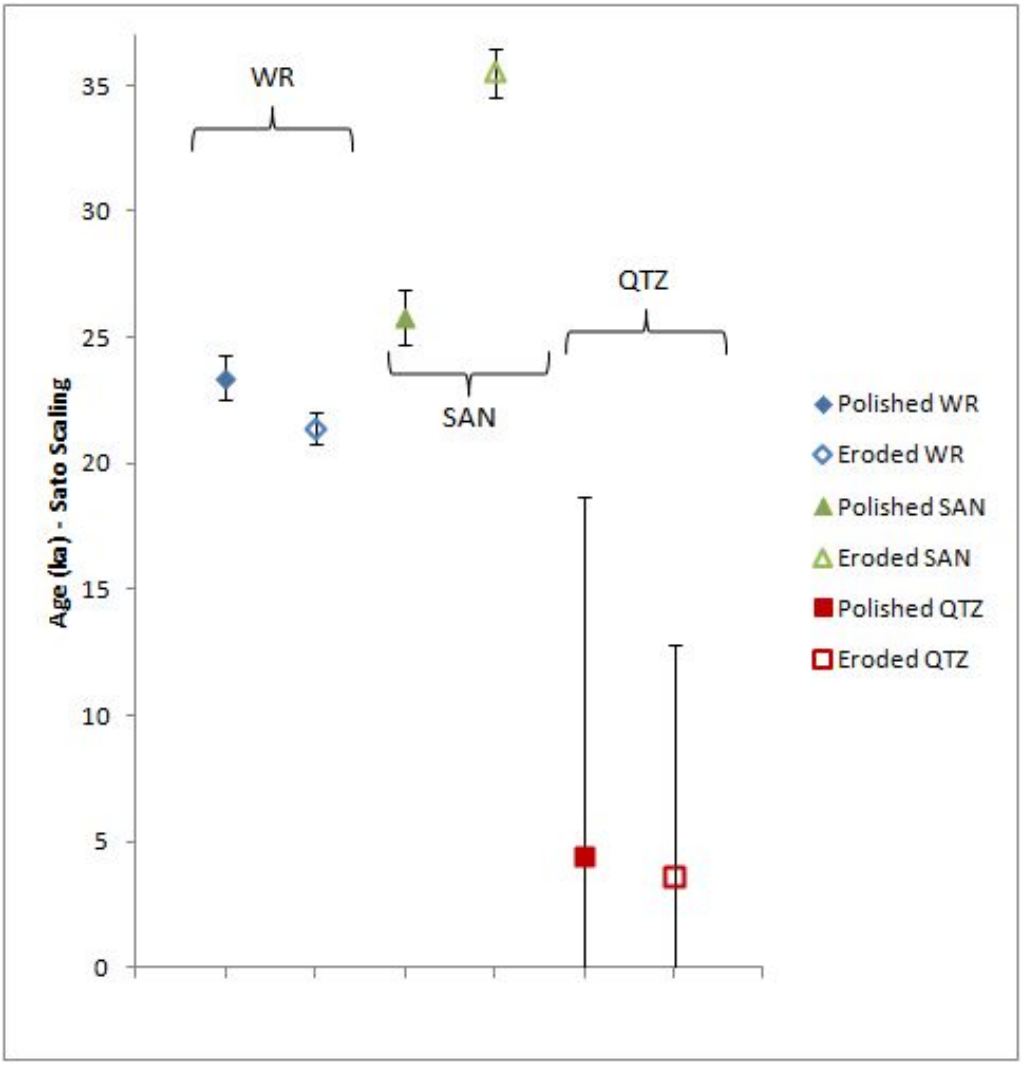

Figure 6.8: Ages for ^{36}Cl samples from the Peru erosion rate study. Sample ages calculated assuming no erosion. Whole rock (WR), potassium mineral separates (SAN), and quartz mineral separates (QTZ). Eroded SAN sample is plotted but is considered an outlier and is thus not used to determine erosion rate.

bedrock was eroded and polished during the extended glacial occupation of the area.

Exposure ages that pre-date the last glacial maximum likely indicate some inherited component in the cosmogenic nuclide inventory. Figure 6.10 shows hypothetical profiles to demonstrate the effect of inheritance on the erosion rate calculation. An inherited component, the profile on the far left, was created by calculating the profile at a surface that had been exposed for 15 ka (prior to the LGM), then subglacially eroded by 50 cm. The figure also shows two pairs of profiles, with the middle pair representing the 'no inheritance' scenario and the right pair representing the 'inheritance' scenario. The two inherited profiles are essentially the sum of the inherited component (far left) and the appropriate middle profile. The location of the measured sample pair on each profile is shown by red (eroded) and green (polished) dots. The value of 22 mm/kyr was calculated assuming a 'no inheritance' scenario, while the actual shapes of the profiles more likely resembles the 'inheritance' scenario instead. The slope of ^{36}Cl concentration with depth is much steeper for the 'inherited' scenario than for the 'no inheritance' scenario, which would lead to the calculation of a much higher erosion rate than the actual rate. The anomalously old apparent ages of these two samples strongly support the inheritance scenario.

The erosion rate calculations performed above assume no inheritance. Inheritance could easily account for the unreasonably high erosion rate calculated for the samples. The erosion rates determined from the stickups and the Be study are much more robust and the erosion rates from those sources will be used in the final calibration dataset.

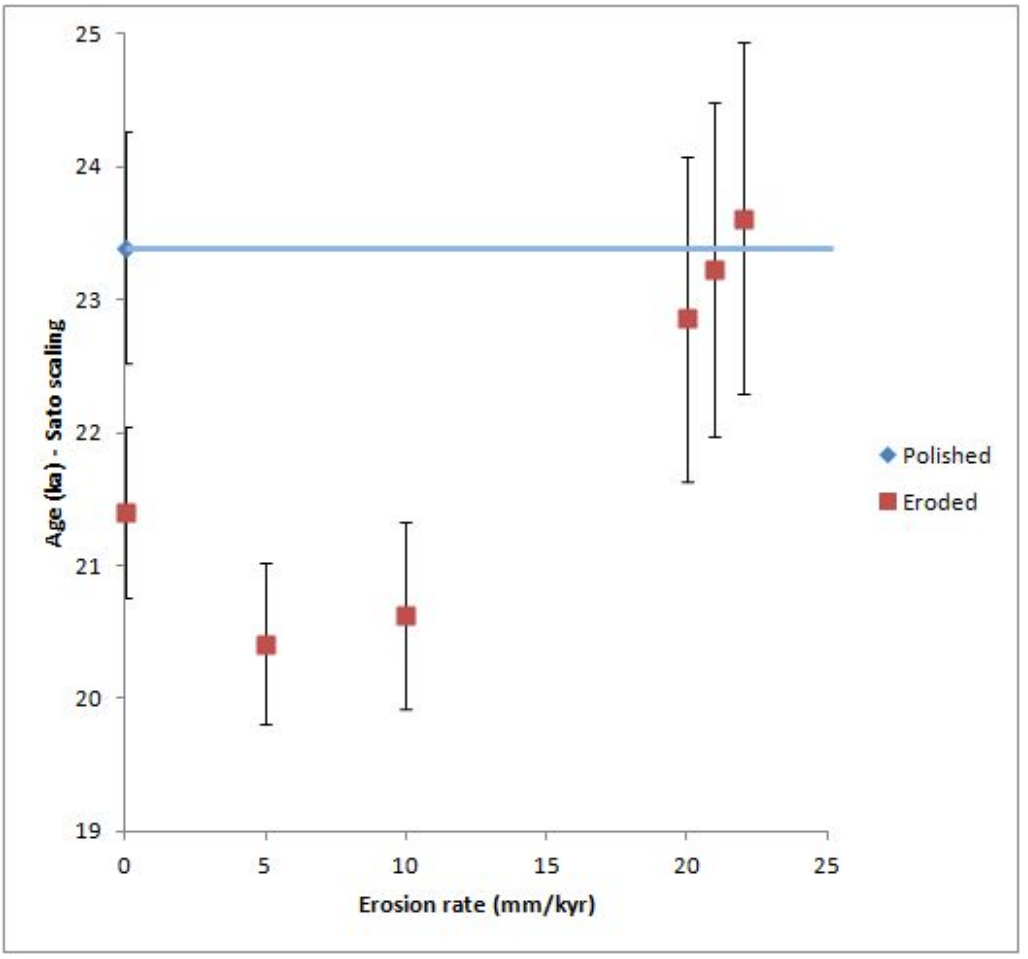

Figure 6.9: Ages for chlorine-36 samples from the erosion-rate study showing the whole-rock sample age variation with erosion rate. The polished-sample is shown at 0 erosion by a diamond and the nominal age of this sample is shown by the blue line. The ages were calculated with the NMT potassium production rate in order to reduce any possible systematic offset. The K spallation production rate does not impact the erosion rate determination.

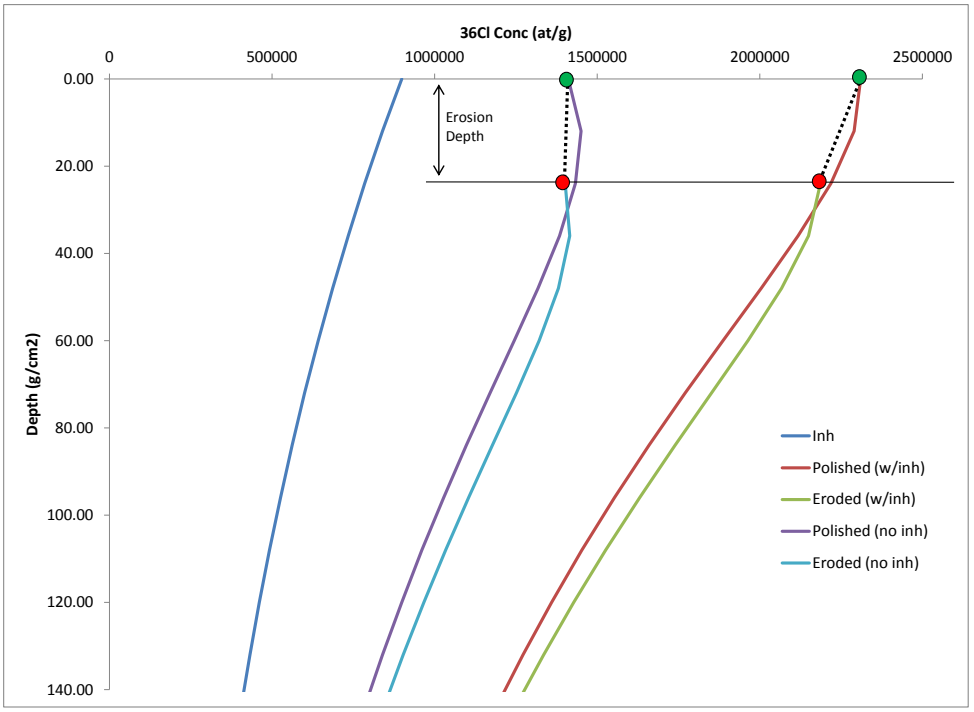

Figure 6.10: Hypothetical profiles indicating the effect of inheritance on the determination of erosion rate at the Huancané site. The profile on the far left is the "inherited" profile remaining after 15 ka of exposure and assuming 50 cm of total erosion. The middle pair of profiles indicates the predicted profiles assuming there is no inheritance in the sample and the surface was exposed for 15 ka. The pair of profiles on the right shows the sum of the inherited component and the 15 ka profile. Samples are all plotted assuming the glacially polished surface is at 0, so both eroded profiles are plotted $\sim$20 g/cm^2 below the surface, which is approximately equivalent to the measured total erosion for these samples. The circles indicate the location of the sample pairs on the hypothetical profiles (red = eroded, green = polished). The dotted lines indicate the difference between the pair of samples as predicted by the inheritance and no inheritance scenarios.

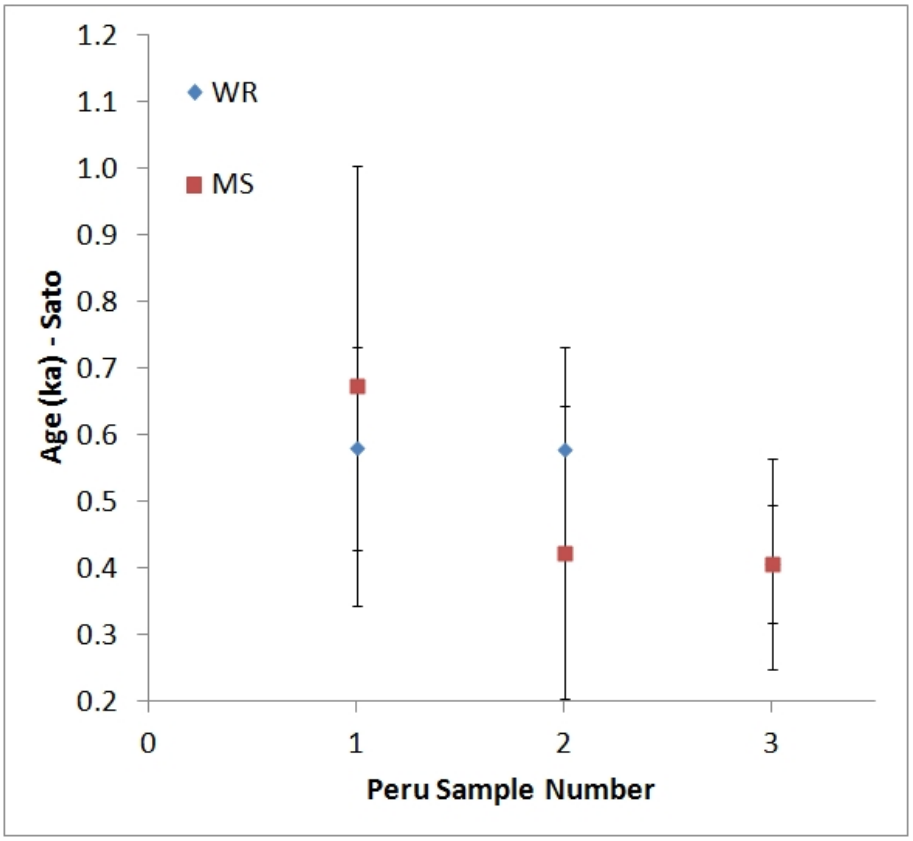

Figure 6.11: Sample ages from the Huancané I moraine processed in the NMT lab. Samples are separated out by lab procedure (potassium feldspar mineral separate (MS) or whole rock (WR)). The whole-rock sample plots directly behind the mineral separate for sample 3. The samples on the plot correspond to samples HU08-18, HU08-19, and HU08-21 as 1, 2, and 3.

6.4.5 Secondary Huancané Samples

Three samples from the Huancané I moraines were also analyzed and are included as extra secondary samples in the final dataset. Figure 6.11 shows the ages of the samples for the NMT lab, as calculated using the final production rates. The ages appear to be internally consistent with an age of approximately 0.51 ka.

6.5 Discussion

The consistency of chlorine-36 data is impossible to assess without accounting for composition. Therefore, the results will be plotted and discussed in two ways. The first method is a normalized composition diagram and the second is the calculated ages of the samples using the final production rates. Both methods rely on the final production rates to some degree. The production rates were produced without information from this analysis, so there is no circularity. This analysis simply presents the data using these two presentation styles in order to ascertain if they are consistent.

The normalized composition diagram plots the concentration of chlorine-36 from the combination of Cl and K (as calculated by the final production rates) divided by the weight percent K_2O of the target versus the percent production from Cl. Production from Ca is subtracted prior to these calculations. Ideally, all the samples would fall along a single line, with the potassium production rate found by extrapolating to 0% production by chlorine. While this is not independent of production rates, it gives a clear picture of whether or not the data are consistent for the production rate calibration. All the samples from all the labs are shown using this plot in Figure 6.12.

In order to assess the whole-rock samples in terms of their consistency with the mineral separates, the whole-rock samples are also plotted on the normalized composition plot. There are two shaded areas that represent where higher chlorine samples, such as whole-rock samples, would plot based on the production rates from mineral separates and assuming a $P_f(0)$ value of approximately 650 n (g air)$^{-1}$yr^{-1}. The difference between the production rate produced by Stone and that produced by Marrero result in two different shaded windows.

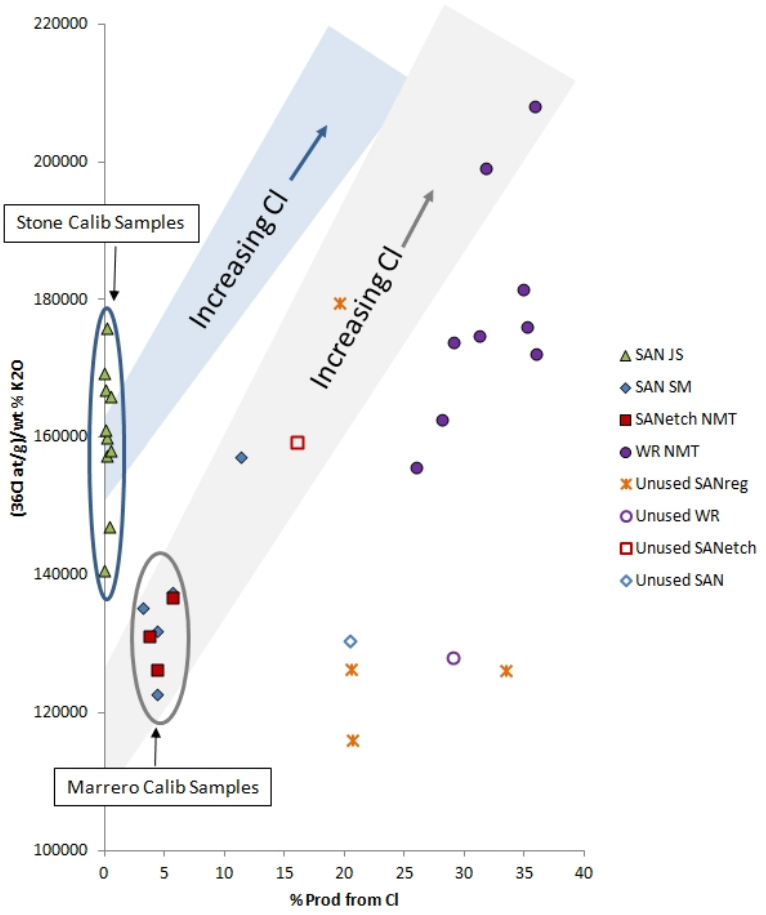

Figure 6.12: All Huancané samples processed for chlorine (NMT & UW), plotted as (at $^{36}Cl/g$)/wt% K_2O vs chlorine concentration. The small amount of production from Ca was subtracted prior to these calculations. The light blue shaded area, which extends from the Stone Calibration samples samples, indicates the range where samples with higher Cl would plot using the potassium production rate determined from the UW data. The gray shaded region, which extends from the Marrero calibration samples, indicates the range where samples with higher Cl would plot using the potassium production rate determined from the NMT data. In both cases, a value of 650 n (g air)$^{-1}$yr^{-1} was assumed for $P_f(0)$. The symbols represent each of the sample groups: SAN JS - John Stone sanidines; SAN SM - Shasta Marrero sanidines etched very completely; SANetch NMT - Shasta Marrero sanidines minimally etched; WR NMT - Shasta Marrero whole-rock samples; Unused SANreg - Shasta Marrero unetched sanidines; 'Unused' indicates samples from the dataset produced by Shasta Marrero at NMT that were not used in the analysis, but follow the naming conventions described above.

The location of higher chlorine samples are shown in light blue if using the Stone production rate and light gray if using the Marrero production rate. These regions are plotted to show that neither potassium production rate is consistent with the whole-rock sample results. There is no value of $P_f(0)$ that would bring the whole-rock samples into alignment with the Stone samples and only an unrealistically low value would make them consistent with the Marrero mineral separates. The whole-rock samples likely have similar analytical problems as the Marrero mineral separates and will not be used for the production rate analysis.

The site production rate for potassium for Peru was found by using the CRONUScalc Matlab program. Due to the fact that the samples are potassium dominated, only the potassium production rate will be discussed. The calibration results were cross-checked using a manual analysis in Excel. Essentially, the production rates can be approximated by fitting a straight line through the data as they are plotted in Figure 6.12. The y-intercept at Cl equal to zero is the production rate from only potassium at the site. The Matlab code does this through chi-squared minimization and selecting the best-fit parameter. The Matlab and Excel results are in very good agreement and only results from the Matlab analysis will be discussed.

The site production rate (scaled to SLHL using the Lifton/Sato scaling) was found for each subset of the Huancané chlorine-36 data. The production rate is 155 at ^{36}Cl(g K)$^{-1}$yr^{-1} for potassium, based on the mineral separates from UW. This rate changes to 120 at ^{36}Cl(g K)$^{-1}$yr^{-1} if the NMT mineral separates are used instead. If both datasets are combined, a rate of 148 at ^{36}Cl(g K)$^{-1}$yr^{-1} is found. These results and the associated p-values are summarized in Table 6.12. When each dataset is analyzed independently, the p-value greater than 0.05 in-

Dataset	K Prod Rate [at (g K)$^{-1}$yr^{-1}]	p-value
UW only	156.1 $\pm$ 2.8	0.14
NMT only	120.3 $\pm$ 5.4	0.9955
Combined	148.8	0.000079

Table 6.12: Chlorine-36 potassium production rates produced by the different labs. Uncertainties are only valid for calibrations that produce an adequate fit to the data. The SLHL production rates were calculated using the Lifton/Sato model.

dicates that each dataset is internally consistent, but they are inconsistent when combined, as seen by the very small p-value.

After the final global calibration of production rates (see Chapter 8), the newly calibrated rates were used to age all the Huancané samples. This is plotted in Figure 6.13. The UW mineral separates were used in the primary calibration, while the samples processed by NMT were removed. The NMT whole rocks were not used because only a spallation calibration was performed and the NMT mineral separates were removed due to the scatter in the dataset and the systematic offset. The same systematic offset between the UW and NMT mineral separates is seen. A possible reason for this offset is an oversubtraction in the blank calculations or other systematic problem or difference in the sample preparation.

6.5.1 Comparison with Other Nuclides

Beryllium-10 samples were run in four CRONUS-Earth labs. The ages from these samples are compared to the chlorine ages in Figure 6.14. The beryllium-10 samples for Huancané appear to provide more consistent ages than any of the chlorine-36 datasets. The mineral separates from UW are closest to the beryllium ages, but there is still more scatter in the chlorine results than in beryllium.

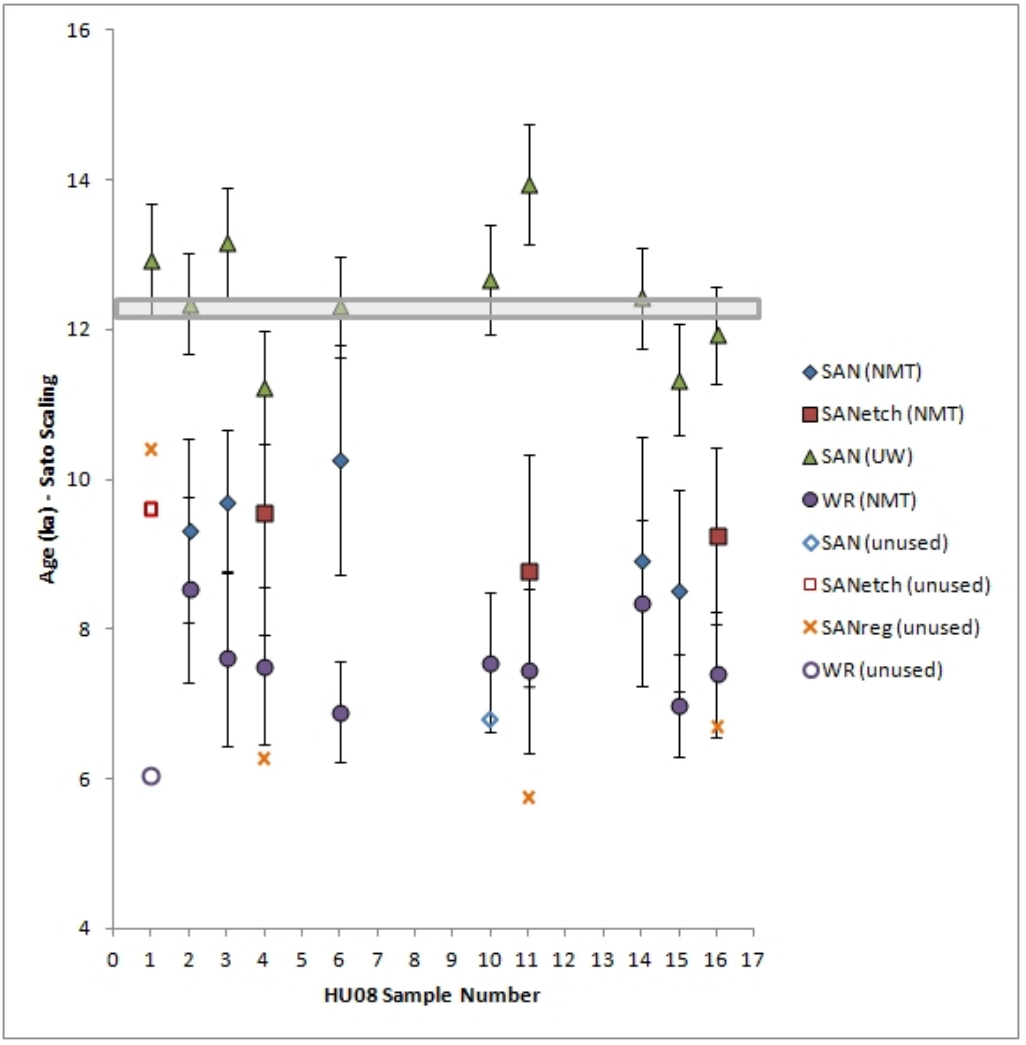

Figure 6.13: Sample ages calculated for all samples using the final calibrated production rates and separated by lab and method used. Samples excluded for any reason are shown as open symbols. The shaded box indicates the independent age bounds for the site.

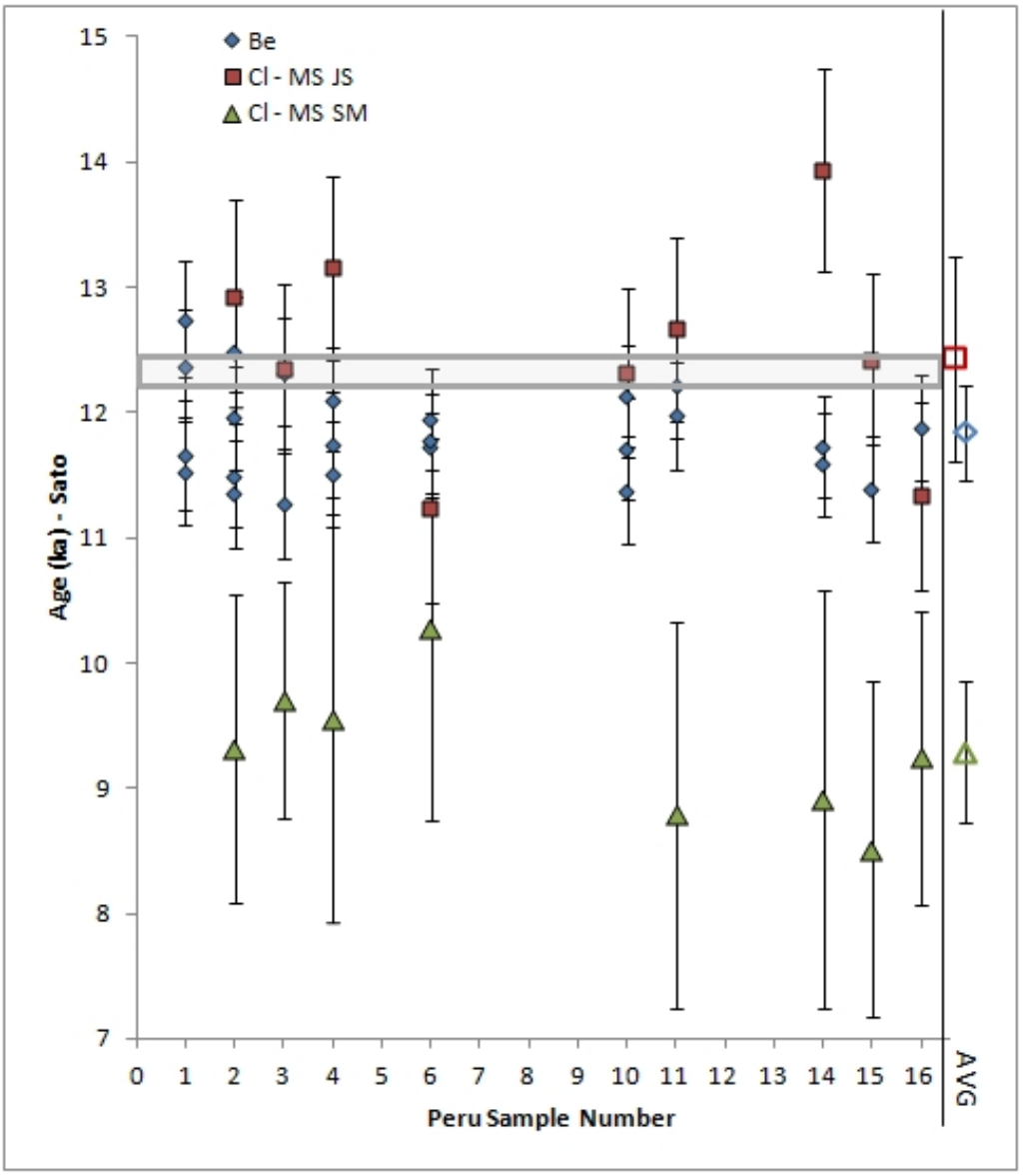

Figure 6.14: Comparison between ages for Be and Cl samples for the Huancané samples. Samples are divided into beryllium-10, John Stone's K mineral separates (Cl - MS JS), and Shasta Marrero's K mineral separates (Cl - MS SM). The shaded box indicates the independent radiocarbon bounds for the site. The open symbols at the right show the mean and standard deviation for the set of samples.

6.6 Peru Conclusions

The Huancané data provides valuable information for potassium chlorine-36 production rate calibration from a low latitude, high elevation site. An offset between chlorine-36 labs is unfortunate and is likely due to blank oversubtraction by NMT, differing processing, or problems with the calibrated values for the $P_f(0)$parameter, which only affects the higher chlorine samples from NMT. The UW mineral separate data was used in the final chlorine-36 production rate calibration, while all other datasets were included in the secondary dataset.

The comparison between chlorine-36 and beryllium-10 data at the Huancané site generally indicates that the beryllium-10 data produces more precise results than the chlorine-36 data. However, the consistency of the beryllium data, despite varying boulder heights, confirms that there should be no problems with snow corrections, exhumation, or other shielding issues.

CHAPTER 7

COPPER CANYON - SITE DESCRIPTION AND DATA

Copper Canyon is not a primary chlorine-36 calibration site, but provides insight into the chlorine-36 $P_f(0)$ parameter. This chapter is designed to provide the background information on the site, including the site description, sample collection, characterization, and an initial analysis of the dataset. Further results from this site will be discussed in the calibration chapter.

7.1 Previous Neutron Activation Studies

Previous chlorine-36 calibration studies have typically either calibrated all three main production pathways simultaneously (Swanson and Caffee, 2001; Phillips et al., 1996, 2001) or have focused on spallation-only pathways (Evans et al., 1997; Licciardi et al., 2008; Schimmelpfennig et al., 2008; Stone et al., 1996). The simultaneous calibrations provided calibrated values for $P_f(0)$, although there were very few samples with compositions appropriate for determining the $P_f(0)$ parameter (i.e. high-Cl, low-Ca, low-K). A study by Swanson and Caffee (2001) contained samples with very low chlorine concentrations in all samples ($<$30 ppm) and a study by Phillips et al. (2001) contained many samples with high-Cl concentrations ($>$300 ppm) but with significant contributions from Ca and K spallation as well.

Two other studies, Dep et al. (1994b) and Bierman et al. (1995), focused on physically isolating the neutron activation pathway for producing chlorine-36. While neither study was a calibration exercise, both developed models of the subsurface and interface to predict production of chlorine-36 from low-energy neutrons. Bierman et al. (1995) developed a model to predict the concentration of chlorine-36 up to 1000 cm into the subsurface due to neutron activation. Although not quantitative, the model accounted for radiogenic neutrons, muon-induced neutrons, and the atmosphere/subsurface interface. The sample processing technique involved crushing samples to release the chlorine in fluid inclusions instead of dissolving the entire sample. Although the samples were reproducible and were generally consistent with the exposure history of the boulders, the results varied by a factor of five from boulder to boulder on the same feature. Ultimately, the variability was likely due to the chlorine extraction technique, geologic heterogeneity of the debris-flow fan that was sampled, or variable erosion rates, but could not be attributed conclusively to any one of these sources.

Dep et al. (1994b) processed quartz mineral separates from a 60 cm deep core from the Bollinger Meteor Crater, AZ. The goal of the project was to physically isolate Cl-containing fluid inclusions by dissolving the rock as compared to the crushing and leaching procedure used by Bierman et al. (1995). Although the measured results were in general agreement with Monte Carlo modeling, this study also had significant scatter in the results. Modeling results from this study did indicate a region of the chlorine profile that is insensitive to erosion rate, making the case for using chlorine-36 depth samples in environments where the erosion history cannot be well-constrained.

Finally, the only calibration exercise that physically isolated the low-energy neutron production pathway was Evans (2001). In the $P_f(0)$ calibration study,

chi-squared minimization was used on eight quartz mineral separate samples from Scotland in order to calibrate the $P_f(0)$ parameter. The value of 740 $\pm$ 54 fast neutrons (g air)$^{-1}$yr^{-1} obtained in the Evans (2001) study was higher than the value of 626 $\pm$ 43 obtained by Phillips et al. (2001), but lower than the 762 $\pm$ 28 value obtained by Swanson and Caffee (2001). This discrepancy between the calibrated values for $P_f(0)$ provides the motivation for this study.

All of the calibration studies mentioned above were performed on surface samples, which are subject to certain limitations. Specifically, the effects of erosion can be significant and samples collected from surfaces with anything other than 2π geometry are at risk for low-energy neutron leakage. New information about the $P_f(0)$ parameter, gained by using a new calibration method, may help resolve the discrepancy. By using a depth profile and combining results from chlorine with results from beryllium, there should be fewer unknowns leading to better constraints on the value of $P_f(0)$.

7.2 Sample Location

The Magdalena Mountains are located in central New Mexico to the west of Socorro (see Figure 7.1). The block-faulted mountains trend N-S and are located within the Rio Grande graben in the Basin and Range province (Krewedl, 1974). The central region of the mountains, thoroughly described by Krewedl (1974), was faulted and tilted in the Late Oligocene. The faults controlled the emplacement of stocks, dikes, and hydrothermal solutions. Of interest are quartz veins that formed as a result of silication alteration that occurred at the end of the Late Oligocene volcanism. The regional uplift of the Magdalenas began sometime after 11 Ma and continues to this day. Considering the long time period

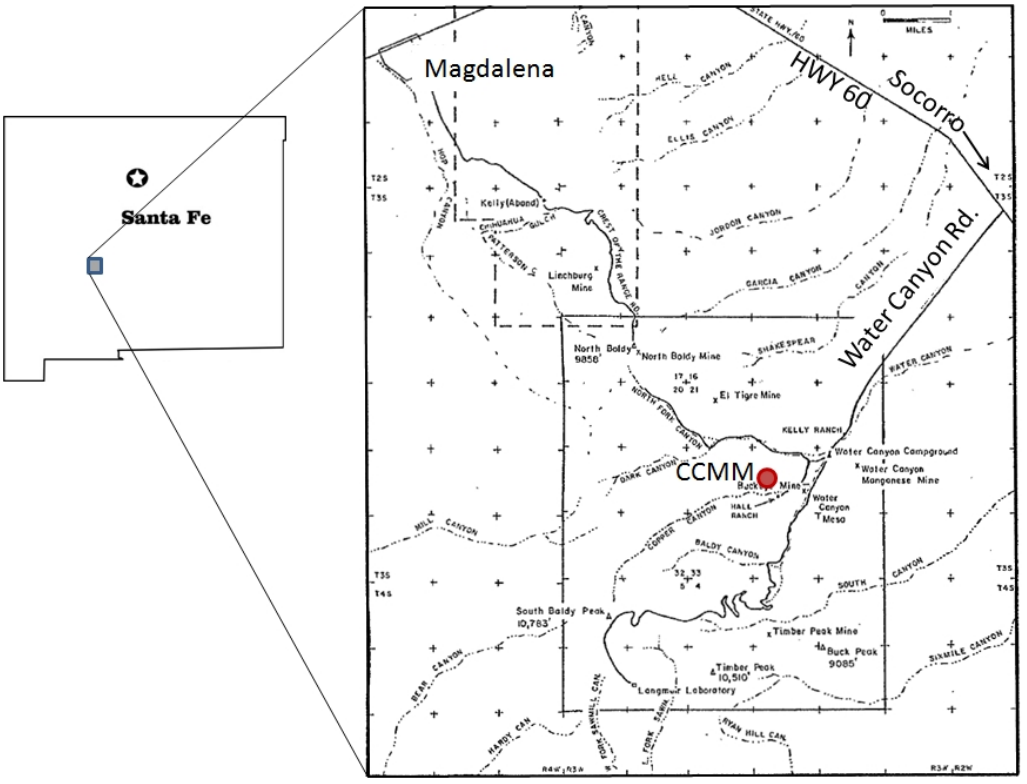

Figure 7.1: Map showing location of the Copper Canyon site in the state of New Mexico. The map shows the Copper Canyon site. Major landmarks, including the access roads to the site, have been relabeled for clarity. Original map from Krewedl (1974).

since initiation of the current conditions, the production of both ^{10}Be and ^{36}Cl should be in equilibrium with the erosion rate at the site.

The Magdalena mining district produced lead, zinc, copper, and manganese from the mineralized zones. Significant mineralization occurred primarily along faults in the Kelly limestone; limestone in the Magdalenas thus became known as the "ore-bearing" lithology, leading to numerous unproductive prospect pits in areas unrelated to faults (Krewedl, 1974). One of these prospect pits provides access to a quartz vein profile almost 2 meters deep. The limestone rock at the sampling site is likely the Pennsylvanian Madera Limestone, described as being well-exposed in Copper Canyon by Krewedl (1974), although

it could also be the Kelly Limestone.

Copper Canyon is located at an elevation of 2206m, with coordinates of 34.01986N,-107.14505W. The pit is located on a south-facing, 30° slope about three-quarters of the way up to the top of the canyon side. The pit itself is approximately two meters deep with the geometry as shown in Figure 7.3. The excavated material was piled on the downhill side of the pit, leaving the uphill side of the pit essentially untouched.

In the area surrounding the pit, there is a very small amount (<10 cm) of overburden/soil on the hillside. In some areas near the pit, areas of exposed bedrock material extend up approximately 30-50 cm above the sloping ground surface. Many of these resistant outcrops are composed of quartz.

7.3 Methods

The Copper Canyon investigation had unique needs as far as sample collection and processing were concerned. The novel methods used at this site that are different from those described in the methods chapter are described in detail here.

7.3.1 Sample Collection and Trimming

The sample material was a small (∼100 cm in width) vein of quartz in a limestone host rock. Depth to the sample was measured as precisely as possible in the field by setting up a horizontal baseline (checked with a level) across the pit and then measuring down from that line to each sample. Each sample was photographed and documented in the field notebook. The samples were removed

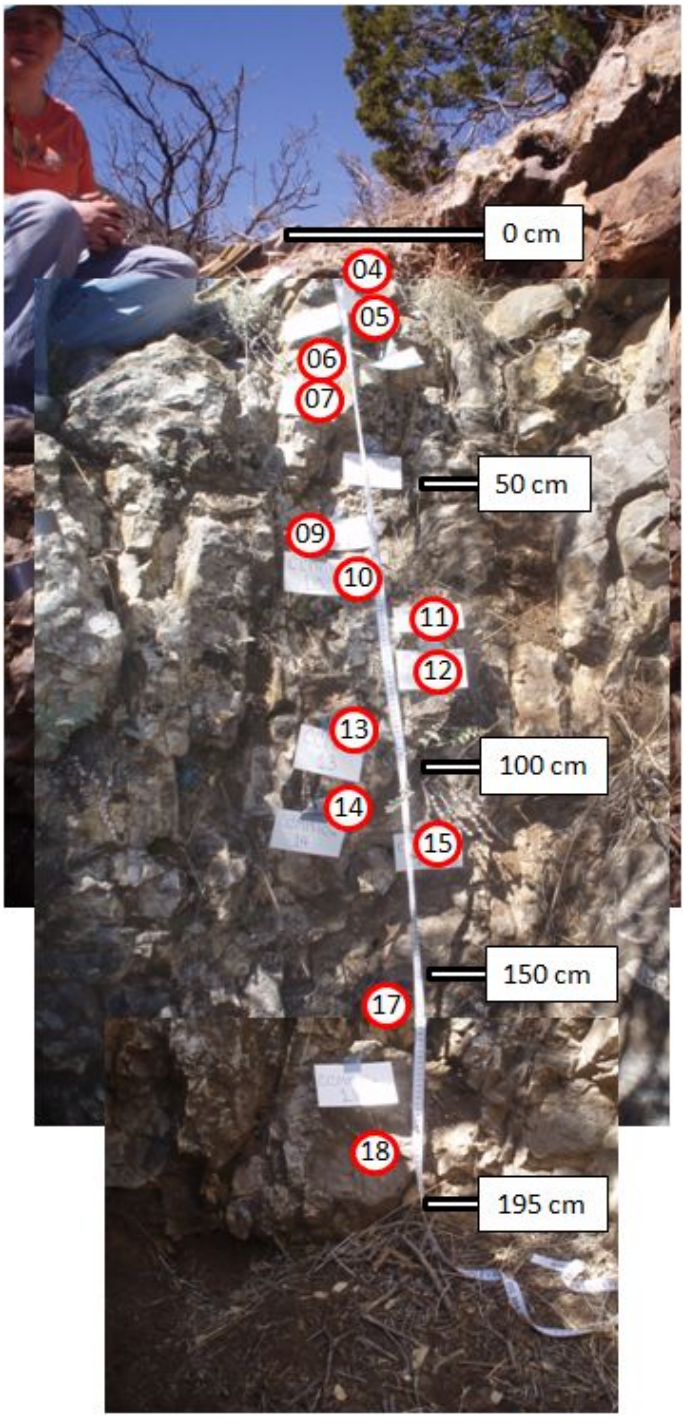

Figure 7.2: Photo collage of the pit showing sample locations. Approximate depths and sample locations are shown on the photo.

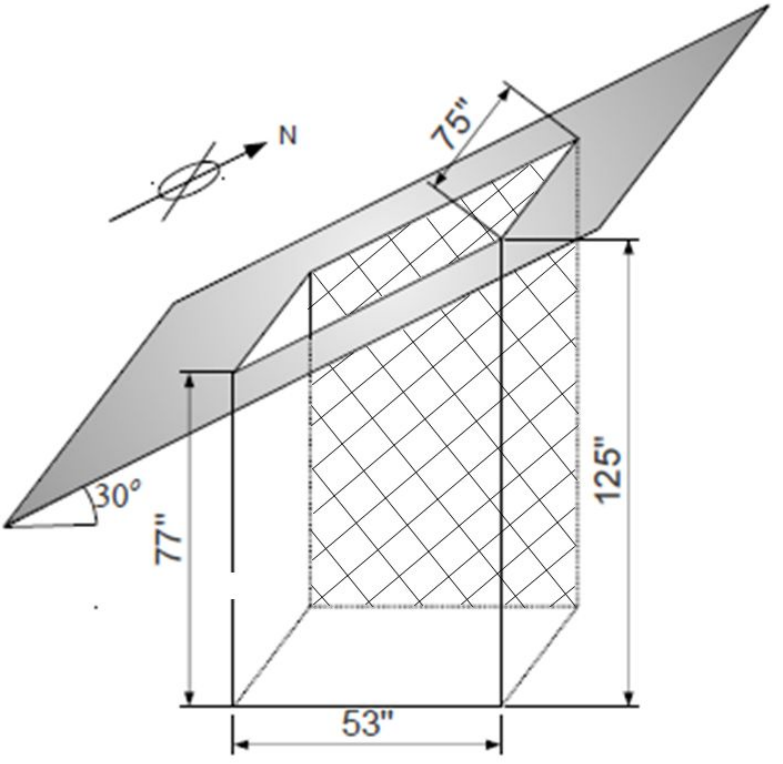

Figure 7.3: Diagram of the pit showing dimensions and angles. Hashed face indicates the sampled pit wall.

Sample	Depth [vert cm]	Depth [perp g/cm^2]
CCMM10-04	0.4	1
CCMM10-05	7.4	16
CCMM10-06	22	48
CCMM10-07	29	63
CCMM10-09	64	138
CCMM10-10	65	140
CCMM10-11	72	156
CCMM10-12	79	171
CCMM10-14	98	212
CCMM10-15	120	260
CCMM10-17	160	346
CCMM10-18	193	417

Table 7.1: Copper Canyon sample depths. The second column gives the depth down in the pit, or vertical cm. The third column is the depth converted to depth perpendicular to the surface in g/cm^2. This uses the average slope of 30° as well as the average density of the profile (2.3 g/cm^3).

by chisel and single jack when possible. In most cases, fractures encouraged the removal of large blocks containing more than one sample. The samples were collected in the following block sets: 4/5, 6/7, 9/10, 11/12, 13/14, 15. The deepest two samples, CCMM17 and CCMM18, were collected using a paleomagnetic sampling drill to remove small cores and then chisel out the rest of the sample. A paleomagnetic drill was necessary for these samples due to the lack of fractures near the bottom of the pit.

Samples were repositioned in their original orientation and marked with horizontal lines in order to collect samples at a single depth interval. Samples were sawed at the marked lines using tile and trim saws in order to collect each sample at the appropriate depth. The larger pieces of the excess material were labeled in case more material was eventually needed. During trimming, adjustments to the actual sample location were made for practical reasons (size of saw

Figure 7.4: Copper Canyon sample showing a void in sample CCMM07 filled with well-defined quartz crystals. Crystal lengths range from 3-10mm.

blades) and the sample depth was recalculated. Final samples were typically 1.0-1.5 cm thick.

7.3.2 Sample density

In order to determine the cosmic-ray flux reaching each depth in the depth-profile, the profile density needs to be measured accurately. In this case, heterogeneous porosity is a possible cause for concern. There are significant pockets that contain cleanly-formed quartz crystals inside a void (Figure 7.4). Many of these voids were observed during trimming. If these voids are significant, the larger blocks should have a more representative density than the smaller pieces.

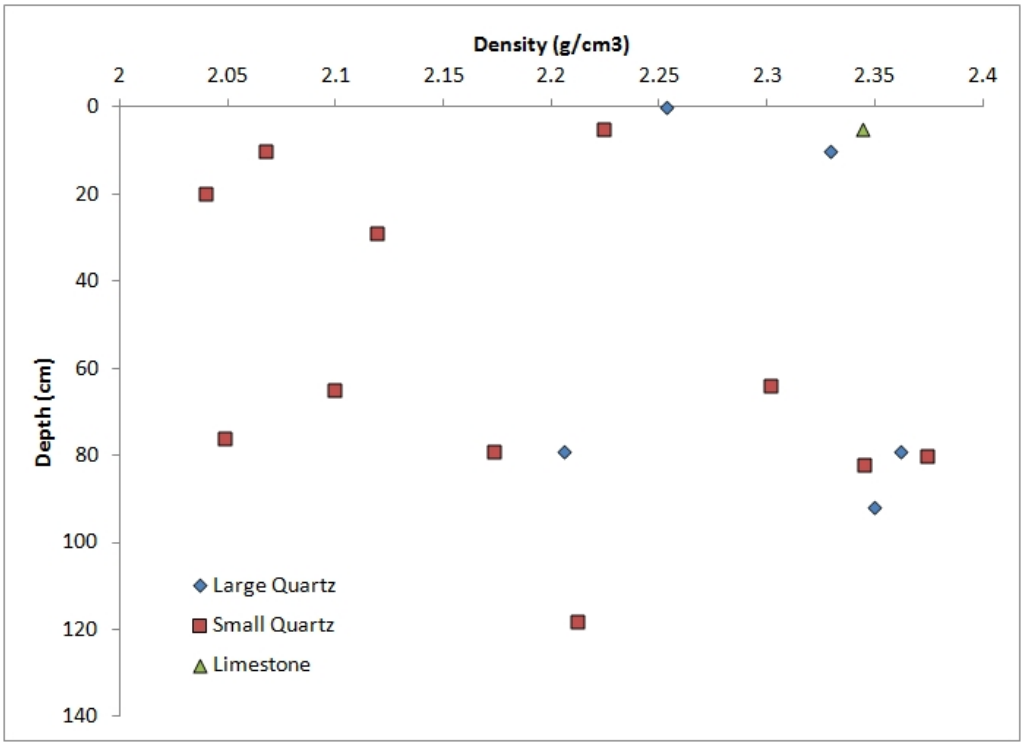

Figure 7.5: Density of Copper Canyon samples. The limestone sample is the host rock. Large pieces are arbitrarily defined as >900 g. See text for more details. Final density was based on the average of the large pieces.

The sample density was determined by sampling many pieces from different depths in the profile. The mass was measured for each sample and then any holes or voids were sealed with wax. The sample displacement volume was measured for the wax-coated samples. The mass for each sample was divided by its displacement volume and a density was calculated. These values were plotted against depth in Figure 7.5. There do not appear to be any trends with depth.

The sample densities ranged from 2.04 to 2.37 g/cm^3; however, the range is much smaller (2.20-2.35) if only large pieces are considered. The larger pieces are more likely to have a representative density than the smaller pieces due to the void spaces and the insignificant contribution of the wax to the density measurement due to the larger sizes of the samples. The results from the largest samples,

arbitrarily defined as >900 g for this experiment, were averaged to yield 2.30 g/cm^3. The significant density variations for the smaller samples indicate the likelihood of heterogeneous porosity in the profile. For this reason, the average of the large samples was applied to all samples in the profile.

7.3.3 Sample Crushing & Cleaning

The trimmed samples were crushed to a grain size of 250-1000 microns. For all samples with sufficient material, only the sample fraction between 500 and 1000 microns was used for the chlorine analyses. An initial cleaning, overnight leaching in 3% HNO_3, was used to clean the sample and remove any limestone. Prior to any treatment, a homogeneous aliquot of each sample was collected for XRF, along with a sample of the limestone host rock.

The quartz samples were etched for 2-3 cycles of 3-day etches in 1% HF, keeping the samples in an ultrasonic bath as frequently as possible. The sample purity was checked by ICP prior to dissolution for the first batch of samples. All remaining samples were etched for similar, or longer, periods of time and were not verified by ICP prior to dissolution. All sample compositions were verified by ICP prior to the final computation of results (see the methods Section 3.4 for details). Final samples were rinsed thoroughly with water and leached overnight in 3% HNO_3, followed by a brief ($\sim$15 minute) leach in 10% NaOH. The samples were rinsed until neutral and dried in the oven at low temperature.

7.3.4 Sample Dissolution

Preliminary samples collected at the Copper Canyon site prior to the official sampling trip indicated a chlorine content of $\sim$20-25 ppm. Based on this,

the decision to process the Copper Canyon samples using the traditional sample processing techniques, as discussed in Chapter 3, were used on the initial set of Copper Canyon samples. However, the results from these new samples showed considerably lower Cl concentrations than expected (<10ppm) and the results had relatively high uncertainties due to the relatively large blank subtractions and the type of spike added to the samples. Based on these results, other procedures for the remaining low-Cl Copper Canyon samples were developed in an attempt to obtain more accurate results from the AMS measurements.

We developed three different types of sample treatments, referred to as the normal, mixed, and no-spike procedures. The initial method was to treat the sample normally, using the traditional IDMS spiking procedure. The samples that were processed using this procedure had a ^{35}Cl spike with an A_0, defined as the atom ratio of ^{35}Cl to ^{36}Cl, of 0.9996 and HF acid, brand EM, was used to dissolve them. As a result of the lower-than-predicted chlorine concentrations in the samples, the "mixed" samples were processed using a ^{35}Cl spike with an atom ratio, A_0, of 0.9636 and HF, brand BDH, was used to dissolve them. The third group of samples were processed without any spike and were dissolved with HF acid, brand BDH, in order to test the ratios without the need for large corrections. Unfortunately, these samples were of necessity very large (>120 g) and still required a significant blank correction due to chloride in the HF.

7.3.5 Blank Subtraction

Due to the low natural chloride concentration in the samples (∼10 ppm Cl) and large amounts of acid required for dissolution, there is a significant blank correction for each sample. General blank correction procedures are discussed in

Section 3.7. Corrections were performed individually for total chloride as well as chlorine-36. The chlorine-36 blank subtraction was relatively small compared to the subtraction for total chloride. The initial and final values are shown in Table 7.2. In both cases, the uncertainty in the values was propagated using standard error uncertainty formulas (Bevington and Robinson, 1992). It was assumed that the covariance between uncertainties, discussed in Section 3.5, was not affected by the blank subtraction process.

The size of the total chloride blank was based on the blanks that were processed with a particular method and typically processed in the same batch as the samples. The two preparations used in the lab (normal and mixed blanks) had different total chloride blank subtractions. The "normal method blank" was prepared using a combination of the regular spike, HF, and a ^{36}Cl-dead salt (Week's Island Halite) and had a blank of 0.004 mg Cl/mL HF. The uncertainty on the blank amount was based on the variation between blanks and was determined to be approximately 50% of the mass of the blank itself.

The total chloride blank for the mixed spike method was determined by treating the HF blank as an IDMS sample and adding spike. Due to the low concentration of chlorine, the sample required a new Matlab code using Monte Carlo methods to determine the uncertainty in the blank. This Monte Carlo routine has replaced the original method for calculation of IDMS uncertainties. The blank concentration and uncertainty determined in this way were used directly as the blank value. This method resulted in a smaller blank of 0.00020 ± 0.00018 mg Cl/mL HF.

The value for the chlorine-36 blank was based on a sample that was processed using no halite blank, but was spiked with ^{35}Cl spike and had HF added.

SSample	Analytical Cl (ppm)	Analytical ^{36}Cl ($\times 10^4$ at/g)	HF (mL)	Blank Type	BC Cl (ppm)	BC ^{36}Cl ($\times 10^4$ at/g)	$\sigma_{36,total}$
CCMM10-04	25.9 $\pm$ 0.3	38.73 $\pm$ 0.98	100	REG	10.6 $\pm$ 7.6	36.40 $\pm$ 2.50	260000
CCMM10-05	12.2 $\pm$ 0.4	58.80 $\pm$ 2.30	146	MIXED	10.8 $\pm$ 1.4	53.90 $\pm$ 5.40	89000
CCMM10-06	27.5 $\pm$ 0.4	42.80 $\pm$ 1.60	117	REG	8.7 $\pm$ 9.4	40.40 $\pm$ 2.90	440000
CCMM10-07	10.3 $\pm$ 0.2	40.70 $\pm$ 1.30	191	MIXED	9.2 $\pm$ 1.1	37.70 $\pm$ 3.30	56000
CCMM10-09	27.3 $\pm$ 0.4	44.60 $\pm$ 1.30	108	REG	9.0 $\pm$ 9.2	42.10 $\pm$ 2.90	430000
CCMM10-10	14.5 $\pm$ 0.4	40.30 $\pm$ 1.80	203	MIXED	13.5 $\pm$ 1.1	37.70 $\pm$ 3.20	44000
CCMM10-11	13.3 $\pm$ 0.2	39.20 $\pm$ 1.20	197	MIXED	12.3 $\pm$ 1.0	36.70 $\pm$ 2.90	41000
CCMM10-12	31.1 $\pm$ 0.5	34.31 $\pm$ 0.92	233	REG	13.5 $\pm$ 8.8	33.20 $\pm$ 1.50	220000
CCMM10-14	8.9 $\pm$ 0.3	16.58 $\pm$ 0.73	192	MIXED	7.9 $\pm$ 1.0	13.90 $\pm$ 2.70	32000
CCMM10-15	23.8 $\pm$ 0.7	8.91 $\pm$ 0.38	296	REG	6.8 $\pm$ 8.5	8.05 $\pm$ 0.95	100000
CCMM10-17	14.6 $\pm$ 0.2	5.18 $\pm$ 0.27	300	MIXED	13.8 $\pm$ 0.8	3.80 $\pm$ 1.40	15000
CCMM10-18	4.9 $\pm$ 0.1	3.63 $\pm$ 0.23	303	MIXED	4.1 $\pm$ 0.9	2.10 $\pm$ 1.50	16000

Table 7.2: Analytical and blank-corrected (BC) ^{36}Cl and stable Cl values for Copper Canyon chlorine-36 samples. Blank type refers to the different preparation methods and blanks applied to the sample. 'REG' indicates the standard processing as discussed in the text; 'MIXED' indicates the processing technique that uses the The $\sigma_{36,total}$ represents the total uncertainty used in the final model in order to account for the uncertainty in the chlorine concentration (see text).

This was performed for each preparation method that involved spike. The chlorine-36 was assumed to be added on a "per sample" basis and to not be related to the amount of reagents added to the sample. This was confirmed by the lack of correlation between chlorine-36 (total atoms per blank sample) and the volume of reagents added to the blank (see the methods chapter, Chapter 3, for more detail).

The Matlab code used for the calibration of $P_f(0)$ only accounts for the uncertainties on the chlorine-36 concentration and does not account for uncertainties in other parameters, including the chloride concentration. This is reasonable if the uncertainties in the chlorine concentration are small; however, other modifications need to be made if there is significant uncertainty in the chlorine concentrations. For this reason, it was necessary to transfer any uncertainties in the chloride concentration to the uncertainties in the chlorine-36 concentration so that the total uncertainty in the fitted values remained correct and accounts for both uncertainties. This was done using Equations 7.1-7.4.

$$\sigma_{36} = \sqrt{(\sigma_{blank36})^2 + (\sigma_{sample36})^2} \tag{7.1}$$

$$\sigma_{Cl} = \sqrt{(\sigma_{blankCl})^2 + (\sigma_{sampleCl})^2} \tag{7.2}$$

$$\sigma_{36,equiv} = \frac{\sigma_{Cl}}{C_{Cl}} * N36 \tag{7.3}$$

$$\sigma_{36,total} = \sqrt{(\sigma_{36})^2 + (\sigma_{36,equiv})^2} \tag{7.4}$$

Where: σ_{36} is the uncertainty from the sample measurement uncertainty and from the blank subtraction. $\sigma_{blank36}$ is the ^{36}Cl blank subtraction uncertainty while $\sigma_{sample36}$ is the sample measurement uncertainty. σ_{Cl} represents the total uncertainty from Cl sources, specifically blank subtraction $\sigma_{blankCl}$ and the measurement uncertainty $\sigma_{sampleCl}$. $\sigma_{36,equiv}$ is the new uncertainty on chlorine-36 concentration from the transfer from chloride uncertainty. C_{Cl} is the concentration of chlorine in the sample and N36 is the measured concentration of chlorine-36 in the sample. Finally, $\sigma_{36,total}$ is the total chlorine-36 uncertainty that combines all sources of uncertainty from the chlorine and chlorine-36.

7.3.6 Copper Canyon Characterization

The chlorine-36 measurements required specific information on the properties of the samples, including composition and density. The characterization of the samples and site were performed using various techniques. All the results are summarized in this section.

The target elements of all the samples were measured using ICP-OES on small aliquots of the final samples, as completely prepared for dissolution. The results from the measurements showed very low levels of all the major target elements for chlorine-36 production (Ca, K, Fe, Ti). J. Stone (pers. comm., June 29, 2010) ICP measurements in similarly cleaned aliquots confirm these low concentrations. It is clear that the target element levels in the samples are sufficiently low that spallation from Ca or K is not significant compared to production from the low-energy pathway. The actual measured concentrations are shown in Table 7.3.

Sample	K_2O $\times 10^{-4}$ wt %	CaO $\times 10^{-4}$ wt %	TiO_2 $\times 10^{-5}$ wt %	Fe_2O_3 $\times 10^{-4}$wt %
CCMM4	6	7	8	16
CCMM5	15	19	14	27
CCMM6	4	6	5	9
CCMM7	15	23	14	29
CCMM9	4	9	10	6
CCMM10	11	33	18	22
CCMM11	4	18	5	8
CCMM12	4	19	7	14
CCMM14	5	23	13	44
CCMM15	18	20	20	47
CCMM17	7	7	18	27
CCMM18	23	17	29	75

Table 7.3: Target elements for the NMT chlorine samples as measured using ICP-OES at the New Mexico Bureau of Geology chemistry lab.

The major and trace element compositions of each sample layer, as well as the limestone host rock, was determined using XRF with an ICP-OES finish. Additional samples were also analyzed in order to look at the widest range of possible heterogeneities in the samples. The complete target, bulk-rock, and trace element compositions for the samples can be found in Tables 7.4, 7.5, and 7.6, respectively. In general, the major element compositions are consistent throughout the profile. There is one sample that shows some variability in the trace element composition, but it appears to be isolated and could not be recreated when additional aliquots were sent for analysis. These outliers are indicated by asterisks (*) in the tables. Other than the obvious difference in major element concentration due to the lithology, the main difference between the limestone wall rock and the quartz vein rock is the slightly higher concentrations of Sm, Gd, and U in the host limestone as compared to the vein quartz. There is also significantly less Cr and Li in the host limestone as compared to the vein quartz. There does not appear to be significant differences among any of the samples sent specifically to test

for heterogeneity (labeled as METAL, POROUS, DARK, or NORMAL in order to discuss the particular heterogeneity being sampled).

The behavior of thermal neutrons depends on the chemistry of the rock and is measured by two main compositional analyses: bulk rock XRF and trace element ICP. Due to the unique situation of the Copper Canyon quartz vein, there are several possible scenarios. Two endmember scenarios and one intermediate scenario were used to determine the variability in the $P_f(0)$ parameter due to the composition of the surrounding bulk rock. The two endmember scenarios (shown in Figure 7.6) are a) the quartz vein is small enough to be considered infinitely thin in terms of neutron transport properties and b) the quartz vein is large enough that only the quartz affects the neutron transport properties. Somewhere in between these two endmember scenarios is the more realistic scenario containing an irregularly shaped quartz vein (labeled (c)). The neutron transport properties are likely to be somewhere between the two endmember scenarios. The quartz vein is typically $\sim$1 m, so the quartz composition was used in the final analysis and discussion.

7.4 Copper Canyon Calibration Results

The calibration of the $P_f(0)$ parameter from the two nuclide profiles is a two-step process. First, the beryllium-10 profile is used to fit an attenuation length and an erosion rate for the site. These parameters and then fixed for the chlorine-36 profile and only the $P_f(0)$ parameter is calibrated. This reliance on beryllium-10 does link the $P_f(0)$ parameter to the beryllium-10 production rate. This is a possible issue because there is still some uncertainty on the beryllium-10 production rate. However, beryllium-10 has the best-known production rate

Sample	Ca wt%	Fe wt%	K wt%	Ti wt%
CCMM04	<0.1	0.35	0.2	<0.01
CCMM05	<0.1	0.35	0.2	<0.01
CCMM06	<0.1	0.53	0.2	<0.01
CCMM07 normal	<0.1	0.2	0.2	<0.01
CCMM09	0.1	0.31	0.2	<0.01
CCMM10 normal	<0.1	0.21	0.1	<0.01
CCMM10 metal	0.1	0.43	<0.1	<0.01
CCMM11	<0.1	0.06	<0.1	0.01
CCMM12 normal	0.1	0.23	0.2	<0.01
CMM12 porous	0.2	0.26	<0.1	<0.01
CCMM13 normal	<0.1	0.25	<0.1	<0.01
CCMM13 dark	<0.1	0.27	<0.1	<0.01
CCMM15	0.4	0.23	0.2	0.01
CCMM17	<0.1	0.95	0.1	<0.01
DUP-CCMM17	<0.1	0.97	0.1	<0.01
CCMMWall2	>35	0.3	0.2	0.01

Table 7.4: Table showing bulk rock concentrations for target elements as determined using XRF, as measured for bulk samples specifically chosen to represent all possible variability. Samples listed with DUP were duplicates of the same aliquot at the analyzing lab. Samples listed twice (CCMMWall and CCMMWall2) are separate aliquots sent to be analyzed at different times. Other sample labels indicate types of samples used to look at heterogeneities in the samples and are as follows: NORMAL - appears to be pure quartz; METAL - visible amounts of some sort of shiny material; POROUS - area of extra porosity and maybe different material; DARK - material looks dirty.

Sample	SiO_2 wt %	TiO_2 wt %	Al_2O_3 wt %	Fe_2O_3 wt %	MnO wt %	MgO wt %	CaO wt %	Na_2O wt %	K_2O wt %	P_2O_5 wt %	LOI wt %
CCMM05	98.1	<0.01	0.89	0.5	0.01	0.09	0.04	<0.01	0.23	<0.01	0.47
CCMM07	98.14	0.02	1.16	0.19	0.01	0.07	0.14	0	0.21	0.01	0.03
CCMM10 normal	98.3	0.01	0.72	0.32	0.04	0.07	0.07	<0.01	0.14	0.01	0.34
CCMM10 metal	97.8	<0.01	0.59	0.67	0.02	0.07	0.15	<0.01	0.1	0.05	0.5
CCMM12 normal	97.7	0.01	0.84	0.31	0.03	0.09	0.13	<0.01	0.18	0.05	0.31
CMM12 porous	98.1	<0.01	0.16	0.39	0.11	0.06	0.26	<0.01	0.04	0.01	0.47
CCMM13 normal	98.1	<0.01	0.56	0.37	0.01	0.07	0.11	<0.01	0.1	0.03	0.34
CCMM13 dark	98.6	<0.01	0.3	0.39	0.03	0.05	0.05	<0.01	0.03	<0.01	0.16
CCMMWall	4.42	0.05	0.82	0.48	0.42	0.44	56.11	0	0.31	0.06	36.87
CCMMWall2	4.94	0.03	0.68	0.47	0.42	0.41	51.3	<0.01	0.22	0.04	40.3

Table 7.5: Major elements for Copper Canyon, as determined by XRF analysis. Samples listed with DUP were duplicates of the same aliquot at the analyzing lab. Samples listed twice (CCMMWall and CCMMWall2) are separate aliquots sent to be analyzed at different times. Other sample labels indicate types of samples used to look at heterogeneities in the samples and are as follows: NORMAL - appears to be pure quartz; METAL - visible amounts of some sort of shiny material; POROUS - area of extra porosity and maybe different material; DARK - material looks dirty. LOI - Loss on ignition.

Sample	B ppm	Sm ppm	Gd ppm	U ppm	Th ppm	Cr ppm	Li ppm
CCMM04	20	0.4	0.56	0.5	0.6	150	40
CCMM05	10	0.2	0.3	0.14	0.2	140	40
CCMM06	20	0.3	0.38	0.41	0.5	180	40
CCMM07	-	31.25*	88.14*	287.0*	192.0*	220	-
CCMM07 normal	10	0.4	0.44	0.35	0.6	170	50
CCMM09	20	1.9	2.89	0.71	1	300	50
CCMM10 normal	20	0.7	0.96	0.22	0.4	130	50
CCMM10 metal	20	0.9	1.55	0.36	0.2	150	40
CCMM11	10	0.5	0.78	0.45	0.9	<10	40
CCMM12 normal	20	1.1	1.52	0.44	0.5	210	50
CMM12 porous	10	0.6	0.81	0.11	<0.1	250	<10
CCMM13 normal	20	0.9	1.61	0.32	0.2	230	40
CCMM13 dark	20	0.2	0.24	<0.05	<0.1	260	30
CCMM15	10	2	2.54	0.57	0.7	170	50
CCMM17	10	0.4	0.45	0.26	0.4	330	40
DUP-CCMM17	20	0.4	0.47	0.24	0.3	320	40
CCMMWall	10	1.75	2.06	0.9	0.6	10	-
CCMMWall2	<10	2	2.68	0.48	0.4	20	<10

Table 7.6: Table showing trace element concentrations for NMT Copper Canyon samples as measured using ICP-OES at SGS Labs. Samples listed with DUP were duplicates of the same aliquot at the analyzing lab. Samples listed twice (CCMMWall and CCMMWall2) are separate aliquots sent to be analyzed at different times. Other sample labels indicate types of samples used to look at heterogeneities in the samples and are as follows: NORMAL - appears to be pure quartz; METAL - visible amounts of some sort of shiny material; POROUS - area of extra porosity and maybe different material; DARK - material looks dirty.

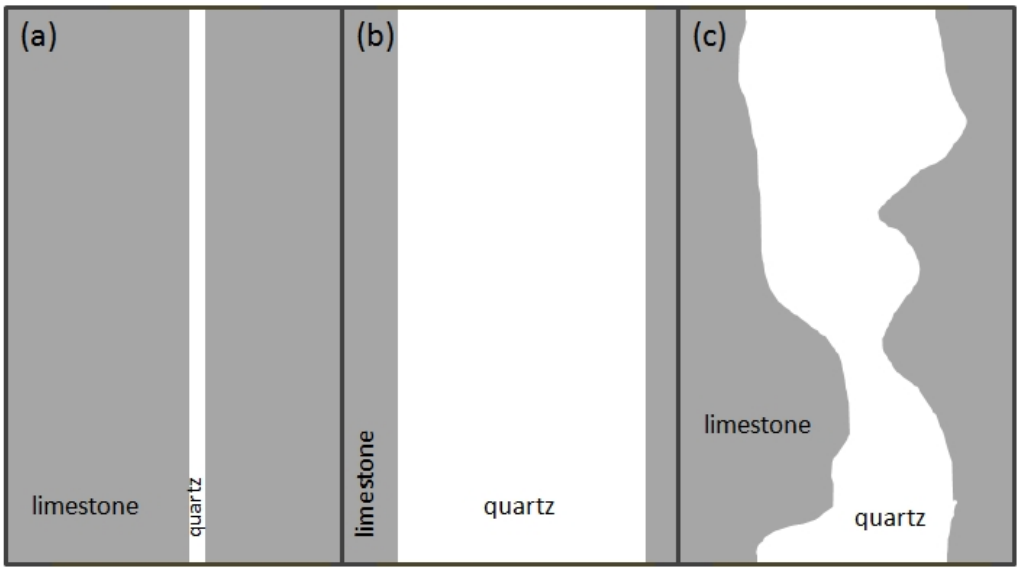

Figure 7.6: Figure showing the hypothetical end members for quartz vein geometry. (a) Theoretical vein geometry with a very thin vein, indicating that the bulk rock is best represented by limestone; (b) Theoretical vein geometry with a large vein thickness, indicating that bulk rock is best represented by quartz; (c) An irregular vein geometry, indicating that the neutron transport properties will likely be in between the two endmembers.

of any of the cosmogenic nuclides and the uncertainty on that parameter is far smaller than the uncertainty in the $P_f(0)$ parameter and so this is an acceptable link between the production rates.

The beryllium-10 profile was fitted using chi-squared minimization to find the attenuation length and the erosion rate at the site. The beryllium-10 profile is internally consistent and yields an attenuation length of 140 $\pm$ 3 g/cm^2 and an erosion rate of 1.34 $\pm$ 0.04 g/cm^2/kyr ($\sim$5.7 mm/kyr). The best-fit attenuation length and erosion rate were used to predict the beryllium profile, as shown in Figure 7.7. Additional profiles using higher and lower erosion rates are also plotted on the figure for comparison.

A similar chi-squared minimization was performed for the chlorine-36 profile, using the ^{10}Be-determined attenuation length and erosion rate as fixed

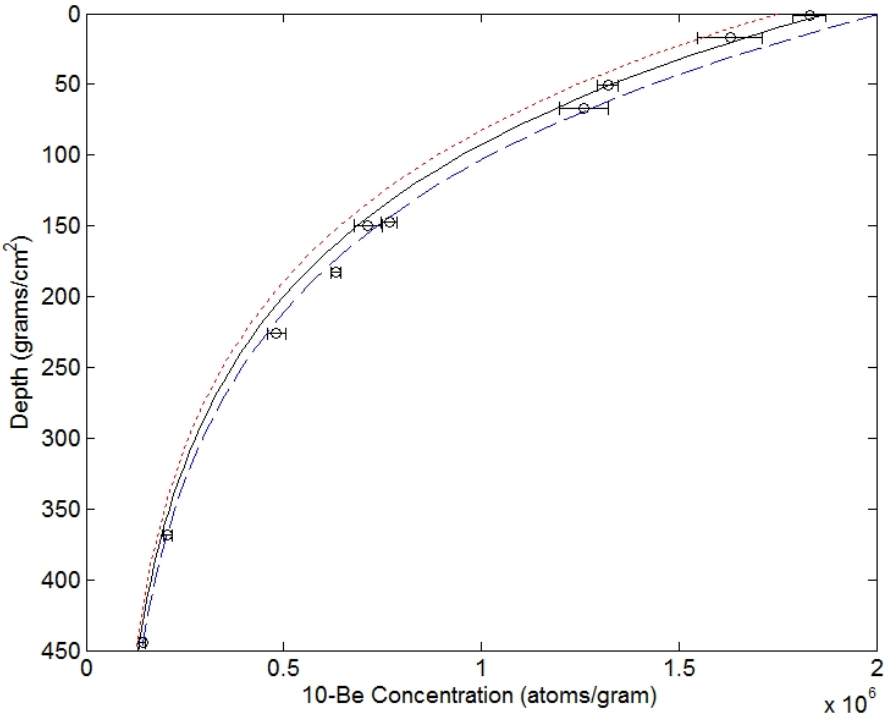

Figure 7.7: The predicted versus measured beryllium-10 concentrations for the Copper Canyon profile. Open circles indicate sample measurements and uncertainty. Lines indicate the values predicted by the model, with the best-fit erosion rate (1.34 g/cm^2) shown by the solid line, the high erosion rate (1.44 g/cm^2, found by taking the best-fit +3*uncert) is shown by a red dotted line, and the low erosion rate (1.18 g/cm^2, found by taking the best-fit - 3*uncert) is shown by the blue dashed line.

parameters. The chlorine-36 profile yields a $P_f(0)$ value of 679 $\pm$ 54 fast neutrons (g air)$^{-1}$yr^{-1} (this unit will be abbreviated as n g^{-1}yr^{-1} for the remainder of this chapter). This value is consistent with other calibrations of $P_f(0)$.

The p-value of 0.0015, based on a chi-squared of 30.2 for 12 samples, indicates that the fit to the chlorine data is not statistically adequate, although visual inspection indicates that the value and uncertainty seem reasonable based on the data. Figure 7.8 shows the predicted concentrations for two values of $P_f(0)$ (the Copper Canyon fitted parameter and another value discussed in the calibration

chapter, Chapter 8) plotted against the measured concentrations.

Another way to visualize the calibration results is a normalized profile, shown in Figure 7.9, which accounts for the varying composition of the samples in the profile. The variability in the production rates due to composition differences between samples were eliminated by normalizing the measured concentrations. This was done by dividing the measured sample concentrations were normalized by a factor based on the predicted production of the actual composition of a particular sample in the profile compared to the production predicted for an average composition. The average composition is found simply by taking the average of all the samples in the profile. This removes the variability due to different concentrations of target elements, trace elements, and bulk elements so that all the points can be compared against a single profile. The predicted profiles for the average composition for various values of $P_f(0)$ are plotted on the normalized plot. It is clear that a range of values between 600-800 n $g^{-1}yr^{-1}$ are consistent with the Copper Canyon data.

In order to assess the possible sources of uncertainty from assumptions made for this profile, a sensitivity analysis was performed for the bulk-rock composition, the water content, the hillslope angle, and possible outliers in the profile. The bulk-rock composition and water content of the profile could both affect the calculation of the low-energy neutron flux, thus influencing the calibrated value of $P_f(0)$.

The two endmember compositions discussed earlier, quartz and limestone, and a 'mixed' composition were each used to calibrate a value for $P_f(0)$. The change in composition to limestone results in a $P_f(0)$ value of 806 ± 68 n $g^{-1}yr^{-1}$, which is a 19% change from the quartz profile value. However, the 'mixed' composition (limestone bulk rock with the quartz trace elements) produces a $P_f(0)$

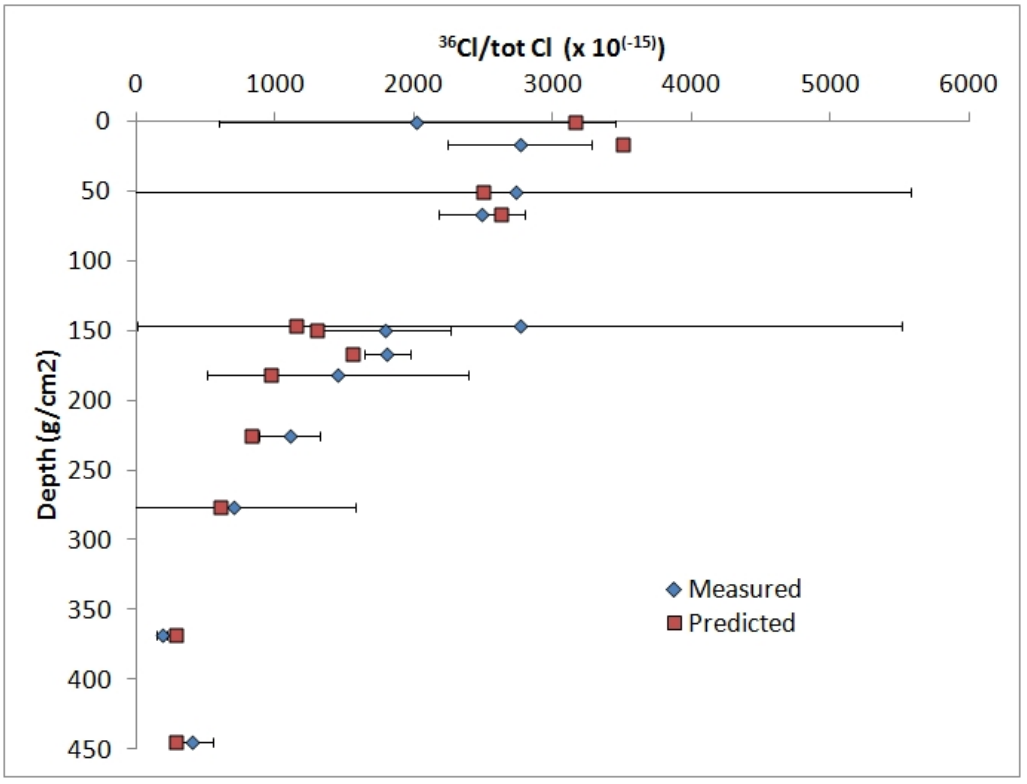

Figure 7.8: The predicted and measured ratios for the chlorine-36 Copper Canyon depth profile. Uncertainties are shown on the measured ratios.

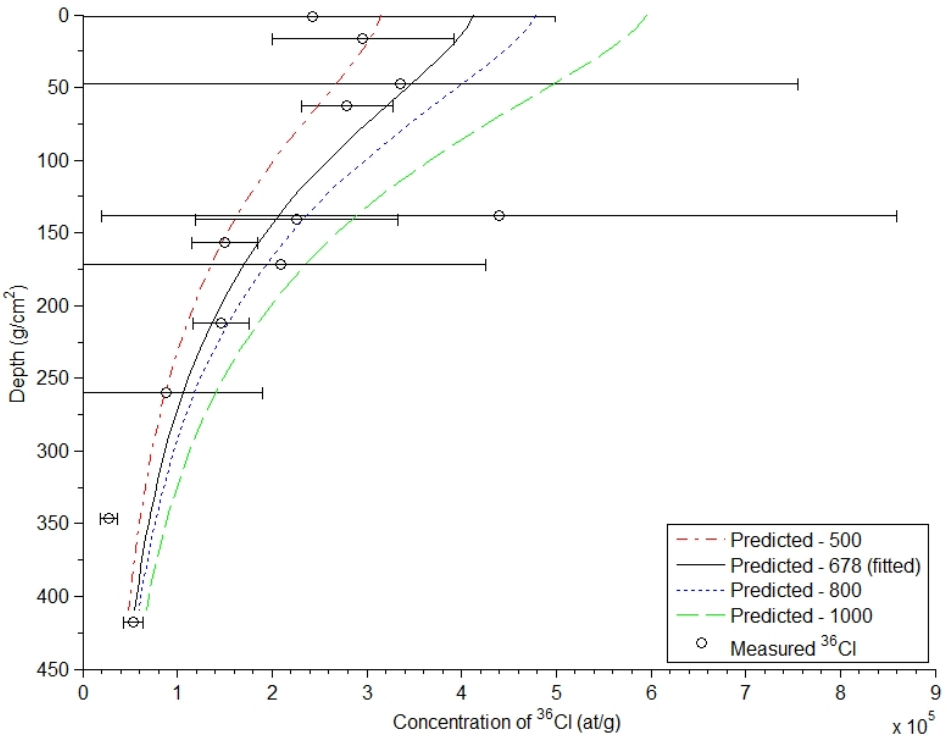

Figure 7.9: Normalized measured concentrations (open symbols with error bars) plotted against depth. Predicted profiles for several values of $P_f(0)$ are also plotted, including the fitted value based on the measurements. Units for $P_f(0)$ are fast n (g air)$^{-1}$ yr^{-1}.

value of 1016 $\pm$ 77 n $g^{-1}yr^{-1}$, which is a 50% increase. It is clear that the resulting $P_f(0)$ parameter is sensitive to bulk-rock composition.

In order to test the effect of a higher water content on the profile, it was run with a 5% water content instead of the original value of 0.5 vol % water. This resulted in a value of 893 n $g^{-1}yr^{-1}$, a 23% increase in the calibrated $P_f(0)$ parameter as compared to the 0% water content scenario, that provided a value of 726 n $g^{-1}yr^{-1}$, and 32% larger than the value with 0.5% water content. Water content could have a significant effect on the calibrated value of $P_f(0)$.

Although the slope was measured, the terrain roughness (vegetation and rocks) made it difficult to accurately determine the slope angle to better than 5°. The perpendicular depths of the samples were recalculated for hillslopes of 25° and 35° and the entire fitting procedure was performed again. The beryllium attenuation lengths and erosion rates were refit and then the chlorine $P_f(0)$ parameter was calibrated. For the 25° and 35° hillslopes, the results vary less than 0.3% so this does not affect the calibrated value of $P_f(0)$ significantly.

A large portion of the calibration is pinned on the values of the bottom two samples. The points are not in agreement with one another, but there is no indication from the laboratory processing or geologic notes to warrant removal of either point. As a sensitivity analysis, each point was removed and the profile was recalibrated with only the 11 remaining points and assuming the quartz composition. Removing point CCMM18 does essentially nothing and gives a value of 676 $\pm$ 54 n $g^{-1}yr^{-1}$; however, removing sample CCMM17 gives a significantly higher value of 800 $\pm$ 59 n $g^{-1}yr^{-1}$. This uncertainty is on the same order of magnitude as the effect of the change in water discussed above.

Based on the uncertainties at this site, primarily the issues of the bulk composition, water content, and blank subtractions, it was downgraded from a primary calibration site to a secondary site. The large blank subtractions necessary on many of the samples leads to uncertainties that are difficult to quantify in the resulting ^{36}Cl concentration values. Instead of being used to determine the value of $P_f(0)$ in the main calibration, the values of $P_f(0)$ determined using other methods (see Chapter 8) will be compared to these results from Copper Canyon.

7.5 Copper Canyon Conclusions

The Copper Canyon site, which had many complicating factors that did not appear until later in the study, produced a $P_f(0)$ value of 678 ± 54 n g^{-1}yr^{-1}. Uncertainties due to blank subtractions, water content, varying composition, and inconsistent data points contributed to the decision to classify this site as a secondary site. Sensitivity studies based on the factors listed above produce values of $P_f(0)$ that vary by up to 50% compared to the nominal value of 678 n g^{-1}yr^{-1}. The nominal value is consistent with the value of $P_f(0)$ calibrated as part of the CRONUS-Earth study discussed in Chapter 8.

CHAPTER 8

CHLORINE-36 CALIBRATION

8.1 Abstract

Chlorine-36 is a versatile cosmogenic nuclide, but has been plagued by conflicting production rates from different geological calibration studies (Phillips et al., 2001; Swanson and Caffee, 2001; Evans et al., 1997; Stone et al., 1996). The CRONUS-Earth Project is designed to improve upon the general knowledge of cosmogenic systematics and to provide the cosmogenic user community with a uniform platform for use and interpretation of all cosmogenic nuclides.

The CRONUS-Earth Project has provided high-quality geological calibration sites, including Lake Bonneville, Peru, and Scotland, for a large-scale calibration of chlorine-36. Three primary sites were used to calibrate the spallation pathways (K and Ca) for chlorine-36 production yielding production rates of 56.0 $\pm$ 2.2 at ^{36}Cl (g Ca)$^{-1}$yr^{-1} for Ca spallation, 157 $\pm$ 6 at ^{36}Cl(g CK)$^{-1}$yr^{-1} for potassium spallation. The third major production rate parameter for the low-energy production pathway, $P_f(0)$, was calibrated separately using CRONUS-Earth data from the Bonneville and Baboon Lakes sites and yielded a value of 704 $\pm$ 141 neutrons (g air)$^{-1}$yr^{-1}. There was significant uncertainty associated with the third pathway due to the presence of site-to-site variability and possible factors to explain this are discussed in detail.

The resampling of the Puget Lowlands site allowed for the analysis of samples comparable to Swanson and Caffee (2001). The new analyses, performed by two different labs, are consistent with the calibrated production rates produced in this study and are therefore not consistent with the previously published rates in Swanson and Caffee (2001). The most likely source for this discrepancy is a systematic analytical problem with the original samples. The maximum discrepancy for the previously published chlorine-36 calibration studies is reduced from 40% to 27% if Swanson and Caffee (2001) is excluded.

The chlorine-36 calibration uses the CRONUScalc program (see Chapter 2, an open-source multi-nuclide Matlab program that helps with the interpretation of cosmogenic nuclide results, to produce the results. Muon production rate parameters consistent with the code were recalculated from published profiles for both Ca and K. The minimum uncertainty on the chlorine-36 technique was assessed independently for the spallation and $P_f(0)$ calibrations using a secondary dataset with independent ages. The goodness of fit for the primary calibration is reported as well. The uncertainty associated with the chlorine-36 technique is assessed using a combination of analytical uncertainty and the scatter in the secondary dataset when the dataset is aged using the final parameters.

8.2 Introduction

In-situ terrestrially produced cosmogenic nuclides are commonplace tools in an increasing number of scientific fields, indicating the need for continued improvement of the technique. Despite the widespread use of cosmogenic nuclides, the results are applied and interpreted using a large number of different methods that may implement very different production rates, lab methods, and scal-

ing methods among others. The NSF-funded CRONUS-Earth (Cosmic-Ray prOduced NUclide Systematics on Earth) Project is designed to improve the general knowledge of cosmogenic nuclide systematics and to provide the cosmogenic user community with a uniform platform for use and interpretation of all cosmogenic nuclides. The consistent interpretation is facilitated by the production of CRONUScalc, an open-source multi-nuclide Matlab program that helps with the interpretation of cosmogenic nuclide results. A large part of the CRONUS-Earth Project is the calibration of cosmogenic nuclide production rates using geological calibration locations. This paper discusses the results from the chlorine-36 production rate calibration project.

Chlorine-36 is unique among the cosmogenic nuclides because of its versatility. The use of chlorine-36 is not limited to a specific lithology and can be used on limestone, which is impossible to date reliably using other cosmogenic isotopes. The applicable age range of chlorine-36 is between $\sim$5 ka and 500 ka, providing dating opportunities for landforms that are too old for carbon-14 and too young for argon dating. However, the reason that chlorine-36 is versatile is due to the complex production pathways, specifically production of chlorine-36 from three main target elements (K, Ca, and Cl) and the different types of reactions (high energy neutrons, low-energy neutrons, and muons). The complexity of the production contributes to the lack of consensus on the production rate parameters for chlorine-36.

Published production rates for the three main chlorine-36 production pathways are in some cases in poor agreement, with the most extreme cases differing by more than 40%. Previous chlorine-36 production rate studies and their published results are shown in Table 8.1. The geological calibration studies that produced the discrepant rates have been limited in geographical scope, sometimes

Source	Location	Landform	h	Lat	Age	Meth.	$P_{m,k}$
Phillips et al. (2001)	Utah	Basalt Flow	1445	39°N	16.5	WR	Ca: 66.8 ± 6.8
	Idaho	Basalt flow	1367-1798	44°N	2.1-13.7		
	New Mexico	Basalt flow	2058-2578	35°N	3-18.2		K: 137 ± 60
	Wales	Boulder on beach	375	52 °N	11.8		
	Ellesmere Island	Glacial erratic boulder	80-100	80°N	9		$P_f(0)$: 626 ± 43
	Northwest Territories	Glacial polished bedrock	20	68°N	14.8		
	Arizona	Meteor Crater ejecta	1730	35°N	49		
Evans et al. (1997)	Sierra Nevada	Glacial bedrock	3000-3600	38°N	13.1	MS	K: 170 ± 25
	Scotland	Glacial bedrock	520	58°N	11.6		
	Antarctica	Bedrock	2000-2200	70°S	SS		K: 241 ± 9
Stone et al. (1996)	Utah	Basalt flow	1445	39 °N	17.3	MS	Ca: 48.8 ± 4.8
Evans (2001)	Scotland	Glacial bedrock	520	58 °N	11.6	MS	$P_f(0)$: 740 ± 63
Swanson and Caffee (2001)	WA state	Moraine boulders and glacial bedrock	10-140	48°N	15.5	WR	Ca: *91 ± 5; K: *228 ± 18; $P_f(0)$: 762 ± 28
Licciardi et al. (2008)	Iceland	Basalt flow	30-500	64 °N	4-10	WR	Ca: 57 ± 5
Schimmelpfennig (2009)	Sicily	Basalt flow	2000	38°N	10	MS	Ca: 50 ± 4
	Argentina	Basalt flow	2300-2500	36 °S	15		K: 142 ± 13

Table 8.1: Summary of previous chlorine-36 calibration studies. h indicates the elevation in meters. Method is the method used to prepare the samples: WR indicates whole rock samples and MS indicates mineral separates. $P_{m,k}$ is the production rate for nuclide m from target k as calibrated from the study (as published). All studies shown here used Lal (1991) scaling. *Indicates that the production rate includes muons. Units for Ca are atoms (g Ca)$^{-1}$ yr^{-1}, K are atoms (g K)$^{-1}$ yr^{-1}, and $P_f(0)$ are fast neutrons (g air)$^{-1}$ yr^{-1}.

focusing on only one location, and they have rarely included large numbers of samples from a wide variety of latitudes and elevations worldwide. The authors of the production rate studies have also attributed the discrepancies between the chlorine-36 production rates to many factors including mineralogy/composition (Evans, 2001), scaling (Swanson and Caffee, 2001), independent age constraints (Gosse and Phillips, 2001; Swanson and Caffee, 2001), preparation methods (Gosse and Phillips, 2001; Schimmelpfennig et al., 2009), differences in partitioning chlorine-36 between pathways (Licciardi et al., 2008; Schimmelpfennig et al., 2009), new technological methods (Marrero, 2009), among others. Despite the numerous possibilities for the source of the discrepancies, there is currently no consensus on the underlying cause(s).

8.2.1 Calibration Description/Summary

This production rate calibration study corrects some of the problems in previous studies and ultimately produces chlorine-36 production rate parameters for the three main production pathways (spallation of Ca, spallation of K, and thermal neutron absorption). This study focuses on three primary sites and a secondary site (Scotland, Peru, and Bonneville as primary; Baboon Lakes as secondary) that cover a wide range of elevations (300-4500 m) and latitudes (13-57°N or S). The sites cover a variety of compositions, providing production rates for all three main production pathways. Two previously published depth profiles are also reanalyzed here to provide calibrated muon production parameters consistent with the model used in this study. A secondary dataset composed of sites not used in the main calibration but possessing independent ages is used to assess the calibrated parameters and provide a realistic uncertainty estimate for

the chlorine-36 technique. For the first time in a multi-site chlorine-36 calibration, the goodness of fit is reported quantitatively along with a physical estimate of uncertainty. The final production rates are used in CRONUScalc in order to distribute the results in an easy-to-use format.

8.3 Background

8.3.1 Chlorine-36 Systematics

Cosmic-ray interactions with minerals at the earth's surface produce *in-situ* cosmogenic nuclides. These surfaces can be dated and used to investigate processes in the natural world, assuming the production rates of the nuclides are known. The production of cosmogenic nuclides is dependent on the sample position in space (i.e., dip and direction of dip of the sample) and the original incoming cosmic-ray flux, which varies as a function of geographic position and time (Nishiizumi et al., 1989; Gosse and Phillips, 2001). The production also typically decreases with increasing depth in the sample material due to attenuation of the cosmic-ray flux through interactions with matter. These interactions of cosmic rays with matter produce cosmogenic nuclides through three types of reactions: spallation, low-energy neutrons, and muons.

Spallation is generally the most common type of reaction and all of the common cosmogenic nuclides (^{26}Al, ^{10}Be, ^{36}Cl, ^{14}C, ^{3}He, ^{21}Ne) are produced in large part through this pathway. For the production of cosmogenic nuclides, spallation can be defined as the interaction of a high-energy neutron with a nucleus that eject protons and nuclides to produce a lighter nucleus. The production of cosmogenic nuclides by this process is defined in Equation 8.1. Element k is the

target element (i.e., Ca for the production of ^{36}Cl) and m represents the resulting cosmogenic nuclide. The production of the cosmogenic nuclide for the high-energy reactions decreases exponentially with depth to $\sim$ 2 m. The $P_{\mathrm{m,k}}$ parameter is the production rate parameter and is calibrated independently for each nuclide using data from geological calibration sites. This calibration is discussed further in Section 8.7.2.

$$P_{\mathrm{s,m}}(Z) = S_T \sum S_{el,s} P_{\mathrm{m,k}}(0) C_{\mathrm{k}} \exp\left(-\frac{Z}{\Lambda_{\mathrm{f,e}}}\right) \tag{8.1}$$

Where $P_{\mathrm{m,k}}$ is the production rate of species m by spallation of element k; S_T is the topographical shielding factor; $S_{el,s}$ is the scaling factor for spallation reactions for the particular reaction of interest; C_{k} is the concentration of the target element k; and $\Lambda_{\mathrm{f,e}}$ is the effective attenuation length for fast neutrons. The production is summed for all target elements k that produce nuclide m to give the total spallation production rate.

Spallation reactions that produce chlorine-36 are primarily from the target elements of calcium (Ca) and potassium (K), although spallation also occurs on titanium (Ti) and iron (Fe). In this study, only the spallation production rates for Ca and K will be calibrated. Nominal values for spallation production from iron (1.9 at ^{36}Cl (g Fe)$^{-1}$ yr^{-1}) (Stone, 2005) and titanium (3.8 at ^{36}Cl (g Ti)$^{-1}$ yr^{-1}) based on scaling the geological calibration of Stone (2005) according to the relative amounts predicted by the model of Masarik (2002) are used. The combined contributions from Ti and Fe are typically less than 1-2%.

Thermal and epithermal neutrons (grouped here as low-energy neutrons) can be absorbed by ^{35}Cl to produce chlorine-36. This pathway is complicated by

the sensitivity of the incoming low-energy neutron flux to water and composition of the sample. These reactions are discussed in detail in Sections 2.36 and 2.39. Equation 8.2 shows the simplified production equation. This equation is generalized in order to apply to both thermal or epithermal neutrons.

$$P_{\mathrm{e,m}}(Z) = \frac{f_{\mathrm{e}}}{\Lambda_{\mathrm{e,ss}}} * \Phi_{\mathrm{e,ss,total}} \tag{8.2}$$

Where e indicates the energy level of the parameter (either thermal or epithermal), $\Phi_{\mathrm{e,ss,total}}$ is the epithermal or thermal neutron flux in the subsurface; f_{e} is the fraction of absorbed neutrons of energy e that are taken up by the target element to produce chlorine-36; $\Lambda_{\mathrm{e,ss}}$ is the effective attenuation length for neutrons of energy e. The neutron flux accounts for the diffusion of neutrons at the atmosphere/subsurface interface as well as low-energy neutrons produced as a product of muon absorption reactions. The details of the low-energy production pathways are discussed in Chapter 2, Sections 2.4.2, 2.4.3, and 2.4.4.

The parameter that is fitted for the low-energy reactions is called $P_f(0)$. This parameter, defined as the fast neutron flux in the atmosphere directly above the atmosphere/subsurface interface with units of neutrons (g air)$^{-1}$ yr^{-1}, is what ultimately quantifies the low-energy neutron flux. As the fast neutron flux is moderated by the nuclear interactions with the atoms comprising the sample, it transitions into the epithermal and thermal neutron fluxes, which depend on the composition of the rock. $P_f(0)$ is chosen as the calibration parameter specifically because it is not composition dependent. The calibration of this parameter is discussed in Section 8.7.3.

Although production of cosmogenic nuclides by muons is not typically large at the surface, it can be significant for younger surfaces, high erosion areas,

or in determining inheritance. Muons, which are leptons with a mass approximately 200 times that of an electron, penetrate very deeply into the subsurface, as shown by their very large attenuation length ($\sim$1300 g/cm^2)(Heisinger et al., 2002b). The inclusion of the ability to date single samples of any depth and depth-profile calculators in CRONUScalc has increased the necessity for accurate muon models. In the CRONUScalc code, muon production is calculated using production equations from Heisinger et al. (2002b,a) and scaled according to Lifton (2012). The production rate from fast muons is shown in Equation 8.3.

$$P_{\mu,fast} = \phi_{\mu,total}\beta(Z)(\bar{E}(Z))^{\alpha}\sigma_0 \mathrm{N}_{t,i} \tag{8.3}$$

Where β and $\bar{E}$ are depth-dependent constants described in Heisinger et al. (2002b). $\mathrm{N}_{t,i}$ is the concentration of the target element in atoms g^{-1} and $\phi_{\mu,total}$ is the total muon flux in units of muons cm^{-2} yr^{-1}. The parameter, σ_0, is the cross-section in 10^{-24}cm^2 at 1 GeV. σ_{190}, the cross-section at an energy of 190 GeV, was used to calculate the initial σ_0 values based on Equation 8.4 (Equation 13 in Heisinger et al. (2002b)). In Heisinger et al. (2002b), values for σ_{190} are given for all the common terrestrial cosmogenic nuclides except potassium. The σ_0 parameter is the calibrated parameter in the muon model and is discussed in Section 8.7.1.

$$\sigma(E) = \sigma_0 E^{\alpha} \tag{8.4}$$

Where E is the muon energy in GeV and the exponent (α is listed as 0.75 in Heisinger et al. (2002b), although an exponent of 1 was chosen by the CRONUS-Earth group (details in Section 2.4.4).

Slow muons are produced according to Equation 8.5 (Heisinger et al., 2002a). In this equation, $\phi_{\mu-}$ is the negative muon flux in units of stopped muons g^{-1}

yr^{-1}, $f_{i,C}$ is the compound factor, and $f_{i,D}$ is the probability that the negative muon does not decay in the K-shell before it is captured by the nucleus. The parameter, f_i^*, is the effective probability for particle emission to the radionuclide after the negative muon is captured. Values based on laboratory experiments are provided in Heisinger et al. (2002a) for chlorine-36 (both K and Ca) and other nuclides. The calibration of the slow muon production parameter, f_i^*, is discussed in Section 8.7.1.

$$P_{\mu-} = \phi_{\mu-} f_{i,C} f_{i,D} f_i^* \tag{8.5}$$

Muons can produce chlorine-36 through interaction with Ca, K, Fe, and Ti. For the main two muon reaction targets, Ca and K, previously published depth profiles allow the calibration of the muon production rate parameters for these two pathways, as discussed above. There are currently no studies or models to predict the production of chlorine-36 by muons from Fe and Ti. Fe and Ti muon production rates are assumed to be insignificant and these are not included in the production model.

Chlorine-36 production rate calibration is complicated by the fact that there are multiple target elements and by three reaction types. In many samples, the results are complicated by the presence of multiple target elements. Physical separation can be used to isolate a single mineral phase, which typically enriches the sample in a particular target element, reducing or eliminating the other possible targets that were present in the bulk sample. The use of mineral separates reduces the uncertainty of the partitioning of chlorine-36 between different target elements. For this reason, mineral separate samples were chosen for the spallation calibration.

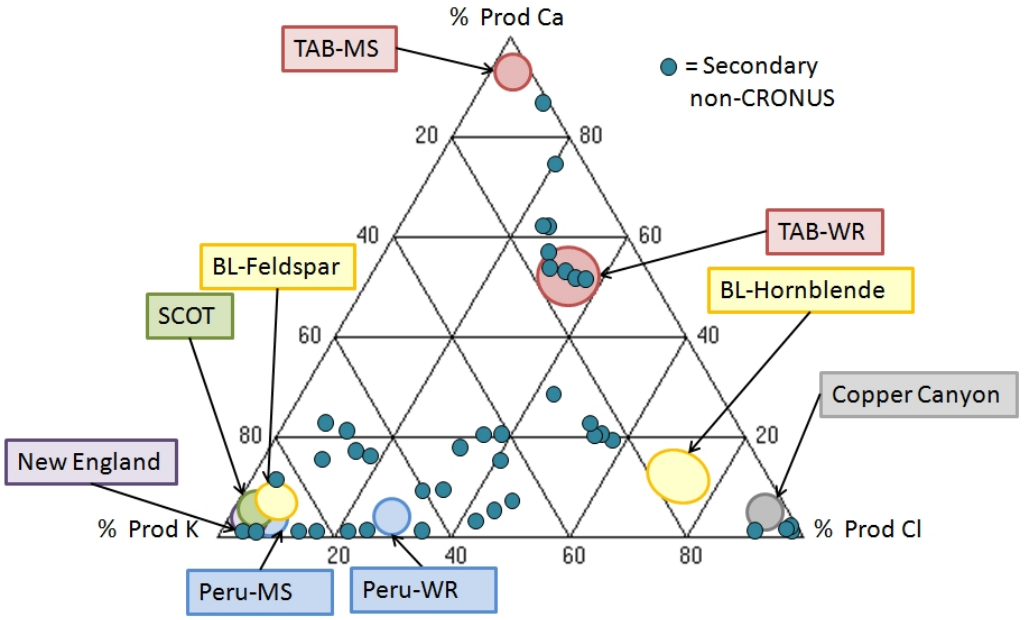

Figure 8.1: Ternary diagram showing the CRONUS-Earth sample compositions. The figure includes both primary and secondary CRONUS-Earth data. Secondary non-CRONUS sites are shown as unlabeled smaller blue circles. Abbreviations refer to the site: TAB - Tabernacle Hill, UT; BL - Baboon Lakes, CA; Peru - Huancané, Peru; SCOT - Isle of Skye and Scottish Highlands, Scotland; New England - Littleton-Bethlehem moraine; Copper Canyon - Copper Canyon, NM. Additional abbreviations refer to the composition of the samples: MS - plagioclase or feldspar mineral separates; WR - whole rock.

The compositions of the rocks chosen for this calibration are a deliberate attempt to have samples representing the three main target elements for chlorine-36 production. The ternary diagram in Figure 8.1 shows the percent production from each main pathway (Ca, K, and Cl) for all the CRONUS calibration sites, separated into primary and secondary sites. The percent production was calculated using the final calibrated production rate parameters from this study. For this calibration, we have tried to isolate as many samples as possible at each of the three corners of the diagram, indicating production limited to a single target element.

Cosmogenic nuclide scaling allows for the application of a production rate

determined at one location to be applied at a different location. It uses the physics governing the modulation of the cosmic ray flux by atmospheric mass and the terrestrial and solar magnetic fields to provide scaling factors as a function of location and exposure time, which is used to create appropriate production rates. Numerous scaling models have been proposed in order to correct for latitude, elevation, atmospheric pressure anomalies, geomagnetic field changes, dipole effects, and solar modulation. Results from production rate calibrations are completely dependent on the scaling model used to produce the results. All previous chlorine-36 production rate calibrations have used the Lal (1991) or Lal (1991)/Stone (2000) scaling model. Other common scaling models are discussed in Chapter 2, Section 2.6.

The most recent model by Sato et al. (2008) provides an energy-dependent breakdown of incoming cosmic rays at any point on the earth's surface and has led to the creation of a new scaling model. While the equations provided in the paper were not originally intended for this purpose, Lifton (2012) has modified the Sato model to incorporate the geomagnetic models and the solar modulation effects so that it can be used as a cosmogenic nuclide scaling model. Using this combined model, referred to as the Lifton/Sato model, we are able to calculate the neutron and muon flux at any site given latitude, longitude, and elevation. The model also allows for the use of a nuclide-dependent scaling model, which incorporates the individual reaction cross-sections for each cosmogenic nuclide-producing reaction. The nuclide-dependent Lifton/Sato model is used here for all results, unless otherwise indicated.

8.3.2 Factors Affecting $P_f(0)$

The calibration of the $P_f(0)$ parameter is challenging for many reasons. Issues such as the water content, geometry, and composition are important for samples with moderate to high chlorine contents, although the definition of "high" is somewhat arbitrary and depends on sample composition. Samples with low chlorine concentrations are exempt from these issues due to the lack of dependence on $P_f(0)$.

Water content can significantly affect the calculated low-energy neutron fluxes (Hendrick and Edge, 1966) and is therefore an important factor. Despite this fact, the water content of a sample is commonly an estimated parameter. In a study by Zreda et al. (2008), neutron detectors were used to determine the average water content of very large areas (hectometers). The water content of the soil clearly affects the the neutron flux, indicating that water content in a relatively large area around the sample may be affecting the cosmic-ray flux reaching the sample.

Several studies have shown that water content in a sample can lead to significant changes in the cosmic-ray flux. Masarik et al. (2007) presented GEANT and MCNPX models for the thermal neutron flux in the ground for 3% water and for dry conditions. The 3% water content increased the thermal neutron flux by 30% compared to dry conditions. Dep et al. (1994a) showed that the thermal neutron flux varied by a factor of two depending on the composition and water content of a sample. Even for low-porosity samples, such as granite, uncertainties in the water content lead to a 15% uncertainty in the production from low-energy neutrons, with even larger uncertainties possible for high-porosity rocks.

The difficulty in measuring current water content and the inability to measure its change through time makes this issue serious (Evans, 2001). We commonly estimate low-water conditions for many of the samples, assuming a volumetric water content of 0.5% for crystalline rock lithologies if no other information is provided. In some areas with different climates or lithologies, the water content may be consistently higher or lower.

An issue related to water content is the presence of snow on top of a sample. Snow shielding is a relatively common correction for many samples, including some used in the secondary dataset of this study, but is typically only used to change the shielding factor of a sample. This is a sufficient correction in samples without low-energy production (spallation-dominated samples), but requires an additional correction for low-energy production to account for the changing flux. Thermalization by the snow will change the proportion of fast to slow incoming neutrons, increasing the proportion of low-energy neutrons as compared to fast neutrons. The increase in low-energy production is similar to that seen by increasing the water content of the rock.

D. Desilets (pers. comm., February 27, 2012) used fast and slow neutron detectors to measure the changing neutron fluxes detected above a site as snow cover increased. The results are plotted in Figure 8.2. One neutron detector was placed under to the snow in order to measure the effect of the amount of snow cover present (plotted as water equivalent in panel (a)). The above-ground probes were then used to determine the changing flux as the snow cover increased. The proportion of slow neutrons to fast neutrons, plotted in panel (c) as the ratio of slow/fast neutrons, increased in the presence of a small amount of snow and then changed very little for additional snow. As the amount of snow increased, there

was general attenuation of both fast and slow neutrons after the initial changes in the fluxes. The implications for these studies on cosmogenic nuclide studies are significant. Small amounts of snow present at a site (1-2 cm snow water equivalent) can dramatically change the incoming flux of both fast and slow neutrons. The current snow-correction model (Gosse and Phillips, 2001) only adjusts for the snow shielding of a sample, assuming that both the fast and slow neutrons scale similarly. There is no model that accounts for the increased thermal neutron flux in the presence of snow.

The geometry of surfaces is also important, especially for diffusive low-energy neutrons. Masarik et al. (2000) calculated relative production rates on a flat surface and for hemispheres of 1 and 3m in diameter for beryllium-10. The hemispheres represent boulders, a typical cosmogenic nuclide sampling site. Despite the fact that Be-10 is produced by fast neutrons, the models indicate a surface concentration 12% lower for the 1 m hemisphere as compared to an infinite plane and a 7% decrease for a 3 m hemisphere. In Masarik and Wieler (2003), different boulder shapes were also modeled, but the general conclusion was that production at the surfaces of boulders can be up to 12% lower than that seen in an ideal, infinite, flat surface. For typical boulder sizes and sampling locations (top surface of boulder), corrections are on the order of 4%. This is larger than most of the topographic corrections that are routinely made for samples, so the authors argued that this is a significant correction. The 4% was calculated for a spallation-dominant nuclide, which means that high-chlorine samples may result in a correction much greater than a 4% difference in production rates. In Evans (2001), samples from the center and edge of a boulder were compared to each other and the edge sample produced a 35% lower concentration than the center sample. The geometry effects have the possibility to be significant, but are extremely hard to quantify without extensive modeling of each sample.

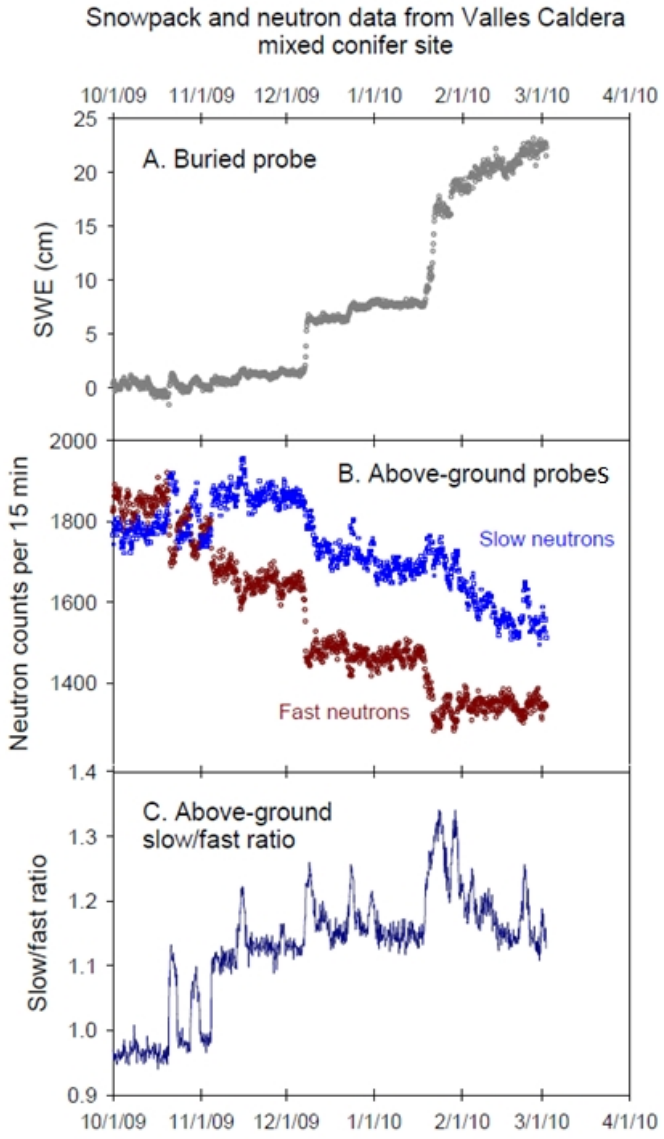

Figure 8.2: Figure showing the effect of snow on the fast and thermal neutron fluxes. A - Readings from a buried neutron probe were used to determine the SWE (snow water equivalent) through time. B - Two probes (one measuring slow and one measuring fast neutrons) from above the snow provide the 15-min average of the neutron counts through time. C - The ratio of the slow neutron counts to the fast neutron counts through time. Individual slow and fast neutron fluxes under the snow were not provided. Figure provided by D. Desilets (pers. comm., February 27, 2012).

8.4 Puget Sound Study

The most significant single contributor to the discrepancy in the production rates is the study by Swanson and Caffee (2001). Swanson and Caffee (2001) used 37 samples from the Puget Lowlands divided into three groups based on the dominant production pathway to calibrate all three main chlorine-36 production pathways. The production rates from that study (83.8±5 at (g Ca)$^{-1}$yr^{-1}, 211±18 at (g K)$^{-1}$yr^{-1}, 762±28 n (g air)$^{-1}$yr^{-1}) were very high compared to all previous production rate calibrations. The possible reasons provided in the paper included inheritance, temporal variability of paleomagnetic field, scaling, erosion, or poorly constrained independent ages. One additional possibility is a systematic analytical problem.

Part of the CRONUS-Earth project resampled some of the same, or similar, locations as those presented in Swanson and Caffee (2001). The samples from the first group, samples PUG01 to -03, are the Saratoga erratic and the Coles Road erratic and the samples are directly comparable to the Jolly-Breedlove erratic samples from the Swanson study (JB samples). The second site, Mt. Erie, represents bedrock samples from an area composed of highly resistent gabbroic rock that was glaciated by the Cordilleran ice sheet (Briner and Swanson, 1998). The third site, Cattle Point, was from poorly preserved boulders that were collected from a flight of uplifted beach terraces and may have originally been covered by sand or other sediment. These samples were crushed, homogenized, and distributed to several labs for processing. Both the NMT lab and the Purdue lab produced results, which are plotted in Figure 8.3. These results are plotted using the final calibrated production rates, as discussed later in this chapter. The samples are grouped by site, as indicated on the figure.

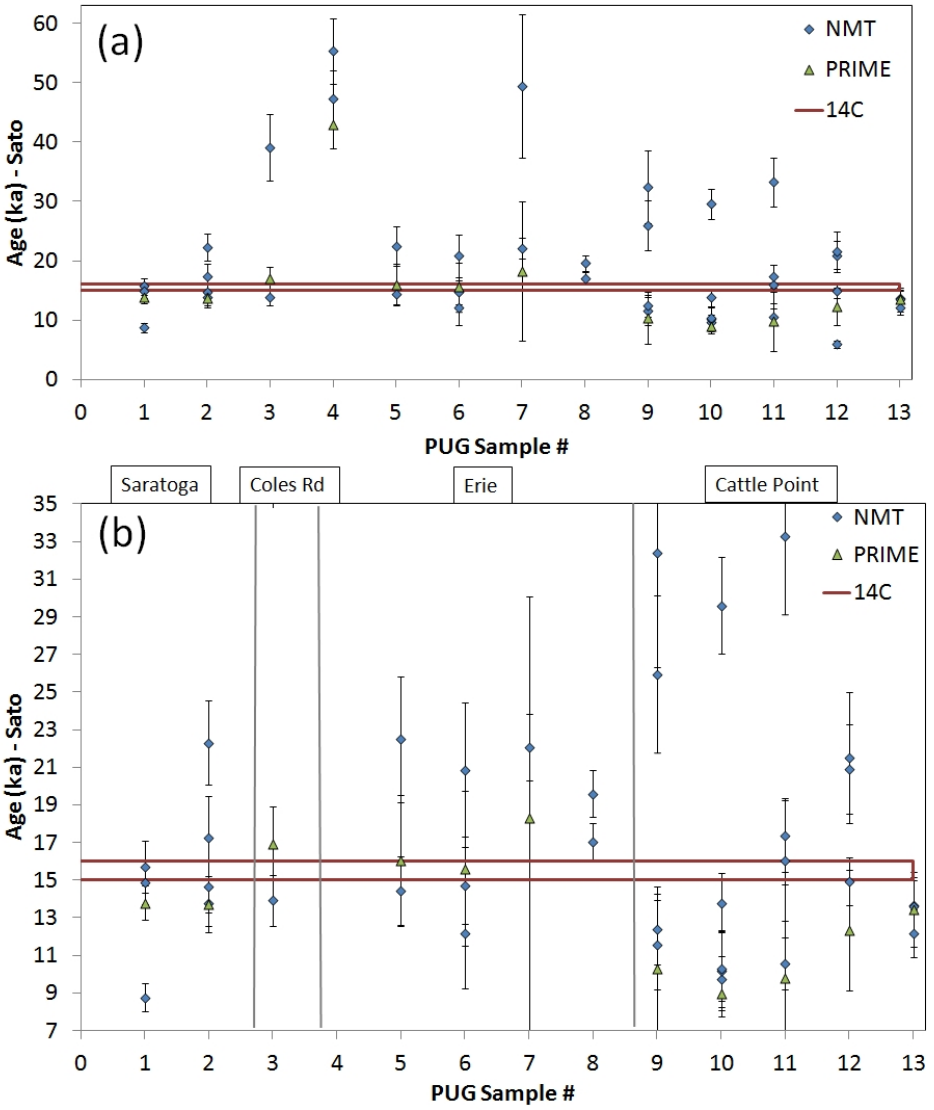

Figure 8.3: (a) Graph showing all the ages (as produced with the final calibrated production rates) for the the Puget Lowlands site. (b) Graph showing only the region surrounding the independent age bounds. Samples are grouped by site by vertical gray lines with the site name indicated above the graph. The horizontal red lines are the independent age bounds (15.0 ± 0.5 ka). Blue diamonds are the NMT results by Michelle Hinz and green triangles are samples from Purdue.

In the cases where there are more than two results from NMT, there are commonly two samples that produce ages very close to each other while a third sample is significantly offset from that result. Although there is significant scatter in the Hinz NMT data, the Purdue results appear to corroborate the replicable results in many cases. The Purdue results appear to be more consistent (less scattered) than the NMT results. Sample 4 appears to be an outlier with a consistently high age from all runs at either lab, likely due to inheritance. Regardless of the scatter, it is clear that the samples plot relatively close to the independent age bounds of 15.5 ± 0.5 ka.

Each sampling location within the Puget Lowlands site is relatively internally consistent. The first site, the erratic boulders, are very close to the independent age bounds. The second location, Mt. Erie, contains most of the possible outliers and has a much older average age than expected based on the independent age bounds. Both the outliers and the older age could be due to incomplete erosion during the glaciation of the region (Briner and Swanson, 1998). Finally, the third location, Cattle Point, has a slightly younger age than the independent age bounds. The fact that these samples outcrop in a series of uplifted shorelines indicates that they may have emerged later than the date indicated by radiocarbon and the samples may have originally had some sand or sediment cover, leading to younger apparent ages.

In order to compare these samples with the previously produced production rates, the samples were plotted using three different production rates. The first set of production rates are those determined in this study to be the best-fit rates (as discussed later in this chapter). The other two sets of rates were from the Swanson study. The ages were determined using the published rates, unchanged

Study	Ca Rate [at (g K)$^{-1}$ yr^{-1}]	K Rate [at (g Ca)$^{-1}$ yr^{-1}]	$P_f(0)$ Rate [n (g air)$^{-1}$ yr^{-1}]
This Study	56.0 ± 2.2	157 ± 6	704 ± 141
Swanson (published)	91 ± 4	228 ± 18	762 ± 28
Swanson (recalibrated)	77.5 ± 2.7	217 ± 6	1007 ± 26

Table 8.2: The production rates for the Puget samples that were used to produce Figure 8.4. The Swanson published rates represent exactly what was published in the paper with no correction for the change in scaling model. The Swanson recalibrated rates represent the rates produced by using the original Swanson calibration dataset, but recalibrating using the CRONUScalc program.

for the scaling model, as well as a new calibration using the same method applied in this study but applied to the original Swanson calibration dataset. These rates are shown in Table 8.2.

Only samples 01-03 from this study are directly comparable to samples used in Swanson and Caffee (2001), so these samples are used as a comparison between ages produced by different production rates (shown in Figure 8.4. The samples were aged using the production rates produced in this study, the original published rates of Swanson and Caffee (2001) with no adjustment to account for scaling, and the recalibrated rates found by using the original data from Swanson and Caffee (2001) in the CRONUScalc model. It is clear that the production rates determined in this study fit the sample data better than either of the Swanson production rate sets. The differences between the original Swanson and Caffee (2001) and the recalibrated rates can be attributed to the differences in scaling as well as the fact that the simultaneous calibration used did not separate the samples into groups.

The original samples from Swanson and Caffee (2001) were aged using the new production rates and plotted using a camel plot (see Balco (2011) for details on type of plot) in Figure 8.5. The ages are all considerably higher than

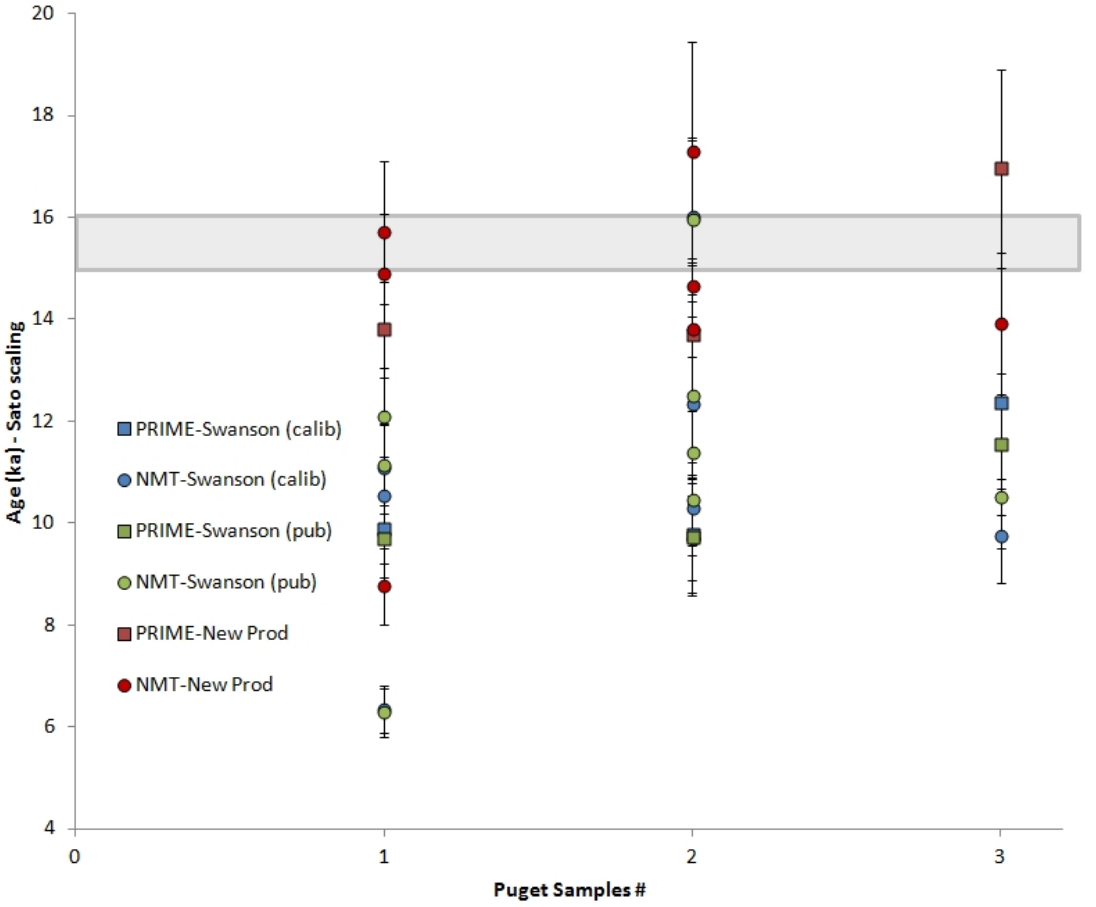

Figure 8.4: Graph showing the ages of the new CRONUS erratic samples as calculated using three different production rates: this Cl calibration (red), the published Swanson rates with no adjustment for different scaling model (green), and the results of using the Swanson data recalibrated using this same code and scaling model (blue). The shaded gray box shows the independent age of 15.0 $\pm$ 0.5 ka.

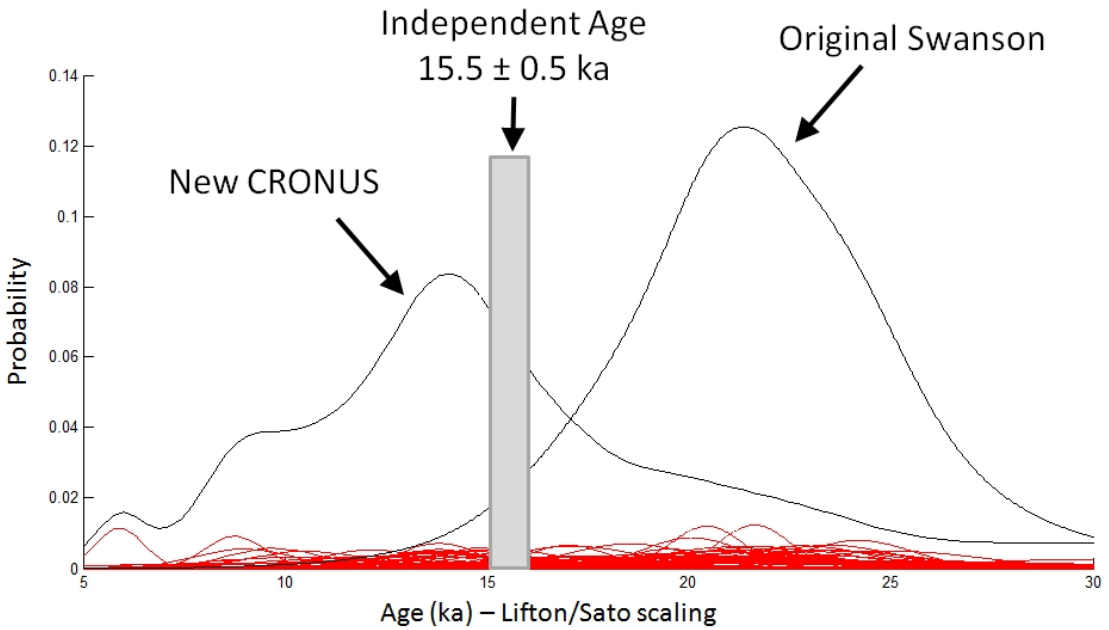

Figure 8.5: Camel plot showing the ages of the original Swanson and Caffee (2001) samples and the new CRONUS Puget samples both aged using the new production rates from this study. The gray box indicates the independent age bounds from the Swanson and Caffee (2001) study of 15.5 $\pm$ 0.5 ka. Uncertainties used on all the samples are the final production rate uncertainties (presented in Section 8.8).

the independent age bound (shown as a gray box). The combination of these high ages on the original samples and the relatively reasonable ages produced by the resampling (labeled as "New CRONUS" in the diagram) indicates that the discrepancy is likely due to analytical problems and was not reproduced during this reanalysis of the site.

Although few people use the Swanson and Caffee (2001) production rates to calculate exposure ages outside of the local region, it has still caused significant concern over the production rates for chlorine-36. Based on resampling and analysis of the data at two labs, it seems clear that the results from the original calibration study were not reproducible and our current results appear to be consistent with the production rate parameters in other regions of the world. If

Swanson and Caffee (2001) is not included, the discrepancy among the previous calibrations is reduced to only 27%, at most.

8.5 Chlorine-36 Interlab Comparison

As part of the CRONUS-Earth project, interlaboratory comparison materials were issued for beryllium-10, aluminum-26, and carbon-14 in the form of a pure quartz sample. This material was analyzed by many labs and the uncertainty on samples due to the different processing techniques was statistically assessed based on the results. This type of analysis ensures that all labs are producing equivalent results. Unfortunately, no intercomparison materials were issued for chlorine-36 until late in the project and there are currently not enough results to produce a statistically valid result.

In lieu of official intercomparison materials for chlorine-36, real geological samples that were processed by several labs are used to produce an estimate of the interlab uncertainty. The only samples that were processed by more than two labs was the Tabernacle Hill whole-rock material. Between the three labs, there are 24 analyses of 7 distinct samples from the same basalt flow. The comparison for chlorine-36 cannot be done using concentrations due to the possible variations in the sample compositions. Instead, the samples are aged and the resulting ages are used to compute the differences between the labs, as seen in Figure 8.6. In this case, the coefficient of variation resulting from the analysis of data from three labs was 5.0%. The maximum of either this value or the actual uncertainty is applied as the new uncertainty on the concentration measurement in order to incorporate the variability due to differences in different lab techniques.

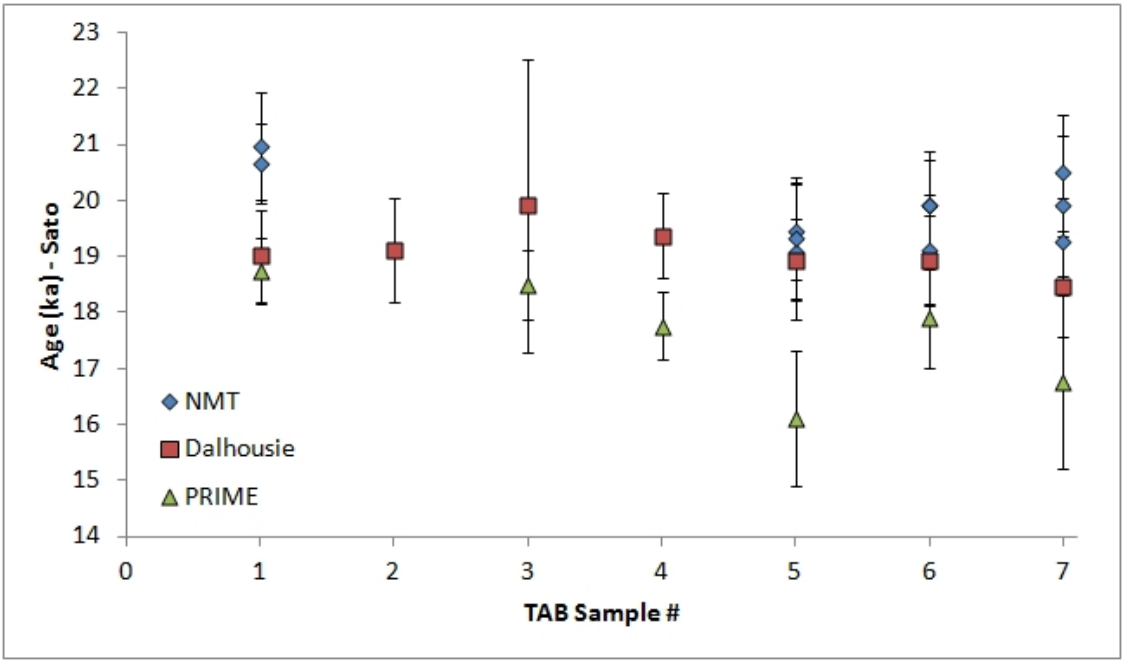

Figure 8.6: Tabernacle Hill whole-rock sample ages (calculated using nuclide-dependent scaling (Lifton, 2012) and final production rates) plotted showing all three labs for all samples. The plotted uncertainties include no production rate uncertainty.

8.6 Calibration Datasets

In general, a good chlorine-36 calibration dataset needs to be internally consistent with no outliers and it needs to represent a variety of compositions as well as a variety of latitudes and elevations. There should be little uncertainty in the parameters (such as erosion rate, location, independent age constraints, etc.). The sites that fit this set of criteria are defined as primary calibration sites. In order to test the calibrated production rate parameters, a second dataset was created. The secondary dataset contains additional sites with independent age constraints, but were not used during the main calibration of production rate parameters. These samples are also important because they can be used in conjunction with the primary dataset to calculate the realistic uncertainty in the dating technique.

The complete set of CRONUS-Earth sites were categorized based on site quality. The best sites, those fitting the criteria discussed above, were classified as 'primary' sites and the data was placed into the primary dataset. There are three CRONUS sites in the primary chlorine-36 dataset: Lake Bonneville, Huancané, and Scotland. The remaining chlorine sites (New England and Baboon Lakes) were classified as 'secondary' sites. The secondary sites are still considered good sites, but were discarded from the primary list for a particular reason, such as large uncertainty on the erosion rate or unknown amounts of snow cover at a site. In addition to the CRONUS-Earth sites, additional high-quality sites from the literature were added to the secondary site list in order to have a wide range of samples for comparisons. These datasets were updated if necessary and, in cases, the authors were contacted in order to verify the information or provide missing details for the samples. Figure 8.7 shows the location of all the sites

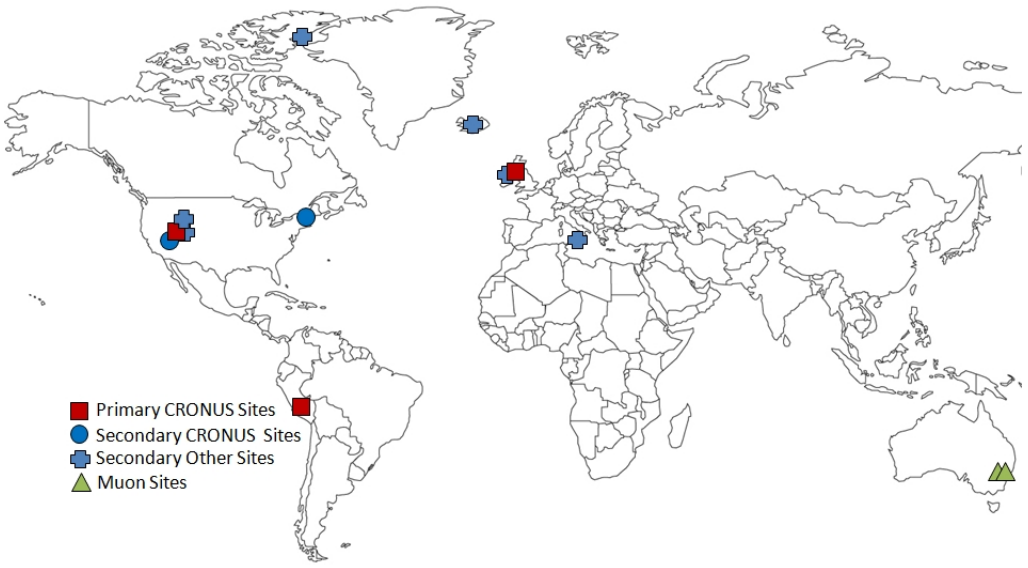

Figure 8.7: Map showing locations of the chlorine-36 calibration sites. The primary sites are indicated by red squares, the CRONUS-Earth secondary sites are indicated by blue circles, other secondary sites (those from publications) are indicated by blue crosses, and the muon calibration sites are shown by green triangles.

used in the chlorine calibration. Each primary and secondary chlorine-36 site is summarized briefly below.

8.6.1 Primary Calibration Sites

Lake Bonneville, Utah The Lake Bonneville, Utah, site contains two distinct sampling sites, Promontory Point and Tabernacle Hill. For chlorine-36, only samples from Tabernacle Hill (39°N and 1450 m elevation) are being used in the calibration. This basalt flow erupted into the Provo-level Pleistocene lake. This eruption is well constrained by the maximum limiting age of the Bonneville flood and the minimum limiting age of tufas collected from the edges of the basalt flow. The limiting ages constrain the eruption of the basalt to 18,200 $\pm$ 300 years before

2010 (see Chapter 4). Calcium feldspar mineral separates were prepared by John Stone at the University of Washington. Whole rock samples were prepared at New Mexico Tech by Shasta Marrero, at LDEO by John Gosse, and at the PRIME Lab at Purdue University. Mineral separates were used in the spallation calibration and the whole-rock samples were used for the $P_f(0)$ calibration. A summary of this site, including primary references and discussion of the complete datasets, can be found in Chapter 4.

Huancané, Peru The Huancané, Peru, site is located in the central Peruvian Andes at approximately 13 °S and very high elevation (4850 m). The Quelccaya ice cap created several sets of moraines, with these samples taken from the middle set. These moraines are known as the Huancané II moraines. The moraines have a well-constrained age based on radiocarbon found in peats and lake cores. The maximum and minimum bracketing ages yield a site age of 12,320 $\pm$ 110 years before 2010 (see Chapter 6). Potassium feldspar mineral separates were prepared by Shasta Marrero at New Mexico Tech and John Stone at the University of Washington. The mineral separates by Stone had significantly lower chlorine and less scatter than those from NMT, so the NMT mineral separates were removed from the primary dataset. Whole rock samples were also prepared at New Mexico Tech by Shasta Marrero. These whole rock samples produced concentrations that were much lower than reasonably expected. These samples also show significant scatter in the results so the Huancané whole rock samples were not used in the final calibration for chlorine-36. A summary of this site, including primary references and discussion of the complete datasets, can be found in Chapter 6.

Scotland The Isle of Skye and Scottish Highlands sites are part of the primary Scotland site. The Isle of Skye, Scotland site is located in the Inner Hebrides along the northwest coast of Scotland. Additional samples were collected on the mainland, in the Scottish Highlands, located in northwestern Scotland. The samples are at approximately 57°N with sample elevations ranging from 300-450 m. These samples were collected from rockfall boulders carried either sub- or supra-glacially and exposed at the end of the Loch Lomond readvance. The age assigned to these samples is 11,700 $\pm$ 300 based on varve counting, radiocarbon, pollen analysis, and correlation with the Greenland Ice Core. The independent age control is not local, but is well-constrained for deglaciation of the larger region. A set of four potassium feldspar mineral separate samples were analyzed by John Stone at the University of Washington. For a complete summary of this site, including primary references and a discussion of the complete dataset, see Chapter 5.

8.6.2 Secondary Sites

High-quality sites that do not meet the criteria discussed above (low uncertainty on all input parameters and well-constrained independent ages) are categorized as secondary sites. The CRONUS-Earth secondary sites are New England and Baboon Lakes. However, numerous papers outside the CRONUS-Earth Project report chlorine-36 results that include reasonably secure independently constrained ages. For the most part, these papers represent previous calibration efforts. These additional sites can provide valuable information on the quality of the main calibration.

New England (CRONUS Secondary Site) The Littleton-Bethlehem moraine site in New England (latitude of 44°N, elevation 400m) is a bouldery moraine complex. The independent age comes from the associated till sheet that is stratigraphically bracketed by varved sediments. The sediment ages restrict the age of the moraine complex to 13900 $\pm$ 250 years before 2010. There was some concern about excessive erosion and cover by snow and moss at this site, so it was not included in the primary calibration dataset. Previous results from other nuclides and more detailed site information is included in Balco et al. (2009). The sample data, including location and chemical composition, are included in Appendix C.3.

Baboon Lakes (CRONUS Secondary Site) The Baboon Lakes are located in the Sierra Nevada, CA, at a latitude of 37°N and an elevation of 3400m. The features that were sampled are glacial moraines from the Recess Peak advance. The details of the chronology are presented in Phillips (2011) giving an age for these samples of 13310 $\pm$ 250 years before 2010. This site is not ideal due to heavy winter snow accumulation. Snow corrections were also performed for all three samples, as discussed in Phillips (2011). The sample data, including location and chemical composition, are included in Appendix C.3.

Evans et al. (1997) (Non-CRONUS Secondary Site) These Sierra Nevada samples (latitude of 38°N, elevation 3000-3600m) were collected from boulders on moraines located as close as possible to the samples reported in Nishiizumi et al. (1989). The radiocarbon chronology of the Nishiizumi et al. (1989) samples, which have the same chronology as the Evans et al. (1997) samples, was re-evaluated in

Phillips (2011). These samples are from valley floor settings that were exposed by final retreat of the Tioga IV glacier, which has been assigned an age of 15810 $\pm$ 250 years before 2010. There are two datasets presented in this paper: a low-Cl potassium feldspar dataset and a high-Cl leachate dataset. Both datasets are being used as secondary datasets. The sample data, including location and chemical composition, are included in Appendix C.3.

Evans (2001) (Non-CRONUS Secondary Site) Evans (2001) calibrated potassium production rates as well as $P_f(0)$ using data from Scotland (latitude of 58°N, elevation 100-500m). The moraines in Scotland were likely exposed around 12400$\pm$300 years before 2010, which has a chronology similar to the CRONUS Scotland site. The samples added to the secondary dataset are quartz samples used to calibrate $P_f(0)$. These samples have production entirely from the low-energy neutron pathway. The sample data, including location and chemical composition, are included in Appendix C.3.

Phillips et al. (2009) (Non-CRONUS Secondary Site) The Sierra Nevada, California, site is located in western California at approximately 37°N and an elevation range of 2400-3600 m. The original chlorine data was published by Phillips et al. (2009), although the site chronology and site-specific details are comprehensively covered in the report by Phillips (2011). The dataset in Matlab format is included in Appendix C.3. Although these samples were not collected as part of the CRONUS-Earth project, these samples are geographically close to the Baboon Lakes CRONUS-Earth site and supplement the relatively limited dataset from that site. In addition, high-quality samples with high chlorine contents and

well-constrained ages were necessary in order to constrain the $P_f(0)$ parameter in the calibration. The subset used here was chosen from the larger dataset presented in Phillips et al. (2009) due to the internal consistency, composition and clear independent age context. Three sets of samples from the Humphreys Basin, the Middle Fork of Bishop Creek, and the Bishop Creek drainage were chosen as secondary calibration samples. These samples were collected from several well-dated moraines representing the Recess Peak terminal position, Tioga IV final deglaciation, and the Tioga IV terminal position, with assigned ages of 13310 $\pm$ 250, 15810 $\pm$ 500, and 16060 $\pm$ 500 years before 2010, respectively. The independent age constraints were primarily radiocarbon ages from cores in both local and regional lakes, although there is supporting evidence from pollen and shoreline outcrops that is consistent with the radiocarbon chronology. The chlorine samples have a wide range of compositions (from K to Ca), but contain higher chlorine concentrations (16-120 ppm) as well. The whole rock samples were processed at the New Mexico Tech laboratory.

Legacy Phillips data (Non-CRONUS Secondary Site) Initial introduction of the data can be found in Phillips et al. (1996) and the reevaluation of the sites and calibration can be found in Phillips et al. (2001). The calibration contains seven locations (Utah, Idaho, New Mexico, Wales, Ellesmere Island, Northwest Territories, and Arizona) that correspond to a variety of landforms (basalt flows, meteor crater, glacial boulders, glacial bedrock, and beach deposits). The dataset spans a variety of latitudes (19.8-80°N) and elevations (20-2578 m). In general, the dataset uses radiocarbon ages to constrain the site age, but there are some thermoluminescence and K/Ar dates as well, with the assigned calibrated ages ranging from 2.1-49 ka, but most sites are younger than 16 ka.

After talking with the author, some samples were removed based on new information about the landforms obtained since the publication. The main reason for removing samples was doubt about independent age constraints. Removed samples include Meteor Crater (MC), Mauna Kea (MK), and Wales (CW). The sample data, including location and chemical composition, are included in Appendix C.3.

8.7 Calibration

The CRONUS-Earth geological calibrations were originally designed to contain numerous sites (>10), varying lithologies, and a good geographic distribution over elevation and latitude in order to produce production rates and assess scaling models. During the project, the sample sites were re-evaluated and prioritized so that the most important sites would be sampled first. Out of 17 proposed sites, only five were sampled as part of the CRONUS-Earth Project and an additional three sites that were not originally on the list were added and sampled. This resulted in only eight CRONUS sites, with only six (Scotland, Peru, Tabernacle Hill, Puget Lowlands, Copper Canyon, Baboon Lakes, and New England) completed and applicable to chlorine at the time of publication (Hawaii has been sampled, but analyses have not been completed).

The compositions of these samples includes the following numbers of sites for each target element: Ca - 2, K - 3, Cl - 4, not including the Puget Lowlands samples, which were not intended as calibration samples but only to examine the discrepancy between the Swanson and Caffee (2001) and other chlorine-36 calibrations. After sample processing and analysis (see Chapters 5, 6, 4, and 7 for details), the remaining distribution is: Ca - 1, K - 2, Cl - 2. In addition, not all

of the available sites were designated as 'Primary' sites, those designated for use in the calibration, but were only 'Secondary' sites, those to be used for checking calibrated parameters. In this case, both the chlorine sites are secondary sites. Unfortunately, this resulted in insufficient numbers of sites and samples to perform the calibration as it was originally designed. Alternative methods had to be devised to work around these problems.

There were several calibration methods available in CRONUScalc. The original chlorine-36 calibration was designed to rely on the Copper Canyon value of $P_f(0)$ and then calibrate the spallation production rates using that as a fixed parameter. Once this method was excluded due to the large uncertainties in the Copper Canyon study, other options were explored, including a simultaneous calibration of surface samples to yield all three production rate parameters. The lack of primary calibration sites for $P_f(0)$ and significant variability in the samples used to constrain the value of $P_f(0)$ informed the decision to calibrate the spallation parameters separately and not as part of a simultaneous calibration. The production rates from the spallation parameters are insensitive to the value of $P_f(0)$ so they can be calibrated prior to the calibration of $P_f(0)$. After the calibration of the spallation production rates, the value for $P_f(0)$ is calibrated using secondary CRONUS datasets.

Site-to-site variability that far exceeds the intra-site variability caused significant problems in the calibration as well as the assignment of uncertainties to the final calibrated parameters. In order to statistically assess uncertainty on the calibrated production parameters, it must be shown that the data fits the model reasonably well, typically by calculating the p-value for the calibration. Even with acceptable p-values, there should be no bias between sites. The calibration

model shows some degree of site-to variability, especially in the $P_f(0)$ calibration. Due to this variability, the statistical uncertainties produced by the calibration code were not valid. New methods to determine the uncertainties on the production rate parameters based on the secondary dataset were developed.

The chlorine-36 calibration was carried out as a multi-step process. The calibration of spallation production rates from both Ca and K was performed on a low-Cl mineral separate dataset. Using a separate dataset for calcium, which included mineral separates from Tabernacle Hill, and another dataset for potassium, which included mineral separates from Peru and Scotland, the spallation production rates were calibrated. During this step, the $P_f(0)$ value was fixed at the value in Phillips et al. (2001) of 626 neutrons (g air)$^{-1}$ yr^{-1}. The value of $P_f(0)$ had very little effect on the spallation calibrations due to the very low concentration of Cl in the mineral separate samples.

Using previously published deep profiles, the model was reparameterized so that the muon production parameters were consistent with the new muon formulation. The spallation production rates and the muon parameters were not completely independent of one another. The muon production rates for Ca and K were calibrated iteratively with the spallation production rates until there was no change in the calibrated parameters.

After the spallation calibrations were complete, the spallation production rates were fixed and then the $P_f(0)$ parameter was calibrated using the CRONUS-Earth samples from Tabernacle Hill and Baboon Lakes. The whole-rock samples from Tabernacle Hill and the hornblende mineral separates from Baboon Lakes had significant production from chlorine (35-40% and $\sim$75%, respectively) and so they were able to constrain the $P_f(0)$ parameter. Due to the large difference in

total sample numbers at the sites (24 samples from 3 labs at Tabernacle Hill and 3 samples from 1 lab at Baboon Lakes), the $P_f(0)$ parameter was calibrated at each site individually and then averaged to obtain a representative value. This value was then compared with that obtained from the CRONUS-Earth Copper Canyon site.

The uncertainty on the calibrated parameters was obtained using the comparison to the secondary dataset. The secondary dataset was analyzed using the distribution of the normalized ages and the uncertainties were inferred from fitted normal distributions. Constraints on the uncertainty of the chlorine-36 technique were found using the root mean square error (RMSE) on the primary (minimum uncertainty) and secondary (maximum uncertainty) datasets.

8.7.1 Muon Calibration

In order to calibrate muon production using geologic samples, deep profiles are necessary in order to analyze samples below the depth of contribution from spallation (Stone et al., 1998). Previous calibrations for chlorine-36 have produced some calibrated parameters for muon production (Stone et al., 1998; Evans, 2001), but the current muon model in CRONUScalc (see Section 2.4.4 for details) is not parameterized in the same way, so those calibrations are no longer applicable. Even though the values of σ_0 (calculated from σ_{190}) and f* have been experimentally determined in some cases (Heisinger et al., 2002a,b), the values do not always agree with geological data. For ^{10}Be, the values reported in Heisinger et al. (2002b,a) predict ^{10}Be production at depth that is higher, by a factor of two or more, than the values measured by Stone (pers. comm., April 15, 2012) (see

Section 2.4.4 for more details). Based on this information, it was decided to calibrate the two parameters of σ_0 and f* for all reactions where there is appropriate data available.

As part of the CRONUS-Earth Project, a 30 m deep, dolerite core was scheduled to be collected in the Dry Valleys of Antarctica. Unfortunately, the drilling was halted at only 2 m depth due to loss of fluid circulation and the need to comply with environmental restrictions. This core was intended to provide the calibrated parameters necessary for chlorine-36 production from calcium, but the short length of the core prevents this.

Instead of using the CRONUS-Earth core from Antarctica for muon calibration, two previously published studies were used, one each for calcium and potassium. In both cases, the near-surface depth profile data (<2 m) was used to calibrate an erosion rate and attenuation length for the site. These two parameters were applied as constants while the deeper data was used to calibrate the muon production parameters of σ_0 and f* orthogonal distance regression. Once the calibration using both cores is complete, the muon production parameters are used in the spallation calibration and the calibrations are iterated until neither spallation or muon parameters change. Another possible method currently being developed for muon calibration is a simultaneous calibration of all fitted parameters, which would likely produce an even better fit to the data. However, the muon production contribution to the surface samples used in this calibration is minimal so the two-part fitting is adequate. Papers published from this chlorine-36 calibration may be updated to use the new method and may not reflect the calibration shown here.

Potassium Muon Calibration The potassium muon depth profile, originally published in Evans (2001) and summarized here, was collected from a granite quarry face in Australia (148°55'E, 34°02'S) at an elevation of 540 m. Sixteen samples were collected down to 1600 g cm^{-2} ($\sim$6 m) below land surface. The very geomorphically stable area was assumed to be at steady-state with respect to chlorine-36 concentrations. Additional surface samples were taken near the quarry in order to determine the erosion rate and overburden depth by comparison to undisturbed samples. The chlorine, beryllium, and aluminum concentrations in the surface samples yielded an overburden depth of 15 g cm^{-2} and an erosion rate of 2.64-7.91 mm kyr^{-1}, depending on the geomorphic location of the sample. However, Evans (2001) also fitted an erosion rate of 8.5 mm/kyr to the profile, which is in agreement with the surface sample erosion rate of 7.91 mm/kyr. The average density from ten measurements was calculated to be 2.643 g cm^{-3}. For simplicity, the complete set of original measurements from this core are included in Matlab-ready format in Appendix C.3.

In this study, an erosion rate and attenuation length were calculated using all the samples with depths $<$2 m (the uppermost six samples from the profile). The calibrated erosion rate and attenuation length were 1.44 $\pm$ 0.13 g cm^{-2} (5.4 $\pm$ 0.5 mm kyr^{-1})and 175 $\pm$ 11 g cm^{-2}, respectively. The p-value of 0.28 indicates an acceptable fit to the data. From the deeper portion of the core, the muon parameters of σ_0 and f* were (25.8$\pm$79) x 10^{-30} m^2 and 4.6 $\pm$ 10.6 %. With a p-value of 0.9989, the fit to the data is good, but the uncertainties on the calibrated parameters, which are larger than the value itself) indicate that the data does not constrain the values well. Figure 8.8 shows the predicted concentration using these calibrated parameters (black 'X'), and the measured values (open circles).

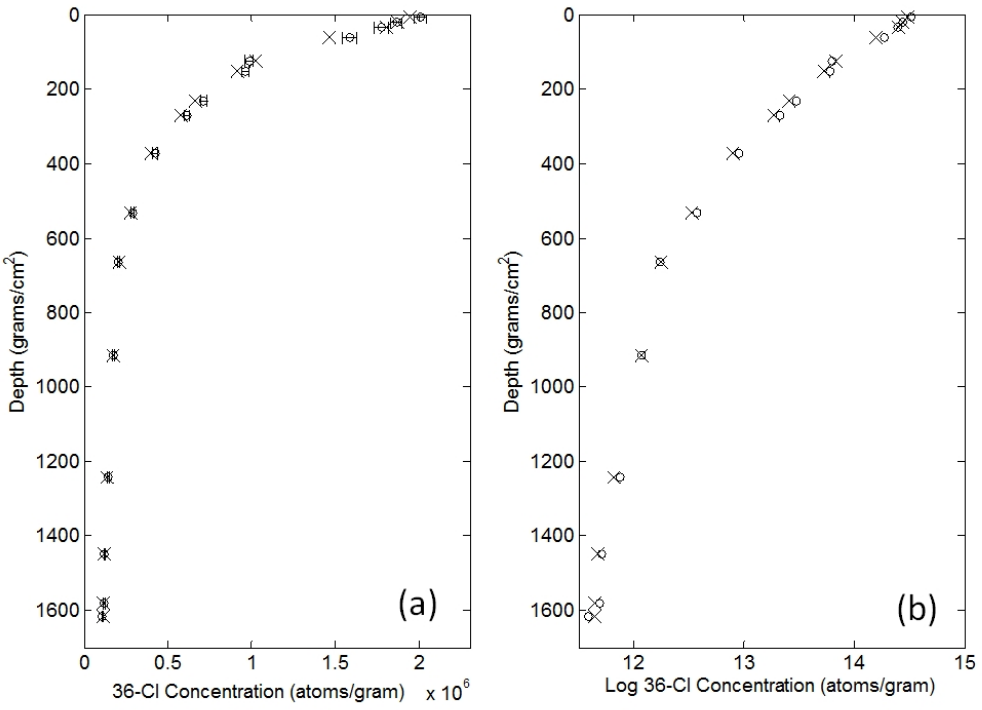

Figure 8.8: The calibrated potassium muon model (shown by symbol 'X') compared to the measured sample data (open circles). The calibrated parameters were $\sigma_{0,K}$ and f_K^*. (a) Comparison on a linear plot. (b) Comparison on a semilog plot. There were no published potassium parameters for the model provided in Heisinger et al. (2002b), so there is no comparison with previous models presented here.

Evans (2001) calibrated the muon production parameter, Y_k (defined in Equations 8.6 and 8.7), and got a value of (5.80 $\pm$ 0.21) x 10^{-2} at ^{36}Cl per stopped negative muon. The author cautioned that the calibrated value of Y_k is composition-dependent, so applying it to other areas introduces uncertainty. As this is a reinterpretation of the original dataset, the calibrated values can be directly compared. When an equivalent value is calculated for our calibration, the value is 0.43 x 10^{-2} at ^{36}Cl per stopped negative muon based on the following values: f_c=0.08-0.09 depending on composition of each sample, f_d= 0.802, and f* = 0.058 $\pm$ 0.050. The difference in the values is not due to differences in the negative muon stopping rate, calculated at depths of 100 and 1000 g/cm^2 to be 182 and 68 negative muons g^{-1} yr^{-1} using the equation presented in Stone et al. (1998) and 187 and 93 negative muons g^{-1} yr^{-1} using the CRONUScalc program. Other possible factors that could contribute to these discrepancies include a different spallation production rate and the fact that we calibrated both fast and slow muon parameters simultaneously, while Evans (2001) assumed that muon production was due entirely to slow, negative muon capture.

$$P_{\mu-,k} = \phi_{\mu-} Y_k = \phi_{\mu-} (f_C f_i^* f_D) \tag{8.6}$$

$$Y_k = f_C f_i^* f_D \tag{8.7}$$

Calcium Muon Calibration The calcium depth profile, published in Stone et al. (1998), was collected from the wall of an abandoned quarry in the southeastern highlands of Australia (149°58'E, 34°19'S) at an elevation of 620 m. The site is

very geomorphically stable, with a reasonable assumption of steady-state conditions for chlorine-36 concentrations. The erosion rate could not be determined by independent methods and quarry activity made it difficult to determine if overburden was present. By using nearby surface samples from undisturbed outcrops, the erosion rate was calculated to be 20 mm kyr^{-1} and the overburden depth was calculated to be 174 g cm^{-2}. The density was measured as 2.68 g cm^{-2} and the composition was determined to be almost pure carbonate (>99.8 weight %). The samples were taken from the surface down to a depth of 5400 g cm^{-2} in marble ($\sim$ 20 m). The shielding was calculated by the original authors using the topography of the area as well as the 20° slope of the hillside. The complete set of measurements from this core are included in Matlab-ready format in Appendix C.3.

The calibrated erosion rate of 7.97 $\pm$ 1.3 g cm^{-2} kyr^{-1} (29.7 mm/kyr) was very similar to the rate of 26 mm/kyr determined in the original study. The calibrated attenuation length of 193 $\pm$ 26 g cm^{-2} is also within uncertainty of the 170 g/cm^2 assumed in the original study. The large uncertainty on the erosion rate and attenuation length is due to the very small number of samples (6) in the shallow depth range. The lower part of the profile produced values of σ_0 and f* of (0.84$\pm$0.45) $\times 10^{-29}$ m^2 and 1.68 $\pm$ 1.18 %, respectively. While the fit to the data is very good (p-value = 1.0), the uncertainties are still quite large. Figure 8.9 shows the old fit to the data based on values from Heisinger et al. (2002b,a) (red triangles), the new fit using these calibrated parameters (black 'X'), and the measured values (open circles with error bars).

In Stone et al. (1998), the calibration produced a value of Y_{Ca} equal to 0.012 $\pm$ 0.002 negative muons g^{-1} yr^{-1}. Reanalyzing this data using our current model

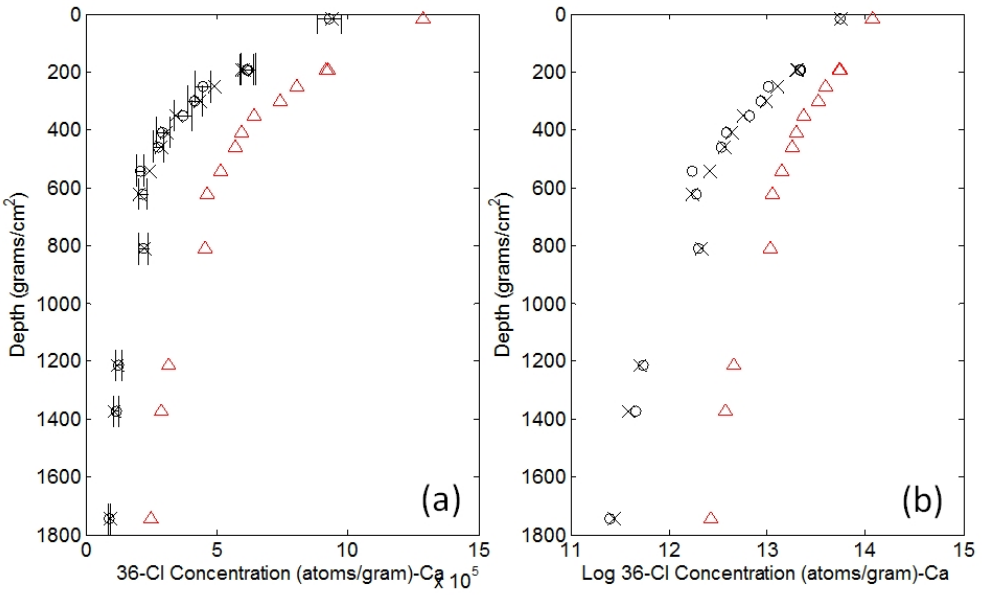

Figure 8.9: A comparison of the pre-calibration calcium muon model from Heisinger et al. (2002b,a) (red triangles) with the newly calibrated model from this study (black 'X') and the measured sample data (open circles with error bars). (a) Comparison on a linear plot. (b) Comparison on a semilog plot. The calibrated parameters were $\sigma_{0,Ca}$ and f^*_{Ca}. The profiles are not smooth due to the changing composition of the samples.

Parameter	K		Ca	
	Calibrated	Previous	Calibrated	Previous
σ_0 [mb]	258±790	NA	84±52	0.027±0.006
f* [–]	0.046±0.106	0.035±0.005	0.0168±0.0118	0.045±0.005

Table 8.3: Table showing the calibrated muon production rate parameters and the previously published values. NA indicates that the value was not published.

produced an equivalent value of 0.0051 negative muons g^{-1} yr^{-1}, using the following values: f_D=0.8486, f_C=0.35-0.36, and f^*=0.017. The total production is calculated by multiplying Y_{Ca} by the negative muon stopping rate. The difference in the values is not due to differences in the negative muon stopping rate, calculated at depths of 100 and 1000 g/cm^2 to be 182 and 68 negative muons g^{-1} yr^{-1} using the equation presented in Stone et al. (1998) and 195 and 97 negative muons g^{-1} yr^{-1} using the CRONUScalc program. While these values are not identical, they are similar and do not explain a difference in an order of magnitude. The small differences in flux are due to the new Heisinger/Sato muon model (introduced in Section 2.4.4). The possible differences are the same as those given in the discussion of calcium muon calibration: we calibrated both slow and fast muon parameters from this profile and the spallation production rates are different between the calibrations.

The complete set of previously published muon production parameters are shown in Table 8.3 along with the newly calibrated values resulting from the reinterpretation of the depth profiles.

8.7.2 Spallation Calibration

Orthogonal distance regression (ODR) was used to produce the calibrated production rates. ODR allows both dependent variables (in this case, sample

data) and independent variables (independent age constraints) to have uncertainty in the curve-fitting process by minimizing the orthogonal distances to the curve instead of minimizing purely vertical or horizontal distances to the curve (Boggs et al., 1987). This method of calibration improves upon previous calibrations that used only the least-squares method and leads to smaller overall uncertainties on the final fitted parameters.

We used the Lifton (2012) scaling model in the CRONUScalc code to produce the production rates for the two spallation production pathways. The calibration of each element individually yields production rates of 157 $\pm$ 5 at (g K)$^{-1}$yr^{-1} and 56.0 $\pm$ 1.4 at (g Ca)$^{-1}$yr^{-1}. The chi-squared value is 18.1 and 5.08 for K and Ca, respectively, (reduced chi-squared of 1.5 and 0.63, respectively), giving a p-value of 0.15 and 0.83, which indicates that the predicted values based on the new calibrated parameters fit the data adequately. P-values around 0.5 indicate very good fits to the data (Bevington and Robinson, 1992). Although the exact lower limit for an acceptable p-value is somewhat arbitrary, we assume that any p-value greater than $\sim$ 0.05 is considered to be an adequate fit.

In order to check for bias in the calibration, ages were calculated for the samples in the primary dataset using the final fitted parameters. The samples were plotted as normalized ages (calculated age/independent age) versus the parameters of site, latitude, elevation, and independent age (Figure 8.10). There are no trends in latitude, elevation, or independent age. For two of the three calibration sites, the normalized ages are distributed evenly above and below one. On the other hand, the normalized ages from Scotland all plot slightly above one, indicating the possibility of site bias. However, it is also possible that the apparent bias is simply due to the small number of samples from the site. There

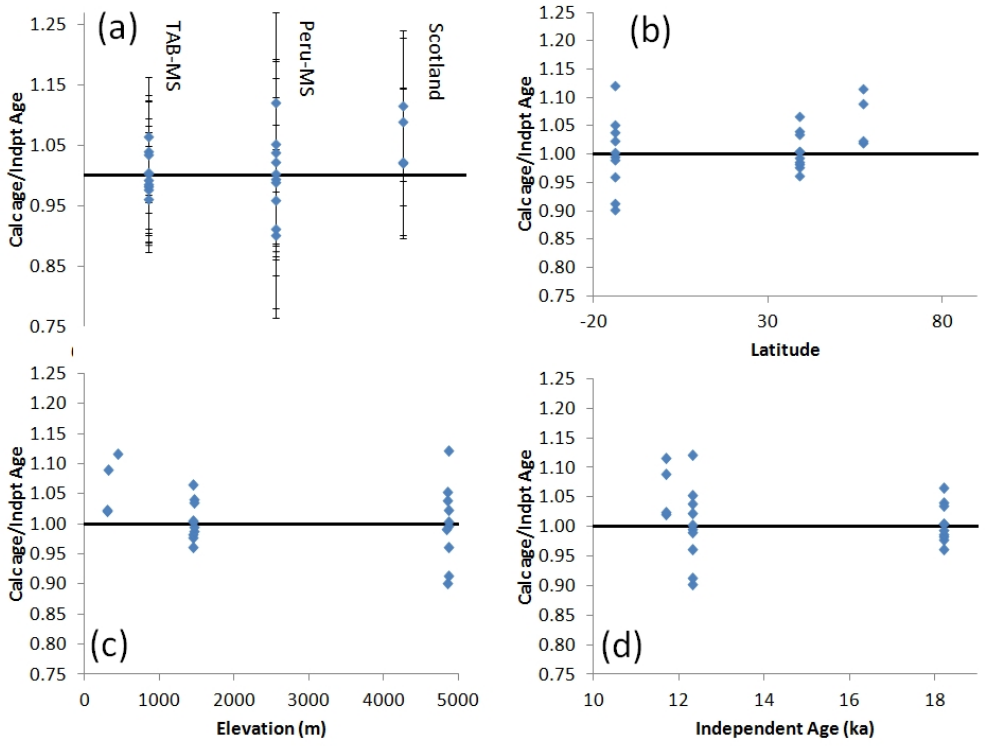

Figure 8.10: Primary calibration dataset ages shown plotted by (a) site (from left to right: Tabernacle Hill plagioclase mineral separates, Huancané, and Scotland), (b) latitude, (c) elevation, and (d) independent age. Uncertainties are only shown in panel (a), but are the same for all other plots in this figure.

are only four samples from the Scotland site, whereas there are ten Peru samples and ten TAB samples. Based on the plots, there is no clear indication of bias.

Cross-validation exercises, performed for all other nuclide spallation calibrations (Borchers and Stone, 2012), were not possible for the chlorine-36 dataset. During leave-one-out cross-validation, one dataset is removed and the remaining sites are used to calibrate new production rates. Then, those production rates are used to predict the ages of the removed site. In other calibrations, cross-validation was performed in order to check for site bias in the dataset. For the chlorine calibration, each site has a dominant production mechanism. The dominant mechanism at Tabernacle Hill is calcium and Peru and Scotland are

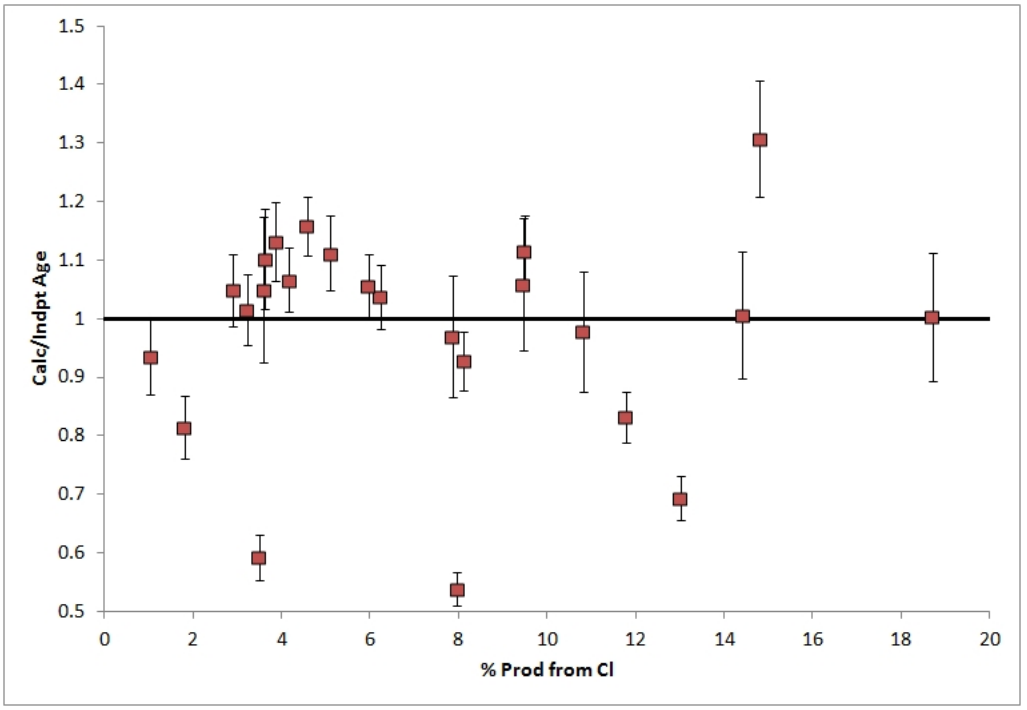

Figure 8.11: Normalized ages (Lifton (2012) scaling) for the low-Cl quantitative secondary dataset. Ages were calculated using the final spallation production rates and plotted as normalized ages against % production from chlorine. Only samples with <20% production from chlorine are included in this dataset.

potassium-dominated. There are insufficient sites to adequately constrain the production rates of both spallation rates if any one of the sites is removed. For this reason, no cross-validation was performed for chlorine.

The secondary datasets provide another way to assess the calibrated production rate parameters. The low-Cl secondary samples, defined as those samples with a % production from Cl $\leq$20, were aged using the newly calibrated spallation parameters and plotted in Figure 8.11. There is a group of samples that plot above the line and dispersed samples that plot significantly below the line, but the samples generally scatter relatively evenly around one.

8.7.3 Low-Energy Neutron Calibration

$P_f(0)$ from CRONUS Sites A single value for the $P_f(0)$ parameter is necessary for the code. Unfortunately, there is significant variability between the two CRONUS sites with regard to the final calculated values of $P_f(0)$. There was no a-priori reason to prefer one of these sites over the other, therefore the value was calibrated using the data from both of the CRONUS sites (Baboon Lakes hornblende separates and Tabernacle Hill whole-rock samples) and the average of these two values was used. The Baboon Lakes site has the advantage that the preponderance of the production is from Cl ($\sim$75%), but there are a very limited number of individual analyses. The Tabernacle Hill whole-rock samples are numerous, but only $\sim$40% of the ^{36}Cl production is from Cl. As discussed in the site description and Chapter 6 for Huancané, Peru, the whole-rock samples from that site were not used due to to the unrealistically low ^{36}Cl concentrations that were measured.

The Baboon Lakes high-Cl mineral separates (only three samples) produced a $P_f(0)$ of 594 n (g air)$^{-1}$ yr^{-1}. Samples from Phillips et al. (2009), located in the same region as the Baboon Lakes, confirm that the region is not anomalous with respect to cosmogenic nuclide production and the region produces ages that are consistent with the production rates discussed here, as seen by the normalized age plot in Figure 8.12. Tabernacle Hill whole-rock samples from all labs (24 samples total) produced a $P_f(0)$ value of 814 n (g air)$^{-1}$ yr^{-1}. These two values were averaged to obtain a CRONUS site $P_f(0)$ value of 704 n (g air)$^{-1}$ yr^{-1}. Due to the large differences in the values between sites, the samples could not be calibrated in the same dataset or the result would have been skewed by the different

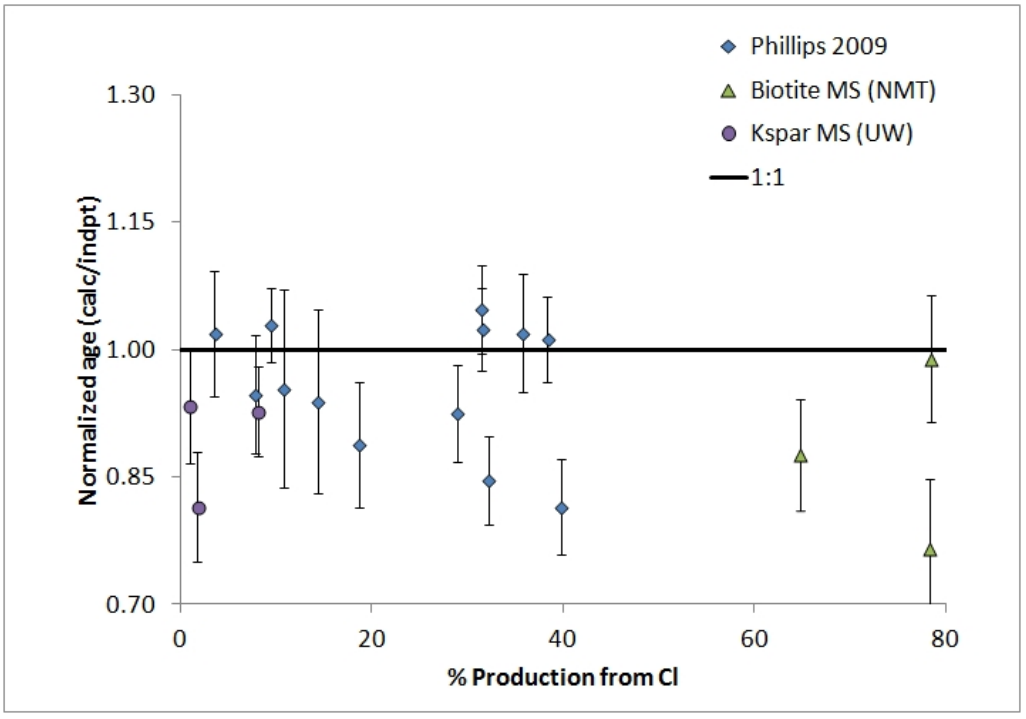

Figure 8.12: Normalized ages (Lifton (2012) scaling) for the Sierra Nevada (Phillips et al., 1997) dataset as calculated using the final spallation production rates and plotted as % production from chlorine. The UW potassium feldspar mineral separates and the NMT biotite mineral separates are also plotted for reference.

numbers of samples at each site. The uncertainty on this parameter is discussed in Section 8.8.

The reasons for the site-to-site variability include most of the factors discussed in Section 8.3.2. With respect to the individual sites, a likely factor is water content of the surrounding area or the geometry of the landforms sampled. The surface sites include the Tabernacle Hill basalt where samples were taken from the tops of tumuli and the region is relatively arid. The Baboon Lakes samples were collected from the tops of granite boulders, but the area and all three samples are corrected for a moderate amount of snow in the winter, resulting in a 1-2% correction. Snow corrections are important and if they are incorrect, they can misapportion the chlorine-36 inventory between fast and slow neutrons.

$P_f(0)$ from Copper Canyon The chlorine-36 $P_f(0)$ calibration site is in Copper Canyon, NM, and was designed to provide an independent constraint on the low-energy neutron production rate parameter, $P_f(0)$. The site was an abandoned mine prospect pit into a quartz vein hosted in limestone. Samples were taken down to a depth of approximately 2 m from a quartz vein in a limestone matrix. The pit was dug into a surface sloping at 20° with essentially no other topographic shielding. Depths to the samples were measured in the vertical (the orientation of the mine pit) but were recalculated as depths perpendicular to the sloping surface in order to be consistent with the formulations of the production equations within the Matlab code. The geomorphically stable surface was assumed to be in equilibrium with respect to both ^{10}Be and ^{36}Cl concentrations. The beryllium-10 profile (Figure 8.13) is consistent with a saturated sample and yielded a calibrated erosion rate of 1.3 $\pm$ 0.04 g cm^{-2}kyr^{-1} (5.7 mm/kyr) and

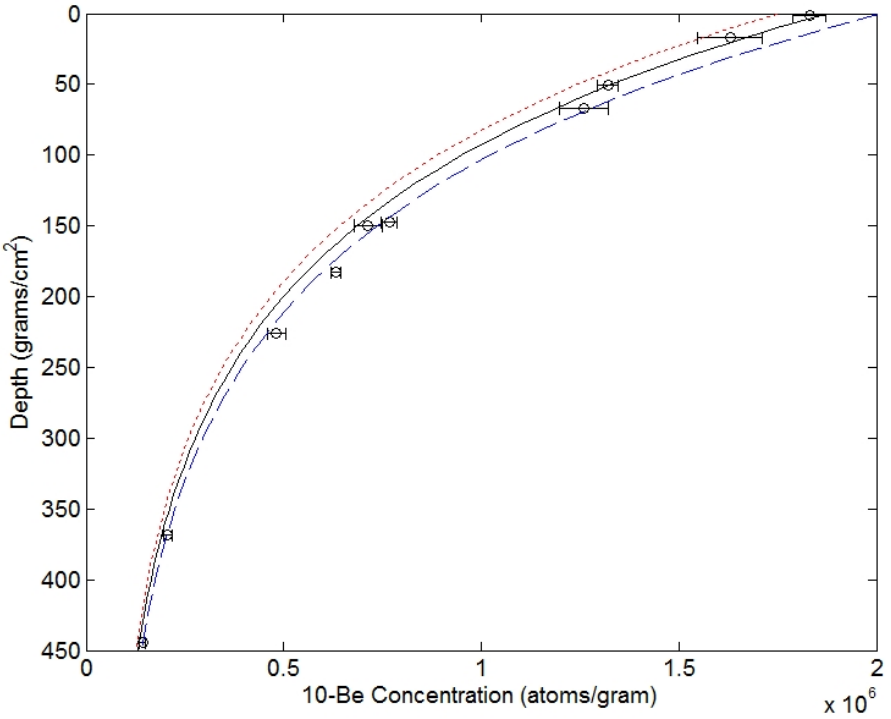

Figure 8.13: The calculated (solid line) versus measured (open circles) beryllium-10 concentrations of the profile. The dashed (and dotted) lines indicate the predicted profile for a lower (or higher) erosion rate.

attenuation length of 140 $\pm$ 3 g/cm^2 at the site. This is very similar to the predicted attenuation length value of 143 g/cm^2 predicted by the attenuation length module (details in Section 2.4.1).

Chlorine-36 samples were processed from the depth profile and were used to calibrate the thermal neutron production rate parameter, $P_f(0)$. The value of $P_f(0)$ from the profile was 679 $\pm$ 54 n (g air)$^{-1}$yr^{-1}. The measured and predicted profiles for chlorine-36 are shown in Figure 8.14. The fit to the profile was not technically acceptable (p-value of 0.001), but it is also not unreasonable, as seen in Figure 8.14. There are some complications with the profile that has diminished its usefulness as a calibration site. The complications include the geometry of

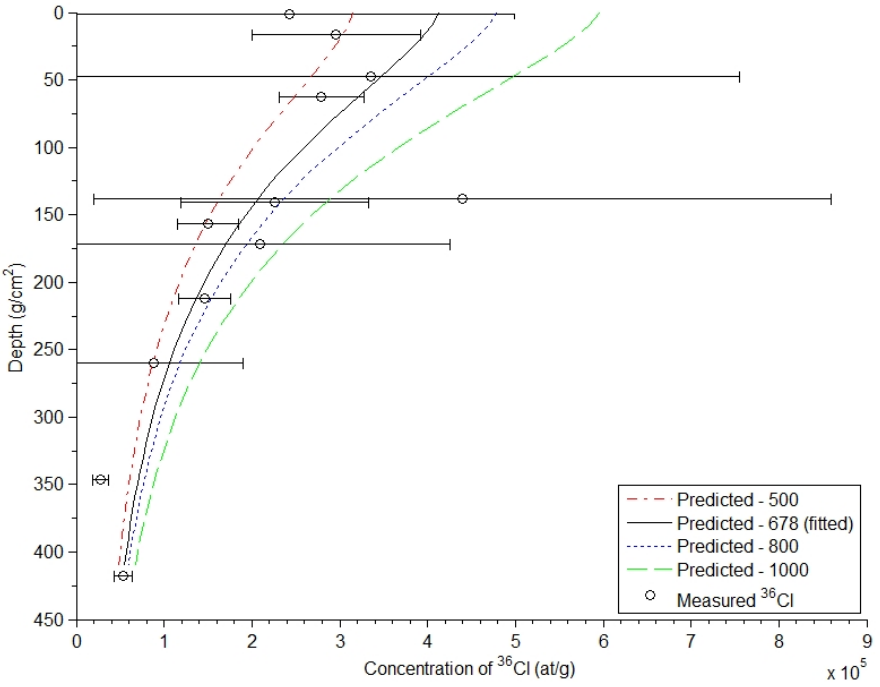

Figure 8.14: The predicted (colored lines) versus measured (open circles with error bars) chlorine-36 concentrations of the profile. The calibrated value based on the profile is shown, along with several values of $P_f(0)$ above and below the calibrated value.

the vein, water content in the area, large blank corrections, and the slope of the surface. The results are summarized briefly here with full details provided in Chapter 7.

The irregular geometry of the quartz vein has made the assignment of bulk rock composition difficult. The bulk rock should be the average composition of the material seen by the cosmic rays before they reach the sample. Due to the irregular vein geometry, it is unclear if the bulk composition should be the limestone host rock or the quartz vein itself. The sensitivity of the calculated value of $P_f(0)$ to rock composition was explored by recalculating $P_f(0)$ for two alternative compositions: limestone bulk+limestone trace element, yielding 805 $\pm$ 68 n

(g air)$^{-1}$yr^{-1}, and limestone bulk+ quartz trace element, yielding 1016 $\pm$ 77 n (g air)$^{-1}$yr^{-1}. It is clear that the observed degree of variation in the composition of the bulk rock and trace elements is significant. Given that the width of the quartz vein in most parts of the profile is $\sim$1 m, and hence the calculations based on only the quartz chemistry were considered to be most representative of the environment controlling the low-energy neutron flux passing through the samples. The value of 679 $\pm$ 54 n (g air)$^{-1}$yr^{-1} will therefore be used for the discussion and sensitivity analyses.

The sensitivity to water content was examined by calibrating the profile at three different water contents, 0, 0.005, and 0.05 volumetric water content. The resulting $P_f(0)$ values are 725 $\pm$ 62, 678 $\pm$ 54, and 893 $\pm$ 71 n (g air)$^{-1}$yr^{-1}. The lower water content samples (0 and 0.5 %) are within uncertainty of one another. With a larger increase in water content, the value of $P_f(0)$ increases signficantly. This is likely due to the decreased calculated thermal neutron flux reaching the sample due to the high stopping power of water. The estimate of 5% water content is a conservative bound and the lower values represent a more realistic estimate.

Initial measurements of Cl indicated concentrations of 20 ppm in the quartz samples. This necessitated dissolution of large masses of sample in order to obtain sufficient Cl for AMS analysis. However, determination of the Cl concentration by isotope dilution mass spectrometry on the AMS samples showed that Cl concentrations were only 5-10 ppm. The large masses of acid required to dissolve the large sample masses, combined with the unexpectedly low Cl concentrations, resulted in undesirably large Cl-blank corrections. Most of the chlorine-36 blank corrections were on the order of 3-10% and the stable Cl-blank

corrections ranged from 3 to 70%. This combination lead to increased uncertainties on sample measurements.

The slope of the hill is used in the calculation of the depths of the samples. The uncertainty of this measurement (approximately 5°) leads to an uncertainty in $P_f(0)$ of 0.3%. This uncertainty is not significant compared to analytical uncertainty or uncertainty on other parameters, as discussed above. Results will only be presented for a slope of 30°.

The average of the two CRONUS-Earth datasets produced a value of 704 n (g air)$^{-1}$yr^{-1} for $P_f(0)$. The value produced by the Copper Canyon study, 679$\pm$54 n (g air)$^{-1}$yr^{-1} is completely consistent with that value. However, the Copper Canyon study had large uncertainties on the composition of the bulk rock and uncertainties due to large blank subtractions, so the results are not being used as a primary control on the value of $P_f(0)$. For this reason, the final value of $P_f(0)$ adopted in this study is 704 n (g air)$^{-1}$yr^{-1}.

8.8 Calibration Discussion

Several methods were used in order to analyze how well the calibrated parameters fit both the primary and secondary datasets and how they compare to previous calibrated parameters.

In order to test for bias in the main calibration datasets, all the samples used for calibration were aged using the final calibrated production rates. Figure 8.15 shows the normalized ages of all the samples as plotted by site, latitude, elevation, and independent age. There do not appear to be any clear trends, although both the Baboon Lakes and Scotland sites plot to one side of the line. This

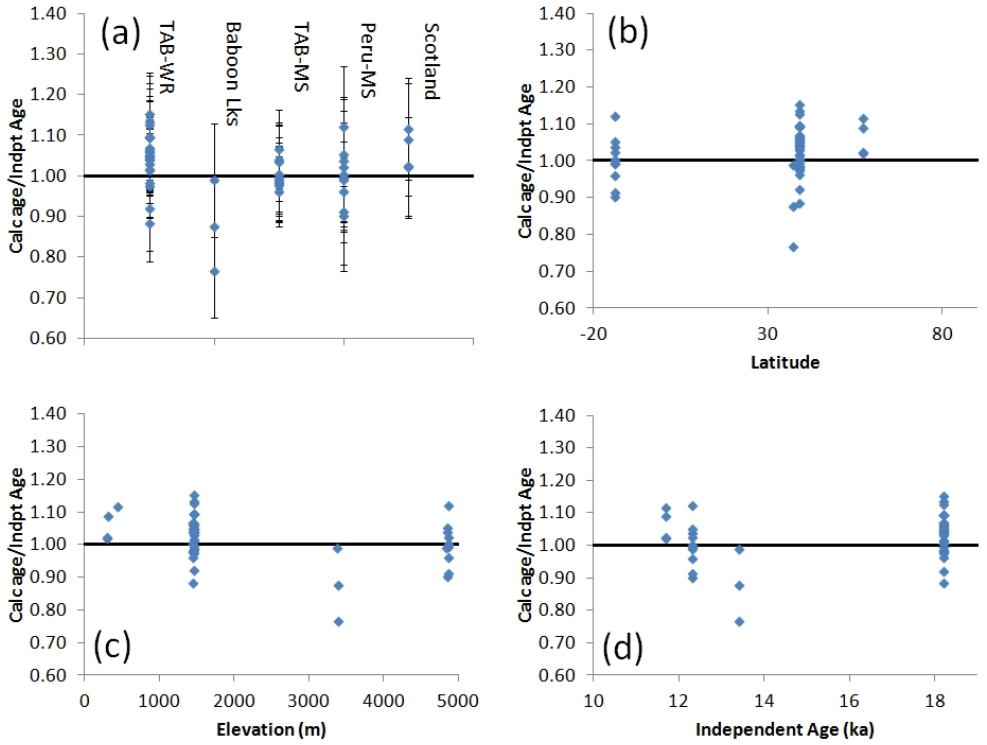

Figure 8.15: The main calibration dataset ages, including the samples used to calibrate $P_f(0)$, shown plotted by (a) site (from left to right: Tabernacle Hill plagioclase mineral separates, Huancané, and Scotland), (b) latitude, (c) elevation, and (d) independent age. Uncertainties are only shown in panel (a), but are the same for all other plots in this figure.

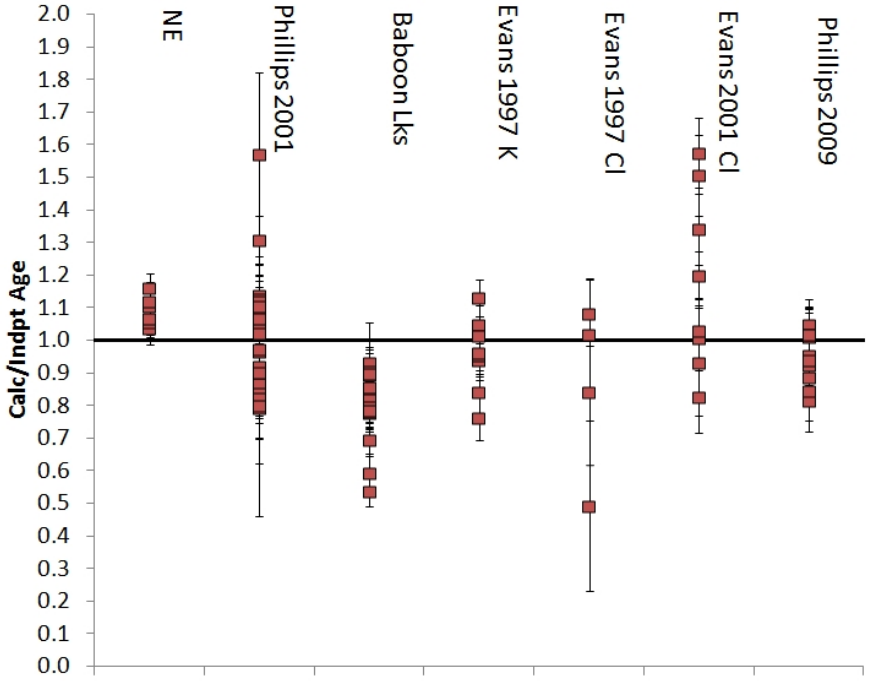

Figure 8.16: The normalized (calculated/independent) ages of the samples in the secondary - quantitative dataset. The data from Evans et al. (1997) is broken into potassium feldspar samples (Evans, 1997-K) and leachate samples (Evans, 1997-Cl).

pattern could also be due to the scatter and the small number of samples at each site (3-4), so there is no clear indication of bias.

A completely independent dataset that was not used for calibration, the secondary quantitative dataset, was used to assess the primary calibration parameters as well. The quantitative secondary dataset was aged using the final production rates and the normalized ages are plotted by site in Figure 8.16. Most sites plot evenly around one, although the New England site plots slightly above the line and the Baboon Lakes (all samples other than hornblende) site plots slightly below the line.

The general validity of the estimate of $P_f(0)$ derived from the CRONUS

Dataset	$P_f(0)$
Baboon Lakes	594
Tabernacle Hill WR	814
Average (TAB + BL)	704
Copper Canyon (quartz)	679

Table 8.4: Comparison of calibrated values of $P_f(0)$ for different datasets. For all calibrations here,the spallation values were fixed and the $P_f(0)$parameter was calibrated. The Lifton/Sato scaling method was used for all the calibrations shown here. These are not directly comparable to previously published values due to the differences in scaling method.

dataset can be tested by comparison with the secondary dataset. We performed this test by aging the secondary quantitative dataset using the CRONUS $P_f(0)$ value (704 n (g air)$^{-1}$yr^{-1}) and alternative values of the parameter. A graph showing the normalized ages of the secondary dataset, as plotted by percent production from Cl, is shown in Figure 8.17 in order to test for bias in the secondary dataset. For comparison, the same plot is shown with the Copper Canyon quartz composition result shown.

In order to assess the accuracy of the calibrated $P_f(0)$ value, the secondary dataset ages were calculated using the $P_f(0)$ value. If there is a problem with the value for $P_f(0)$, a deviation from the 1:1 line will be apparent. A graph showing the normalized ages, as calculated using the value calibrated from the CRONUS value, is plotted in Figure 8.17. The figure also shows the normalized ages as calculated for Copper Canyon (mixed composition). The plot for the CRONUS value shows no bias with an increase in the percent production from chlorine. On the other hand, the plot for the mixed composition value from Copper Canyon shows a clear downward trend with increasing chlorine. Although the mixed composition from Copper Canyon is not the best-fit composition, it does a good job illustrating the misfit of higher (or lower) $P_f(0)$ values to the secondary dataset.

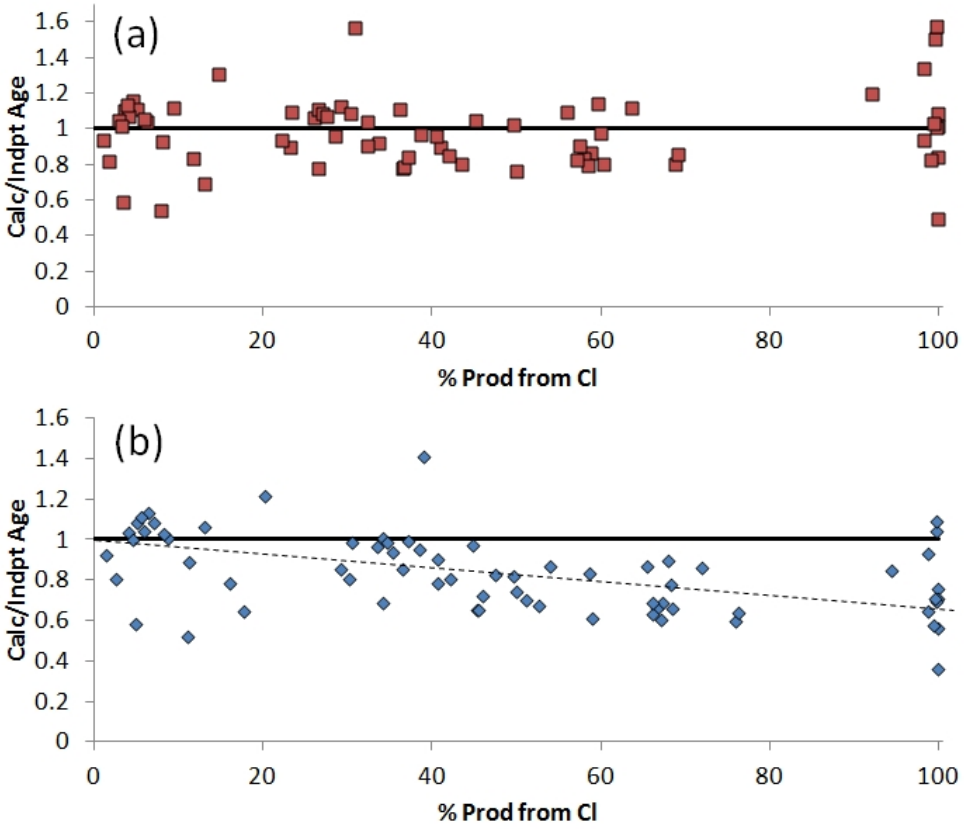

Figure 8.17: The normalized (calculated/independent) ages of the samples in the secondary - quantitative dataset. (a) Normalized ages plotted using $P_f(0) = 704$ n (g air)$^{-1}$yr^{-1}. (b) Normalized ages plotted using $P_f(0) = 1016$ n (g air)$^{-1}$yr^{-1}, the value from the mixed composition calibration from Copper Canyon. The dashed line represents the general downward trend seen in the dataset and is not a best-fit line.

The uncertainty on the chlorine-36 technique is bounded by the root mean square error of the calibration and secondary datasets. The minimum uncertainty in the ages is determined by the RMSE on the calibration dataset, which is 7.5%. The maximum uncertainty in the chlorine-36 technique is represented by the RMSE of the secondary quantitative dataset, which is 20.0%. The uncertainty for chlorine-36 is likely somewhere between these two bounds.

An alternative for assessing the uncertainty associated with the $P_f(0)$ parameter is to use the distributions of the normalized sample ages and determine the overall amount of unattributed variation. The unattributed variation is used to estimate the $P_f(0)$ uncertainty using following method.

The samples in the quantitative secondary dataset (no calibration samples included) were each aged using the final calibrated production rate parameters. The uncertainty was propagated for all input parameters, with the production rate uncertainties intentionally set to 0. The samples were broken into categories based on the range of percent production from Cl (Column 1 in Table 8.5. The propagated uncertainties were averaged and the percent uncertainty for each category was placed in the second column of Table 8.5. The sample ages were plotted using a 'camel plot' (Balco, 2011), and then summed for each category. These sums were plotted and then a normal distribution was fitted to those samples by means of minimizing the absolute value of the difference of the calculated and observed distributions, assuming the mean of the calculated distribution was one, shown in Figure 8.18. The difference between the reported uncertainties and the actual standard deviation of the fitted distribution (Column 3 in Table 8.5) is the unattributed variation (Column 4 in Table 8.5).

This additional spread of the data beyond the uncertainties propagated for all of the other parameters results from a combination of the uncertainty associ-

% Production from Cl	Avg Calc Age Uncertainty	Avg Fitted Age Variability	Unexplained Variability	3% Indpt Age Error Subtracted
0-10%	5.5	11	5.5	2.5
10-35%	6.50	19	7.5	4.5
35-80%	9.0	15	10.5	7.5
90-100%	13.4	28	14.6	11.6

Table 8.5: Data for calculation of sample variation as a function of percent production from Cl. See text for detailed description. Note: there are no samples in the 80-90% production from Cl range.

ated with the value of Pf(0) and errors in the assigned values for the independent ages of the samples. Errors in the assignment of independent ages were assumed to contribute 3% to the uncertainty based on calculations of the independent ages for the quantitative dataset, with the remainder corresponding to uncertainty in the age due to uncertainty on the $P_f(0)$ parameter (Column 5 in Table 8.5). The unattributed variation increases with increasing percent production from Cl, as seen in Figure 8.19. The two limits of this plot represent the uncertainties for spallation reactions (0% production from Cl) and chlorine reactions (100% production from Cl). This observed unattributed variation, that is unexplained by uncertainty in any other parameters, can be converted into uncertainties on the production rate parameters. However, a 2% uncertainty in the age is not equivalent to a 2% uncertainty in the production rate. The production rates uncertainties were increased proportionally (within rounding error) until the observed variability matched the unattributed variability. The final production rate uncertainties are 4% for spallation parameters and 20% for $P_f(0)$, which corresponds to parameters and uncertainties of 56.0 ± 2.2 at (g Ca)$^{-1}$yr^{-1}, 157 ± 6 at (g K)$^{-1}$yr^{-1}, and 704 ± 141 n (g air)$^{-1}$yr^{-1}. These values change slightly depending on the number of groups used in the analysis. Four groups with approximately equal numbers of samples are used to determine the final uncertainties. The parameter

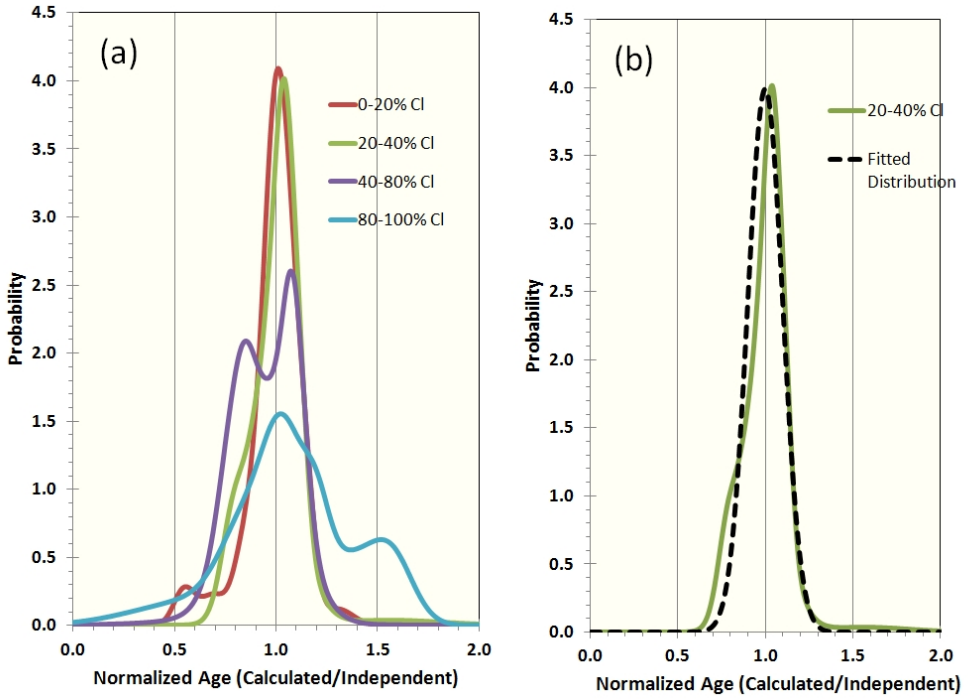

Figure 8.18: (a) The observed probability distributions of the normalized ages of all the samples in the secondary quantitative dataset, subdivided by percent production from Cl. (b) An example of the fitted line for the 20-40% production from Cl group. The dashed line indicates the fitted normal distribution.

uncertainty for $P_f(0)$ is consistent with the maximum uncertainty limit of 20% calculated using the RMSE.

The variation in the reduced chi-squared value with changing $P_f(0)$ is shown in Figure 8.20. The values were based on the samples in the quantitative secondary dataset that had >50% production from Cl, as calculated using a $P_f(0)$ value of 704. The figure shows a minimum between ~700-750 n (g air)$^{-1}$yr^{-1}. The shaded region indicates the range of $P_f(0)$ values based on the value and uncertainties presented here. The calibrated $P_f(0)$ very clearly covers the minimum chi-squared value, corresponding to reduced chi-squared values of ~1.9-2.4. Based on the figure, the calibrated value for $P_f(0)$ appears to be a relatively conservative estimate.

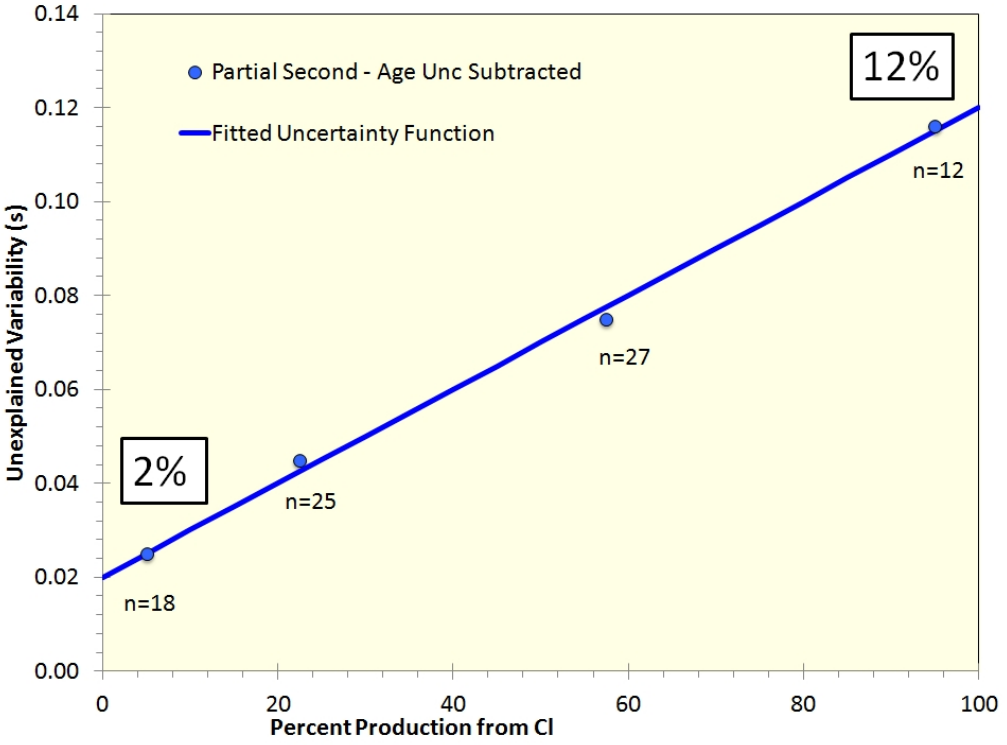

Figure 8.19: Plot illustrating the dependence of the unexplained (or "unattributed") variability of the secondary quantitative dataset as a function of percentage production from Cl. The circles are the secondary quantitative dataset with the samples used to calibrate $P_f(0)$ (TAB whole rock and Baboon Lakes hornblende) removed.

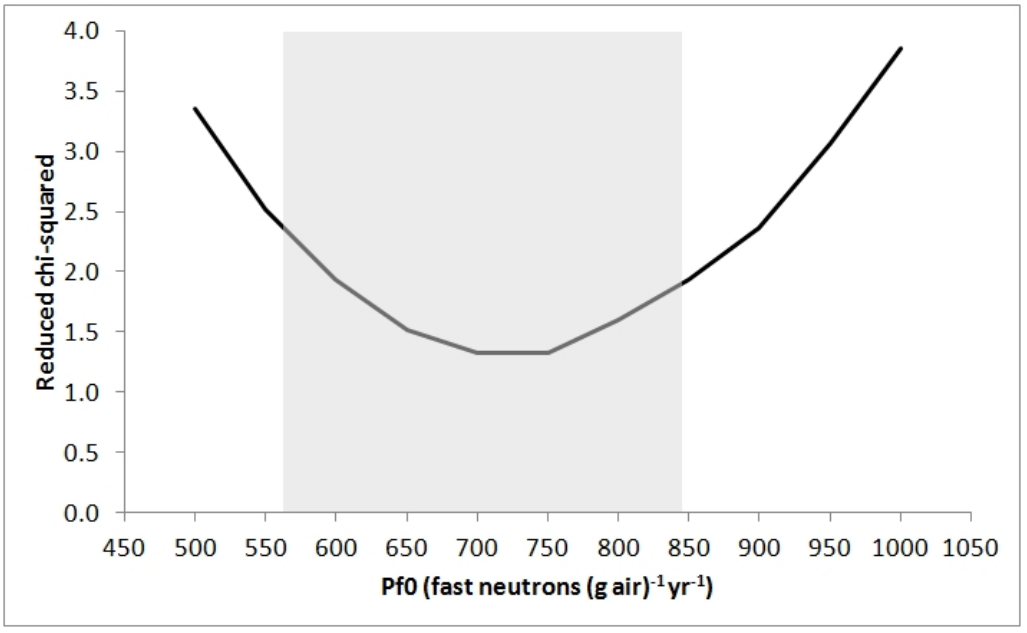

Figure 8.20: The chi-squared value as a function of $P_f(0)$, calculated from samples with >50% production from Cl when calculated using a $P_f(0)$ of 700. Shaded region indicates the final uncertainties assigned to the $P_f(0)$ parameter.

In order to look at possible bias due to composition, the samples were plotted on a ternary diagram (see Figure 8.21) and color-coded to show the normalized ages using the final calibrated production rates. Most samples are very close to one. Although there are several low ages that plot together in the high-potassium corner, there are no clear trends visible in the composition plot that indicate bias based on target element.

The qualitative secondary dataset, which contains whole-rock samples from Licciardi et al. (2008) and mineral-separate samples from Schimmelpfennig et al. (2009), are aged using the new production rates and graphed as normalized ages in Figure 8.22. These datasets were excluded from the quantitative secondary dataset due to large uncertainties on the independent age constraints (Schimmelpfennig et al., 2009) or scatter in the dataset and sample cover (moss) that may affect the low-energy flux (Licciardi et al., 2008). The mineral separates plot

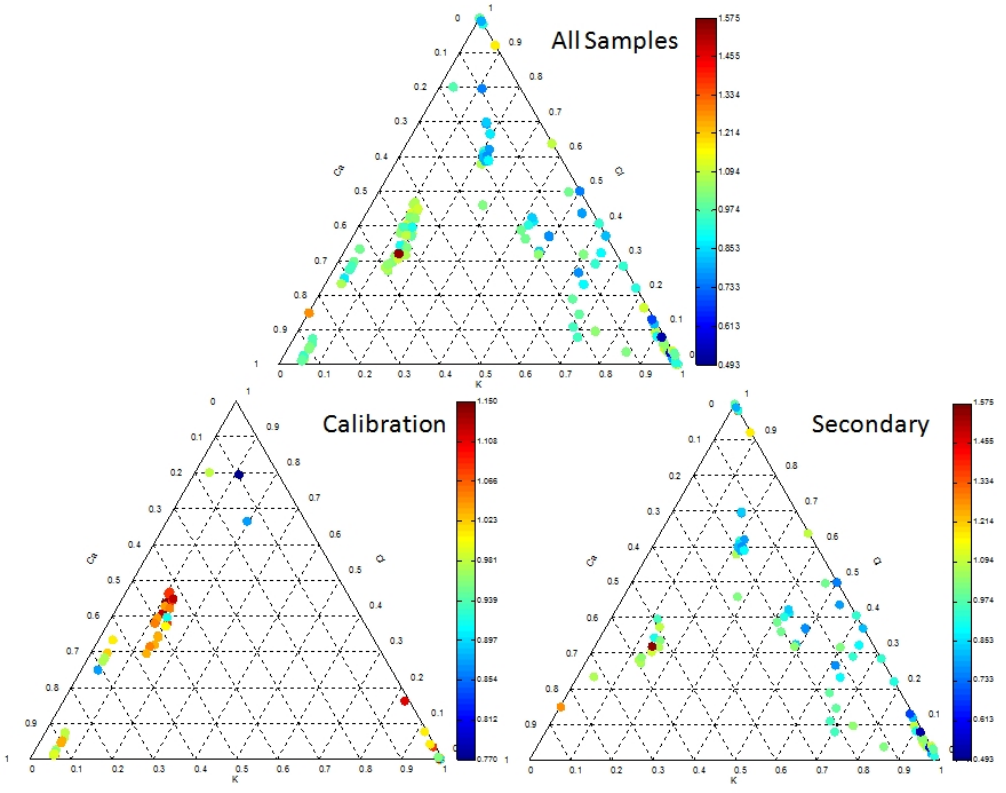

Figure 8.21: Ternary diagram showing the normalized ages for all the calibration and secondary dataset samples. The top plot shows the combined calibration and secondary datasets. The Calibration plot shows all samples used for calibration (includes the Baboon Lakes hornblende and Tabernacle Hill whole-rock samples) and the Secondary plot shows the quantitative secondary dataset. Note: The color scale is not the same for all plots. Data was plotted using Theune (2005).

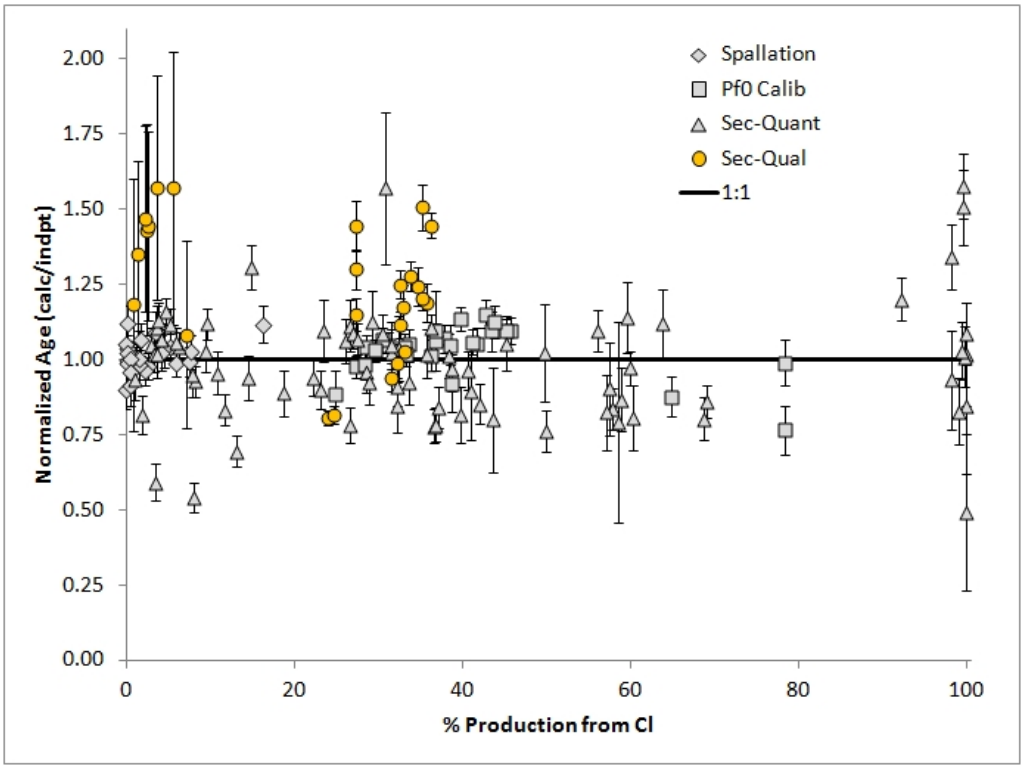

Figure 8.22: Normalized ages for the secondary-qualitative dataset (yellow circles). The other datasets are plotted as gray symbols, including spallation calibration, $P_f(0)$ calibration

very close to the 0 percent production from Cl and show some scatter. This group is offset from the 1:1 line, although the large uncertainties on the samples means that many of the samples are still within uncertainty of the line. The whole-rock samples plot between 20-40% production from Cl. These samples are show significant scatter, although some of the samples still plot close to one. In neither case are the samples completely inconsistent with the calibrated production rates.

After formatting data from published calibration papers, new calibrations were performed on those samples using the same method as the primary calibration. The results from the calibration studies discussed here are shown in Table 8.6. The Phillips et al. (2001) study had a very low p-value, whereas the Swanson and Caffee (2001) study has a reasonable fit to the data with a p-value

of 0.023. The potassium production rate from the Phillips data is consistent with the current study; however, the other production rates are significantly different, including those from the Swanson study.

Other calibrations, such as those by Evans et al. (1997), used mineral separates so that one target element dominates the production. This means that only one production rate parameter can be calibrated in a single study. Using the updated Evans dataset (as discussed in Section 8.6.2), the potassium production rate has been reevaluated and is consistent with the results from this study, despite the p-value equal to zero. Stone et al. (1996) was not used as a comparison dataset because those samples are incorporated into this study.

Goodness of fit was not assessed quantitatively in previous calibration studies, so there is no published basis for comparison. Direct comparison of previously produced production rates is also impossible due to the use of different scaling models. There are seven possible scaling models presented in the CRONUScalc program (see Chapter 2), but only the Lifton/Sato nuclide dependent model has been used to produce the results shown here. There will be small variations in the actual values produced by each scaling model, but the comparisons and trends discussed in this chapter should remain consistent throughout all the models. In order to properly implement each scaling model in the program, the production rates must be calibrated from the original data using the each scaling model. In the CRONUScalc program, this is done using identical calibration datasets for each nuclide in order to provide consistent results. The methods outlined in this chapter will be used to produce a set of consistent production rate parameters for each possible scaling model. These final production rates will be distributed with the final CRONUScalc code.

Study	Ca	K	$P_f(0)$	p-value
This study	56.0 ± 2.2	157 ± 5	704 ± 140	0.83 (Ca)/0.15 (K)
Phillips et al. (2001)	$72.5 \pm$ NA	$153.2 \pm$ NA	$613.4 \pm$ NA	1.3×10^{-7}
Swanson and Caffee (2001)	77.5 ± 2.7	217.0 ± 5.8	1006.8 ± 26.0	0.023
Evans et al. (1997)		$167 \pm$ NA		0

Table 8.6: Final production rates recalculated using Lifton (2012) scaling. Uncertainties not shown for studies with a very low p-value.

8.8.1 Implications of Uncertainty Analysis for Sample Ages and Uncertainties

The implications for a quantitative uncertainty estimate for the chlorine-36 technique are significant. This assessment provides the first opportunity to present realistic uncertainties on sample ages. The broad bounds on the maximum and minimum uncertainty, found by calculating the RMSE on the calibration and secondary datasets (see Section 8.8), limit the overall uncertainty to between 7.5 and 20.0%.

The analytical uncertainty from the AMS and input sources can be combined with the uncertainty on the production rates to provide a better estimate of the total uncertainty for each sample. The primary and secondary datasets were aged both with and without the production rate uncertainties. The results show that the increase in uncertainty was between 4-20%. In most samples, this additional uncertainty from the production rate parameters is some combination of the uncertainty on the spallation and $P_f(0)$ parameters. Although the uncertainty on $P_f(0)$ is 20%, few samples will see this uncertainty because few samples have >40% production by Cl. Most sample uncertainties remain relatively low (<10%). Although this is larger than the commonly presented AMS uncertainties of 3-6%, this is a more realistic value and better represents the accuracy of the chlorine-36 technique.

8.9 Sensitivity Analysis

A sensitivity analysis was performed in order to determine the influence of input parameters on final results. This was accomplished by calculating partial derivatives for each parameter with respect to age, holding all other parameters

constant. A wide assortment of the calibration samples were used in order to include differing compositions and locations. The derivatives were calculated for each parameter in terms of kyr age change per one unit change in the parameter. For each sample, the derivative was then multiplied by a reasonable uncertainty for that particular parameter. The parameters and their uncertainties are listed in Table 8.23. These were fairly conservative uncertainties, but they were designed to test the broadest possible impact on any given sample.

The samples were divided into three categories and the major, minor, and non-contributing factors were determined for each group. The results are summarized in Figure 8.23. The major factors contributing to the uncertainty on the age, arbitrarily defined as parameters that have more than a 2.5% effect on sample age, were the nuclide concentration and average atmospheric pressure. Uncertainty on nuclide concentration can be reliably estimated, whereas the pressure was an unexpected major contributing factor. Each of these parameters contributes up to 8% uncertainty to the age. Minor contributing factors, defined as parameters that affect most of the samples in the group by 1-2%, include erosion rate, shielding, attenuation length, thickness, and density. For high-Cl samples, such as whole-rock basalts, the composition parameters are also minor contributing factors. For composition parameters that contribute significantly, the composition of the sample determines the actual impact of the particular parameter.

Hypothetical depth-profile samples were created by analyzing two surface samples as if they were at depths of 25, 50, 75, 100, 250, 300, and 400 g/cm^2. The results are similar in many ways to the surface sample sensitivity analysis discussed above. Many of the major contributing factors, such as uncertainty in concentration and pressure, still contribute significantly to the uncertainty of the

Input	Sample Range	uncert	units	Whole Rock	Min Sep	High Cl - depth	Low-Cl - depth
Conc	Actual	Actual	at/g				
erate	0.05-1.9	0.5*actual	g/cm^2				
water cont	0.5	1	vol %				
density	2.3-2.8	0.3	g/cm^3				
thick	3-8	1	cm				
press	565-974	5	hPa				
shielding	0.98-1.00	0.005	--				
Λ_{eff}	140-170	10	g/cm^2				
Bulk Na_2O	3-4	0.4	wt %				
Bulk Al_2O_3	14-19	0.4	wt %				
Bulk K_2O	0.5-5	0.4	wt %				
Bulk CaO	0.2-10	0.4	wt %				
Bulk TiO_2	0.2-2	0.4	wt %				
Bulk MnO_2	0.01-.15	0.4	wt %				
Bulk Fe_2O_3	1-11	0.4	wt %				
B	0-100	10	ppm				
Sm	2-13	2	ppm				
Gd	2-13	2	ppm				
U	0.3-10	2	ppm				
Th	1-12	2	ppm				
Cr	0-400	20	ppm				
Targ K	0.2-13	0.1	wt %				
Targ Ca	0.2-10	0.1	wt %				
Targ Cl	1-700	0.5	ppm				
Depth	0-400	5 cm equiv.	g/cm^2				

Figure 8.23: Figure showing the relative influence of realistic uncertainties on the ages of four types of samples: whole-rock (high-Cl) surface samples, mineral separate (low-Cl) surface samples, high-Cl depth samples, and low-Cl depth samples. The red boxes indicate major influence (>2.5%), blue indicates minor influence (0.5-2.5%), white indicates non-contributing parameters, and the gray indicates that the parameter changes in influence with depth and are minor contributors. Only parameters that contribute to the uncertainty in some way are shown. All other input parameters are considered "non-contributing" to the uncertainties on samples. The uncert represents the actual level of the uncertainty applied in the analysis, with units also shown. 'Targ' indicates the target composition. Depth uncertainties of the equivalent of 5 cm were used only for depth-profile samples. 'Erate' indicates the erosion rate.

sample. However, there are additional factors that contribute to uncertainty that were not significant in the previous analysis, such as attenuation length, which is more important in depth profiles than surface samples, and depth to top of sample. Once again, the difference between high-Cl and low-Cl samples is clear. The high-Cl profile uncertainties depends significantly on the composition parameters and water content, while the spallation-dominated profile uncertainties depend more on the target composition.

The implications of the sensitivity analysis are twofold. First, high-Cl sample results depend significantly on the compositional parameters, especially trace elements. This is an expected result, but it does highlight the importance of measuring these parameters accurately if samples contain high Cl. Second, mean atmospheric pressure is the single biggest contributing factor other than the measured concentration of the nuclide. The pressure variability through time is difficult to tightly constrain and the history likely varies from site-to-site. This offers a possible explanation for previously unexplained site-to-site variability. If future work could lead to the reduction of pressure uncertainty, the uncertainties on the ages of the samples could also be reduced.

8.10 Internuclide Comparison

One of the goals of the CRONUS-Earth Project was to compare results between nuclides, beyond the typical Al/Be pair. Aliquots of the CRONUS samples were distributed to many labs for analysis of as many nuclides as possible for a given lithology. One pair of results that has not been compared in the past is beryllium-10 and chlorine-36 in the same sample. This comparison is performed for both published studies (Section 8.10.1) and for the CRONUS-Earth dataset (Section 8.10.2).

8.10.1 Cl and Be Comparison

Sample information from published studies containing both nuclides (^{36}Cl and ^{10}Be) processed on the same sample, when possible, or the from the same site was extracted for this comparison. For landforms with significant scatter, such as glacial moraines, the average ages computed from each nuclide were used instead of the individual ages from each sample. The results were plotted as the chlorine-36 age vs the beryllium-10 age, as seen in Figure 8.24. The sources of the data are given in the caption, with the full datasets provided in Appendix C.3.

Most of the ^{36}Cl-^{10}Be pairs in Figure 8.24 show good correspondence in the calculated ages. However, a subset of the samples are characterized by significantly older ^{10}Be there appears to be a very strong bias in the older samples, with the ^{10}Be than ^{36}Cl ages. This is especially clear in the Phillips et al. (1997) and Benson 2004/06 datasets. The CRONUS-Earth samples, which have well-constrained independent ages and well-known sample parameters, show no apparent bias. This indicates several possibilities for the anomalous samples. It is possible that there is a problem with older samples, so the CRONUS-Earth samples, which are restricted to ages <19 ka, would not reveal a problem. The 'Sierra Comp' samples as well as the 'Rood-Old' samples (defined in the caption for Figure 8.24) also plot very near the 1:1 line.

The other possible reasons for the discrepancy include incorrectly assessed erosion rates or local spatial variability. A large portion of the anomalous samples (14 out of 15 points) are from central/southern Rocky Mountains, including Benson 2004/2005, Rood 2011, and Phillips 1997. The sample input information was taken directly from the original papers, although many assumptions were necessary in order to run the CRONUScalc program to calculate ages. Parameters

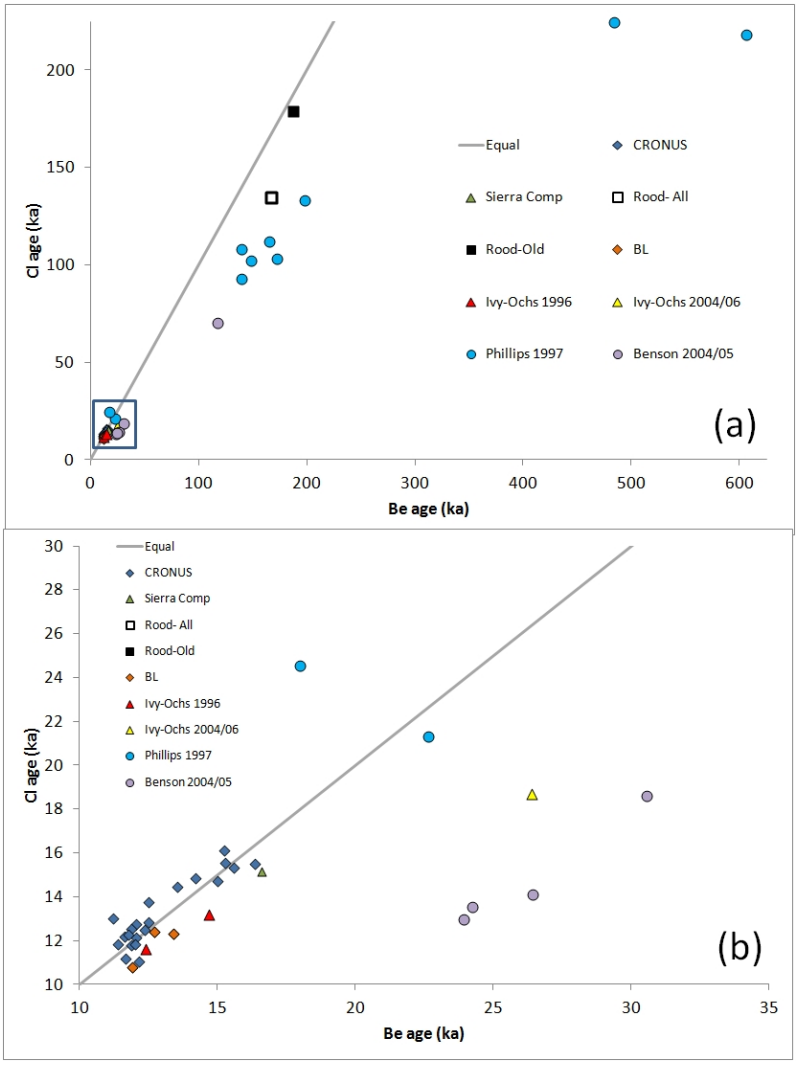

Figure 8.24: Figure showing compared ages of chlorine and beryllium samples that were processed on the same samples or comparative samples. The inset shows the enlargement of the younger samples. (a) All Cl-Be sample pairs. The box indicates the location of plot (b). (b) Close-up of the younger samples. The CRONUS samples represent the New England, Huancané, and Scotland. The 'Sierra Comp' samples are a comparison of the average of the Phillips et al. (2009) and the average of the revised Nishiizumi et al. (1989). The 'Rood-All' dataset is the average of the Rood et al. (2011) Buckeye Creek outwash terrace (Tahoe) compared to the average of the Tahoe moraine in the Bishop Creek drainage samples in Phillips et al. (2009). 'Rood-Old' compares only the oldest four samples on each of the moraines in the Rood-All dataset. The other datasets are Ivy-Ochs et al. (1996), Ivy-Ochs 2004/06 is the combination of Ivy-Ochs et al. (2004) and Ivy-Ochs et al. (2006), Phillips et al. (1997), and Benson 2004/05 is the combination of Benson et al. (2004) and Benson et al. (2005).

like erosion rate, full composition, water content, shielding, and snow correction were not always clearly listed in the paper. If the assumptions were incorrect, the resulting ages could be systematically biased for the affected sites.

A possible source of bias is processing procedures. Samples in the Phillips et al. (1997) study were dissolved for a pre-determined period of time. It is possible that these samples were processed prior to complete dissolution, which could lead to bias in the results. Details are not available to determine if this actually occurred.

Aspects of the code, such as nuclide-dependent scaling factors and production rates of both nuclides, have been assessed and found not to be the cause of the bias. Other sections of code were checked for bugs and were also not the cause of the bias. Currently, the source is unknown and additional investigation is necessary. Despite the discrepancy in some samples, many comparison samples fall close to the 1:1 line and do not show any significant bias.

8.10.2 Internuclide Comparison: Chlorine-Beryllium Ratios

Another comparison of the ^{36}Cl and ^{10}Be pair is the ratio of the nuclide concentrations in the sample. The raw sample ratios are calculated by simply dividing the total concentration of chlorine-36 by the total concentration of beryllium-10. The raw ratio is plotted in Figure 8.25, along with the raw ratio predicted by the flux-only scaling model and the nuclide-dependent scaling model of Lifton (2012), discussed in Section 2.6. The predicted concentrations are calculated using the CRONUScalc code that accounts for the half-life of each nuclide, so no additional adjustments are made here. The ratios predicted by the nuclide-dependent scaling model appear to be closer to the measured points for Scotland and New

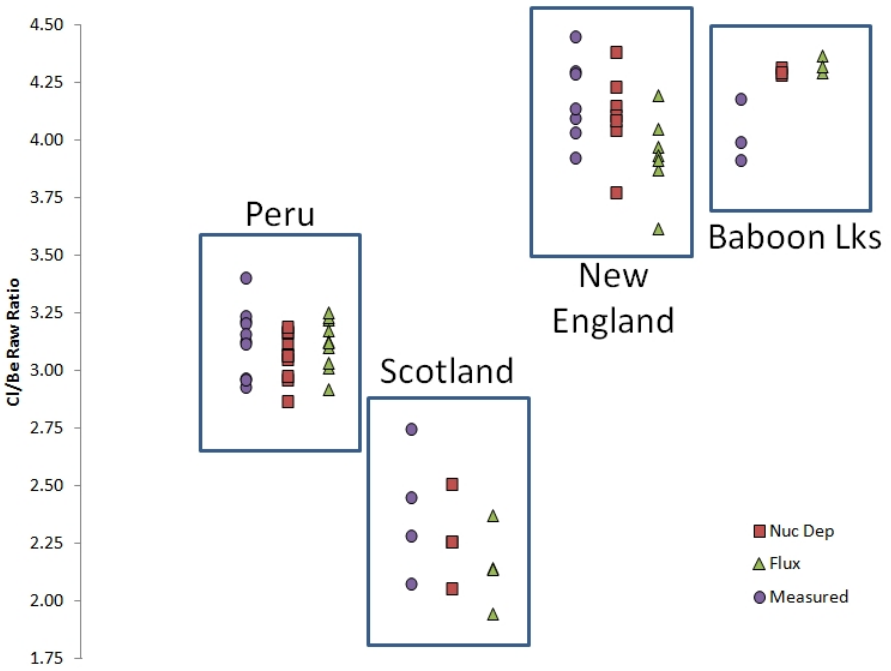

Figure 8.25: Ratios calculated for the measured concentrations of chlorine-36/beryllium-10 (represented as circles). The ratios were also predicted by the CRONUScalc program using the Lifton/Sato flux-only scaling (triangles) and the nuclide-dependent (squares) scaling models. For a discussion of scaling models, see Section 2.6. In all cases, potassium feldspar mineral separates are compared against the beryllium concentrations.

England than those predicted by the flux-only scaling. While this is not conclusive, it is certainly suggestive that concentrations predicted by the nuclide-dependent scaling matches the data better than the predictions from the flux-only scaling model.

A recent transect study on basalts on Kilimanjaro volcano by Schimmelpfennig et al. (2011) compared measured ratios from three different nuclides and concluded that the ratios did not scale differently with altitude. However, in our results, we have four sites represented and at least two (Scotland and New England) of those four sites suggest that nuclide-dependent scaling is more appro-

priate than flux-only scaling. Two of the sites (Peru and Baboon Lakes) are inconclusive, although both are consistent with the nuclide-dependent scaling models. Based on our results from these four sites, the use of the Lifton/Sato nuclide-dependent scaling is supported.

8.11 Conclusion

The multi-step chlorine-36 calibration produced a complete set of chlorine-36 parameters. The calibration of spallation production rates was performed using a low-Cl dataset composed of mineral separates from Tabernacle Hill, UT (for Ca), Scotland and Peru (for K). The calibration appears to be very robust, insensitive to the $P_f(0)$ parameter, and it fits the secondary low-Cl dataset well. The inclusion of a low-latitude, high-elevation site (Peru) in the potassium calibration is significant and allows allows a much clearer discrimination between the various scaling models than was possible with previous calibration datasets.

Two previously published chlorine-36 muon calibration profiles were reanalyzed here to provide more accurate muon production parameters parameterized to match the new Heisinger/Sato formulation. The reanalysis of the calcium profile provided in Stone et al. (1998) yielded σ_0 and f* values of $(0.84\pm0.45)\times10^{-29}$ and $1.68\pm1.18\%$, respectively. The reanalysis of the potassium profile in Evans (2001) yielded σ_0 and f* values of $(25.8\pm79)\times10^{-30}$ and $4.6\pm10.6\%$, respectively. Although the uncertainties on these parameters is relatively large, the newly calibrated rates fit the profiles better than the published values from Heisinger et al. (2002b,a).

The calibration of $P_f(0)$, the low-energy neutron production parameter, was more complicated than the other parameters. There is evidence to indicate

that there may be some site-to-site variability that is not currently explained by the model used in the CRONUScalc program (described in Chapter 2). Possible explanations for this are water content and geometry of the sampling sites. However, for most sample analyses, especially low-chlorine samples, these variations will be small and an average value of $P_f(0)$ is sufficient. The value produced by the average of the CRONUS-Earth datasets (Tabernacle Hill basalt whole-rock samples and the Baboon Lakes hornblende mineral separates) is 704 n (g air)$^{-1}$ yr^{-1}. This value appears to provide a reasonable fit to all the samples in the secondary dataset. The data from Copper Canyon, an independent set of chlorine-36 depth-profile samples, is also consistent with this value of $P_f(0)$. Future work is necessary to produce a better model of the low-energy neutron flux, especially concerning water content, in order to improve the model.

The uncertainty of the full chlorine-36 technique can be assessed in two ways. The overall bounds on the uncertainty can be determined by using maximum and minimum constraints on the uncertainty from calculated RMSE values. The minimum uncertainty is found by aging the samples used in the calibration and computing the RMSE (7.5%), which is used as the minimum uncertainty. For the maximum uncertainty, the same procedure is applied to the secondary dataset (20.0%). These uncertainties likely constrain the overall uncertainty on the chlorine-36 technique. In order to assign uncertainties to the production rate parameters, normal distributions were fitted to subsets of the samples as a function of percent production from Cl and the amount of 'unattributed variation' was determined. This uncertainty, minus an estimated 3% uncertainty due to independent age constraint uncertainty, was attributed to production rate parameters. Using samples grouped by percent production from chlorine, uncertainties for the spallation production parameters (3%) and $P_f(0)$ (20%) were estimated.

The final calibrated production rate parameters, including uncertainties are 56.0 $\pm$ 2.2 at (g Ca)$^{-1}$yr^{-1}, 157$\pm$ 6 at (g K)$^{-1}$yr^{-1}, and 704 $\pm$ 141 n (g air)$^{-1}$yr^{-1}. Studies quantifying the inter- and intra-lab variability would be useful for estimating the portion of total uncertainty due to processing and measurement techniques.

New results from a CRONUS project to re-examine the Puget Lowlands calibration location, originally presented in Swanson and Caffee (2001), are consistent with the calibrated production rates presented here. The samples were analyzed by two different labs and are not consistent with the production rates published in Swanson and Caffee (2001) or with the recalibrated version of those production rates using the original samples and the CRONUScalc model. It is possible that the original study had some sort of systematic analytical problems.

8.12 Future Work

Although the CRONUS-Earth project had many sub-projects, there are additional projects that were not covered in the scope of this project. One of the remaining uncertainties in the chlorine-36 technique is repeatability and variability due to processing. Three parts of this include repeatability in a single lab, differences in procedures between labs, and variability between labs. A study using a single geologic sample measured repeatedly over time would yield a better understanding of the uncertainty that comes from the processing technique. A systematic analysis of how each processing step affects the procedure would help in the creation of a single, accurate procedure for chlorine-36 processing. A complete intercomparison involving as many labs as possible using both Ca and K materials would be useful in assessing the variability that currently exists and in assessing the improvements as new processing procedures are implemented.

Over the long term, this type of study could help reduce the scatter or bias between labs.

The site-to-site variability in the value of $P_f(0)$ could be due to many different factors, including a high water content in the rock or soil. By using a neutron detector, the thermal neutron flux could be measured at calibration locations and compared to the values predicted by the code as well as the geological samples.

Current snow corrections for cosmogenic nuclides account only for the change in attenuation length for fast neutrons and not for the thermalization of neutrons. A snow-correction model that accounts for the change in the energy spectrum of neutrons reaching the sample would be an improvement for snow-corrected chlorine-36 samples.

The current CRONUScalc code is designed to age samples with any one of five nuclides, but it would be useful to have a calculator that could incorporate information from two or more nuclides in a single sample or from a single surface to provide the best-fit age. This also applies to depth-profile calculations where it might be useful to be able to calculate the best-fit parameters given two nuclide profiles. Another feature that should be incorporated into CRONUScalc is an erosion-rate calculator for surface samples.

APPENDIX A

CRONUSCALC PROGRAM APPENDIX

A.1 Glossary of Terms and Equations

Table A.1: Glossary of terms and equations

Term	Definition
General parameters and subscripts	
bulk	In reference to the bulk rock composition of the sample
C_k	Mass concentration of element k [g element k/(g material)]
eth	Subscript used to denote the "epithermal" production pathway, defined as neutrons with energies of 0.5 eV to 0.1 MeV.
h	Atmospheric depth $[g/cm^2]$
k	Subscript used to denote a particular cosmogenic-producing element
m	Subscript used to denote a particular cosmogenic nuclide
m	Molar concentration
μ	Subscript used to denote the "muon" production pathway
ρ	Density $[g/cm^3]$
s	Subscript used to denote the "spallation" production pathway
target	In reference to the particular target fraction of the sample, specifically in the case of mineral separates
th	Subscript used to denote the "thermal" production pathway, defined as neutrons with energies of <0.5 eV.
z	Ordinary linear distance $[cm]$

Continued on next page

Table A.1 – continued from previous page

Term	Definition
Z	Mass depth below the surface $[g/cm^2]$ $$Z(z) = \int_0^z \rho(z)dz \quad \text{(A.1)}$$
Cosmic Rays	
c	Speed of light (see eqn 2.1)
e	Particle charge (see eqn 2.1)
p	Particle momentum (see eqn 2.1)
R	Rigidity of a particle (see eqn 2.1)
S_{el}	Latitude/Elevation scaling coefficient (see scaling scheme section) $[unitless]$
S_T	Topographic scaling coefficient describing the shielding from surrounding topography [unitless]
θ	Inclination angle from the horizontal $[degrees]$
z_p	Vertical penetration depth $[g/cm^2]$ $$z_p = \Lambda_{f,p} cos\phi \quad \text{(A.2)}$$
Spallation	
$I(\theta)$	Intensity. See eqn 2.3. I_0 is the intensity of I for a sample with 0 dip.
$\Lambda_{\text{f,e}}$	Effective attenuation length for fast neutrons. See section 2.4.1.
$P_{s,m}$	Production rate for spallation of nuclide m. See eqn 2.2.
$P_{m,k}$	Production rate of nuclide m from target element k. See eqn 2.2.
θ	Sample dip/inclination as measured from the horizontal. See eqn 2.3.
Epithermal Production	
$\bar{A}_{ss}$	Average atomic weight of the bulk rock [g/mol] $$\bar{A}_{ss} = \frac{\sum_k A_k N_{k,ss,bulk}}{\sum_k N_{k,ss,bulk}} \quad \text{(A.3)}$$

Continued on next page

Table A.1 – continued from previous page

Term	Definition
$\bar{A}_a$	Average atomic weight of the atmosphere; constant = 14.5 $[g/mol]$ (Phillips and Plummer, 1996)
A_k	Atomic weight of element k [g/mol]
$\Delta(\mathscr{F}\Delta\Phi)^*_{eth,ss}$	Difference between $\mathscr{F}\Delta\Phi)^*_{eth}$ in the atmosphere $(\mathscr{F}\Delta\Phi)^*_{eth,a})$ and the subsurface $(\mathscr{F}\Delta\Phi)^*_{eth,ss})$ $$\Delta(\mathscr{F}\Delta\Phi)^*_{eth,ss} = (\mathscr{F}\Delta\Phi)^*_{eth,a} - (\mathscr{F}\Delta\Phi)^*_{eth,ss} \quad \text{(A.4)}$$
$\Delta\Phi^*_{eth,ss}$	Difference between the hypothetical equilibrium epithermal neutron fluxes in atmosphere and rock $[neutrons/cm^2/yr]$ $$\Delta\Phi^*_{eth,ss} = \Phi^*_{eth,a} - \Phi^*_{eth,ss} \quad \text{(A.5)}$$
$\Delta\Phi^*_{eth,a}$	Difference between the hypothetical equilibrium epithermal neutron fluxes in atmosphere and rock $[neutrons/cm^2/yr]$ $$\Delta\Phi^*_{eth,a} = \Phi^*_{eth,ss} - \Phi^*_{eth,a} \quad \text{(A.6)}$$
$\Delta\Phi^{**}_{eth,ss}$	Adjusted difference between the hypothetical equilibrium epithermal neutron fluxes in atmosphere and rock. $[neutrons/cm^2/yr]$ $$\Delta\Phi^{**}_{eth,ss} = \Phi^*_{eth,a} - \frac{D_{eth,ss}}{D_{eth,a}}\Phi^*_{eth,ss} \quad \text{(A.7)}$$
$\Delta\Phi^{**}_{eth,a}$	Adjusted difference between the hypothetical equilibrium epithermal neutron fluxes in atmosphere and rock. $[neutrons/cm^2/yr]$ $$\Delta\Phi^{**}_{eth,a} = \Phi^*_{eth,ss} - \frac{D_{eth,a}}{D_{eth,ss}}\Phi^*_{eth,a} \quad \text{(A.8)}$$

Continued on next page

Table A.1 – continued from previous page

Term	Definition
$D_{eth,ss}$	Diffusion coefficient for epithermal neutrons in subsurface $[g/cm^2]$ $$D_{eth,ss} = [3\Sigma_{sc}(1 - \frac{2}{3\bar{A}})]^{-1} \quad \text{(A.9)}$$
$D_{eth,a}$	Diffusion coefficient for epithermal neutrons in air $[g/cm^2]$ can be calculated using values of (sc,a)=0.3773 $[cm^2/g]$ (Phillips and Plummer, 1996). (A.10)
$(F\Delta\Phi)^*_{eth,ss}$	Difference between the epithermal neutron flux if there was no boundary ($\Phi^*_{eth,ss}$) and the actual epithermal neutron flux at the atmosphere/subsurface interface (see equation 2.13) $[neutrons/cm^2/yr]$ $$(F\Delta\Phi)^*_{eth,ss} = \frac{\Delta\Phi^*_{eth,ss} D_{eth,a}/L_{eth,a} - \Delta\Phi^{**}_{eth,a} D_{eth,ss}/\Lambda_{f,e}}{D_{eth,a}/L_{eth,a} + D_{eth,ss}/L_{eth,ss}} \quad \text{(A.11)}$$
$(F\Delta\Phi)^*_{eth,a}$	Difference between $\Phi^*_{eth,a}$ (the epithermal neutron fluxin the atmosphere if there was no boundary) and $\Phi_{eth,a}$ (the actual epithermal neutron flux at the atmosphere/subsurface interface) $[neutrons/cm^2/yr]$ $$(F\Delta\Phi)^*_{eth,a} = \frac{\Delta\Phi^*_{eth,a} D_{eth,ss}/L_{eth,ss} - \Delta\Phi^{**}_{eth,a} D_{eth,ss}/\Lambda_{f,e}}{D_{eth,a}/L_{eth,a} + D_{eth,ss}/L_{eth,ss}} \quad \text{(A.12)}$$
$(\mathscr{F}\Delta\Phi)^*_{eth,ss}$	Describes the difference between $\Phi^*_{eth,ss}$ and the actual flux due to the shape of the epithermal neutron profile across the atmosphere/subsurface interface $$(\mathscr{F}\Delta\Phi)^*_{eth,ss} = \frac{p(E_{th})_a R_{th,ss} (F\Delta\Phi)^*_{eth,ss}}{\Lambda_{eth,ss}(\Sigma_{th,ss} - D_{th,ss}/L^2_{eth,ss})} \quad \text{(A.13)}$$

Continued on next page

Table A.1 – continued from previous page

Term	Definition
$(\mathscr{F}\Delta\Phi)^*_{eth,a}$	Describes the difference between $\Phi^*_{eth,a}$ and the actual flux due to the shape of the epithermal neutron profile across the atmosphere/subsurface interface $$(\mathscr{F}\Delta\Phi)^*_{eth,a} = \frac{p(E_{th})_a R_{th,a}(F\Delta\Phi)^*_{eth,a}}{\Lambda_{eth,a}(\Sigma_{th,a} - D_{th,a}/L^2_{eth,a})} \quad (A.14)$$
$f_{eth,m,ss}$	Fraction of total epithermal neutrons absorbed per unit mass of rock that react to produce nuclide m; compositionally dependent $[unitless]$ $$f_{eth,m,ss} = \frac{N_{k,ss} I_{a,k}}{I_{eff}} \quad (A.15)$$
$\Gamma_{eth,m,ss}$	Total rate of epithermal neutron absorption in subsurface $[n/(g*yr)]$
$I_{a,k}$	Dilute resonance integral for absorption of epithermal neutrons by element k $[10^{-24} cm^{-2}]$
$I_{eff,ss}$	Effective/macroscopic resonance integral for absorption of epithermal neutrons in subsurface $[cm^{-2}g^{-1}]$ $$I_{eff} = \sum_k I_{a,k} N_{k,bulk} \quad (A.16)$$
$\Lambda_{eth,ss}$	Effective epithermal neutron attenuation length in subsurface, accounting for both absorption and moderation $[g/cm^2]$ $$\Lambda_{eth,ss} = [\xi(I_{eff,ss} + \Sigma_{sc,ss})]^{-1} = \Sigma^{-1}_{eth,ss} \quad (A.17)$$
$\Lambda_{eth,a}$	Effective epithermal neutron attenuation length in the atmosphere, accounting for both absorption and moderation $[g/cm^2]$ $$\Lambda_{eth,a} = [\xi(I_{eff,a} + \Sigma_{sc,a})]^{-1} = \Sigma^{-1}_{eth,a} \quad (A.18)$$

Continued on next page

Table A.1 – continued from previous page

Term	Definition
$L_{eth,ss}$	Diffusion length for epithermal neutrons in the subsurface(g/cm^2) $$L_{eth,ss} = (\sqrt{3\Sigma_{sc,ss}\Sigma_{eth,ss}})^{-1} \quad \text{(A.19)}$$
$L_{eth,a}$	Diffusion length for epithermal neutrons in the air(g/cm^2) $$L_{eth,a} = (\sqrt{3\Sigma_{sc,a}\Sigma_{eth,a}})^{-1} \quad \text{(A.20)}$$
$N_{k,ss,bulk}$ $N_{k,ss,target}$	Atomic concentration of element k in subsurface (target or bulk specified as additional subscript) $[at/g]$
$N_{k,a}$	Atomic concentration of element k in air $[at/g]$
$P_{eth,m}$	Production rate for epithermal production of nuclide m. See eqn 2.32.
$\Phi_{eth,ss}(z)$	Epithermal neutron flux in subsurface $[n/(cm^2 * yr)]$
$\Phi^*_{eth,ss}$	Epithermal neutron flux that would be observed at the land surface if the properties of the medium did not change (e.g. identical to the subsurface).) $[neutrons/cm^2/yr]$ (See equation 2.10) $$\Phi^*_{eth,ss} = \mathrm{P}_f(0)\frac{R_{eth,ss}}{\Sigma_{eth,ss} - \frac{D_{eth,ss}}{\Lambda^2_{f,e}}} \quad \text{(A.21)}$$
$\Phi^*_{eth,a}$	Epithermal neutron flux that would be observed at the land surface if the properties of the medium did not change (e.g. atmosphere identical to the air).) $[neutrons/cm^2/yr]$ $$\Phi^*_{eth,a} = \mathrm{P}_f(0)\frac{R_{eth,a}}{\Sigma_{eth,a} - \frac{D_{eth,a}}{\Lambda^2_{f,e}}} \quad \text{(A.22)}$$
$P_f(Z)$	Production rate of epithermal neutrons from fast secondary cosmogenic neutrons as a function of depth. [neutrons (g air)$^{-1}$yr^{-1}]

Continued on next page

Table A.1 – continued from previous page

Term	Definition
$P_f(0)$	is P_f at depth equal to 0 and is a calibrated production rate parameter. [neutrons (g air)$^{-1}$yr^{-1}]
$p(E_{th})_{ss}$	Resonance escape probability in the subsurface - probability that a neutron will pass through the epithermal energy range to the thermal range without being absorbed [unitless] $$p(E_{th}) = exp[-\frac{I_{eff}}{\sum_k \xi_k N_{k,bulk} \sigma_{sc,k}}] \quad \text{(A.23)}$$
$p(E_{th})_a$	Resonance escape probability in the air - probability that a neutron will pass through the epithermal energy range to the thermal range without being absorbed [unitless]. Value is 0.56 according to Phillips and Plummer (1996). (A.24)
$R_{eth,ss}$	Ratio of epithermal neutron production in the rock to that of the atmosphere $[unitless]$ $$R_{eth,ss} = \sqrt{\frac{\bar{A}_{ss}}{A_a}} \quad \text{(A.25)}$$
$R_{eth,a}$	Ratio of epithermal neutron production in the atmosphere to that of the atmosphere $[unitless]$. Equal to 1. $$R_{eth,a} = \sqrt{\frac{\bar{A}_a}{A_a}} \quad \text{(A.26)}$$
$\Sigma_{eth,ss}$	Effective epithermal loss cross-section in subsurface, by both absorption and energy moderation $[cm^2/g]$
$\Sigma_{eth,a}$	Effective epithermal loss cross-section in air, by both absorption and energy moderation $[cm^2/g]$

Continued on next page

Table A.1 – continued from previous page

Term	Definition
$\Sigma_{sc,ss}$	Macroscopic neutron scattering cross-section in subsurface $[cm^2/g]$ $$\Sigma_{sc,ss} = \sum_k N_{k,bulk}\sigma_{sc,k} \quad \text{(A.27)}$$
$\Sigma_{sc,a}$	Macroscopic neutron scattering cross-section in air. Constant = 0.3773 $[cm^2/g]$
$\sigma_{sc,k}$	Neutron scattering cross-section for element k [1×10^{-24} cm^2]
$\bar{\xi}_{bulk}$	Macroscopic average log decrement neutron energy loss per collision for the bulk rock $$\bar{\xi}_{bulk} = \frac{\sum_k \xi_k \sigma_{sc,k} N_{k,ss,bulk}}{\sum_k \sigma_{sc,k} N_{k,ss,bulk}} \quad \text{(A.28)}$$
ξ_k	Average log decrement of energy loss for element k
Thermal Production	
$D_{th,ss}$	Diffusion coefficient for thermal neutrons in the subsurface $[unitless]$ $$D_{th,ss} = [3\Sigma_{sc,ss}(1 - \frac{2}{3A_s s})]^{-1} \quad \text{(A.29)}$$
$D_{th,a}$	Diffusion coefficient for thermal neutrons in the atmosphere $[unitless]$ $$D_{th,a} = [3\Sigma_{sc,a}(1 - \frac{2}{3A_a})]^{-1} \quad \text{(A.30)}$$
$\Delta\Phi^*_{th,ss}$	Describes the difference between the hypothetical equilibrium thermal neutron flux in the air and the subsurface $[neutrons/(cm^2 yr^{-1})]$ $$\Delta\Phi^*_{th,ss} = \Phi^*_{th,a} - \Phi^*_{th,ss} \quad \text{(A.31)}$$

Continued on next page

Table A.1 – continued from previous page

Term	Definition
$f_{th,ss,m}$	Fraction of thermal neutrons absorbed per unit mass by target k that react to form cosmogenic nuclide m $[unitless]$ $$f_{th,ss,m} = \frac{\sigma_{th,k} N_{k,ss,target}}{\Sigma_{th,ss}} \quad (A.32)$$
$(\mathscr{F}\Delta\Phi)^*_{th,ss}$	Describes the difference between $\Phi^*_{th,ss}$ and the actual flux due to the shape of the thermal neutron flux profile across the interface. See equation 2.20
$\Lambda_{th,ss}$	Effective thermal neutron attenuation length for medium i [fix so -1 and th,i are above and below sigma, not in front] $[g/cm^2]$ $$\Lambda_{th,ss} = \sum_{th,ss}^{-1} \quad (A.33)$$
$L_{th,ss}$	Diffusion length for thermal neutrons in the subsurface $[g/cm^2]$ $$L_{th,ss} = \sqrt{\frac{D_{th,ss}}{\Sigma_{th,ss}}} \quad (A.34)$$
$P_{th,ss,m}$	production rate of nuclide m by thermal neutrons $[atoms/(g*yr)]$
$L_{th,a}$	Diffusion length for thermal neutrons in the air $[g/cm^2]$ $$L_{th,a} = \sqrt{\frac{D_{th,a}}{\Sigma_{th,a}}} \quad (A.35)$$
$\Phi_{th,ss}(Z)$	Thermal neutron flux at depth Z $[n/(cm^2 yr)]$
$\Phi^*_{th,ss}$	Thermal neutron flux that would be observed at the land surface if the properties of the atmosphere and subsurface were identical [neutrons/cm^2/yr] $$\Phi^*_{th,ss} = \frac{p(E_{th})_a R_{th,ss} \Phi^*_{eth,ss}}{\Lambda_{eth,ss}(\Sigma_{th,ss} - \frac{D_{th,ss}}{\Lambda^2_{eth,ss}})} \quad (A.36)$$

Continued on next page

Table A.1 – continued from previous page

Term	Definition
$\Phi^*_{th,a}$	Thermal neutron flux that would be observed at the land surface if the properties of the medium did not change and were identical to the atmosphere [neutrons/cm^2/yr] $$\Phi^*_{th,a} = \frac{p(E_{th})_a R_{th,a} \Phi^*_{eth,a}}{\Lambda_{eth,a}(\Sigma_{th,a} - \frac{D_{th,a}}{\Lambda^2_{eth,a}})} \quad \text{(A.37)}$$
$R_{th,ss}$	Ratio of thermal neutron production in the rock to that in the atmosphere [unitless] $$R_{th,ss} = \frac{p(E_{th,ss})}{p(E_{th,a})} \quad \text{(A.38)}$$
$\sigma_{th,ss,k}$	Elemental thermal neutron cross-section for the sub-surface $[barns]$ 1 barn = $10^{-24} cm^2$
$\sigma_{th,a,k}$	Elemental thermal neutron cross-section for the air $[barns]$ 1 barn = $10^{-24} cm^2$
$\Sigma_{th,ss}$	Macroscopic neutron absorption cross section $[cm^2/g]$ $$\Sigma_{th,ss} = \sum_k \sigma_{th,k} N_{k,ss,bulk} = \Lambda^{-1}_{th,ss} \quad \text{(A.39)}$$
$\Gamma_{th,ss,m}$	Total rate of thermal neutron absorption $[ng^{-1}yr^{-1})]$
Muons	
f^*_i	Probability for particle emission to the radionuclide. See Heisinger et al. (2002a).
$f_{i,D}$	Fraction of muons stopped by element k and absorbed by the nucleus before decay of the muon (Fabryka-Martin, 1988) $[unitless]$

Continued on next page

Table A.1 – continued from previous page

Term	Definition
$f_{i,C}$	Chemical compound factor $[unitless]$ Chemical compound factor (for Be, Al, C, see Heisinger et al. (2002a)); values computed on a sample by sample basis for chlorine-36 due to variations in composition using values from von Egidy and Hartmann (1982). $$f_{i,C} = \frac{M_{k,bulk}\Omega_k}{\sum jM_{j,bulk}\Omega_j} \quad \text{(A.40)}$$
N_{atoms}	Atom number density of the target atom $[at/g]$
Ω	Atomic number of the element. Subscript k refers to the target element and j refers to all elements in the rock.
P	Average probability of muon capture by a nucleus relative to that of oxygen (von Egidy and Hartmann, 1982) $[unitless]$
$P_{\mu-,m}$	Production rate for negative muon production of nuclide m. See eqns 2.7 and 2.36.
$P_{\mu,fast,m}$	Production rate for fast muon production of nuclide m. See eqn 2.28.
$P_{n,\mu}$	Production rate for muon-induced neutrons. See eqn 2.33.
$P_{n,\mu}(Z)$	Total muon-induced neutron production at depth Z $[neutrons/cm^2/yr]$; value at surface is $P_{n,\mu}(0)$ $$P_{n,\mu}(Z) = Y_s\Psi_\mu(Z) + 5.8 \times 10^{-6}\Phi_{\mu f}(Z) \quad \text{(A.41)}$$
$\Phi_{\nu,0}$	Vertical muon flux at SLHL as a function of depth. Only valid for depths of <200,000 g/cm^2. See equation 2.21. $[cm^{-2}s^{-1}sr^{-1}]$
$\phi_{\mu f}(Z,\theta)$	Fast muon flux at depth Z $[muonsg^{-1}yr^{-1}]$; calculated from the muon code
$\Psi_{\mu-}(Z)$	Slow negative muon stopping rate at depth Z $[muonsg^{-1}yr^{-1}]$; calculated from the muon code
$R_{\mu-}(h)$	Rate of negative muons stopping at an atmospheric depth of h

Continued on next page

Table A.1 – continued from previous page

Term	Definition
$R_\mu(Z)$	Ratio of muon production to epithermal neutron production $[unitless]$ $$R_\mu(Z) = \frac{S_{el,\mu} P_{n,\mu}(Z)}{S_{el} P_f(0) R_{eth}} \quad \text{(A.42)}$$
R'_μ	Ratio of the muon production rate to the production rate for thermal neutrons. $[unitless]$ See eqn 2.37. $$R'_\mu = \frac{p(E_{th})_a}{p(E_{th})} R_\mu \quad \text{(A.43)}$$
σ_{190}	Cross-section for fast muon production at 190 GeV $[mb]$. Note: 1 barn=1×10^{-24} cm^2
Y_s	Average neutron yield per stopped negative muon [neutrons/(stopped negative muon)] $$Y_s = \sum_k f_{c,k,bulk} f_{d,k} Y_{n,k} \quad \text{(A.44)}$$
$Y_{n,k}$	Average neutron yield per captured muon for element k - (Fabryka-Martin, 1988)
Radiogenic Production	
$F_{k,bulk}$	Fractional abundance of element k in ppm in the bulk rock
P_r	Total radiogenic production from all mechanisms in a particular sample. (equation 2.41)
$P_{n,\alpha}$	Production rate of neutrons from alpha particles in neutrons/g/yr
$P_{n,sf}$	Neutron production rate due to the spontaneous fission of ^{238}U
S_k	Mass stopping power of element k for α-particles of a given energy
X	Neutron production factors related to the light isotope composition of the rock matrix. See equation 2.44.
Y	Neutron production factors related to the light isotope composition of the rock matrix. See equation 2.45.
Y_n^U	Neutron yields of element i per ppm U in equilibrium
Y_n^{Th}	Neutron yields of element i per ppm Th in equilibrium

Continued on next page

Table A.1 – continued from previous page

Term	Definition
Accumulation	
D	Depth of the sample with 'old' representing the original sample depth and 'new' is the updated sample depth, accounting for erosion during the time period
Δt	Time step in the CRONUScalc program.
ϵ	Erosion rate [g/cm^2]
f_{decay}	Decay factor that accounts for the fact that some of the nuclides produced at the beginning of the time period will have decayed by the end of the period. (equation 2.47)
λ	Decay constant for the nuclide
N_{tot}	Total inventory in the sample up to the current time step
N_{prev}	Inventory from all previous time steps.
P_{tot}	Instantaneous production rate of the nuclide from all mechanisms and is the sum of production from all other mechanisms.

A.2 Table of elemental parameters

The table was originally taken out of Fabryka-Martin (1988). It has been updated using Mughabghab (2006). The columns correspond to the following parameters:

1. Ai=Atomic weight of element
2. Average log decrement of energy per neutron collision with element i
3. Neutron scattering cross-section of element i
4. Thermal neutron absorption cross-section of element i

5. Dilute resonance integral for element i
6. Mass stopping power of element i for alpha particles of a given energy
7. neutron yield of element i per ppm U in radioequilibrium
8. Neutron yield of element i per ppm Th in radioequilibrium
9. Km, 602/atomic weight of sample, used to convert to at/g from ppm
10. Stoichiometry ratio of oxide (oxygen to element i)
11. Atomic number
12. Average capture probability relative to oxygen

Note that the average capture probability relative to oxygen for C was determined by back calculating based on a compound factor from Heisinger et al. (2002a) and values from von Egidy and Hartmann (1982).

A.3 Attenuation lengths by latitude and elevation

Table A.3 shows the attenuation length table used in the CRONUScalc program. Interpolation requires both atmospheric depth and cutoff rigidity.

Element	A_i	ξ_i	$\sigma_{sc,i}$	$\sigma_{th,i}$	$I_{a,i}$	S_i	$Y^u_{n,i}$	$Y^{th}_{n,i}$	K_m	*Stoichiometry*	#	**P**
–	$[g/mol]$	$[-]$	$[1\times10^{-24}]$	$[1\times10^{-24}]$	$[1\times10^{-24}]$	$[-]$	$[-]$	$[-]$	$[-]$	$[-]$	$[-]$	
O	16	0.120004104	3.761	0.00019	0.0002693	539	0.23	0.079	0	0	8	1.00
H	1.01	1	20.49	0.3326	0	1542	0	0	0	0.5	1	0.00
C	12.01	0.157760474	4.74	0.0035	0.0018	573	0.45	0.18	13.691	2	6	0.36
Na	22.99	0.084543589	3.038	0.517	0.311	454	14.5	6.8	19.42	0.5	11	1.00
Mg	24.31	0.08009077	3.414	0.0666	0.038	463	5.8	2.6	14.94	1	12	0.93
Al	26.98	0.072337427	1.413	0.231	0.17	449	5.1	2.6	11.812	1.5	13	0.76
Si	28.09	0.069559975	2.044	0.171	0.082	455	0.69	0.335	10.01	2	14	0.84
P	30.97	0.063210393	3.134	0.165	0.079	444	0	0	8.48	2.5	15	1.04
K	39.1	0.050295528	2.04	2.1	1	432	0.45	0.305	12.78	0.5	19	1.54
Ca	40.08	0.049086179	2.93	0.43	0.233	436	0	0	10.73	1	20	1.90
Ti	47.87	0.041208508	4.09	6.41	3.1	367	0	0	7.53	2	22	2.66
Mn	54.94	0.035968204	2.06	13.36	13.4	351	0	0	8.486	1	25	2.73
Fe	55.85	0.035390922	11.35	2.56	1.36	353	0.19	0.205	7.54	1.5	26	3.28
Cl	35.45	0.055371497	15.8	33.14	13.83	420	0	0	16.98	0	17	1.32
B	10.81	0.174236264	4.27	767	343	537	62.3	19.2	55.68	0	5	0.25
Sm	150.36	0.013242694	38	9640 1400	0	0	0	4.004	0	62	4.4	
G	157.25	0.012664667	172	41560	390	0	0	0	3.828	0	64	5.8
U	238.03	0.008378873	9.08	2.68	277	0	0	0	2.529	0	92	4.7
Th	232.04	0.008594581	13.55	7.34	83.3	0	0	0	2.594	0	90	3.0
Li	6.9	0.264	0.95	70.5	0.0	548	21.1	9.6	86.731	0.0	3	0.18
Cr	52.0	0.038	3.38	3.1	1.6	0.0	0.0	0.0	11.578	0.0	24	2.98

Table A.2: Table of constants used for elemental parameters.

Depth/Cutoff Rigidity	**1100**	**1000**	**900**	**800**	**700**	**600**	**500**	**400**
0	136	136	137	138	139	142	146	154
4	136	137	138	140	143	147	154	166
8	139	142	144	147	151	157	166	183
12	145	148	150	154	158	165	176	195
16	151	152	155	159	164	171	183	205
20	151	153	156	160	165	172	185	207

Table A.3: The table used for the interpolation of attenuation lengths based on the given atmospheric depth (g/cm^2) and cutoff rigidity (GeV). Values obtained using the spreadsheet that accompanied Sato et al. (2008).

APPENDIX B

METHODS

B.1 Tufa preparation procedure

Acid pretreatment methods used on the Tabernacle Hill tufa samples from A. Hudson (pers. comm., January 10, 2012).

1. Subsamples of whole tufa chunks were oriented and cut into stratigraphic 'top' (younger) and 'bottom' (older) square sections of $\sim$2 cm width and $\sim$0.5 cm in height, with stratigraphic 'center' material removed and retained, using a lapidary saw. This was to limit the amount of time-averaging of the dated material and to assess how much time was represented by the whole stratigraphic thickness of tufa.

2. Top and bottom subsamples were placed in 50 mL plastic centrifuge vials and rinsed with Milli-q water 5 times alternating with 10 second periods of sonication to remove adhering fine particles.

3. Samples were then dried overnight in a 70°C drying oven.

4. Sample slabs were crushed to coarse sand size using a mortar and pestle and sieved so that only grains $>$0.15 mm were retained. Coarse particles were used only to limit surface area for contamination of the primary material.

5. Samples were again rinsed and sonicated with Milli-q 5 times to remove adhering fine particles and dried overnight at 70°C.

6. Sample mass was measured and enough 1N HCl was added to each sample to dissolve 50% based on sample mass, following the equation:

   $CaCO_3$+2HCl = $CaCl_2$+H_2O+CO_2

   This follows the procedure outlined in Oviatt and Nash (1989).

7. Samples were then allowed to react to completion overnight at 70°C, and subsequently rinsed 5 times with Milli-q and dried overnight in a drying oven at 70°C.

8. Approximately 4 grains of each sample ($\sim$20 mg) were then separated for radiocarbon dating.

9. These grains were evacuated on our extraction line to $<2\times10^{-5}$ torr pressure, then sealed and reacted with 100% H3PO4 in a heat bath until the reaction was visibly complete.

10. The CO2 from the reaction was then extracted under vacuum on our extraction line, run through one dry ice water trap ($\sim$-100°C) to remove water.

11. Sample CO2 gas was passed through a 600°C Cu/Ag furnace to further remove contaminant gases, frozen in liquid nitrogen (LN) and sealed in glass tubes. Purified CO2 samples were then graphitized using 100 mg of zinc powder and Fe powder in a 2:1 proportion to the mass of carbon in the sample following the procedure outlined in Slota et al. (1987).

Sample Name	JQ number	AA#	Graph. Date	Mass Fe (mg)	Max P (psi)	Min P (psi)	% Yield
TAB 11/01 Top	2252	94394	5/25/2011	2720	6.86	0.03	0.995626822
TAB 11/01 Bottom	2253	94395	5/25/2011	2740	7.05	0.06	0.991489362
TAB 11/02 Top	2254	94396	5/25/2011	2620	6.24	0.14	0.977564103
TAB 11/02 Bottom	2255	94397	5/25/2011	2310	5.16	0.02	0.996124031
TAB 11/03 Top	2257	94399	5/26/2011	2680	6.94	0.04	0.994236311
TAB 11/03 Bottom	2258	94400	5/26/2011	2740	6.48	0.17	0.973765432
TAB 11/02 Top B	2256	94398	5/26/2011	2510	6.22	0.02	0.996784566

Table B.1: Table accompanying the TAB tufa processing description.

B.2 Sample splitting

Splitting Procedure

1. Homogenize the sample 3 times
2. Split the sample once into two parts: named 1 & 2.
3. Split the two samples into four parts each and name them 1,2,3,4.
4. Combine parts 1 & 3, and 2 & 4.
5. Split 1 & 3 into two parts, and 2 & 4 into two parts.
6. Repeat this procedure until the sample has been split into the appropriately sized sample.

B.3 Contact Information for Compositional Analyses

Contact information for SGS Labs (major element XRF, trace element ICP-OES):

SGS Toronto
1885 Leslie St.
Toronto, Ontario
M3B 2M3
Canada
Contact: Bonnie White
Phone: 416-445-5755

Contact information for Michigan State University XRF Lab (major element XRF only):

Tyrone Rooney
Department of Geological Sciences
211 Natural Sciences Building
Michigan State University
East Lansing, MI 48824-1115
Phone: 517-432-5522

APPENDIX C

ELECTRONIC APPENDIX

C.1 CRONUScalc Matlab Code

Title: "CRONUScalc" Folder

The CRONUScalc Matlab code is included in its current form. Future versions may be slightly different due to reorganization or updated methods. See the Function Appendix (Appendix D.4) for descriptions of the major code pieces and how they work. The current version of the code only has the Sa (Lifton/Sato nuclide dependent scaling) scaling method set up. Future versions will have all 7 possible scaling methods.

C.2 Laboratory Procedures

Title: "CompleteNMTProcedure.doc"

This document contains the silicate and carbonate procedures for processing whole-rock and mineral-separate chlorine-36 samples.

C.3 Dissertation Excel Datasheets

Title: "Marrero2012datasets.xlsx"

This document contains the final datasets for all the samples discussed in the dissertation. The sheets are described below:

1. `PrimaryDataset` - Contains the Ca spallation, K spallation, and $P_f(0)$ calibration datasets.

2. `calib36secQuant` - Contains the quantitative secondary dataset.

3. `calib36secQual` - Contains the qualitative secondary dataset.

4. `K muons` - Contains the data for the reparameterization of the potassium muon production parameters. Data originally from Evans (2001).

5. `Ca muons` - Contains the data for the reparamterization of the calcium muon production parameters. Data originally from Stone et al. (1998).

6. `CCMM-Cl` - Contains the chlorine-36 datasets for the main Copper Canyon calibration as well as the datasets for the sensitivity analyses.

7. `CCMM-Be` - Contains the beryllium-10 datasets for the main Copper Canyon calibration as well as the datasets for the sensitivity analyses.

8. `Peru` - Contains the datasets for the primary Peru calibration, the NMT/Marrero samples that were not used in the primary calibration, the Peru erosion rate samples, and the Huancané 1 samples.

9. `Puget Lowlands` - Contains all the data from the resampling of the Puget Lowlands for the CRONUS-Earth Project. Includes data from the NMT and PRIME labs.

10. `Swanson 2001 Legacy` - Contains the sample data for the samples originally published in Swanson and Caffee (2001).

11. `BeClcompCl data` - Contains the chlorine-36 sample data for the beryllium-chlorine comparisons. Contains samples from the CRONUS datasets as well as Ivy-Ochs et al. (1996, 2004, 2006); Phillips et al. (1997); Benson et al. (2004, 2005).

12. `BeClcompBe data` - Contains the beryllium-10 data for the beryllium-chlorine comparisons. Contains samples from the CRONUS datasets as well as Ivy-Ochs et al. (1996, 2004, 2006); Phillips et al. (1997); Benson et al. (2004, 2005).

13. `PPT` - Contains the chlorine-36 sample data for the four Promontory Point samples.

14. `TAB 3He` - Contains the helium-3 data from Goehring et al. (2010b).

APPENDIX D

FUNCTION APPENDIX

D.1 IDMS Calculator

The IDMS calculator has been encoded into Matlab following the equations in Thomas (2005). Format the dissolution data according to the template (see the Excel sheet named "Template36Cl"). Copy this information into Matlab to create the variable that will be the input.

Run the Matlab code `spiketoconcmc`. The main output is the following:

1. chlorine-36 concentration - this is the sample concentration of chlorine-36 in units of at/g.
2. chlorine-36 uncertainty - this is the uncertainty in the chlorine-36 concentration in units of at/g.
3. chlorine concentration - this is the sample stable chlorine concentration in units of ppm.
4. chlorine uncertainty - uncertainty in the chlorine concentration in ppm.
5. covariance - this is the covariance between the uncertainties on chlorine-36 concentration and the stable chlorine concentration.

D.2 Inputs

D.2.1 Chlorine-36

The inputs for chlorine-36 include three variables for regular samples and an additional independent age variable for calibration samples. The four possible inputs include `nominal36`, `uncerts36`, `cov36`, and `indages36`. `nominal36` is set up with one row for each sample and each column is a different input parameter, as defined below.

1. Sample 36-Cl concentration (atoms of 36-Cl/g of target) - This should be the blank-subtracted chlorine-36 concentration of the sample.

2. Inheritance (atoms 36-Cl/g of target) - This is zero except in some rare instances.

3. erosion-rate epsilon ($(g/cm^2)/kyr$) - This is the erosion rate in mass depth units. Do not use mm/kyr or similar units.

4. fractional volumetric water-content (unitless) - This is the pore water content of the rock given as a fraction. Example: A rock that is 1% saturated would have an input value of 0.01.

5. bulk density (g/cm^3) - This is the density of the sample. For depth profiles, use the individual layer density here.

6. sample thickness (cm) - This is the thickness of the sample that was used for analysis. For depth profiles, use the thickness of the collected layer here.

7. Latitude (decimal degrees)

8. Longitude (decimal degrees)

9. Elevation (meters) - This is not used as an input to the code, but is collected for the record.

10. Pressure (hPa) - The pressure should be calculated from the elevation unless it has been directly measured. The current recommended model is ERA40 (see Matlab function `ERA40atm.m`).

11. Shielding factor for terrain, snow, etc. (unitless) - This is the shielding correction factor. If necessary, use the `topooriginal.m` file to calculate this value.

12. $\lambda_{f,e}$ Effective neutron attenuation length (g/cm^2) - The effective attenuation length should account for the location of the sample (use the `attenuationlength.m` or `attenuationlengthraw.m` file as an initial estimate of the attenuation length. This value should then be adjusted to account for the changes in the horizon.

13. Weight % CO_2 - This is the bulk rock weight %, typically measured using XRF.

14. Weight% Na_2O - This is the bulk rock weight %, typically measured using XRF.

15. Weight% MgO - This is the bulk rock weight %, typically measured using XRF.

16. Weight% Al_2O_3 - This is the bulk rock weight %, typically measured using XRF.

17. Weight% SiO_2 - This is the bulk rock weight %, typically measured using XRF.

18. Weight% P_2O_5 - This is the bulk rock weight %, typically measured using XRF.

19. Weight% K_2O - This is the bulk rock weight %, typically measured using XRF.

20. Weight% CaO - This is the bulk rock weight %, typically measured using XRF.

21. Weight% TiO_2- This is the bulk rock weight %, typically measured using XRF.

22. Weight% MnO - This is the bulk rock weight %, typically measured using XRF.

23. Weight% Fe_2O_3 - This is the bulk rock weight %, typically measured using XRF.

24. Cl (ppm) - This is the blank-subtracted chlorine concentration for the bulk rock. If doing whole-rock, this should be the same value as the target Cl concentration.

25. B (ppm) - This is the trace element composition for the bulk rock, typically measured using ICP.

26. Sm (ppm) - This is the trace element composition for the bulk rock, typically measured using ICP.

27. Gd (ppm) - This is the trace element composition for the bulk rock, typically measured using ICP.

28. U (ppm) - This is the trace element composition for the bulk rock, typically measured using ICP.

29. Th (ppm) - This is the trace element composition for the bulk rock, typically measured using ICP.

30. Cr (ppm) - This is the trace element composition for the bulk rock, typically measured using ICP.

31. Li (ppm) - This is the trace element composition for the bulk rock, typically measured using ICP.

32. Target element %K_2O - This is the target element composition and should be exactly the composition of the dissolved material. This is typically measured by XRF.

33. Target element %CaO - This is the target element composition and should be exactly the composition of the dissolved material. This is typically measured by XRF.

34. Target element %TiO_2- This is the target element composition and should be exactly the composition of the dissolved material. This is typically measured by XRF.

35. Target element %Fe_2O_3- This is the target element composition and should be exactly the composition of the dissolved material. This is typically measured by XRF.

36. Target element Cl (ppm) - This is the blank-subtracted chlorine concentration for the sample. If doing whole-rock, this should be the same value as the bulk rock Cl concentration.

37. Depth to top of sample (g/cm^2) - This is the depth to the top of the sample in units of mass depth. For depth profiles, the depth to top of sample should incorporate any changes in density throughout the profile.

38. Year Collected (AD) - This is the calendar year the sample was collected.

D.3 Outputs

Using cosmogenic nuclides to obtain surface exposure ages is probably one of the most common functions. For this reason, the outputs discussed here are the outputs from the aging routine `cl36age.m`.

1. age (kyr) - This is the best-fit sample age.

2. age uncertainty - This is the uncertainty incorporating the propagation of uncertainties in the input parameters as well as any production rate parameter uncertainties incorporated into the code.

3. Elevation/latitude scaling factor for fast neutrons for Ca(unitless)

4. Elevation/latitude scaling factor for fast neutrons for K(unitless)

5. Elevation/latitude scaling factor for fast neutrons for Ti(unitless)

6. Elevation/latitude scaling factor for fast neutrons for Fe(unitless)

7. Elevation/latitude scaling factor for epithermal neutrons (unitless)

8. Elevation/latitude scaling factor for thermal neutrons (unitless)
9. Avg elevation/latitude scaling factor for fast muons (unitless)
10. Elevation/latitude scaling factor for slow muons (unitless)
11. Contemporary depth avg prod rate, Ca, spallation (atoms/g/yr)
12. Contemporary depth avg prod rate, K, spallation (atoms/g/yr)
13. Contemporary depth avg prod rate, Fe, spallation (atoms/g/yr)
14. Contemporary depth avg prod rate, Ti, spallation (atoms/g/yr)
15. Contemporary depth avg prod rate, Ca, muons (atoms/g/yr)
16. Contemporary depth avg prod rate, K, muons (atoms/g/yr)
17. Contemporary depth avg prod rate, Cl, low energy (atoms/g/yr)
18. $\Sigma_{th,ss}$ (cm^2/g) - This is an intermediate parameter discussed in the text and output for comparison to other programs.
19. $\Sigma_{eth,ss}$ (cm^2/g) - This is an intermediate parameter discussed in the text and output for comparison to other programs.
20. $\Sigma_{sc,ss}$ (cm^2/g) - This is an intermediate parameter discussed in the text and output for comparison to other programs.
21. Qs (unitless) - This parameter is not used in the code, but an equivalent is calculated here for comparison.
22. Qth (unitless) - This parameter is not used in the code, but an equivalent is calculated here for comparison.

23. Qeth (unitless) - This parameter is not used in the code, but an equivalent is calculated here for comparison.

24. Qmu (unitless) - This parameter is not used in the code, but an equivalent is calculated here for comparison.

25. Cosmogenic 36-Cl (atoms/g of target) - This is only the cosmogenically produced component of the chlorine-36 inventory.

26. Radiogenic 36-Cl (atoms/g of target) - This is only the radiogenic component of the chlorine-36 inventory.

27. Measured 36-Cl (atoms/g of target) - This is the input concentration and is simply repeated in the output list for convenience.

D.4 Matlab Functions

The Matlab code, named CRONUScalc, is organized into several folders based on function. In order to use the complete code, you must use the `addpath` command to add all the folders. The function list is organized into the same categories with specific descriptions of each function included. In many cases, there are similar code pieces for chlorine-36, aluminum-26, beryllium-10, etc. When the descriptions for the same, the nuclide number will be replaced with 'XX' to indicate that it applies to all the nuclides. For example, there are several codes for calibrating each nuclide including `calibrate10`, `calibrate26`, `calibrate36`, etc. These codes are discussed as a group under the heading `calibrateXX`. A similar method, only using 'aa' instead of 'XX', is used for code that is named using the two-letter indicator for the nuclide. For example, `al26uncert.m` becomes

aaXXuncert.m when the generic code is discussed. Only the main functions used in the calibrations or discussed in the paper are discussed here. A more complete function list and user manual will be published on with the interface on the website when the code is finalized.

D.4.1 Calib

The calib folder contains code used to perform calibrations and age the primary and secondary datasets after calibration.

agecalibsetXX.m This code computes ages for the calibration dataset.

Inputs: There are no inputs to this code. The calibration dataset is hard-coded at the beginning in the line that starts with "load." The required input is the "calibration input" that consists of three variables. The three variables are nominalXX, uncertsXX, and indagesXX. For chlorine-36, there is an additional variable called cov36. These are covered in detail in the excelformatting section.

Details: The code first collects some basic information about the independent ages of the samples. The uncertainties on the concentrations are updated using the uncertsXX function. The ages and nominal uncertainties are computed using the aaXXage.m function. Other output parameters that are recorded are the scaling factors for the spallation production rate and the percent production from muons based on the contemporary production rates.

The code also calculates the RMSE (root mean square error) for the entire calibration dataset. This is calculated by the following formula: For each sample:

percenterror=100*(computedages-INDAGES)/INDAGES; The vector containing the all the percenterror values is the percenterrors variable.

RMSE=sqrt(mean(percenterrors^2))

A variable named 'total' is created that contains one column for each of the following variables:

- Computed ages
- Computed uncertainties
- Spallation scaling factor
- Average muon scaling factor
- Percent production from muons

`calibrateXX.m` This script calibrates the production rate from the calibration dataset.

Input: There is no input to this script. The calibration dataset is hard-coded at the beginning in the line that starts with "load." The required input is the "calibration input" that consists of three variables. The three variables are nominalXX, uncertsXX, and indagesXX. For chlorine-36, there is an additional variable called cov36. These are covered in detail in the excelformatting section.

Output: The production rates for the appropriate reaction.

Details: The code first stores some variables into global variables. The code gathers information about the independent ages of the samples. The uncertainties on the concentrations are updated using the `uncertsXX` function. The necessary factors are precomputed by calling the `sampparsXX`, `physpars`, `scalefacsXX`,

and compparsXX. The calibration values are initialized using the variable pinit. The first value in pinit is the calibrated production rate. The other values in pinit are the concentration residuals (difference between the predicted and measured concentrations).

The lm.m code fits the parameters. The covariance matrix is calculated using odrfunXX.m and odrjacXX.m and a p-value is calculated.

maxiter is the variable that determines the maximum number of iterations to be performed during the calibration. It is set to 100 for final calibrations, but can be modified if desired.

D.4.2 excelformatting

This folder contains the Excel template for each nuclide as well as the matlab code that converts from the Excel information block to the appropriate matlab files. The data in the included Excel sheet is already properly formatted to be used with these codes. Instructions are included in each file. In general, the createageXX.m functions create only the nominal input parameters and the uncertainties. createcalibXX.m creates an additional parameter that contains the independent ages for each sample and the uncertainties on those ages. Finally, createcalibXXxval.m creates all the variables from the createcalibXX.m code, but adds additional datasets for cross-validation purposes.

D.4.3 muoncalib

This folder contains files used to calibrate the Al, Be, Cl from Ca, and Cl from K muon parameters using the depth profiles discussed in the CRONUS publications. In this dissertation, the chlorine-36 profiles were calculated in multiple

steps. The first step calculated the attenuation length and the erosion rate. The codes that do this are `cal36Cacoreatten.m` and `cal36Kcoreatten.m`. Then those parameters were used to calibrate the lower portion of the profile producing σ_0 and f* muon parameters. The codes that perform the lower portion of the profile are `calClmuonsCa.m` and `calClmuonsK.m`. To plot the entire profile, use the `plotcoreCa.m` and `plotcoreK.m` codes.

D.4.4 `pf0calib`

This folder contains the code necessary to calibrate the Copper Canyon profile and plot the results.

In order to calibrate the Copper Canyon profile, first calibrate the 10Be profile using `calccbecore.m`. This produces an attenuation length and an erosion rate. Modify the appropriate file (`calccpf0.m`) to use these values and then run the Copper Canyon samples. The resulting value is the $P_f(0)$ parameter and the goodness of fit statistics (chi-squared, p-value). The values for $P_f(0)$ can be plotted using the `plotpf0.m` file (or its variants, depending on the type of plotting desired).

D.4.5 `production`

This folder contains the heart of the code, including the pieces necessary to predict the nuclide concentration and perform scaling.

`aaXXuncert.m` This code uses the sample concentration to apply the uncertainties appropriate for the nuclide based on interlaboratory comparisons performed by the CRONUS Project. In most cases, the uncertainty changes depending on the concentration, with higher concentrations having a lower percentage of uncertainty.

`compparsXX.m` cp=comppars36(physpars,samppars,scalefactors,maxdepth)

This code uses physpars, samppars, and scalefacs to calculate all the intermediate parameters necessary (for chlorine-36) and to calculate the muon production table used for interpolation later (all nuclides). Maxdepth can be adjusted so that it is appropriate for the type of reaction.

`get_tdsf.m` This code calculates all the time-dependent scaling factors for all the nuclides.

`getcurrentsf.m` out=getcurrentsf(sf,t)

This code finds the scaling factor for the current time step given all the scaling factors and the time.

`getparsXX.m` [pp,sp36,sf36,cp36]=getpars36(sampledata36,maxdepth)

This code uses the nominal sample input to create all the necessary preliminary information for a particular sample.

`physpars.m` pp=physpars()

This code creates all the constants, such as decay constants and production rates, required for the rest of the code.

`predNXX.m` N36=predN36(pp,sp,sf,cp,age)

This code predicts the concentration of the nuclide given a particular age for the sample. Inputs include the outputs from physpars, samppars, scalefacs, and comppars.

`predNXX.m` N36=predN36depth(pp,sp,sf,cp,age,depths)

This code predicts the concentration of the nuclide at a particular depth(s) for a particular age. Inputs include the outputs from physpars, samppars, scalefacs, and comppars.

`sampparsXX.m` sp=samppars36(sampledata)

This code takes the nominalXX as input and names all the parameters to the correct variables required by the code.

`scalefacs.m` sf=scalefacs36(sp36)

This code creates variables required to call get_tdsf and then calls that code.

D.4.6 `profilecalc`

The profilecalc folder has code that ages depth profiles. Use the XXscript.m file as a template. Change the data file to load and the inheritance, age, and erosion rate bounds the calculator will use. This will be covered in more detail as the depth profile calculator is brought online.

D.4.7 `surfacecalc`

This folder contains necessary files to perform surface sample aging. Example sample files for each nuclide are also included.

`aaXXage.m` [output,derivs]=al26age(sampledata,sampleuncertainties)

This is the main aging routine that creates both age and one standard deviation uncertainty. If you are interested in looking at the derivatives of age with respect to each of the input parameters, you can call the code with two outputs.

`aaXXageraw.m` age=cl36ageraw(sampledata,pp,sf)

This is a simplified version of the aaXXage.m code and it does everything except uncertainty calculations.

REFERENCES

Aruscavage, P. J. and Campbell, E. Y. (1983). An ion-selective electrode method for determination of chlorine in geological materials. *Talanta*, 30:745–749.

Aumer, R. A. (2010). *Calibration of low energy production of ^{36}Cl and the creation of an exposure age calculator*. M.S. Thesis, New Mexico Tech.

Balco, G. (2007). CRONUS-Earth 26 Al- 10 Be exposure age calculator MATLAB function reference Version 2.

Balco, G. (2011). What is a camel diagram anyway? http://cosmognosis.wordpress.com/2011/07/25/what-is-a-camel-diagram-anyway/.

Balco, G., Briner, J., Finkel, R. C., Rayburn, J. a., Ridge, J. C., and Schaefer, J. M. (2009). Regional beryllium-10 production rate calibration for late-glacial northeastern North America. *Quaternary Geochronology*, 4(2):93–107.

Balco, G., Stone, J. O., Lifton, N., and Dunai, T. J. (2008). A complete and easily accessibly means of calculating surface exposure ages or erosion rates from ^{10}Be and ^{26}Al measurements. *Quaternary Geochronology*, 3:174–195.

Ballantyne, C. (2003). A Scottish Sturzstrom: The Beinn Alligin Rock Avalanche, Wester Ross. *The Scottish Geographical Magazine*, 119(2):159–167.

Ballantyne, C. K. (1989). The Loch Lomond Readvance on the Isle of Skye , Scotland : glacier reconstruction and palaeoclimatic implications. *Journal of Quaternary Science*, 4(2):95–108.

Ballantyne, C. K. (2008). *After the Ice: Holocene Geomorphic Activity in the Scottish Highlands*, volume 124.

Ballantyne, C. K., Benn, D. I., Lowe, J. J., and Walker, M. J. C., editors (1991). *The Quaternary of the Isle of Skye: Field Guide*. Quaternary Research Association, Cambridge.

Ballantyne, C. K. and Stone, J. O. (2004). The Beinn Alligin rock avalanche , NW Scotland : cosmogenic 10 Be dating , interpretation and significance. *The Holocene*, 14(3):448–453.

Ballantyne, C. K., Stone, J. O., and Fifield, L. K. (1998). Cosmogenic Cl-36 dating of postglacial landsliding at The Storr, Isle of Skye, Scotland. *The Holocene*, 8(3):347–351.

Benn, D., Lowe, J. J., and Walker, M. J. C. (1992). Glacier response to climatic change during the Loch Lomond Stadial and early Flandrian : geomorphological and palynological evidence from the Isle of Skye , Scotland. *Journal of Quaternary Science*, 7(2):125–144.

Benson, L., Lund, S., Smoot, J., Rhode, D., Spencer, R., Verosub, K., Louderback, L., Johnson, C., Rye, R., and Negrini, R. (2011). The rise and fall of Lake Bonneville between 45 and 10.5 ka. *Quaternary International*, 235(1-2):57–69.

Benson, L., Madole, R., Landis, G., and Gosse, J. (2005). New data for Late Pleistocene Pinedale alpine glaciation from southwestern Colorado. *Quaternary Science Reviews*, 24(1-2):49–65.

Benson, L., Madole, R., Phillips, W., Landis, G., Thomas, T., and Kubik, P. (2004). The probable importance of snow and sediment shielding on cosmogenic ages of north-central Colorado Pinedale and pre-Pinedale moraines. *Quaternary Science Reviews*, 23(1-2):193–206.

Bevington, P. R. and Robinson, D. K. (1992). *Data Reduction and Error Analysis for the Physical Sciences*. McGraw-Hill, Inc., second edition.

Bierman, P., Gillespie, A. R., Caffee, M., and Elmore, D. (1995). Estimating erosion rates and exposure ages with ^{36}Cl produced by neutron activation. *Geochimica et Cosmochimica Acta*, 59(18):3779–3798.

Bierman, P. R. (1994). Using in situ produced cosmogenic isotopes to estimate rates of landscape evolution: A review from the geomorphic perspective. *Journal of Geophysical Research*, 99(B7):13885–13896.

Boggs, P. T., Byrd, R. H., and Schnabel, R. B. (1987). A stable and efficient algorithm for nonlinear orthogonal distance regression. *SIAM Journal on Scientific and Statistical Computing*, 8(6):1052–1078.

Borchers, B. and Stone, J. O. (2012). Calibration of cosmogenic nuclide spallation production rates. *Quaternary Geochronology*, CRONUS(In prep).

Bright, R. C. (1966). Pollen and seed stratigraphy of Swan Lake, southeastern Idaho: Its relation to regional vegetational history and to Lake Bonneville history. *Tebiwa, J. Idaho St. Univ. Mus.*, 9:1–47.

Briner, J. P. and Swanson, T. W. (1998). Using inherited cosmogenic ^{36}Cl to constrain glacial erosion rates of the Cordilleran ice sheet. *Geology*, 26(1):3–6.

Brooks, S. J. and Birks, H. J. B. (2000). Chironomid-inferred Late-glacial air temperatures at Whitrig Bog , southeast Scotland. *Journal of Quaternary Science*, 15(8):759–764.

Cas, R. A. F. and Wright, J. V. (1988). *Volcanic Successions: modern and ancient: A geological approach to processes, products and successions*. Unwin Hyman, London.

Cerling, T. E. (1990). Dating Geomorphic Surfaces Using Cosmogenic ^{3}He. *Quaternary Research*, 33:148–156.

Cerling, T. E. and Craig, H. (1994a). Cosmogenic ^{3}He production rates from 39°N to 46°N latitude, western USA and France. *Geochimica et Cosmochimica Acta*, 58:249–255.

Cerling, T. E. and Craig, H. (1994b). Geomorphology and in-situ cosmogenic isotopes. *Annual Review of Earth and Planetary Sciences*, 22:273–317.

Charalambus, S. (1971). Nuclear transmutation by negative stopped muons and the activity induced by the Cosmic-Ray muons. *Nuclear Physics*, A166:145–161.

Craig, G. Y., editor (1991). *Geology of Scotland*. The Geological Society, London, 3rd edition.

CRONUS (2005). Draft Sampling Issues and Protocols. Technical report.

Currey, D. R., Oviatt, C. G., and Plyler, G. B. (1983). Lake Bonneville stratigraphy, geomorphology, and isostatic deformation in west-central Utah. In *Geologic Excursions in Neotectonics and Engineering Geology in Utah*, pages 63–82. Utah Geol. Min. Surv. Spec. Stud., 62 edition.

Deer, W. A., Howie, R. A., and Zussman, J. (1974). *An introduction to the Rock Forming Minerals*. Longman Group Limited, London, 7th edition.

DeGrey, L., Miller, M., and Link, P. (2008). Lake Bonneville flood. http://geology.isu.edu/Digital_Geology_Idaho/Module14/mod14.htm.

Dep, L., Elmore, D., Fabryka-Martin, J. T., Masarik, J., and Reedy, R. (1994a). Production rate systematics of in-situ-produced cosmogenic nuclides in terrestrial rocks : Monte Carlo approach of investigating ^{35}Cl(n,γ)^{36}Cl. *Nuclear Instruments and Methods in Physics Research B*, 92:321–325.

Dep, L., Elmore, D., Lipshutz, M., Vogt, S., Phillips, F., and Zreda, M. G. (1994b). Depth dependence of cosmogenic neutron-captured-produced ^{36}Cl in a terrestrial rock. *Nuclear Instruments and Methods in Physics Research B*, 92:301–307.

Desilets, D. and Zreda, M. G. (2001). On scaling cosmogenic nuclide production rates for altitude and latitude using cosmic-ray measurements. *Earth and Planetary Science Letters*, 193:213–225.

Desilets, D. and Zreda, M. G. (2003). Spatial and temporal distribution of secondary cosmic-ray nucleon intensities and applications to in situ cosmogenic dating. *Earth and Planetary Science Letters*, 206:21–42.

Desilets, D., Zreda, M. G., Almasi, P. F., and Elmore, D. (2006a). Determination of cosmogenic ^{36}Cl in rocks by isotope dilution: innovations, validation and error propagation. *Chemical Geology*, 233:185–195.

Desilets, D., Zreda, M. G., and Prabu, T. (2006b). Extended scaling factors for in situ cosmogenic nuclides: New measurements at low latitude. *Earth and Planetary Science Letters*, 246:265–276.

Dorman, L. I., Valdes-Galicia, J. F., and Dorman, I. V. (1999). Numerical simulation and analytical description of solar neutron transport in the Earth's atmosphere. *Journal of Geophysical Research1*, 104:22417–22426.

Dunai, T. (2001a). Influence of secular variation of the geomagnetic field on production rates of in situ produced cosmogenic nuclides. *Earth and Planetary Science Letters*, 193:197–212.

Dunai, T. J. (2000). Scaling factors for production rates of in situ produced cosmogenic nuclides: a critical reevaluation. *Earth and Planetary Science Letters*, 176:157–169.

Dunai, T. J. (2001b). Reply to comment on 'Scaling factors for production rates of in situ produced cosmogenic nuclides: a critical reevaluation' by Darin Desilets, Marek Zreda, and Nathaniel Lifton. *Earth and Planetary Science Letters*, 188:289–298.

Dunai, T. J. (2010). *Cosmogenic Nuclides: Principles, Concepts and Applications in the Earth Surface Sciences*. Cambridge University Press.

Dunbar, N. W. (1999). Cosmogenic ^{36}Cl-determined age of the Carrizozo lava flows, south-central New Mexico. *New Mexico Geology*, 21(2):25–29.

Dunbar, N. W. and Phillips, F. (2004). Cosmogenic 36Cl ages of lava flows in the Zuni-Bandera volcanic field, north-central new mexico, U.S.A. *New Mexico Bureau of Geology & Mineral Resources*, Bulletin 160:309–318.

Dunne, A., Elmore, D., and Dep, L. (1996). A Server-based Code for In-Situ-Produced Nuclides that Incorporates Irregular Geometries. *Radiocarbon*, 38(1):25.

Dunne, J., Elmore, D., and Muzikar, P. (1999). Scaling factors for the rates of production of cosmogenic nuclides for geometric shielding and attenuation at depth on sloped surfaces. *Geomorphology*, 27:3–11.

Eidelman, S. (2004). Review of Particle Physics*1. *Physics Letters B*, 592(1-4):1–5.

Elmore, D., Fulton, B. R., Clover, M. R., Marsden, J. R., Gove, H. E., Naylor, H., Purser, K. H., Kilius, L. R., Beukens, R. P., and Litherland, A. E. (1979). Analysis of ^{36}Cl in environmental water samples using an electrostatic accelerator. *Nature*, 277:22–25.

Elmore, D. and Phillips, F. M. (1987). Accelerator mass spectrometry for measurement of long-lived radioisotopes. *Science*, 236(i):543–550.

Elsheimer, H. N. (1987). Application of an Ion-Selective Electrode Method to the Determination of Chloride in 41 International Geochemical Reference Materials. *Geostandards Newsletter*, 11(1):115–122.

Evans, J. M. (2001). *Calibration of the production rates of cosmogenic 36Cl from potassium*. PhD thesis, The Australian National University, Canberra. Doctorate of Philosophy.

Evans, J. M., Stone, J. O. H., Fifield, L. K., and Cresswell, R. G. (1997). Cosmogenic chlorine-36 production in K-feldspar. *Nuclear Instruments and Methods in Physics Research B*, 123:334–340.

Fabryka-Martin, J. (1988). *Production of radionuclides in the earth and their hydrogeologic significance, with emphasis on chlorine-36 and iodine-129*. PhD thesis, University of Arizona, Hydrology and Water Resources, Tucson. Doctor of Philosphy with a major in Hydrology.

Farber, D. L., Hancock, G. S., Finkel, R. C., and Rodbell, D. T. (2005). The age and extent of tropical alpine glaciation in the Cordillera Blanca, Peru. *Journal of Quaternary Science*, 20(7-8):759–776.

Farber, D. L., Mériaux, A.-S., and Finkel, R. C. (2008). Attenuation length for fast nucleon production of ^{10}Be derived from near-surface production profiles. *Earth and Planetary Science Letters*, 274(3-4):295–300.

Feige, Y., Oltman, B. G., and Kastner, J. (1968). Production Rates of Neutrons in Soils Due to Natural Radioactivity. *Journal of Geophysical Research*, 73(10):3135–3142.

Felton, A., Godsey, H. S., Jewell, P. W., Chan, M., and Currey, D. R. (2002). Depositional models for tufa development in Pleistocene Lake Bonneville, Utah. *Geological Society of America, 2002 annual meeting*, 34(6):368.

Felton, A., Jewell, P. W., Chan, M., and Currey, D. R. (2006). Controls on Tufa Development in Pleistocene Lake Bonneville, Utah. *Journal of Geology*, 114:377–389.

Fenton, C. R., Hermanns, R. L., Blikra, L. H., Kubik, P. W., Bryant, C., Niedermann, S., Meixner, A., and Goethals, M. M. (2011). Regional ^{10}Be production rate calibration for the past 12 ka deduced from the radiocarbon-dated Grøtlandsura and Russenes rock avalanches at 69°N, Norway. *Quaternary Geochronology*, 6(5):437–452.

Ford, T. D. and Pedley, H. M. (1996). A review of tufa and travertine deposits of the world. *Earth-Science Reviews*, 41:117–175.

Fretwell, P. T., Smith, D. E., and Harrison, S. (2008). The Last Glacial Maximum British Irish Ice Sheet: a reconstruction using digital terrain mapping. *Journal of Quaternary Science*, 23(3):241–248.

Gaisser, T. K. (1990). *Cosmic Rays and Particle Physics*. Cambridge University Press, Cambridge.

Gilbert, G. K. (1890). Lake Bonneville. *U.S. Geological Survey Monograph*, 1.

Godsey, H. S., Currey, D. R., and Chan, M. A. (2005). New evidence for an extended occupation of the Provo shoreline and implications for regional change, Pleistocene Lake Bonneville, Utah, USA. *Quaternary Research*, 63:212–223.

Godsey, H. S., Oviatt, C. G., Miller, D. M., and Chan, M. a. (2011). Stratigraphy and chronology of offshore to nearshore deposits associated with the Provo shoreline, Pleistocene Lake Bonneville, Utah. *Palaeogeography, Palaeoclimatology, Palaeoecology*, 310(3-4):442–450.

Goehring, B. M., Kelly, M. A., Schaefer, J. M., Finkel, R., and Lowell, T. V. (2010a). Dating of raised marine and lacustrine deposits in east Greenland using beryllium-10 depth profiles and implications for estimates of subglacial erosion. *Journal of Quaternary Science*, 26(6):865–874.

Goehring, B. M., Kurz, M. D., Balco, G., Schaefer, J. M., Licciardi, J., and Lifton, N. (2010b). A reevaluation of in situ cosmogenic ^{3}He production rates. *Quaternary Geochronology*, 5(4):410–418.

Goehring, B. M., Lohne, O. S., Mangerud, J., Svendsen, J. I., Gyllencreutz, R., Schaefer, J., and Finkel, R. (2011). Late Glacial and Holocene Beryllium-10 Production Rates for western Norway. *In Preparation*.

Goldhagen, P., Reginatto, M., Kniss, T., Wilson, J. W., Singleterry, R. C., Jones, I. W., and Steveninck, W. V. (2002). Measurement of the energy spectrum of cosmic-ray induced neutrons aboard an ER-2 high-altitude airplane. *Nuclear Instruments and Methods in Physics Research A*, 476:42–51.

Golledge, N. R. (2010). Glaciation of Scotland during the Younger Dryas stadial: a review. *Journal of Quaternary Science*, 25(4):550–566.

Goodman, A. Y., Rodbell, D. T., Seltzer, G. O., and Mark, B. G. (2001). Subdivision of Glacial Deposits in Southeastern Peru Based on Pedogenic Development and Radiometric Ages. *Quaternary Research*, 56:31–50.

Google (2008). Google earth. http://earth.google.com/.

Gosse, J. C. and Phillips, F. M. (2001). Terrestrial in situ cosmogenic nuclides: theory and application. *Quaternary Science Reviews*, 20:1475–1560.

Granger, D. (2001). Dating sediment burial with in situ-produced cosmogenic nuclides: theory, techniques, and limitations. *Earth and Planetary Science Letters*, 188:269–281.

Hallet, B. and Putkonen, J. (1994). Surface dating of dynamic landforms: Young boulders on aging moraines. *Science*, 265(5174):937–940.

Handwerger, D. A., Cerling, T. E., and Bruhn, R. L. (1999). Cosmogenic ^{14}C in carbonate rocks. *Geomorphology*, 27:13–24.

Heisinger, B., Lal, D., Jull, A. J. T., Kubik, P., Ivy-Ochs, S., Knie, K., and Nolte, E. (2002a). Production of selected cosmogenic radionuclides by muons: 2. capture of negative muons. *Earth and Planetary Science Letters*, 200:357–369.

Heisinger, B., Lal, D., Jull, A. J. T., Kubik, P., Ivy-Ochs, S., Neumaier, S., Knie, K., Lazarev, V., and Nolte, E. (2002b). Production of selected cosmogenic radionuclides by muons: 1. fast muons. *Earth and Planetary Science Letters*, 200:345–355.

Hendrick, L. and Edge, R. (1966). Cosmic-ray neutrons near the Earth. *Physical Review*, 145(4):1023–1025.

Hidy, A. J., Gosse, J. C., Pederson, J. L., Mattern, J. P., and Finkel, R. C. (2010). A geologically constrained Monte Carlo approach to modeling exposure ages from profiles of cosmogenic nuclides: An example from Lees Ferry, Arizona. *Geochemistry Geophysics Geosystems*, 11(September).

Hillas, A. M. (1972). *Cosmic Rays*. Pergamon Press, Oxford.

Idaho State University (2006). Digital Geology of Idaho. http://geology.isu.edu/nsf-isugeol/Modules/Module15/Module15.htm.

Ivy-Ochs, S., Kerschner, H., Reuther, A., Maisch, M., Sailer, R., Schaefer, J. M., Kubik, P. W., Synal, H.-A., and Schlüchter, C. (2006). The timing of glacier advances in the northern European Alps based on surface exposure dating with cosmogenic ^{10}Be, ^{26}Al, ^{36}Cl, and ^{21}Ne. *In Situ-Produced Cosmogenic Nuclides And Quantification of Geological Processes*, Geological:43–60.

Ivy-Ochs, S., Schäfer, J., Kubik, P. W., Synal, H.-A., and Schlüchter, C. (2004). Timing of deglaciation on the northern Alpine foreland (Switzerland). *Eclogae Geologicae Helvetiae*, 97:47–55.

Ivy-Ochs, S., Schlüchter, C., Kubik, P. W., Synal, H.-A., Beer, J., and Kerschner, H. (1996). The exposure age of an Egesen moraine at Julier Pass, Switzerland, measured with the cosmogenic radionuclides ^{10}Be, ^{26}Al ^{36}Cl. *Eclogae Geologicae Helvetiae*, 89(3):1049–1063.

Janecke, S. U. and Oaks, R. Q. (2011). New insights into the outlet conditions of late Pleistocene. *Geosphere*, 7(6):1369–1391.

Jull, A., Scott, E., and Marrero, S. (2011). The CRONUS-Earth inter-comparison for cosmogenic isotope analysis. In *The Twelfth International Conference on Accelerator Mass Spectrometry*, page 242.

Jull, A. and Scott, M. (2012). CRONUS-Earth Interlaboratory Comparison. *Quaternary Geochronology*, In prep.

Kållberg, P., Simmons, A., Uppala, S., and Fuentes, M. (2007). The ERA-40 archive. Technical Report 17, ECMWF.

Kelly, M. A., Lowell, T. V., Applegate, P. J., Smith, C. A., M, F., and Hudson, A. M. (2012). *Submitted*, (8).

Korte, M. and Constable, C. G. (2005). Continuous geomagnetic field models for the past 7 millennia: 2. CALS7K. *Geochemistry, Geophysics, Geosystems*, 6(2):Q02H16.

Krewedl, D. A. (1974). *Geology of the Central Magdalenda Mountains, Socorro County, New Mexico*. Doctor of Philosophy, University of Arizona, Tucson.

Kurz, M. D. (1986). Cosmogenic helium in a terrestrial igneous rock. *Nature*, 320(6061):435–439.

Laj, C., Kissel, C., Beer, J., Channell, J., Kent, D., Lowrie, W., and Meert, J. (2004). High resolution global paleointensity stack since 75 kyr (GLOPIS-75) calibrated to absolute values. *Timescales of the Geomagnetic Field*, pages 255–265.

Lal, D. (1958). *Investigations of Nuclear Interactions Produced by Cosmic Rays*. Phd, Bombay University.

Lal, D. (1988). In Situ-Produced Cosmogenic Isotopes in Terrestrial Rocks. *Ann. Rev. Earth Planet. Sci*, 16:355–388.

Lal, D. (1991). Cosmic ray labeling of erosion surfaces: In situ nuclide production rates and erosion models. *Earth and Planetary Science Letters*, 104:424–439.

Lambeck, K. (1993a). Glacial rebound of the British Isles - I. Preliminary model results. *Geophys. J. Int.*, 115:941–959.

Lambeck, K. (1993b). Glacial rebound of the british isles - II. a high-resolution, high-precision model. *Geophys. J. Int.*, 115:960–990.

Leya, I., Lange, H. J., Neumann, S., Wieler, R., and Michel, R. (2000). The production of cosmogenic nuclides in stony meteorites by galactic cosmic ray particles. *Meteorics & Planetary Science*, 35:259–286.

Licciardi, J. M., Denoncourt, C. L., and Finkel, R. (2008). Cosmogenic ^{36}Cl production rates from Ca spallation in Iceland. *Earth and Planetary Science Letters*, 267:365–377.

Licciardi, J. M., Kurz, M. D., and Curtice, J. M. (2006). Cosmogenic ^{3}He production rates from Holocene lava flows in Iceland. *Earth and Planetary Science Letters*, 246:251–264.

Lifton, N., Smart, D. F., and Shea, M. A. (2008). Scaling time-integrated in situ cosmogenic nuclide production rates using a continuous geomagnetic model. *Earth and Planetary Science Letters*, 268:190–201.

Lifton, N. A. (2005). Bonneville sampling plan.

Lifton, N. A. (2012). Lifton/Sato Scaling. *Quaternary Geochronology*, CRONUS:In prep.

Lifton, N. A., Bieber, J. W., Clem, J. M., Duldig, M. L., Evenson, P., Humble, J. E., and Pyle, R. (2005). Addressing solar modulation and long-term uncertainties in scaling in situ cosmogenic nuclide production rates. *Earth and Planetary Science Letters*, 239(1-2):140–161.

Lifton, N. A., Jull, A. J. T., and Quade, J. (2001). A new extraction technique and production rate estimate for in situ cosmogenic ^{14}C in quartz. *Geochimica et Cosmochimica Acta*, 65(12):1953–1969.

Light, A. (1996). *Amino acid paleotemperature reconstruction and radiocarbon shoreline chronology of the Lake Bonneville basin, USA*. M.S. Thesis, University of Colorado, Boulder, CO.

Liu, B., Phillips, F., Fabryka-Martin, J., Fowler, M. M., and Stone, W. D. (1994). Cosmogenic ^{36}Cl accumulation in unstable landforms 1. effects of the thermal neutron distribution. *Water Resources Research*, 30(11):3115–3125.

MacLeod, A., Palmer, A., Lowe, J. J., Rose, J., Bryant, C., and Merritt, J. (2010). Timing of glacier response to Younger Dryas climatic cooling in Scotland. *Global and Planetary Change*, 79:264–274.

Mark, B. and Seltzer, G. (2005). Evaluation of recent glacier recession in the Cordillera Blanca, Peru (AD 19621999): spatial distribution of mass loss and climatic forcing. *Quaternary Science Reviews*, 24:2265–2280.

Marrero, S. (2009). *Chlorine-36 Production Rate Calibration Using Shorelines from Pleistocene Lake Bonneville, UT*. PhD thesis, New Mexico Tech, Earth and Environmental Science, Socorro. Master of Science in Hydrology.

Masarik, J. (2002). Numerical simulation of in-situ produced cosmogenic nuclides. *Geochimica et Cosmochimica Acta*, 66:A491.

Masarik, J., Kim, K., and Reedy, R. (2007). Numerical simulations of in situ production of terrestrial cosmogenic nuclides. *Nuclear Instruments and Methods in Physics Research Section B: Beam Interactions with Materials and Atoms*, 259(1):642–645.

Masarik, J., Kollar, D., and Vanya, S. (2000). Numerical simulation of in situ production of cosmogenic nuclides: Effects of irradiation geometry. *Nuclear Instruments and Methods in Physics Research Section B: Beam Interactions with Materials and Atoms*, 172(1-4):786–789.

Masarik, J. and Wieler, R. (2003). Production rates of cosmogenic nuclides in boulders. *Earth and Planetary Science Letters*, 216:201–208.

McGee, D., Quade, J., Edwards, R. L., Broecker, W. S., and Cheng, H. (2012a). Lacustrine cave carbonates: novel archives of paleohydrologic change in the Bonneville Basin (Utah, USA). *Earth and Planetary Science Letters*, Submitted.

McGee, D., Quade, J., Edwards, R. L., Broecker, W. S., Cheng, H., and Steponaitis, E. (2012b). Lacustrine cave carbonates: novel, absolute-dated paleohydrologic archives in the Bonneville Basin (Utah, USA). In *Submitted Goldschmidt Abstract*.

Mercer, J. H. and Palacios, O. M. (1977). Geology Radiocarbon dating of the last glaciation in Peru. *Geology*, 5:600.

Miller, D. M., Oviatt, C. G., and McGeehin, J. P. (2011). A new look at the chronology for a classic Pleistocene lake: Lake Bonneville's Provo shoreline. In *Pacific Climate Workshop, March 6-9, Asilomar State Conference Grounds, Pacific Grove, CA*, Pacific Grove, CA.

Mughabghab, S. (2006). *Atlas of Neutron Resonances: Resonance parameters and thermal cross-sections Z=1-100*.

Muzikar, P., Elmore, D., and Granger, D. E. (2002). Accelerator mass spectrometry in geological research. *GSA Bulletin*.

Nishiizumi, K., Winterer, E. L., Kohl, C. P., Klein, J., Middleton, R., Lal, D., and Arnold, J. R. (1989). Cosmic ray production rates of ^{10}Be and ^{26}Al in quartz from glacially polished rocks. *Journal of Geophysical Research*, 94(B12):9.

Oerlemans, J. (2005). Extracting a climate signal from 169 glacier records. *Science*, 308:675–7.

Oviatt, C. G. (1991). Quaternary geology of the Black Rock Desert, Millard County, Utah. *Utah Geol. Min. Surv. Spec. Stud.*, 73.

Oviatt, C. G. (1997). Lake Bonneville fluctuations and global climate change. *Geology*, 25(2):155–158.

Oviatt, C. G., Currey, D. R., and Sack, D. (1992). Radiocarbon chronology of lake bonneville, eastern great basin, USA. *Palaeogeography, Palaeoclimatology, Palaeoecology*, 99:225–241.

Oviatt, C. G. and Miller, D. M. (2005). Lake bonneville: Overview and geomorphic considerations.

Oviatt, C. G. and Nash, W. P. (1989). Late Pleistocene basaltic ash and volcanic eruptions in the Bonneville basin, Utah. *Geological Society of America Bulletin*, 101:292–303.

Oviatt, C. G., Sack, D., and Felger, T. J. (1994). Quaternary geology of the northern Sevier Desert, Millard and Juab Counties, Utah. *Utah Geol. Min. Surv. Spec. Stud.*

Phillips, F., Leavy, B. D., Jannik, N. O., Elmore, D., and Kubik, P. W. (1986). The accumulation of cosmogenic chlorine-36 in rocks: a method for surface exposure dating. *Science*, 231:41–43.

Phillips, F., Stone, W. D., and Fabryka-Martin, J. (2001). An improved approach to calculating low-energy cosmic-ray neutron fluxes near the land/atmosphere interface. *Chemical Geology*, 175:689–701.

Phillips, F., Zreda, M. G., Flinsch, M. R., Elmore, D., and Sharma, P. (1996). A reevaluation of cosmogenic ^{36}Cl production rates in terrestrial rocks. *Geophysical Research Letters*, 23(9):949–952.

Phillips, F., Zreda, M. G., Gosse, J. C., Klein, J., Evenson, E. B., Hall, R. D., Chadwick, O. A., and Sharma, P. (1997). Cosmogenic ^{36}Cl and ^{10}Be ages of Quaternary glacial and fluvial deposits of the Wind River Range, Wyoming. *GSA Bulletin*, 109(11):1453–1463.

Phillips, F. M. (2011). A Report on Re-evaluation of Historic ^{10}Be and ^{26}Al Production-Rate Calibration Samples Collected in the Sierra Nevada, California, in 1986. https://www.ees.nmt.edu/cronus/media/site/samples/sierra/sierra-rpt29-06-11comp.pdf.

Phillips, F. M. and Hudson, A. M. (2012). Quelccaya Ice Cap, Peru.

Phillips, F. M. and Plummer, M. A. (1996). CHLOE: a program for interpreting in-situ cosmogenic nuclide data for surface exposure dating and erosion studies. *Radiocarbon (Abstr. 7th Int. Conf. Accelerator Mass Spectrometry)*, 38:98–99.

Phillips, F. M., Zreda, M. G., Plummer, M. A., Elmore, D., and Clark, D. (2009). Glacial geology and chronology of Bishop Creek and vicinity, eastern Sierra Nevada, California. *Geological Society of America Bulletin*, 121(7-8):1013–1033.

Pigati, J. S. and Lifton, N. (2004). Geomagnetic effects on time-integrated cosmogenic nuclide production with emphasis on in situ ^{14}C and ^{10}Be. *Earth and Planetary Science Letters*, 226:193–205.

Press, F. and Siever, R. (2001). *Understanding Earth*. W. H. Freeman and Company, third edition.

Rasmussen, S. O., Andersen, K. K., Svensson, a. M., Steffensen, J. P., Vinther, B. M., Clausen, H. B., Siggaard-Andersen, M.-L., Johnsen, S. J., Larsen, L. B., Dahl-Jensen, D., Bigler, M., Röthlisberger, R., Fischer, H., Goto-Azuma, K., Hansson, M. E., and Ruth, U. (2006). A new Greenland ice core chronology for the last glacial termination. *Journal of Geophysical Research*, 111(D06102).

Reedy, R. C. (2011). Cosmogenic-Nuclide Production Rates: Reaction Cross Section Update. *Nuclear Instruments and Methods in Physics Research Section B: Beam Interactions with Materials and Atoms*.

Rodbell, D. (2000). Rapid Ice Margin Fluctuations during the Younger Dryas in the Tropical Andes. *Quaternary Research*, 54:328–338.

Rodbell, D. T., Smith, J. A., and Mark, B. G. (2009). Glaciation in the Andes during the Lateglacial and Holocene. *Quaternary Science Reviews*, 28:2165–2212.

Rood, D. H., Burbank, D. W., and Finkel, R. C. (2011). Chronology of glaciations in the Sierra Nevada, California, from ^{10}Be surface exposure dating. *Quaternary Science Reviews*, 30(5-6):646–661.

Rubin, M. and Berthold, S. M. (1961). U.S. Geological Survey radiocarbon dates V. *Radiocarbon*, 3:86–98.

Sack, D. (1999). The Composite Nature of the Provo Level of Lake Bonneville, Great Basin, Western North America. *Quaternary Research*, 52:316–327.

Sato, T. and Niita, K. (2006). Analytical functions to predict cosmic-ray neutron spectra in the atmosphere. *Radiation Research*, 166:544–555.

Sato, T., Yasuda, H., Niita, K., Endo, A., and Sihver, L. (2008). Development of PARMA: PHITS-based analytical radiation model in the atmosphere. *Radiation Research*, 170:244–259.

Schimmelpfennig, I. (2009). *Cosmogenic ^{36}Cl in Ca and K rich minerals: analytical developments, production rate calibrations and cross calibration with ^{3}He and ^{21}Ne*. Doctorale, Universite Paul Cezanne Aix-Marseille III Cerege.

Schimmelpfennig, I., Benedetti, L., Finkel, R., Pik, R., Blard, P.-H., Bourlès, D., Burnard, P., and Williams, A. (2009). Sources of in-situ ^{36}Cl in basaltic rocks. Implications for calibration of production rates. *Quaternary Geochronology*, (6):441–461.

Schimmelpfennig, I., Benedetti, L., Pik, R., Burnard, P., Blard, P., Dunai, T. J., and Bourles, D. L. (2008). In situ cosmogenic ^{36}Cl production rate calibration from Ca and K in lava flows. *Goldschmidt Abstracts*.

Schimmelpfennig, I., Williams, A., Pik, R., Burnard, P., Niedermann, S., Finkel, R., Schneider, B., and Benedetti, L. (2011). Inter-comparison of cosmogenic in-situ ^{3}He, ^{21}Ne and ^{36}Cl at low latitude along an altitude transect on the SE slope of Kilimanjaro volcano (3°S, Tanzania). *Quaternary Geochronology*, 6(5):425–436.

Scott, W. E. (1988). Transgressive and high-shore deposits of the Bonneville lake cycle near North Salt Lake, Utah. *Utah Geol. Min. Surv. Misc. Publ.*, 88(1):38–42.

Shea, M. A. and Smart, D. F. (1983). A world grid of calculated cosmic ray vertical cutoff rigidities for 1980. *Proceedings from the 18th International Cosmic Ray Conference*, 3:415–418.

Slota, P. J., Jull, A. J. T., Linick, T. W., and Toolin, L. J. (1987). Preparation of small samples for ^{14}C accelerator targets by catalytic reduction of CO. *Radiocarbon*, 29(2):303–306.

Stone, J. (2000). Air pressure and cosmogenic isotope production. *Journal of Geophysical Research*, 105(B10):23753–23760.

Stone, J. O. (2005). Terrestrial chlorine-36 production from spallation of iron. In *10th International Conference on Accelerator Mass Spectrometry*, Berkeley, California.

Stone, J. O., Allan, G. L., Fifield, L. K., and Cresswell, R. G. (1996). Cosmogenic chlorine-36 from calcium spallation. *Geochimica et Cosmochimica Acta*, 60(4):679–692.

Stone, J. O. and Borchers, B. (2012). Calibration of muon parameters from depth profiles. *Quaternary Geochronology*, CRONUS(In prep).

Stone, J. O. H., Evans, J. M., Fifield, L. K., Allan, G. L., and Cresswell, R. G. (1998). Cosmogenic chlorine-36 production in calcite by muons. *Geochimica et Cosmochimica Acta*, 62(3):433–454.

Stuiver, M., Reimer, P. J., and Reimer, R. (2005). CALIB radiocarbon calibration.

Swanson, T. W. and Caffee, M. L. (2001). Determination of ^{36}Cl Production Rates Derived from the Well-Dated Deglaciation Surfaces of Whidbey and Fidalgo Islands, Washington. *Quaternary Research*, 56(3):366–382.

Theune, U. (2005). Ternary Plots.

Thomas, T. R. (2005). *A method for preparation of rock samples for measurement of 36Cl by isotope dilution accelerator mass spectrometry*. PhD thesis, New Mexico Tech, Earth and Environmental Science, Socorro. Master of Science in Geochemistry; Independent Study.

Thompson, L. G., Mosley-Thompson, E., and Arnao, B. M. (1984). El Niño-Southern Oscillation Events Recorded in the Stratigraphy of the Tropical Quelccaya Ice Cap, Peru. *Science*, 226:50–53.

Thompson, L. G., Mosley-Thompson, E., Bolzan, J. F., and Koci, B. R. (1985). A 1500-Year Record of Tropical Precipitation in Ice Cores from the Quelccaya Ice Cap, Peru. *Science*, 229:971–973.

Thompson, L. G., Mosley-Thompson, E., Brecher, H., Davis, M., Len, B., Les, D., Lin, P., Mashiotta, T., and Mountain, K. (2006). Abrupt tropical climate change: past and present. *Proceedings of the National Academy of Sciences of the United States of America*, 103:10536–43.

Trustees of Scottish Museums (2012). Scottish Geology. http://www.scottishgeology.com/geo/geology-of-scotland-map/.

Utah Geological Survey (2008). Where was Lake Bonneville, how large was it, and when did it exist? http://geology.utah.gov/online/PI-39/pi39pg01.htm.

Vermeesch, P. (2007). CosmoCalc : An Excel add-in for cosmogenic nuclide. *Terra*, page A1064.

von Egidy, T. and Hartmann, F. J. (1982). Average muonic coulomb capture probabilities for 65 elements. *Physical Review A*, 26(5):2355–2360.

Walker, M. J. C., Ballantyne, C. K., Lowe, J. J., and Sutherland, D. G. (1988). A reinterpretation f the Lateglacial environmental history of the Isle of Skye, Inner Hebrides, Scotland. *Journal of Quaternary Science*, 3(2):135–146.

Walker, M. J. C. and Lowe, J. J. (1990). Reconstructing the Environmental History of the Last Glacial-Interglacial Transition: Evidence from the Isle of Skye, Inner Hebrides, Scotland. *Quaternary Science Reviews*, 9:15–49.

Ziegler, L. B., Constable, C. G., Johnson, C. L., and Tauxe, L. (2011). PADM2M: a penalized maximum likelihood model of the 0-2 Ma paleomagnetic axial diple moment. *Geophys. J. Int., doi: 10.1111/j.1365-246X.2010.04905.x*.

Zreda, M., Desilets, D., Ferre, T. P. A., and Scott, R. L. (2008). Measuring soil moisture content non-invasively at intermediate spatial scale using cosmic-ray neutrons. *Geophysical Research Letters*, 35.

Zreda, M. G. and Phillips, F. (1994). Cosmogenic ^{36}Cl accumulation in unstable landforms 2. simulations and measurements on eroding moraines. *Water Resources Research*, 30(11):3127–3136.